DYNAMICS AND CONTROL OF MOBILE CRANES

A Thesis
Presented to
The Academic Faculty

by

Joshua Vaughan

In Partial Fulfillment
of the Requirements for the Degree
Doctor of Philosophy in the
George W. Woodruff School of Mechanical Engineering

Georgia Institute of Technology
August 2008

DYNAMICS AND CONTROL OF MOBILE CRANES

Approved by:

Dr. William Singhose , Advisor
George W. Woodruff School of
Mechanical Engineering
Georgia Institute of Technology

Dr. Kok-Meng Lee
George W. Woodruff School of
Mechanical Engineering
Georgia Institute of Technology

Dr. Rhett Mayor
George W. Woodruff School of
Mechanical Engineering
Georgia Institute of Technology

Dr. John-Paul Clarke
Daniel Guggenheim School of Aerospace
Engineering
Georgia Institute of Technology

Dr. Patricio Vela
The School of Electrical and Computer
Engineering
Georgia Institute of Technology

Date Approved: July 2nd, 2008

Wherever you are, I hope you're happy now…

ACKNOWLEDGEMENTS

I would like to begin by thanking those that have funded the pursuit of my Ph.D. here at Georgia Tech: *ME2110: Creative Decisions and Design*, the NSF funded STEP program here at Georgia Tech, the ASME Teaching Fellowship, and the Siemens Automation and Drives Fellowship. I would also like to thank the National Science Foundation for funding my research during a four month stay in Tokyo through the Doctoral Dissertation Enhancement Award.

I would like to also thank Dr. Singhose for his guidance and friendship during my time as a graduate student. I also would like to thank all of my labmates, both past and present, for being there to discuss ideas and for making this work fun. To the numerous undergraduate researchers that have worked with me throughout this process, thank you. You often brought a smile to my face when I needed it most. I would also like to thank the Hirose-Fukushima Laboratory at the Tokyo Institute of Technology for being such gracious hosts during my stay in Japan.

To my friends from Hampden-Sydney, you are like brothers to me. We have shared so much. Your support of me through this process should not be underestimated; you all have continued to be teammates long after our playing days have passed.

Finally, I would like to thank my mother, father, and brother for their unwavering support of this pursuit. There are not words to describe what you mean to me.

TABLE OF CONTENTS

LIST OF TABLES

LIST OF FIGURES

NOMENCLATURE

Efficiency of Insensitivity	The Insensitivity of a shaper divided by its normalized duration. Provides a measure of how efficiently a shaper provides Insensitivity.
EI Shaper	**Extra Insensitive Shaper** – An input shaper designed such that the vibration is below some tolerable level (typically 5% of the unshaped case) at the design frequency. Relaxing the vibration constraint from zero increases robustness.
GUI	**Graphical User Interface** – An interface used to control a system, characterized by its graphical nature (as opposed to a text only interfaces).
HME	**Average High-Mode Excitation** – The average of a shaper's sensitivity curve between two and ten times the design frequency.
Input Shaper	A series of impulses designed to create low vibration commands.
Input Shaping	A control method that dramatically reduces motion-induced oscillation by intelligently shaping the reference commands. A series of impulses, called an Input Shaper, is designed using estimates of system natural frequency and damping ratio. The convolution of the input shaper and the original command is then used to drive the system.
Insensitivity	A measure of shaper robustness. It is the width of the sensitivity curve at a given tolerable level of vibration.
I(x%)	The Insensitivity at a tolerable percentage vibration of x% ($V_{tol} = x\%$).
Lowpass Filter	A filter that passes a low frequency band with little modification while attenuating all frequencies above some value.
MI-xxx Shaper	**Multi-Input-xxx Shaper** – An input shaper designed to utilize multiple inputs. The remainder of the name is determined by the vibration and other constraints enforced (*i.e.* MI-ZV).
Multi-Input Vector Diagram	A vector diagram for use with multi-input shapers.
Negative Shaper	An input shaper that contains negative impulses. See UM-xxx and SNA-xxx shapers.

Normalized Duration The duration of an input shaper normalized by the system's period of vibration.

Notch Filter A filter that passes two bands (at high frequencies and low frequencies) with little modification, while attenuating within a stopband, located between the two pass bands. Also known as a band-stop filter.

Overshoot The amount by which a crane payload travels beyond the desired final position.

Overtravel The amount by which a crane trolley travels beyond the desired final position.

Percentage Vibration A measure of the effectiveness of an input shaper. It is the vibration the input shaper will cause normalized by the vibration from a unity magnitude impulse applied at time zero, expressed as a percentage.

PLC **Programmable Logic Controller** – A computer used in automation systems, with inputs and outputs to facilitate sensing and actuation.

Robustness A command's ability to suppress vibration as system parameters vary.

RPL Shaper **Reduced Perceived Lag Shaper** – Input shaping method that improves command rise time over traditional input shaping techniques, reducing the perceived lag caused by using input shaping.

Sensitivity Curve A plot of the percentage vibration caused by an input shaper as system parameters vary from that for which the shaper was designed. It provides a qualitative picture of the robustness of the shaper.

SI Shaper **Specified Insensitivity Shaper** – Input shapers whose Insensitivity is specified as part of the design process. SI shapers are solved via an optimization routine. They provide the shortest duration shaper for given Insensitivity and impulse amplitude requirements.

SI-ZO Shaper **Specified Insensitivity-Zero Overtravel Shaper** – An input shaper that reduces the amount of input shaper induced overtravel to that of the unshaped case, while enforcing specified insensitivity (SI) vibration constraints.

SNA-xxx Shaper — **Specified Negative Amplitude-xxx Shaper** – Input shapers that are designed with impulses alternating between positive values and some specified negative amplitude. The remainder of the name is determined by the vibration constraints enforced (*i.e.* SNA-SI).

SNA(A_{max}) — A Specified Negative Amplitude-Specified Insensitivity (SNA-SI) input shaper with maximum negative amplitude of A_{max}.

Three-Hump EI Shaper — **Three-Hump Extra Insensitive Shaper** – Similar to the Two-Hump EI, but with three humps in its sensitivity curve leading to higher Insensitivity.

Two-Hump EI Shaper — **Two-Hump Extra Insensitive Shaper** – A robust shaper with two humps in its sensitivity curve. It's development followed that of the EI with similar design principles, hence the name.

UM-xxx Shaper — **Unity Magnitude-xxx Shaper** – Input shapers that employ only unity magnitude impulses (± 1), alternating in sign. The remainder of the name is determined by the vibration constraints enforced (*i.e.* UM-ZV).

Vector Diagram — An input shaper design and analysis tool that plots shaper impulses in the phase plane. The summation of the impulses is proportion to the vibration that the impulse sequence will excite.

VNC — **Virtual Network Computing** – A framework to allow a remote user to control a PC via an Internet connection.

V_{tol} — The tolerable amount of vibration that may be induced by an input shaper. Typically represented as a percentage of the unshaped case.

ZV Shaper — **Zero Vibration Shaper** – Input shaper designed with the constraint that there is zero vibration at the design frequency. No robustness constraints are included.

ZV-ZO Shaper — **Zero Vibration-Zero Overtravel Shaper** - An input shaper that reduces the amount of input shaper induced overtravel to that of the unshaped case, while enforcing zero vibration (ZV) constraints.

ZVD Shaper — **Zero Vibration and Derivative Shaper** – An input shaper designed with the constraint that there is zero vibration at the design frequency. An additional constraint that the derivative of the vibration constraint is zero at the design frequency is also enforced to promote robustness.

ZVDD Shaper

Zero Vibration and Double Derivative Shaper – Similar to the ZVD shaper but with two derivative constraints. It is designed with constraints that there is zero vibration at the design frequency and that the first and second derivatives of the vibration equation are zero at the design frequency.

ZVDDD Shaper

Zero Vibration and Triple Derivative Shaper – Similar to the ZVD shaper but with three derivative constraints. It is designed with constraints that there is zero vibration at the design frequency and that the first, second, and third derivatives of the vibration equation are zero at the design frequency.

SUMMARY

The rapid movement of machines is a challenging control problem because it often results in high levels of vibration. As a result, flexible machines are typically moved relatively slowly to avoid such vibration. Therefore, motion-induced vibration limits the operational speed of the system. Input shaping is one method that eliminates motion-induced vibrations by intelligently designing the reference command such that system vibration is cancelled. It has been successfully implemented on a number of systems, including bridge and tower cranes. The implementation of input shaping on cranes provides a substantial increase in the operational efficiency. Unfortunately, most cranes, once erected, have limited or no base mobility. This limits their workspace. The addition of base mobility could help extend the operational effectiveness of cranes and may also expand crane functionality. Mobile cranes may also be better suited for use in harsh and/or distant environments. Teleoperation of oscillatory systems, such as cranes, then becomes another avenue for advancement of crane functionality.

Base mobility in cranes presents both additional control challenges and operational opportunities. A crane with base mobility is redundantly actuated (overactuated), such that multiple combinations of actuators can be used to move a payload from one location to another. This opens the possibility for the selection of a combination of actuation that provides both rapid motion and limited system vibration. The extension of input shaping into this operational domain will provide a method to maximize effective actuation combinations.

Toward addressing these issues, new multi-input shaping methods were developed and applied to a mobile, portable tower crane. During this development, a firm understanding of robust input shaping techniques and the compromises inherent to input shaper design was

formed. In addition, input shaping was compared to other command generation techniques, namely lowpass and notch filtering, and proven to be superior for vibration reduction in mechanical systems. Another, new class of input shapers was also introduced that limit the input shaper induced overshoot in human operated systems. Finally, a series of crane operator studies investigated the application of input shaping techniques to teleoperated cranes. These studies suggested that input shaping is able to dramatically improve remote crane operator performance.

CHAPTER I

INTRODUCTION

Cranes are used to transport heavy loads at construction sites, shipyards, factories, and warehouses throughout the world. All cranes use vertical suspension cables to support the payload, thereby creating the possibility of pendulum-like payload oscillation. To date, the primary method utilized to limit this motion-induced vibration has been to train a skilled operator and to move slowly. While this does serve to reduce payload oscillation and, thereby, increase safety, it does not provide the most efficient operating condition.

Another major drawback of cranes is that they are often difficult and slow to deploy. This fact, when coupled with the limited (or nonexistent) mobility of most cranes, increases construction costs by the time spent moving cranes or leasing additional cranes. A crane with a mobile base could help alleviate this problem, in addition to expanding crane functionality. For example, a rapidly-deployable mobile crane could greatly aid first responders at a disaster scene. Mobile cranes may also be well suited for use in harsh and/or distant environments. Teleoperation of oscillatory systems, such as cranes, then becomes another avenue for advancement of crane functionality.

The addition of base mobility to cranes introduces additional control challenges. Base motion will excite the oscillatory modes of the system. However, the addition of base motion also presents additional control opportunities. A mobile crane will have redundant actuation; multiple combinations of actuators can be used to move the payload from one location to another. Hence, there exists the opportunity to choose a combination of actuation that provides rapid motion and results in low levels of system oscillation. Combinations of actuation could also be chosen to increase the robustness of the control system.

1.1 Research Goals and Methods

The most general goal of this thesis is to advance the state of the art in the control of vibratory systems. The specific application for which the majority of the work is tailored is cranes. Cranes make an excellent application for research for several reasons. The first is the vast number of cranes worldwide, all of which are suseptable to pendulum-like payload oscillations. The ubiquity of cranes and propensity to oscillate also cause cranes to be the bottleneck in many factories, shipyards, and construction sites. As a result, improving the control and efficiency of these cranes will have enormous economic impact. In addition, cranes make an excellent research platform. Crane payload oscillation is easily observable, and reductions in oscillation are equally observable.

Throughout this thesis great importance is placed on the applicability and practically of the methods presented. Where possible experimental trials were conducted with one of the cranes described in Appendix A to verify theoretical predictions. Also, great weight is given to the human interaction with the proposed methods, as almost all cranes are driven by human operators. Methods that are not compatible with human operators are practically useless for cranes.

1.2 Thesis Contributions

This thesis makes significant advancements in crane control, with particular emphasis on mobile cranes. Major contributions include:

- **Dynamic Analysis of Mobile Cranes** – Chapter 5

  The dynamics of a mobile tower crane and a tower crane with double-pendulum payload dynamics are presented. The primary dynamic properties of each are discussed.

- **Methods to design of multi-input shaped commands** – Chapter 6

  Multi-Input shapers create multiple inputs to achieve performance that is not possible with a single input. Multi-input shaping design procedures are introduced that result

in shapers that use secondary actuators to reduce vibration, increase robustness, and speed system motion.

- **Methods to decrease the input shaper overtravel in human operated systems** – Chapter 7

  Traditional input shaping techniques increase the duration of an operator's command. To accurately position an input shaped system, a human operator must estimate the distance the system will travel as a result of this increased command duration. A new class of input shapers is designed to limit the overtravel.

- **A comparison of command filtering methods for vibration reduction via command generation in mechanical systems** – Chapter 4

  Digital filtering and input shaping are both well-known methods for shaping the reference commands for flexible systems. This thesis presents a comparison of digital filters and input shaping, showing that input shaping is the superior approach for vibration reduction in mechanical systems.

- **A new input shaper design method providing a continuous spectrum of solutions for optimizing the robustness, duration, and high-mode excitation compromise inherent in shaper design** – Chapter 3

  There is a fundamental compromise in input shaper design between robustness, shaper duration, and possible high-mode excitation. A new Specified Negative Amplitude-Specified Insensitivity (SNA-SI) shaper is developed to provide the shortest duration shaper for a given Insensitivity and maximum negative impulse amplitude.

1.3 Dissertation Outline

This thesis is organized as follows. Chapter 2 will present a review of cranes, crane control strategies, and input shaping. More specific background information will be included as needed in later chapters.

Chapter 3 presents an in depth evaluation of robust shaping techniques, with special attention to design compromises inherent to input shaping. The evaluation includes both positive and negative input shapers. In addition, a new Specified Negative Amplitude-Specified Insensitivity (SNA-SI) input shaper is introduced.

Chapter 4 presents a comparison of traditional filtering techniques and input shaping for vibration suppression via command generation in mechanical systems. The chapter includes a proof of input shaper superiority and numerous supporting examples, including experimental results.

In Chapter 5, a mathematical model for a mobile tower crane is introduced and evaluated. In addition, a model for a tower crane with double pendulum payload dynamics is developed, analyzed, and experimentally validated. These models are used in simulations in subsequent chapters.

Chapter 6 outlines methods to design multi-input shapers. These multi-input shapers designed allow rapid system motion with low levels of vibration. Methods are presented that account for actuator limits and the contribution of each input to the oscillatory modes of the system. In addition, it is shown that secondary inputs can be used to increase a single input shaper's robustness to parameter changes. Simulations and experiments from a mobile tower crane are used as example cases to demonstrate the methods.

Input shapers that are designed to reduce overshoot in human-operated systems are presented in Chapter 7. In this chapter, equations governing the overshoot induced by shaped commands are developed and experimentally validated. These equations lead to a new constraint that can be included in input shaper formulations, leading to a new class of Zero Overshoot (ZO) input shapers. These new shapers are also experimentally verified.

In Chapter 8, a series of operator studies into the teleoperation of flexible systems, namely cranes, are conducted. The chapter examines the important factors that influence an operator's ability to effectively control a remotely operated crane.

Finally, Chapter 9 presents thesis conclusions, contributions, and a brief summary of

future work.

Detailed specifications for the three cranes used as experimental setups throughout the thesis can be found in Appendix A.

CHAPTER II

BACKGROUND

CHAPTER SUMMARY: *This chapter will provide necessary background information to properly frame the remainder of the thesis. Because cranes are the primary application of the research, an overview of the types of cranes and the associated problems of each is discussed in Section 2.1. Section 2.2 will briefly review the literature on the proposed solutions to these problems. Section 2.3 will present a more detailed overview of a particular solution, input shaping. This method will also serve as the basis for a large portion of the work completed in this thesis.*

2.1 Crane Types and Problems

Cranes can roughly be divided into three categories based upon their primary dynamic properties and the coordinate system that most naturally describes the location of the suspension cable connection point. The first category, bridge cranes , operate in cartesian space, as shown in Figure 1. The trolley moves along a bridge, whose motion is perpendicular to that of the trolley. Bridge cranes that travel on a mobile base are often called gantry cranes. Bridge cranes are common in factories, warehouses, and at shipyards.

The second major category of cranes is boom cranes, shown in Figure 2. Boom cranes are naturally described in spherical coordinates, where a boom rotates about axes both perpendicular and parallel to the ground. In the figure, ψ is the rotation about the vertical Z axis, and θ is the rotation about the Y axis. The payload is supported from a suspension cable at the end of the boom. Boom cranes have the primary advantage of supporting

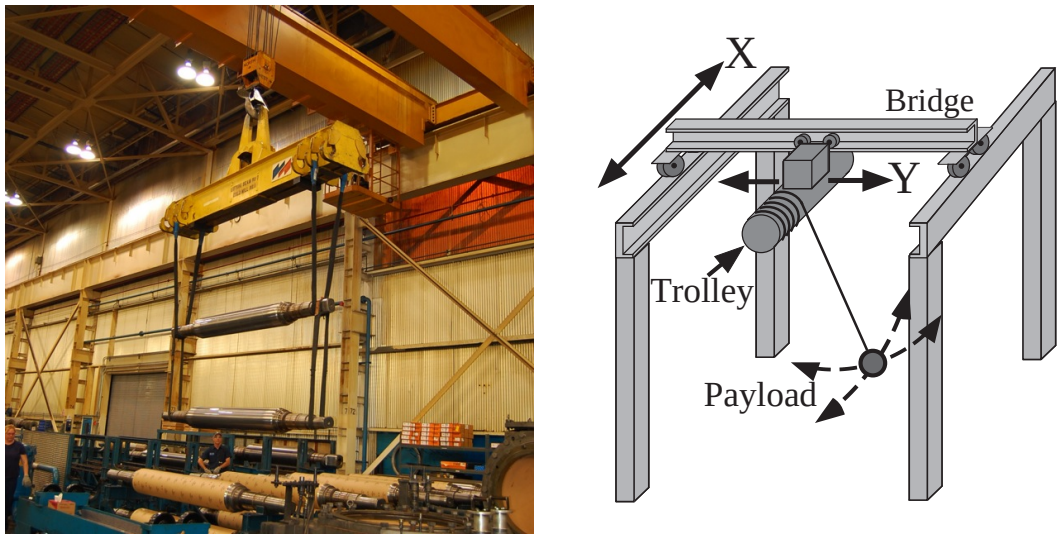

(a) Bridge Crane at Logan Aluminum in Kentucky **(b)** Bridge Crane Sketch

Figure 1: Bridge Cranes

loads in compression. As a result, they are typically more compact than bridge or tower cranes with similar load carrying capacities. Boom cranes are commonly found at building construction sites. Their compact nature also lends well to being mounted on a mobile base. Boom cranes are often mounted on trucks, tracked vehicles, and ships.

The third major category of cranes is tower cranes, like the ones shown in Figure 3. Tower cranes are most naturally described by cylindrical coordinates. A horizontal jib arm rotates around a vertical tower. The payload is supported by a cable from the trolley, which moves radially along the jib arm. Tower cranes are commonly used in the construction of multi-story buildings and have the advantage of having a small footprint-to-workspace ratio. Primary disadvantages of tower and boom cranes, from a control design viewpoint, are the nonlinear dynamics due to the rotational nature of the cranes, in addition to the less intuitive natural coordinate systems for human operators.

A common characteristic among all cranes is that the payload is supported via an overhead suspension cable. While this provides the basic functionality of the crane, it also presents several challenges, the primary of which is payload oscillation. Motion of the crane will often translate to large payload oscillations. These payload oscillations have

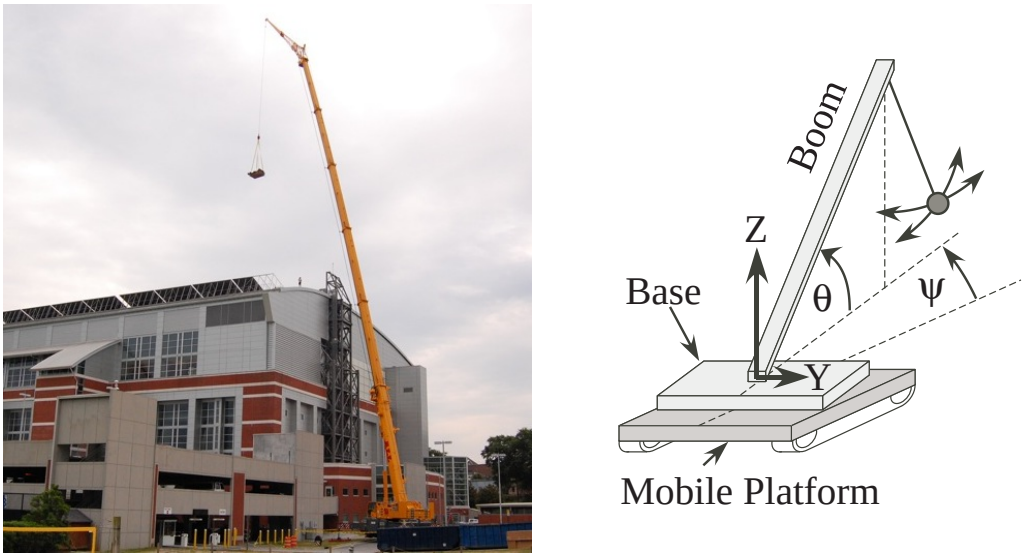

(a) Boom Crane near the CRC at Georgia Tech **(b)** Boom Crane Sketch

Figure 2: Boom Cranes

many detrimental effects including the degradation of payload positioning accuracy, increased task completion time, and decreased safety. Significant research effort has been made into reducing oscillations.

2.2 Crane Control Methods

Crane control is mature research area, with a diversity of published control techniques. An thorough overview of these efforts in crane control, as well as dynamic crane models, is provided in [1]. Crane control methods can divided (as most control can) into open and closed-loop methods. For crane control, the open loop methods can be further divided into optimal trajectory planning and command shaping.

Closed-loop crane controllers use information about the current state of the system (*e.g.* payload swing angle, trolley position, etc.) to generate commands that drive the system toward the desired state. Hazlerigg was one of the first to propose this method [17]. Since then, many researchers have advocated feedback methods for crane control, with proposed solutions ranging from state feedback [49, 90] to learning controllers [13] to wave-based approaches [38]. One primary disadvantage of these methods is that the current state of

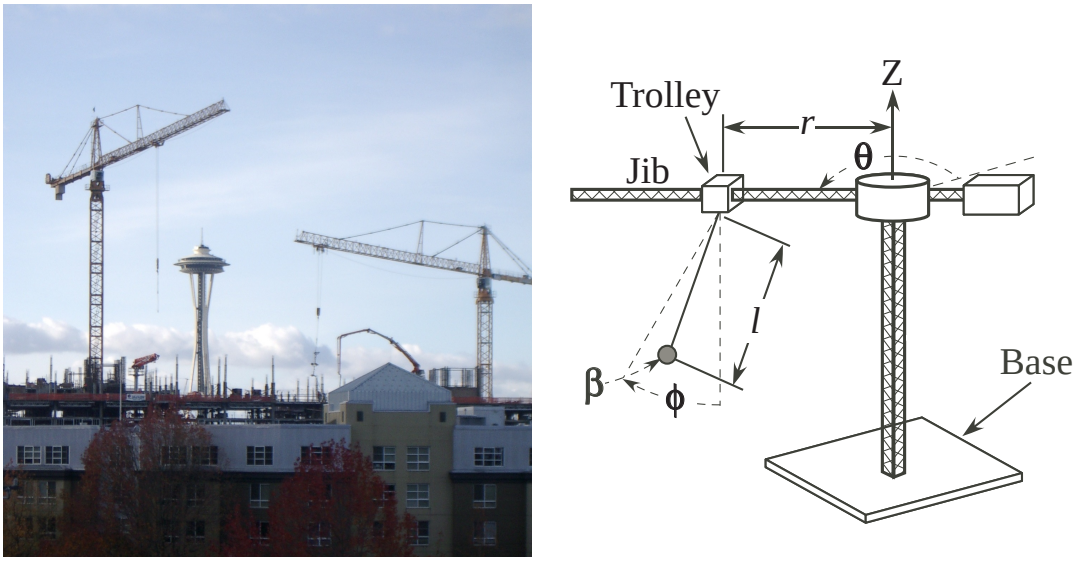

(a) Two Tower Cranes in Seattle, Washington **(b)** Tower Crane Sketch

Figure 3: Tower Cranes

the system must be well known. In practice, this is often difficult to achieve. Of particular difficulty is sensing the hook and payload position.

Optimal trajectory planning methods seek to eliminate vibration, while avoiding the sensing problems of closed-loop methods, by using pre-planned trajectories to move the crane through the workspace. The problem is typically formulated as a minimum time optimization problem, subject to vibration constraints [15, 25]. The primary restriction of this method is that the desired motion of the crane must be known in advance, in addition to the initial conditions of the maneuver. Another major drawback is that generating the optimal profiles can become computationally expensive.

Input shaping is another open loop technique. Unlike optimal trajectory generation, input shaping can be applied in real time. It has been successfully applied to a number of cranes [84, 56, 45, 22, 69, 75, 83]. Input shaping has been implemented on several large bridge cranes at nuclear facilities [56], a 10-ton crane at Georgia Tech [82, 83], tower cranes [44, 7, 30], as well as several portable cranes [29, 30, 85]. A technique similar to input shaping was also successfully tested on a boom crane [45]. Input shaping has also been shown to improve crane operator performance [22, 23]. The next section will present

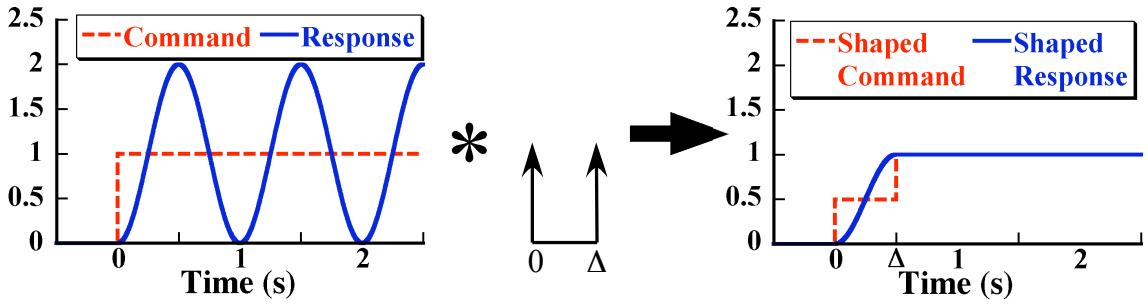

Figure 4: The Input Shaping Process

a more detailed description of input shaping, the primary crane control method covered in this thesis.

2.3 Input Shaping Review

Input Shaping [79, 58] is a control method that dramatically reduces motion-induced payload oscillation by intelligently shaping the reference commands. Using estimates of system natural frequencies and damping ratios, a series of impulses, called the input shaper, is designed. The convolution of the input shaper and the original command is then used to drive the system. This process is demonstrated with a two-impulse input shaper and a step command in Figure 4. Notice that, even though the settling time is drastically reduced, the command rise time is increased by the duration of the impulse sequence. The effects of this increase in command duration are a central topic of this thesis.

2.3.1 General Input Shaping Constraints

In order to determine the impulse amplitudes and time locations of an input shaper, the designer must ensure that they satisfy certain design constraints. The primary design constraint is a limit on the amplitude of vibration caused by the shaper. The vibration amplitude of an underdamped, second-order system from a sequence of n-impulses is:

$$A_{\Sigma} = \frac{\omega}{\sqrt{1-\zeta^2}} e^{-\zeta\omega t_n} \sqrt{\left(\sum_{i=1}^{n} A_i e^{\zeta\omega t_i} \cos(\omega t_i \sqrt{1-\zeta^2}\right)^2 + \left(\sum_{i=1}^{n} A_i e^{\zeta\omega t_i} \sin(\omega t_i \sqrt{1-\zeta^2}\right)^2} \quad (1)$$

where ω is the natural frequency of the system, ζ is the damping ratio, and A_i and t_i are the i^{th}-impulse amplitude and time, respectively.

To form a nondimensional vibration amplitude, (1) is divided by the amplitude of residual vibration from a single impulse of unity magnitude at time zero. The resulting expression gives the ratio of vibration with input shaping to that without input shaping. The amplitude of residual vibration from a single unity-magnitude impulse applied at time zero is simply:

$$A_{\uparrow} = \frac{\omega}{\sqrt{1-\zeta^2}} \tag{2}$$

Dividing (1) by (2) yields the percentage residual vibration (*PRV*) [58, 26]:

$$PRV = V(\omega,\zeta) = \frac{A_{\Sigma}}{A_{\uparrow}} = e^{-\zeta\omega t_n}\sqrt{[C(\omega,\zeta)]^2 + [S(\omega,\zeta)]^2} \tag{3}$$

where,

$$C(\omega,\zeta) = \sum_{i=1}^{n} A_i e^{\zeta\omega t_i}\cos(\omega t_i\sqrt{1-\zeta^2}) \tag{4}$$

$$S(\omega,\zeta) = \sum_{i=1}^{n} A_i e^{\zeta\omega t_i}\sin(\omega t_i\sqrt{1-\zeta^2}) \tag{5}$$

Equation (3) represents the level of vibration induced by an impulse sequence given any value of frequency and any damping ratio less than one. A constraint on residual vibration amplitude can be formed by setting (3) less than or equal to a tolerable level of residual vibration, V_{tol}, at the modeled natural frequency and damping ratio. This can be expressed as:

$$V(\omega,\zeta) \leq V_{tol} \tag{6}$$

Given the transcendental nature of (6) there are an infinite number of solutions. Additional constraints must be imposed to reach a solution. To ensure the fastest solution possible, the time of the last impulse is typically minimized:

$$\min(t_n) \tag{7}$$

Impulses amplitudes are also limited to sum to one, which ensures the shaped command reaches the same set-point as the unshaped command. This constraint is expressed as:

$$\sum_{i=1}^{n} A_i = 1 \tag{8}$$

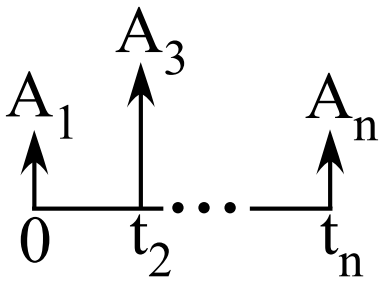

Figure 5: Positive Input Shaper

Additional constraints on impulse amplitude are still required, as those listed thus far will drive impulse amplitudes toward positive and negative infinity.

2.3.1.1 Positive Input Shapers

One impulse amplitude constraint is to limit impulses to having positive amplitude. This results in input shapers that have impulse amplitudes between zero and one, which are typically referred to as positive shapers. A positive input shaper will look similar to the impulse sequence shown in Figure 5. For example, if the above amplitude constraints are applied, while limiting (6) to zero at the design frequency the Zero Vibration (ZV) shaper results [79]. It has the form:

$$ZV = \begin{bmatrix} A_i \\ t_i \end{bmatrix} = \begin{bmatrix} \frac{1}{1+K} & \frac{K}{1+K} \\ 0 & \frac{\tau_d}{2} \end{bmatrix}, \tag{9}$$

where τ_d is the damped oscillation period and

$$K = e^{\frac{-\zeta\pi}{\sqrt{1-\zeta^2}}} \tag{10}$$

2.3.1.2 Negative Input Shapers

The formulation of the ZV shaper above (and all positive shapers) relies upon constraining impulses to have positive ampliutde. If negative impulse amplitude are allowed, there are two primary methods to constrain impulse amplitudes: Unity Magnitude (UM) and Specified Negative Amplitude (SNA). Allowing negative impulses has the primary advantage of decreasing the duration of the input shaper, speeding system response.

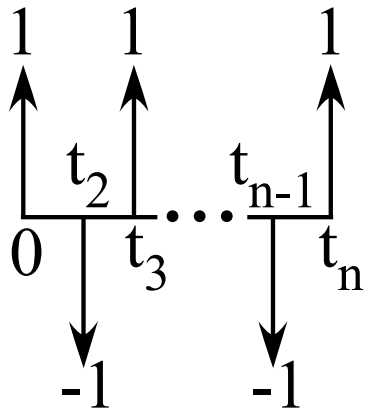

Figure 6: Unity Magnitude Input Shaper

For Unity Magnitude input shapers, the impulse amplitudes are constrained to be ±1 [41, 74]. A unity magnitude shaper will be follow the form of the one shown in Figure 6. The impulse amplitude constraints for UM shapers can be expressed as a combination of (8) and:

$$A_i = (-1)^{i+1} \quad i = 1, \ldots, n \tag{11}$$

where n is the number of impulses contained in the shaper. Additional constraints determine the full name of the shaper. For example, a UM shaper designed for zero vibration at the design frequency, analogous to the ZV shaper shown in (9), is called the UM-ZV Shaper. For undamped systems, it has the form:

$$\begin{bmatrix} A_i \\ t_i \end{bmatrix} = \begin{bmatrix} 1 & -1 & 1 \\ 0 & \frac{\tau}{6} & \frac{\tau}{3} \end{bmatrix} \tag{12}$$

where τ is the vibration period of the system. For a system with viscous damping, the impulse time locations become a function of damping ratio. Table 1 describes the UM-ZV shaper impulse times as a function of system damping.

Another method to remove the positive amplitude constraint is to specify the maximum negative impulse amplitude the input shaper may contain. This constraint can be stated as:

$$0 < A_i \leq 1 \qquad \text{when } i \text{ is odd} \tag{13}$$

$$A_i = -A_{max} \qquad \text{when } i \text{ is even} \tag{14}$$

Table 1: UM-ZV Shaper for Damped Systems
$t_i = (M_0 + M_1\zeta + M_2\zeta^2 + M_3\zeta^3)\tau,\ \tau = \frac{2\pi}{\omega}$

A_i	t_i	M_0	M_1	M_2	M_3
1	t_1	0	0	0	0
-1	t_2	0.16724	0.27242	0.20345	0
1	t_3	0.33323	0.00533	0.17914	0.20125

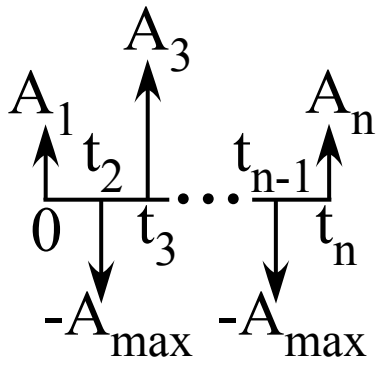

Figure 7: Specified Negative Amplitude Input Shaper

where A_{max} is the maximum negative amplitude allowed. Shapers formed using this amplitude constraint are called Specified Negative Amplitude (SNA) shapers [63] and follow a form similar to that shown in Figure 7. SNA shapers are also named according to the additional constraints used to form them. The SNA-ZV shaper is formed using the zero vibration constraint, analogous to the ZV shaper. For undamped systems, its form is given by:

$$\begin{bmatrix} A_i \\ t_i \end{bmatrix} = \begin{bmatrix} A_1 & -A_{max} & A_3 \\ 0 & \frac{1}{\omega}\cos^{-1}\left(\frac{A_{max}}{2A_1}\right) & \frac{1}{\omega}\cos^{-1}\left(\frac{A_{max}^2}{2A_1^2} - 1\right) \end{bmatrix} \tag{15}$$

where

$$A_1 = A_3 = \frac{1 + A_{max}}{2} \tag{16}$$

2.3.2 Input Shaper Design and Anaysis Tools

2.3.2.1 Vector Diagrams

Due to the nonlinear nature of the constraints used to form input shapers, finding a soluion can be difficult. One tool that seeks to simplify the task is the vector diagram [72]. The vector diagram represents the vibration caused by an impulse as a vector. The vibration

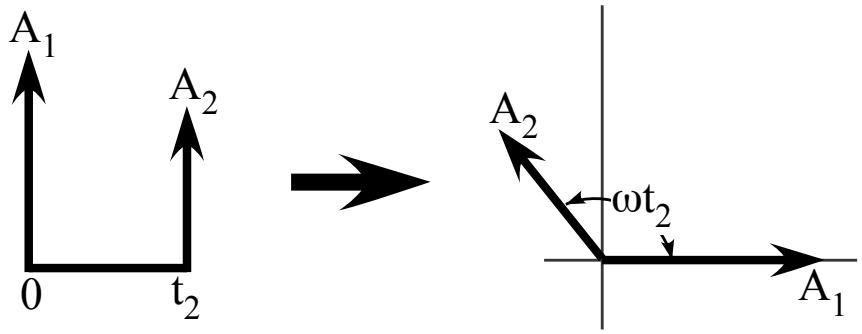

Figure 8: Plotting Impulses on a Vector Diagram

induced by an impulse sequence is represented by the sum of the sequence's representative vectors. The vector diagram can serve as both an input shaper analysis tool, as well as, an input shaper design tool.

The process of plotting an impulse sequence on a vector diagram is shown in Figure 8. Each impulse is plotted on the vector diagram in polar coordinates. The magnitude of each vector on the plot is simply the impulse magnitude. The angle of the vector is:

$$\theta = \omega t_i \tag{17}$$

where ω is the system frequency. The time of the first impulse is always zero, so the resulting angle is zero as well.

To calculate the residual vibration caused by a sequence of impulses, the representative vectors are summed, as shown in Figure 9. The magnitude of the resultant vector, A_R, is proportional to the magnitude of the residual vibration caused by the sequence. The angle of the resultant is equivalent to the phase shift relative to vibration from a single impulse at time zero. For shapers with larger number of impulses, the process is simply expanded to include the entire sequence. This process is demonstrated for a three impulse input shaper in Figure 10. When used in this manner, the vector diagram serves as a tool to analyze the effectiveness of an impulse sequence at suppressing vibration.

The vector diagram can also be used as an input shaper design tool. For example, a third vector can be added to the sequence plotted in Figure 9 to produce zero vibration.

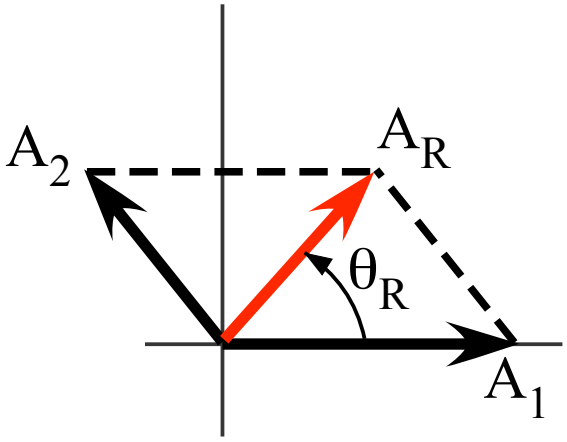

Figure 9: Resultant Vibration Vector from Adding Impulses

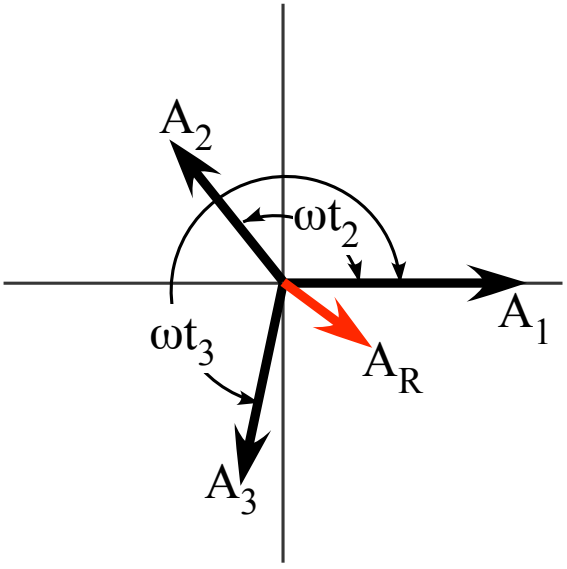

Figure 10: Vector Diagram for Three Impulse Sequence

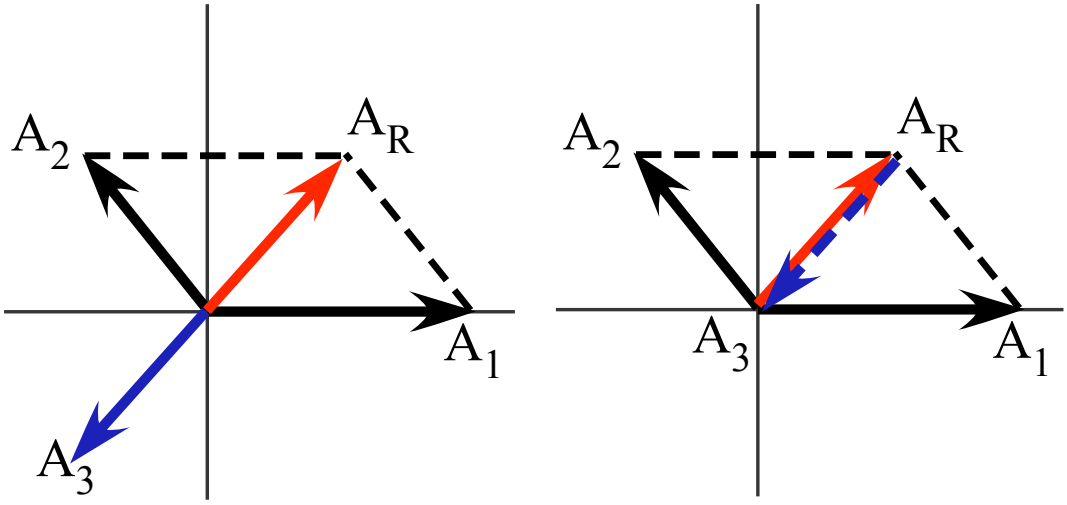

(a) Adding a Positive Impulse **(b)** Adding a Negative Impulse

Figure 11: Designing Input Shapers Using Vector Diagrams

This third vector, A_3, should be placed opposite of A_R, as shown in Figure 11(a). When A_3 is placed this way, the three vectors in the diagram sum to zero, indicating the impulse sequence will excite zero vibration at the design frequency and damping ratio.

Thus far, only positive impulses have been plotted. To plot a negative impulse, the vector simply points toward the origin instead of away. The angle is plotted in a manner just like positive impulses. Another option to design a zero vibration shaper from Figure 9 is to place a negative impulse at A_R. This is shown in Figure 11(b) (note that the vectors have been offset slightly in the figure to allow easier visualization).

2.3.2.2 Sensitivity Curves and Insensitivity

Most measures of input-shaping robustness focus on the sensitivity curve of the input shaper. The natural frequency sensitivity curve for a ZV shaper is shown by the solid line in Figure 12. The vertical axis is the Percent Residual Vibration (PRV) and the horizontal axis is the actual natural frequency, ω, normalized by the modeled frequency, ω_m. The curve indicates how residual vibration changes as a function of modeling errors in frequency. While a sensitivity curve itself is not a measure of robustness, a qualitative picture of the robustness of a command can be obtained from it and quantitative measures can be

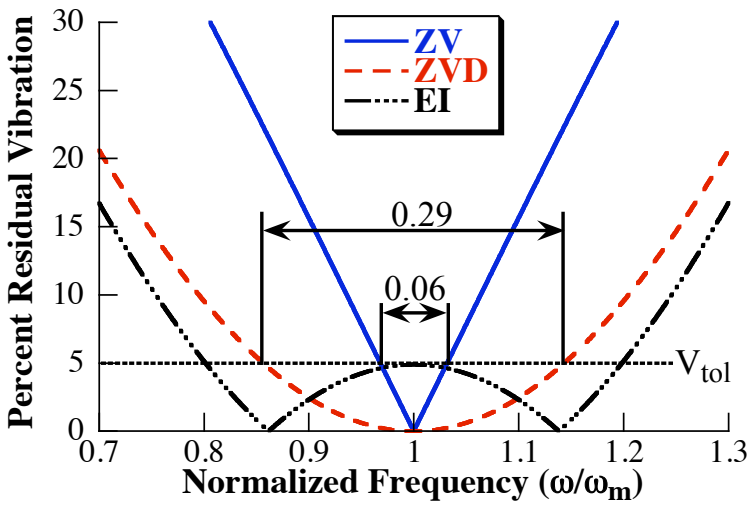

Figure 12: Sensitivity Curves for ZV, ZVD, and EI Shapers

extracted from it.

One key quantitative measure of robustness derived from the sensitivity curve is *Insensitvity* [71, 72]. Insensitivity is the width of the sensitivity curve at a tolerable vibration level, V_{tol}, with respect to the parameter of interest. For example, Figure 12 shows the ZV shaper has an Insensitivity at V_{tol} = 5%, $I(5\%)$, of 0.06. One drawback with this measure is that it can provide misleading results if applied without common sense. For example, if a sensitivity curve has peaks within the considered range (like the one labeled EI in Figure 12), then an automated calculation of Insensitivity may be misleading. Consider the case when the peak occurs at 5.1% instead of 5%. The calculated 5% Insensitivity width will be zero and falsely indicate that the shaper is not robust. Of course, from a common sense perspective, the robustness is essentially the same if the peak in the sensitivity curve occurs at 5.1% or 5.0%.

The large robustness (width of frequency suppression range) provided by both the ZVD and EI shapers shown in Figure 12 does not come without cost. Each of these robust shapers (both of which are discussed in Chapter 3) is longer than the relatively non-robust ZV shaper. This trend continues across all robust shaping methods. This fundamental compromise in input shaper design is discussed in detail in the next chapter.

CHAPTER III

ROBUST INPUT SHAPING

CHAPTER SUMMARY: *This chapter presents a thorough analysis of the fundamental compromises in input shaper design between robustness, shaper duration, and possible high-mode excitation. During this analysis, a new shaper performance measure, the* Efficiency of Insensitivity*, is introduced. After forming a clear understanding of the shaper design compromises, a new Specified Negative Amplitude-Specified Insensitivity (SNA-SI) input shaper is introduced. Experimental results from a portable bridge crane are used to verify the theoretical predictions. The major contribution contained in this chapter is the introduction of the SNA-SI shaper.*

In real applications, the system parameters needed to form an input shaper are not known exactly. This makes modeling system parameters to within the tolerances needed for ZV shapers difficult. This challenge inspired the development of robust shapers. Numerous robust shapers have been proposed, including input shapers specifically designed to address system non-linearities such as friction and non-linear system dynamics [27, 28, 78, 7, 33]. The methods used to develop more general robust shapers fall loosely into four categories: derivative methods, tolerable vibration limit methods, ad hoc methods (*e.g.* MIS methods discussed in Section 3.1.3), and numerical optimization methods. For all robust shapers, an increase in robustness must be traded off against an increase in shaper duration. However,

The experimental results in this chapter were completed with generous help from undergraduate researcher Aika Yano. She also played a key role in the development of the SNA-SI shaper presented in Section 3.5.

the robustness for a given shaper duration will differ between design methods.

This chapter will present a thorough analysis of this compromise for robust shapers, both those with only positive impulses and those with negative impulses. For negative input shapers, the possibility of high-mode excitation is also considered. A new input shaper performance measure, the *Efficiency of Insensitivity* is introduced as part of this evaluation. In addition, a formulation for Specified Negative Amplitude, Specified Insensitivity (SNA-SI) shapers is presented. These shapers provide a continuous spectrum of solutions for the duration/robustness trade-off. Experimental results from a portable bridge crane verify the theoretical predictions.

3.1 Positive Input Shaping Methods

3.1.1 Derivative Methods

The earliest form of robust input shaping was achieved by setting the derivative, with respect to the frequency, of the residual vibration equation (3) equal to zero [58]:

$$\frac{d}{d\omega}\left(e^{-\zeta\omega t_n}\sqrt{[C(\omega,\zeta)]^2+[S(\omega,\zeta)]^2}\right)=0 \tag{18}$$

The resulting shaper is called a Zero Vibration and Derivative (ZVD) shaper. It is described by:

$$ZVD=\begin{bmatrix} A_i \\ t_i \end{bmatrix}=\begin{bmatrix} \frac{1}{1+2K+K^2} & \frac{2K}{1+2K+K^2} & \frac{K^2}{1+2K+K^2} \\ 0 & \frac{\tau_d}{2} & \tau_d \end{bmatrix} \tag{19}$$

Note that the duration of this shaper, $t_3=\tau_d$, is twice that of the ZV Shaper.

The ZVD shaper sensitivity curve shown in Figure 13 has an $I(5\%)$ of approximately 0.29. The zero derivative constraint flattens the sensitivity curve at the modeled frequency and increases the Insensitivity. To further increase Insensitivity, this process can be repeated by taking additional, higher-order derivatives, with respect to frequency. The price for each additional derivative, however, is an increase in shaper duration by one-half period of the natural frequency. The next two derivative-method shapers, the ZVDD and ZVDDD, are

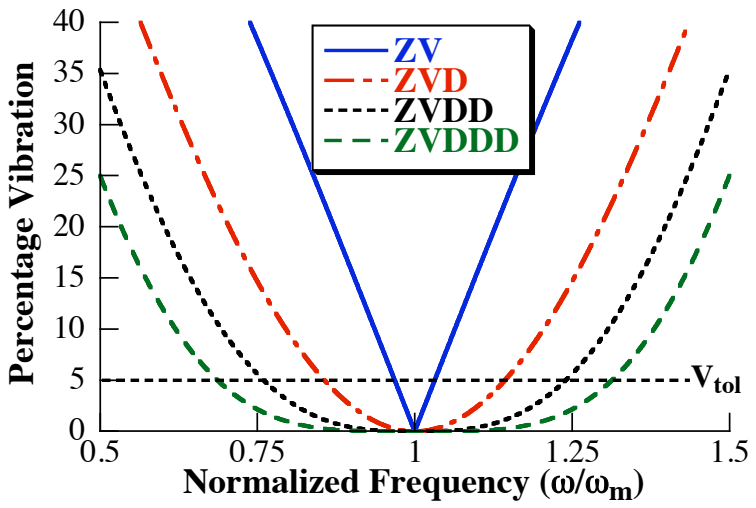

Figure 13: Sensitivity Curves for Derivative Method Shapers

described by:

$$ZVDD = \begin{bmatrix} A_i \\ t_i \end{bmatrix} = \begin{bmatrix} \frac{1}{1+3K+3K^2+K^3} & \frac{3K}{1+3K+3K^2+K^3} & \frac{3K^2}{1+3K+3K^2+K^3} & \frac{K^3}{1+3K+3K^2+K^3} \\ 0 & \frac{\tau_d}{2} & \tau_d & \frac{3}{2}\tau_d \end{bmatrix} \tag{20}$$

and

$$ZVDDD = \begin{bmatrix} A_i \\ t_i \end{bmatrix} = \begin{bmatrix} \frac{1}{D} & \frac{4K}{D} & \frac{6K^2}{D} & \frac{4K^3}{D} & \frac{K^4}{D} \\ 0 & \frac{\tau_d}{2} & \tau_d & \frac{3}{2}\tau_d & 2\tau_d \end{bmatrix} \tag{21}$$

where $D = 1 + 4K + 6K^2 + 4K^3 + K^4$. Their sensitivity curves are shown in Figure 13. The additional Insensitivity gained from each higher-order derivative is evident in the plot.

3.1.2 Tolerable Vibration Methods

To this point, the shapers discussed have been formed using a constraint that there be zero residual vibration at the modeled frequency. However, even in real world systems for which a good model exists, there will be some modeling error and vibration will occur at the design frequency. Realizing this, the designer should relax this constraint to one in which residual vibration remains below some tolerable level, V_{tol}, at the modeled frequency [71, 72].

3.1.2.1 Extra-Insensitive (EI) Methods

The first shaper utilizing this idea was called the Extra Insensitive (EI) shaper [72]. The EI shaper has the same impulse times as the ZVD shaper, but has different amplitude values that lead to greater robustness. For undamped systems, it has the form [72]:

$$EI = \begin{bmatrix} A_i \\ t_i \end{bmatrix} = \begin{bmatrix} \frac{1+V_{tol}}{4} & \frac{1-V_{tol}}{2} & \frac{1+V_{tol}}{4} \\ 0 & \frac{\tau}{2} & \tau \end{bmatrix} \tag{22}$$

where V_{tol} is the tolerable level of vibration ($e.g.$ 0.05 = 5%) and τ is the undamped vibration period of the system. For a system with viscous damping, the EI shaper is described by:

$$EI = \begin{bmatrix} A_i \\ t_i \end{bmatrix} = \begin{bmatrix} A_1 & 1-(A_1+A_3) & A_3 \\ 0 & t_2 & \tau_d \end{bmatrix} \tag{23}$$

where,

$$\begin{aligned} A_1 = {} & 0.24968 + 0.24962V_{tol} + 0.80008\zeta + 1.23328V_{tol}\zeta + \ldots \\ & + 0.49599\zeta^2 + 3.17316V_{tol}\zeta^2 \end{aligned} \tag{24}$$

$$\begin{aligned} A_3 = {} & 0.25149 + 0.21474V_{tol} - 0.83249\zeta + 1.41498V_{tol}\zeta + \ldots \\ & + 0.85181\zeta^2 - 4.90094V_{tol}\zeta^2 \end{aligned} \tag{25}$$

and,

$$t_2 = \frac{1}{\tau_d}\begin{pmatrix} 0.49990 + 0.46159V_{tol}\zeta + 4.26169V_{tol}\zeta^2 + 1.75601V_{tol}\zeta^3 + \ldots \\ +8.57843V_{tol}^2\zeta - 108.644V_{tol}^2\zeta^2 + 336.989V_{tol}^2\zeta^3 \end{pmatrix} \tag{26}$$

The sensitivity curve of the EI shaper is shown in Figure 14. Note that the EI is the same duration as the ZVD shaper, but has much more Insensitivity, as demostrated in Figure 13 and 14.

Shapers that extend this idea have a progressively larger number of humps and are called Multi-Hump EI Shapers [70]. The sensitivity curves for Two-Hump EI and Three-Hump EI shapers are shown in Figure 14. Note that the Three-Hump EI suppresses vibration over the entire range shown. As with the derivative method shapers, the price for increased robustness is a corresponding increase in shaper duration. Note, however, that the penalty

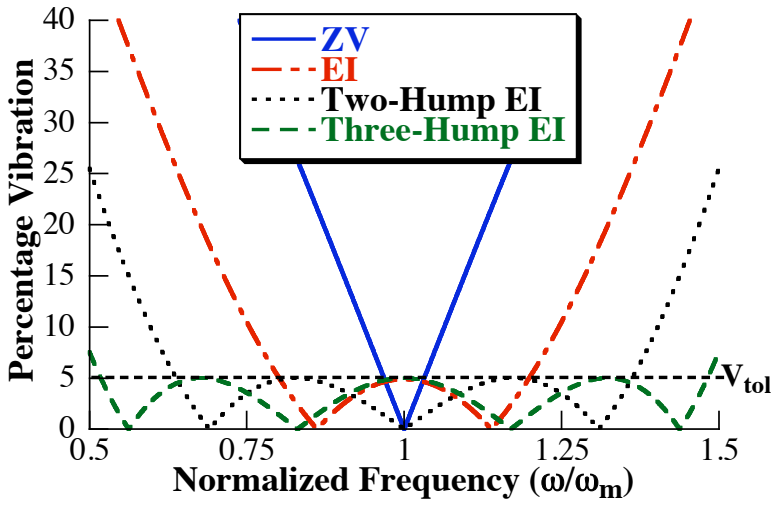

Figure 14: Sensitivity Curves for EI-Method Shapers

is not uniform across all shapers. The Two-Hump EI has the same duration as the ZVDD, and the Three-Hump EI and ZVDDD have the same durations. But, the EI shapers have much more robustness, as can be seen by comparing Figures 13 and 14. This tradeoff will be further discussed in Section 3.6.

For undamped systems, the Two-Hump EI is described by [70]:

$$\text{Two-Hump EI} = \begin{bmatrix} A_i \\ t_i \end{bmatrix} = \begin{bmatrix} A_1 & \frac{1}{2} - A_1 & A_2 & A_1 \\ 0 & 0.5\tau & \tau & 1.5\tau \end{bmatrix}, \tag{27}$$

where,

$$A_1 = \frac{3X^2 + 2X + 3V_{tol}^2}{16X}, \tag{28}$$

and,

$$X = \sqrt[3]{V_{tol}^2 \left(\sqrt{1 - V_{tol}^2} + 1 \right)}. \tag{29}$$

The undamped, three-hump EI shaper is described by [62]:

$$\text{Three-Hump EI} = \begin{bmatrix} A_i \\ t_i \end{bmatrix} = \begin{bmatrix} A_1 & \frac{(1-V_{tol})}{4} & 1 - 2(A_1 + A_2) & A_2 & A_1 \\ 0 & 0.5\tau & \tau & 1.5\tau & 2\tau \end{bmatrix} \tag{30}$$

where,

$$A_1 = \frac{1 + 3V_{tol} + 2\sqrt{2V_{tol}(V_{tol} + 1)}}{16} \tag{31}$$

Table 2: Multi-Hump EI Shapers for $V_{tol} = 5\%$

$t_i = (M_0 + M_1\zeta + M_2\zeta^2 + M_3\zeta^3)\tau,\ \tau = \frac{2\pi}{\omega}$
$A_i = M_0 + M_1\zeta + M_2\zeta^2 + M_3\zeta^3$

Shaper		M_0	M_1	M_2	M_3
Two-Hump EI	t_2	0.49890	0.16270	-0.54262	6.16180
	t_3	0.99748	0.18382	-1.58270	8.17120
	t_4	1.49920	-0.09297	-0.28338	1.85710
	A_1	0.16054	0.76699	2.26560	-1.22750
	A_2	0.33911	0.45081	-2.58080	1.73650
	A_3	0.34089	-0.61533	-0.68765	0.42261
	A_4	0.15997	-0.60246	1.00280	-0.93145
Three-Hump EI	t_2	0.49974	0.23834	0.44559	12.4720
	t_3	0.99849	0.29808	-2.36460	23.3990
	t_4	1.49870	0.10306	-2.01390	17.0320
	t_5	1.99960	-0.28231	0.61536	5.40450
	A_1	0.11275	0.76632	3.29160	-1.44380
	A_2	0.23698	0.61164	-2.57850	4.85220
	A_3	0.30008	-0.19062	-2.14560	0.13744
	A_4	0.23775	-0.73297	0.46885	-2.08650
	A_5	0.11244	-0.45439	0.96382	-1.46000

The amplitudes and time locations for the damped Two-Hump EI ($V_{tol} = 5\%$) shaper and the Three-Hump EI ($V_{tol} = 5\%$) shaper are given in Table 2 as a function of system damping. The curve fits for the two-hump EI shaper have maximum errors in the impulse times and amplitudes of less than 0.5% over the range $0 \leq \zeta \leq 0.3$. The curve fits for the three-hump EI shaper are accurate to within 0.4% over the range $0 \leq \zeta \leq 0.2$.

3.1.2.2 Specified Insensitivity (SI) Methods

It is desirable to tailor the robustness of a shaper to the specific system for which it is being designed. The Specified Insensitivity (SI) Shaper does this by generating constraint equations to match the desired level of robustness [66]. An SI shaper can be generated for any desired level of Insensitivity in one of two ways. The first is an approximation method in which the vibration is limited to below some tolerable level at M points inside the range of parameters desired. This frequency sampling process is shown graphically in Figure 15. Shaper impulse amplitudes and times are then generated using optimization routines. In

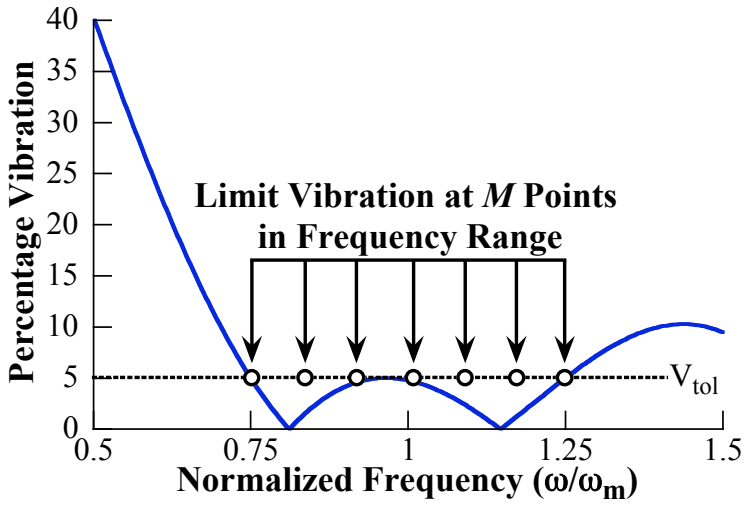

Figure 15: SI Shaper Frequency Sampling Solution Method

theory, an infinite number of points is needed to assure that the vibration remains below the tolerable level. However, in practice, a small number of points can be used to effectively suppress vibration over a wide range of parameters. The second procedure is more complicated and more difficult to implement but it obtains exact solutions [66].

Specified Insensitivity shapers provide the greatest level of robustness for any given shaper duration, a point that will be further discussed in Section 3.6. Another advantage of SI shapers is that they can be designed to have non-symmetric sensitivity curves, such that the shaper is more robust to increases in frequency than decreases, or vice versa. SI shapers can also be designed for any level of tolerable vibration. The sensitivity curves for three SI shapers are shown in Figure 16, including one designed to have an Insensitivity of 0.70 for $V_{tol} = 10\%$ ($I(10\%) = 0.70$). Also included in the figure is the sensitivity curve of a SI shaper with an non-symmetric Insensitivity, (SI ($I_{low} = 0.10, I_{high} = 0.50$)). It was designed to be five times more robust to increases in natural frequency than decreases. Its total Insensitivity is 0.60, but 0.50 of this lies above the design frequency.

One disadvantage of the SI shaper is that an optimization is required to solve for the impulse amplitudes and time locations. This disadvantage, however, is a minor inconvenience. Any number of commonly available software packages can perform the relatively

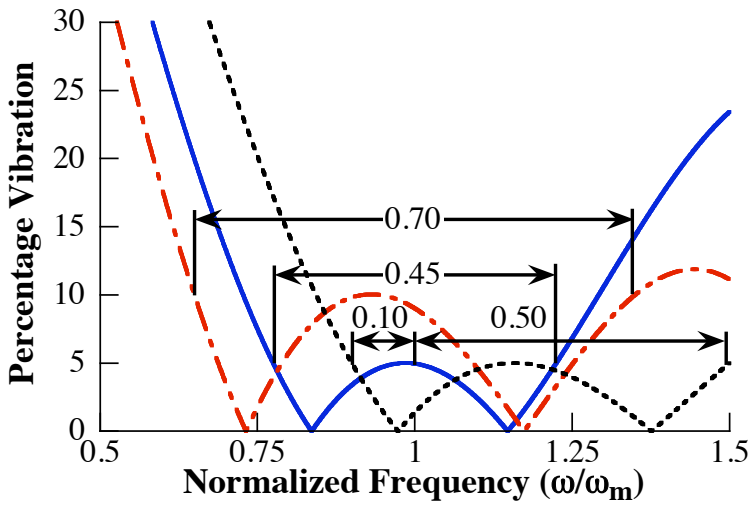

Figure 16: Sensitivity Curves for SI Shapers

easy optimization.

3.1.3 MIS Methods

A Modified Input Shaping (MIS) technique has been proposed that relaxes the constraint requiring the use of the minimum number of impulses [52]. This technique forms MISZV shapers that have zero vibration at the modeled frequency, but have a larger number of impulses and a longer shaper duration than the ZV shaper (which results from limiting the MISZV shaper to two impulses). An N-Impulse MISZV shaper is decribed by:

$$\text{N-Impulse } MISZV = \begin{bmatrix} A_i \\ t_i \end{bmatrix} = \begin{bmatrix} \frac{1}{1+M} & \frac{K_m}{1+M} & \cdots & \frac{K_m^{i-1}}{1+M} & \frac{K)_m^{N-1}}{1+M} \\ 0 & \frac{\tau_d}{N} & \cdots & \frac{(i-1)\tau_d}{N} & \frac{(N-1)\tau_d}{N} \end{bmatrix}, \tag{32}$$

where $K_m = e^{\frac{-2\zeta\pi}{N\sqrt{1-\zeta^2}}}$ (note this is slightly different than the previous K), $M = K_m + \ldots + K_m^{i-1} + K_m^{N-1}$, and $\tau_d = \frac{2\pi}{\omega\sqrt{1-\zeta^2}}$, the damped period of oscillation. The sensitivity plots for two- through five-impulse MISZV shapers are shown in Figure 17. One can see that the additional impulses only provide a minimal increase in shaper Insensitivity.

Zero-derivative MIS (MISZVD) shapers are formed by convolving two MISZV shapers designed for the same frequency. The resulting MISZVD shaper is indicated by the number of impulses of each of the MISZV shapers used to created it. A $N \times M$-Impulse MISZVD is

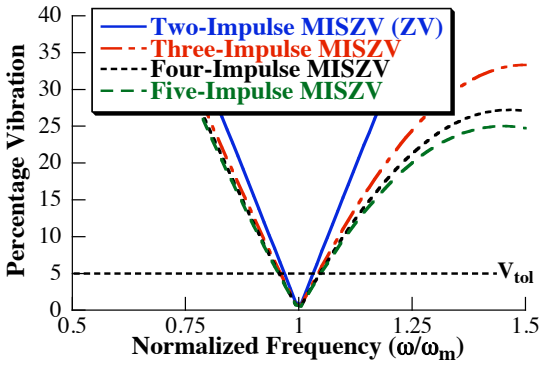

Figure 17: Sensitivity Curves for MISZV Shapers

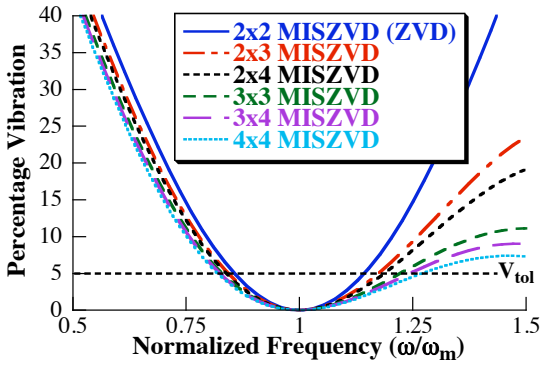

Figure 18: Sensitivity Curves for MISZVD Shapers

formed by convolving an MISZV shaper containing N impulses with a MISZV shaper with M impulses. Convolving MISZV shapers of higher number of impulses results in more robust MISZVD shapers, at the cost of increased shaper duration. It should be noted that a 2×2-Impulse MISZVD shaper is the traditional ZVD shaper. The sensitivity plots for various MISZVD shapers are shown in Figure 18.

3.2 Robustness to Errors in Damping

Input shaper robustness to errors in damping follows very similar trends to robustness to changes in frequency. One difference between the frequency sensitivity plots and the damping ratio plots is that the damping ratio is not normalized. This is because when the modeled damping ratio, ζ, is near zero, small changes in the actual damping ratio, ζ_{act}, result in large changes in the normalized damping ratio, ζ/ζ_{act}. Therefore, insignificant changes in system dynamics, say between $\zeta_{act} = 0.001$ and $\zeta_{act} = 0.002$, show up as large changes in the normalized damping ratio.

The damping sensitivity curves for the ZV and MISZV shapers designed for a damping ratio of 0.1 are shown in Figure 19. One can see that the ZV and MISZV shapers, which are relatively non-robust to errors in natural frequency, are also relatively non-robust to errors in damping. This trend continues across all shaping methods; robustness to errors in natural frequency generally translates into robustness to errors in damping. This is seen in

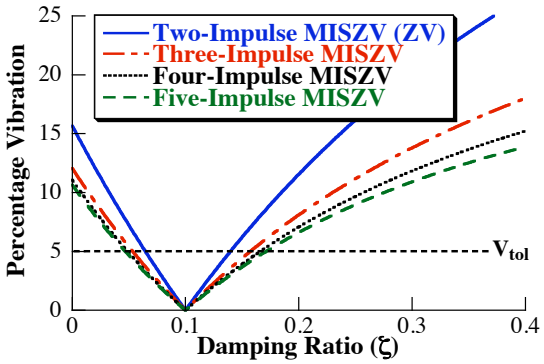

Figure 19: Damping Ratio Sensitivity for ZV and MISZV Shapers ($\zeta_m = 0.1$)

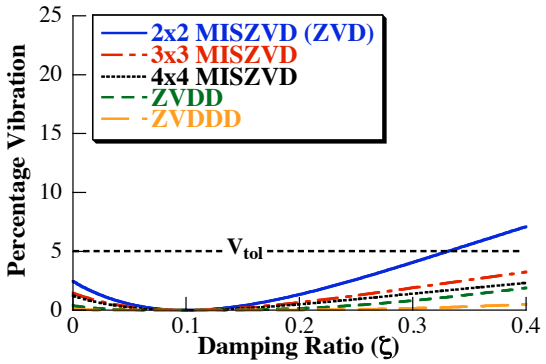

Figure 20: Damping Ratio Sensitivity for Derivative and MISZVD Method Shapers ($\zeta_m = 0.1$)

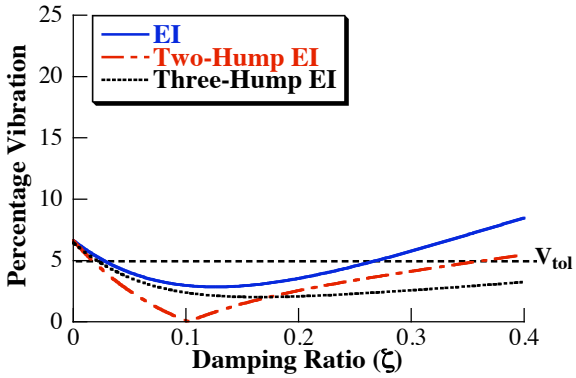

Figure 21: Damping Ratio Sensitivity for EI-Method Shapers ($\zeta_m = 0.1$)

the plots of the sensitivity of the derivative method shapers (including MISZVD) in Figure 20. Notice that the derivative methods have zero slope at the modeled damping ratio and provide a dramatic reduction in vibration for all values of damping shown.

The damping ratio sensitivity curves for the EI-method shapers are shown in Figure 21. Above damping ratios of approximately 0.175, the vibration levels are lower for longer shaper durations (and higher hump numbers), similar to the trends seen in the natural frequency sensitivity plots. However, below 0.175 the level of vibration cannot be predicted solely by shaper duration. Notice that the EI shapers suppress vibration over nearly the entire range of damping ratios shown in the plot. The EI-method shapers in Figure 21 were designed for a $V_{tol} = 3\%$. This is illustrative of the flexibility of the EI-method shapers to design for differing tolerable vibration limits. It is also illustrative of the steps that

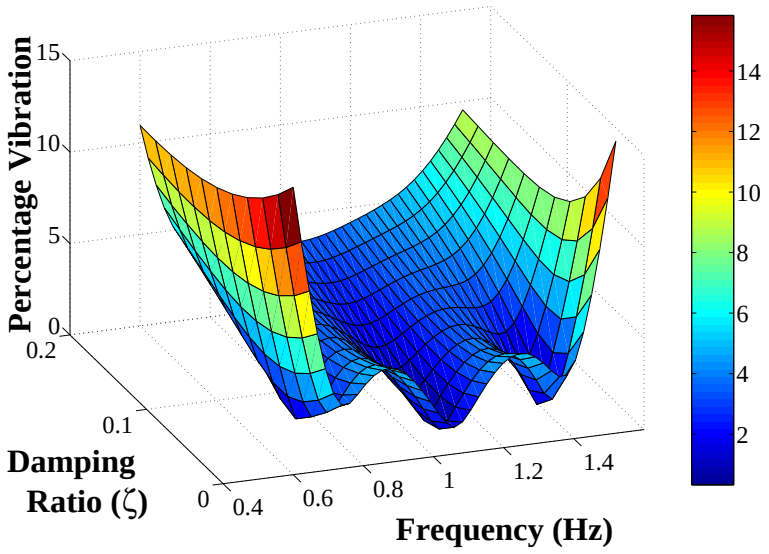

Figure 22: Three-dimensional Sensitivity Curve for an SI Shaper

a designer should take when designing EI-method shapers for systems with dramatically varying damping ratios. One can see from Equations (23) - (26) that choosing a lower V_{tol} has very little effect on shaper duration. The negative consequence of this choice is a decrease in frequency Insensitivity. When V_{tol} is lowered to 0%, the EI shaper becomes the ZVD.

The SI shaper, which was discussed with respect to errors in natural frequency in Section 3.1.2.2, can also be designed to have a specified Insensitivity to damping. Additionally, Insensitivity to errors in damping and frequency can be designed into the same SI shaper. This is done in a manner similar to that discussed in Section 3.1.2.2, by limiting the vibration to below V_{tol} at points within the (ω, ζ) parameter space. Figure 22 shows a three-dimensional sensitivity curve for a SI shaper that was designed to suppress vibration between 0.70 Hz and 1.30 Hz and also over the range of damping ratios between 0 and 0.20.

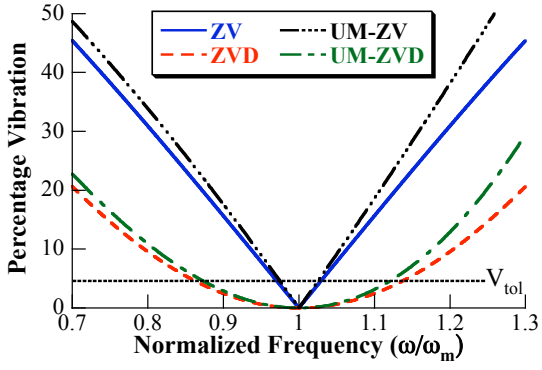

Figure 23: Sensitivity Curves for (UM-)ZV and (UM-)ZVD Shapers

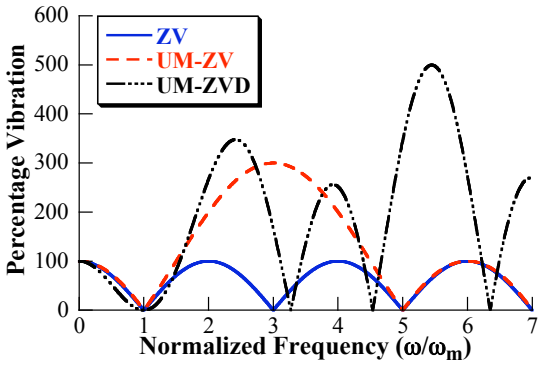

Figure 24: ZV, UM-ZV, and UM-ZVD Sensitivity Curves

3.3 Negative Input Shapers

Allowing negative impulses has the primary advantage of decreasing the duration of the input shaper, thereby speeding system response. If negative impulse amplitude are allowed, then there are two primary methods to constrain impulse amplitudes, Unity Magnitude [74] and Specified Negative Amplitude [63] constraints. Each of these constraint methods was introduced in Section 2.3.1.2

Figure 23 shows the senstivity curves for two Unity Magnitude negative shapers. The sensitivity curves of negative input shapers are similar to their postive counterparts near the design frequency. However, at frequencies much higher than the design frequency significant vibration can occur. This effect is shown in Figure 24, which shows the percentage vibration for frequencies up to seven times the design frequency. Positive input shapers, like the one labeled ZV in Figure 24, can never excite more oscillation than the unshaped case. This is not true, however, for shapers containing negative impulses, as seen in Figure 24 by the UM-ZV and UM-ZVD curves [67, 63].

While it is unlikely that the estimate of the natural frequency of the system used to design the input shaper will be this far from the system's actual frequency, there may be unmodeled higher modes that can be excited. Additionally, higher modes that are known to exist but do not significantly affect system response may be magnified such that they do

so. Therefore, the effect of negative amplitude impulses on higher modes must be taken into account when evaluating negative input-shaping techniques.

3.4 Robust, Unity Magnitude Input Shaping Methods

3.4.1 Derivative Methods

The Zero Vibration and Derivative (ZVD) Shaper was explained in Section 3.1.1. If the same robustness constraints are imposed, but impulse amplitudes are restricted to ±1, then the UM-ZVD shaper results. The impulse times are a complex function of damping ratio, described in Table 3. The sensitivity curve for the UM-ZVD shaper was shown in Figure 23. As with the positive derivative method shapers, setting additional derivatives of (3) equal to zero will provide additional robustness at the cost of increased shaper duration [58].

3.4.2 Tolerable Vibration Methods

Like positive shaper design, relaxing the zero vibration constraint to some tolerable level leads to increased robustness. This section presents two unity magnitude methods with tolerable vibration constraints.

3.4.2.1 Extra-Insensitive (EI) Methods

The Extra Insensitive (EI) shaper was discussed in Section 3.1.2.1 [72, 43, 71]. It has the same duration as the ZVD shaper, but substantially more robustness. The sensitivity curve for the unity magnitude version of this shaper, the UM-EI, is shown in Figure 25. The UM-EI shaper, as a function of damping ratio, is given in Table 4.

Table 3: UM-ZVD Shapers for Damped Systems

$t_i = (M_0 + M_1\zeta + M_2\zeta^2 + M_3\zeta^3)\tau,\ \tau = \frac{2\pi}{\omega}$

A_i	t_i	M_0	M_1	M_2	M_3
1	t_1	0	0	0	0
-1	t_2	0.08945	0.28411	0.23013	0.16401
1	t_3	0.36613	-0.08833	0.24048	0.17001
-1	t_4	0.64277	0.29103	0.23262	0.43784
1	t_5	0.73228	0.00992	0.49385	0.38633

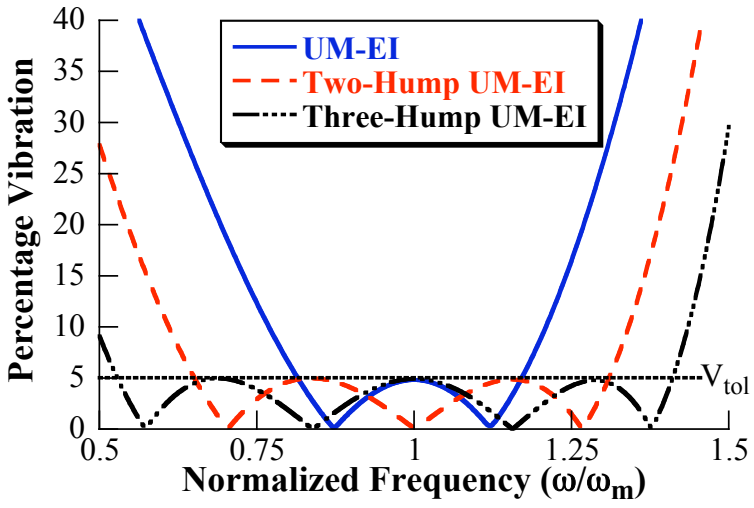

Figure 25: Sensitivity Curves for UM-EI Method Shapers

As with positive shapers, unity magnitude shapers that extend the EI shaper idea have a progressively larger number of humps in their sensitivity curves and are called Multi-Hump UM-EI Shapers [70]. The sensitivity curves for the Two-Hump UM-EI and Three-Hump UM-EI shapers are shown in Figure 25. The impulse times of these shapers are a function of damping ratio, as shown in Table 4.

The price for increased robustness gained with Two and Three-Hump UM-EI shapers is a corresponding increase in shaper duration. As with positive shapers, the penalty for increased robustness is not uniform across all robust shaping methods. For example, the UM-ZVD and UM-EI shapers are approximately the same duraiton. However, the UM-EI provides much greater robustness, as measured by Insensitivity.

3.4.2.2 Specified Insensitivity (SI) Methods

Specified Insensitivity (SI) Shapers are another type of shaper that limits vibration to below some tolerable level over any desired range of parameters, as discussed in Section 3.1.2.2. Figure 26 shows the sensitivity curves for UM-SI shapers designed for several 5% Insensitivities. Like positive SI shapers, two advantages to UM-SI shapers are that they can be designed for any level of tolerable vibration and for un-symmetric Insensitivities. Also like positive SI shapers, one disadvantage is that UM-SI shapers is that an optimization routine

Table 4: UM-EI Shapers for Damped Systems, V_{tol} = 5%

	$t_i = (M_0 + M_1\zeta + M_2\zeta^2 + M_3\zeta^3)\tau,\ \tau = \frac{2\pi}{\omega}$					
Shaper	A_i	t_i	M_0	M_1	M_2	M_3
UM-EI	1	t_1	0	0	0	0
	-1	t_2	0.09374	0.31903	0.13582	0.65274
	1	t_3	0.36798	-0.05894	0.13641	0.63266
	-1	t_4	0.64256	0.28595	0.26334	0.24999
	1	t_5	0.73664	0.00162	0.52749	0.19208
Two-Hump UM-EI	1	t_1	0	0	0	0
	-1	t_2	0.05970	0.31360	0.31759	1.5872
	1	t_3	0.40067	-0.08570	0.14685	1.6059
	-1	t_4	0.59292	0.38625	0.34296	1.2889
	1	t_5	0.78516	-0.08828	0.54174	1.3883
	-1	t_6	1.12640	0.20919	0.44217	0.30771
	1	t_7	1.18640	-0.02993	0.79859	0.10478
Three-Hump UM-EI	1	t_1	0	0	0	0
	-1	t_2	0.04275	0.31845	0.46272	3.3763
	1	t_3	0.42418	-0.05725	0.04989	3.9768
	-1	t_4	0.56353	0.48068	0.38047	4.2431
	1	t_5	0.83047	-0.09785	0.34048	4.4245
	-1	t_6	1.09760	0.38825	0.35290	2.9484
	1	t_7	1.23710	-0.08706	0.81706	2.8367
	-1	t_8	1.61890	0.09964	0.42780	1.3151
	1	t_9	1.66190	-0.09711	0.80045	1.0057

must be used to solve for the shaper.

3.5 The Specified Negative Amplitude-Specified Insensitivity (SNA-SI) Shaper

The faster system motion provided by UM shapers comes at the cost of increased actuator demands and possible high-mode excitation. Specified Negative Amplitude (SNA) shapers provide a method to reduce actuator demands and high-mode excitation, while retaining the benefits of negative impulses [68, 63]. To date, SNA shapers have been developed that fulfill zero-vibration (ZV) and zero vibration and derivative (ZVD) constraints for a specified maximum negative impulse amplitude [68, 63]. To create a shaper that has minimum duration for a given Insensitivity and maximum negative amplitude, SNA and SI constraints can be combined to create a SNA-SI shaper. A graphical representation of

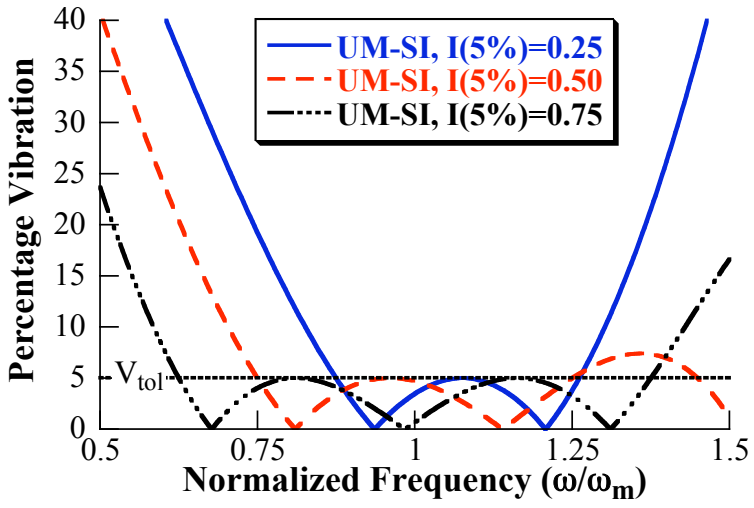

Figure 26: Sensitivity Curves for Several UM-SI Shapers

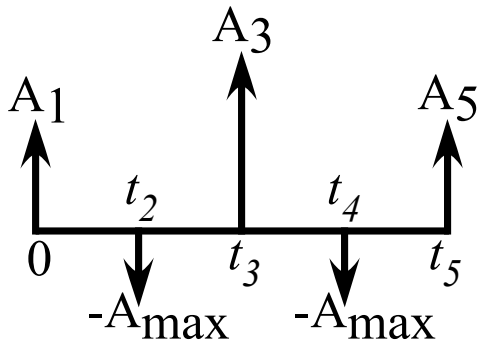

Figure 27: Graphical Representation of a Five-Impulse SNA shaper

a five-impulse SNA-SI shaper is shown in Figure 27. An additional constraint is needed to ensure the shaped command remains within the bounds established by the unshaped command. This constraint limits the running sum of impulse amplitudes to between zero and one:

$$0 \leq \sum_{i=1}^{k} A_i \leq 1 \quad k = 1, \ldots, n \tag{33}$$

where A_i is the i^{th} impulse amplitude, k is the current impulse, and n is the number of impulses contained in the shaper. SNA-SI shapers can be considered a very general form of SI shaping. If the maximum negative amplitude allowed is zero, resulting in only positive impulses, then the positive SI shaper results. If the maximum negative impulse amplitude is set to one, then UM-SI shapers result.

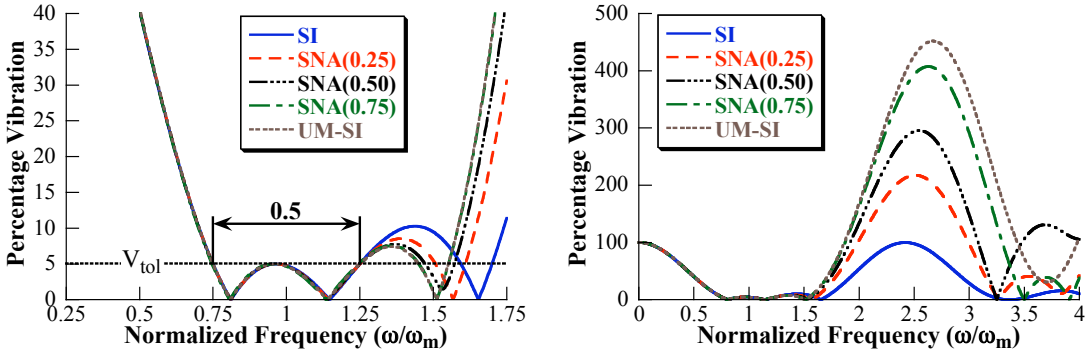

(a) Near the Modeled Frequency

(b) Over a Larger Range of Frequencies

Figure 28: Sensitivity Curves for SI, SNA, and UM-SI Shapers for I(5%)=0.5

For SNA-SI shapers, the maximum negative amplitude allowed is indicated in parenthesis. For example, an SNA-SI shaper with a specified negative amplitude of 0.25 is indicated by SNA(0.25). Figure 28 compares several SNA-SI shapers designed with differing specified negative amplitudes and $I(5\%) = 0.50$. Figure 28(a) shows the sensitivity curves for these shapers near the modeled frequency. One can see that the sensitivity curves for these shapers are nearly identical for frequencies inside the insensitivity range and lower. At higher frequencies, shown in Figure 28(b), SNA shapers with higher maximum negative impulse amplitudes display larger amounts of high-mode excitation. This, along with increased actuator requirements, is the penalty for the decrease in rise time afforded by the larger negative impulse amplitudes. High-mode excitation will be further discussed in Section 3.7.

SNA-SI shapers provide the shortest duration shaper for a given Insensitivity and maximum negative impulse amplitude. As such, they provide the controls engineer with a method to design a shaper that best meets the given requirements on robustness, high-mode excitation, actuator limits, and system rise time.

3.6 Shaper Insensitivity versus Shaper Duration

For each method of generating robust input shapers, the shaper duration increases with Insensitivity. The Insensitivity for a given shaper duration, however, differs between methods,

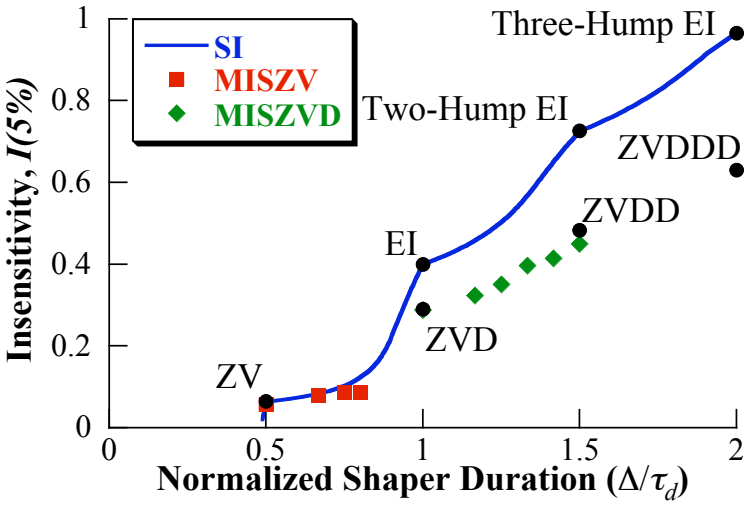

Figure 29: Insensitivity as a Function of Normalized Shaper Duration

indicating the need to thoroughly understand the Insensitivity/duration tradeoff between the various shaping methods. To ensure that this analysis is system independent, the shaper duration is normalized by the damped natural period of the system. A shaper with a duration equal to the modeled damped natural period, like the ZVD and EI shapers, has a normalized duration of one.

3.6.1 Insensitivity versus Shaper Duration for Positive Shapers

Figure 29 shows the 5% Insensitivity, $I(5\%)$, of various positive shapers as a function of normalized shaper duration. The SI shaper is plotted as a line, as it can be designed to have any desired level of Insensitivity. The SI shaper has the minimum duration for any given Insensitivity. Therefore, SI shapers will provide the fastest rise time. Other shapers discussed in this chapter are also shown on the plot. One point of interest is that the EI shapers correspond to nodes on the SI shaper curve. This indicates that they offer the optimal insensitivity for a given shaper duration. Each node is also the point in the solution space where the number of impulses of the SI shaper changes. It is also of interest to note that both the derivative and MIS methods yield shapers that provide substantially less Insensitivity than EI and SI shapers.

In order to further quantify the compromise between insensitivity and shaper duration,

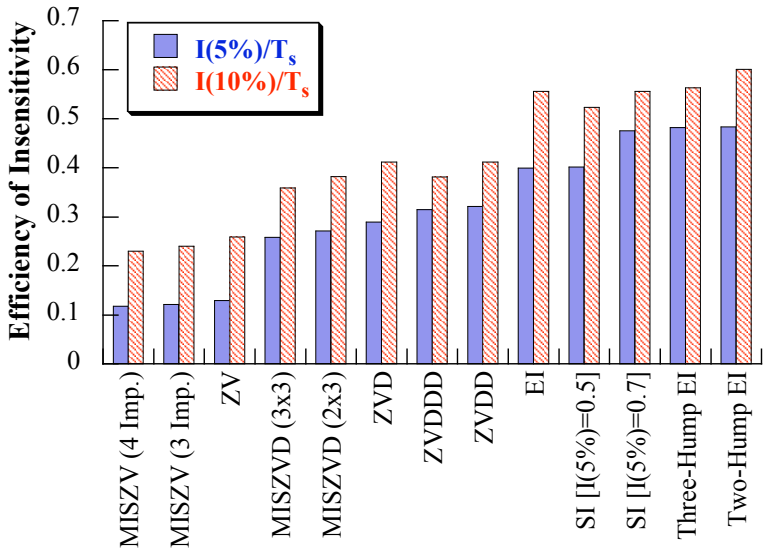

Figure 30: Efficiency of Insensitivity for Positive Shapers

the *Efficiency of Insensitivity* is introduced. The Efficiency of Insensitivity is the Insensitivity of a shaper divided by its normalized duration. Higher numbers indicate that a shaper achieves its robustness more efficiently, in terms of shaper duration. The Efficiency of Insensitivity for five and ten percent vibration tolerance levels is shown in Figure 30. The shapers are sorted from left to right in terms of increasing Efficiency of Insensitivity for $V_{tol} = 5\%$.

As seen in Figure 30, all ZV method shapers, including the MISZV shapers with additional impulses, exhibit a low Efficiency of Insensitivity for $V_{tol} = 5\%$. The efficiency values range between 0.1228 for the Four-Impulse MISZV and 0.1296 for the ZV. Similar trends exist when $V_{tol} = 10\%$. This indicates that of the shapers with low robustness, the ZV shaper achieves its Insensitivity most efficiently.

The evaluation of the Efficiency of Insensitivity for derivative (ZVD) and MISZVD shapers follows the same trend as the ZV method shapers. For $V_{tol} = 5\%$, the Efficiency of Insensitivity of derivative (ZVD) method shapers is greater than that of MISZVD shapers of comparable duration. A similar trend exists when $V_{tol} = 10\%$.

An obvious result from Figure 30 is that the SI and EI shapers, which offer optimal

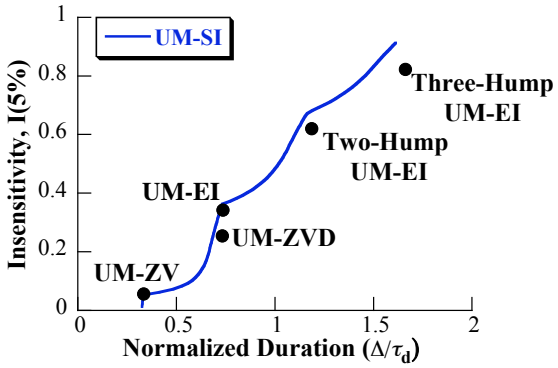

Figure 31: Insensitivity as a Function of Shaper Duration for Unity Magnitude Shapers

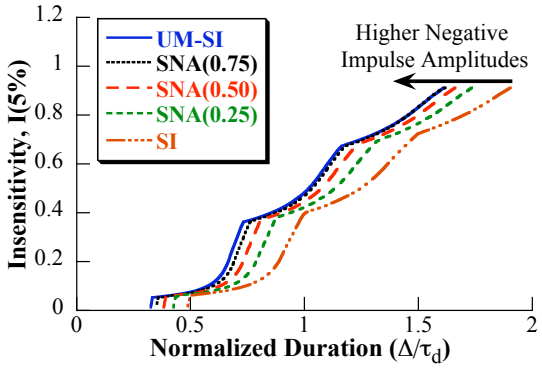

Figure 32: Insensitivity as a Function of Shaper Duration for Several SNA-SI Shapers

Insensitivity for a given shaper duration, also provide the highest Efficiency of Insensitivity, as would be expected. This provides strong evidence that these shapers should be used whenever possible.

3.6.2 Insensitivity versus Shaper Duration for Negative Shapers

Figure 31 shows the 5% Insensitivity, $I(5\%)$, of various unity magnitude shapers as a function of normalized shaper duration. The plot follows very similar trends to positive shaper version shown previously in Figure 29. One point of interest is that the UM-EI shapers do not exactly correspond to nodes on the UM-SI shaper curve, as they do for positive shapers [74]. The nodes of the UM-SI curve correspond to changes in the number of shaper impulses, a point that is an important for consideration of high-mode excitation. Also note that the UM-EI shapers and the UM-ZVD provide less than optimal Insensitivity.

Figure 32 shows the 5% Insensitivity of various SNA-SI shapers as a function of normalized shaper duration. Notice that as higher amplitude negative impulses are allowed the normalized duration for a given Insensitivity decreases. This plot may be extended into three dimensions by plotting the maximum negative amplitude allowed on the third axis, as shown in Figure 33. One can see that the same general trends from Figure 32 continue for all levels of negative impulse amplitude. Note that this plot provides a graphical representation of the maximum 5% Insensitivity possible given a particular shaper duration and

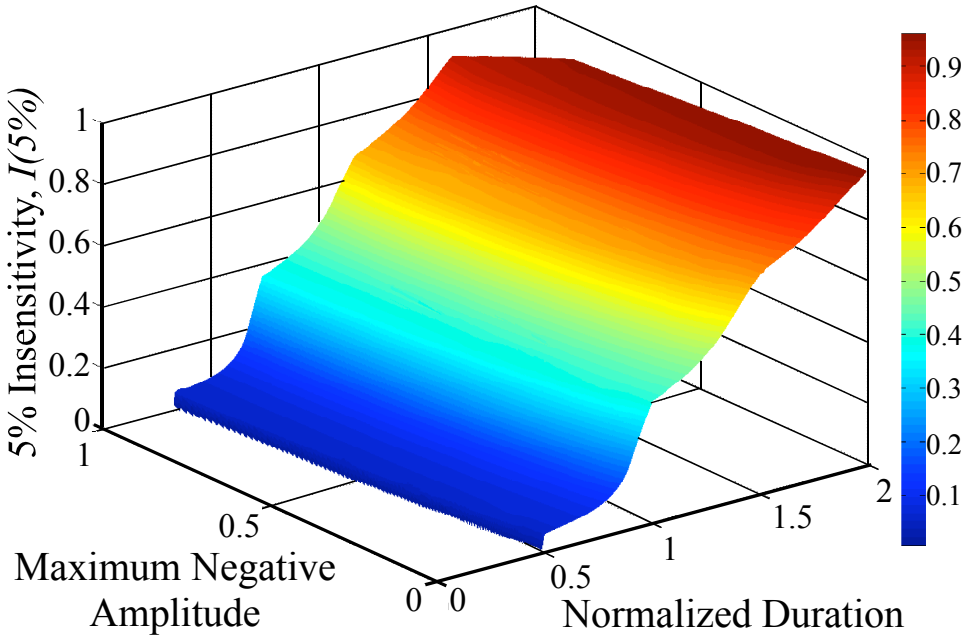

Figure 33: Insensitivity as a Function of Shaper Duration and Maximum Negative Amplitude

maximum negative amplitude.

Figure 34 shows the Efficiency of Insensitivity for $V_{tol} = 5\%$ for various negative shapers. On the left side of the plot are unity magnitude shapers. To the right of the vertical line are SI, SNA-SI, and UM-SI shapers designed for $I(5\%) = 0.65$. Note that the Efficiency of Insensitivity increases as higher magnitude negative impulses are allowed. This indicates that utlizing negative impulses increases the efficiency in which robustness is achieved. This point is further supported by Figure 35, which compares the Efficiency of Insensitivity for five different positive shapers and their unity magnitude equivalents. In all cases the unity magnitude version of the shaper has a higher Efficiency of Insensitivity.

Figure 36 shows Efficiency of Insensitivity for the same series of SNA-SI shapers as Figure 32. The shape of the curves in Figure 32 suggested that there were points where robustness is achieved most effeciently. The local peaks of the curves in Figure 36 are these points. As a result, figure 36 also serves as a valuable input shaper design tool for the controls engineer. It indicates that there are points in the SNA-SI (and UM-SI and

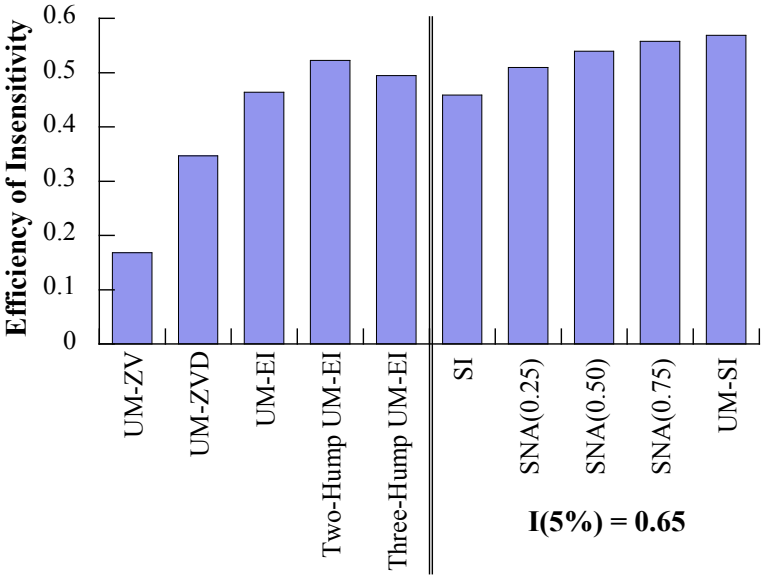

Figure 34: Efficiency of Insensitivity for Negative Shapers

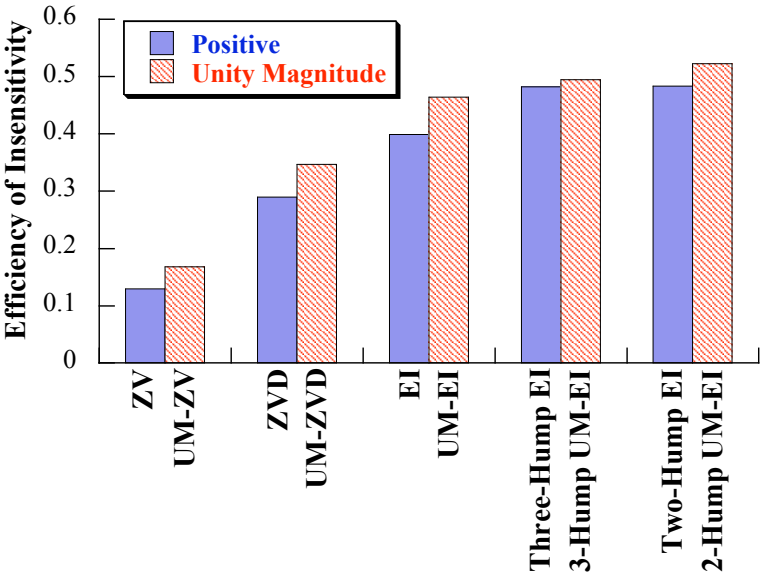

Figure 35: Efficiency of Insensitivity Comparison

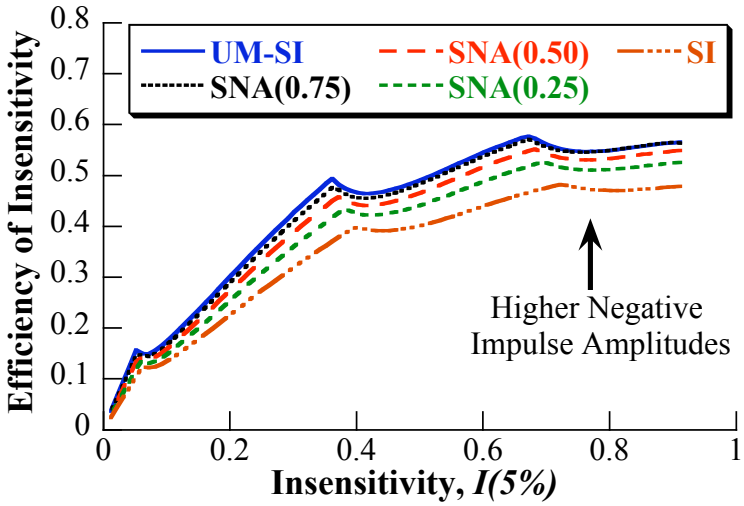

Figure 36: Efficiency of Insensitivity as a function of Insensitivity for SNA-SI Shapers

SI) solution space that best negotiate the duration/robustness compromise. Deviation from these points can lead to large increases in duration, with little increase in robustness. In addition, the Efficiency of Insensitivity is seen to increase at higher amplitude negative impulses for the entire range of Insensitivity plotted.

3.7 High-Mode Excitation

One price for the decrease in shaper duration and increase in Efficiency of Insensitivity afforded by negative impulses is the possibility of high-mode excitation. To characterize the high-mode excitation caused by an input shaper, the average value of the sensitivity curve between 2 and 10 times the design frequency ($2\omega_m$–$10\omega_m$) is used. The average high-mode excitation for the shapers discussed in this chapter is shown in Figure 37. Notice that the positive shapers (ZV, ZVD and SI) average less than 100%. This is expected as the maximum amount of vibration they excite is 100% of the unshaped case. The remaining shapers to the left of the vertical solid line are unity magnitude shapers. All these shapers have high-mode excitation averages above 100%. Note that more robust negative shapers, which require a higher number of impulses, have higher values of average high-mode excitation [63].

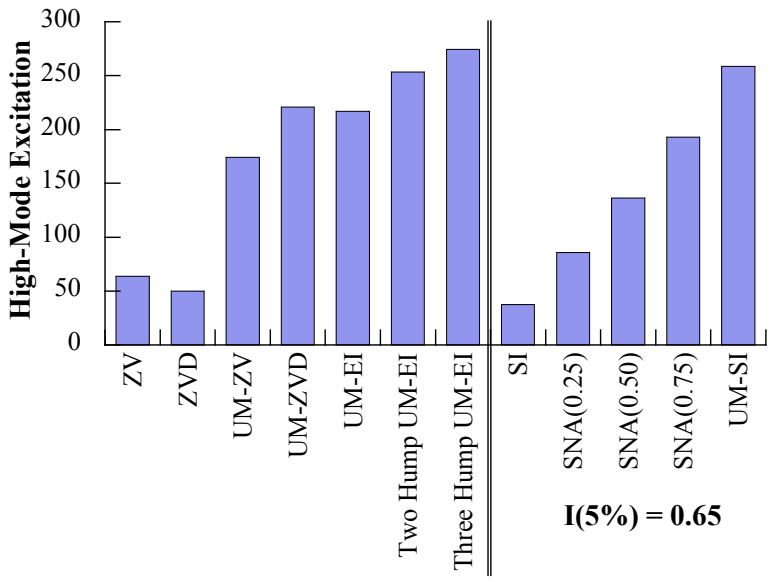

Figure 37: Average High-Mode Excitation

To the right of the solid vertical line are the same SI, SNA-SI, and UM-SI shapers designed for $I(5\%) = 0.65$ from Figure 34. In Figure 34, it was shown that increasing the maximum allowed negative impulse improved the Efficiency of Insensitivity. In Figure 37, the cost of this increased efficiency is shown, as average high-mode excitation increases with maximum negative impulse amplitude. This trend continues for other SNA shapers, as seen in Figure 38, which shows the relationship between average high-mode excitation and maximum negative amplitude for SNA-SI shapers designed for $I(5\%) = 0.25$, $I(5\%) = 0.50$, and $I(5\%) = 0.75$.

The high-mode excitation from the same series of SNA-SI shapers from Figures 32 and 36 is shown in Figure 39(a). This figure provides further documentation of the penalty for increasing negative impulse amplitudes. The average high-mode excitation clearly increases with negative impulse amplitude for all values of Insensitivity shown in the plot. If the range of frequencies over which the high-mode excitation is measured is extended from $10\omega_m$ to $100\omega_m$, the high-mode excitation curves are smoothed, as seen in Figure 39(b). This plot indicates that there are clear transitions in high-mode excitation. These transitions occur at points in which the number of shaper impulses increases, due to increased

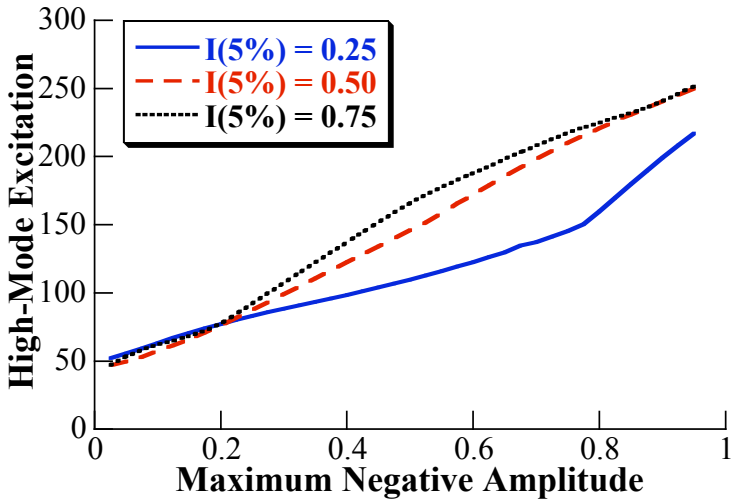

Figure 38: Average High-Mode Excitation as a Function of Negative Impulse Amplitude

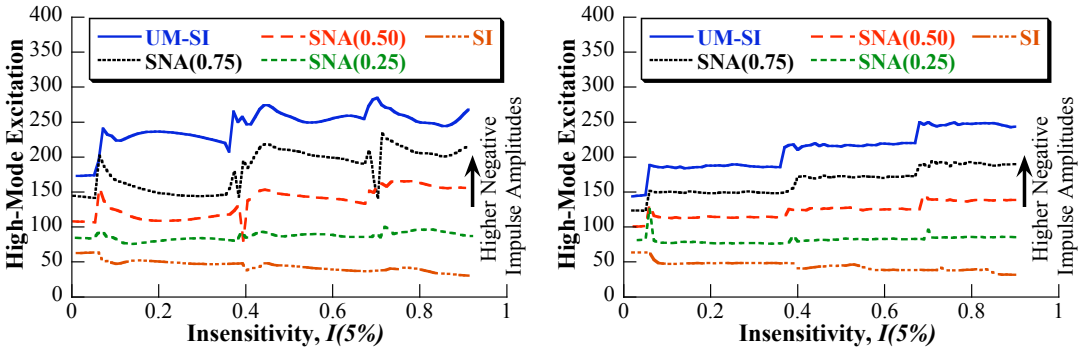

(a) $2\omega_m - 10\omega_m$ **(b)** $2\omega_m - 100\omega_m$

Figure 39: Average High-Mode Excitation as a function of Insensitivity

Insensitivity demands. The transitions also correspond to points of greatest Efficiency of Insensitivity.

3.8 Experimental Comparisons

To this point, all results presented have been theoretical. To rigorously test the various shaping methods, representative shapers from each method were experimentally evaluated using the portable bridge crane shown in Figure 40 [29, 75]. The portable bridge crane has a workspace of approximately 1m×1m×1.6m. The overhead bridge and trolley are driven using Siemens synchronous AC servo motors attached to timing belts that provide motion in

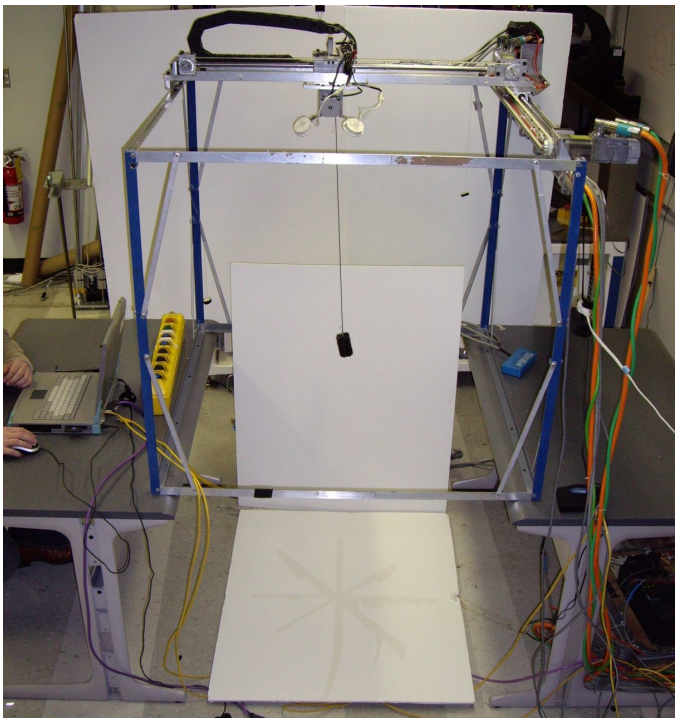

Figure 40: Portable Bridge Crane

the x and y directions. The motors are controlled using a Siemens PLC using Proportional-plus-Integral (PI) Control with feedback from motor-mounted encoders. The crane is also equipped with a vision system to track payload position. More detailed specifications of this crane can be found in Appendix A.

3.8.1 Robust, Positive Shapers

Seven positive input shapers were designed for a system natural frequency of 0.74 Hz and zero damping, corresponding to a suspension cable length of approximately 0.46m (18 in). The seven shapers tested were: ZV, ZVD, EI, Two-hump EI, Four-Impulse MISZV, 2×3 MISZVD, and an SI shaper designed with $I(5\%) = 0.5$. The shapers were evaluated using suspension cable lengths varying between 0.38m and 1.57m (15–62 in).

The vibration amplitudes for unshaped, ZV, and SI-shaped motions are shown in Figure 41. The vibration amplitude is plotted on the vertical axis. Along the horizontal axis, the different natural frequencies resulting from varying the payload suspension cable length

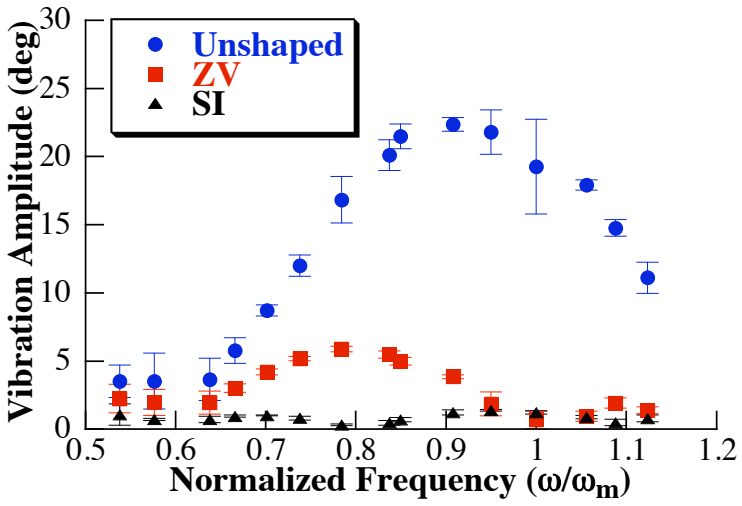

Figure 41: Vibration Amplitudes for Unshaped, ZV, and SI Shaped Motion

are normalized by the shaper design frequency. The points in this figure and the remaining figures in this section are averages of three trials. The error bars represent one standard deviation above and below the average value. Average vibration amplitude for unshaped moves varied between four and twenty-three degrees as the suspension length was changed. One can see that both the ZV and SI-shaped vibration amplitudes remained much smaller than the unshaped motion over the entire range of suspension lengths. Even the relatively non-robust ZV shaper greatly reduced the level of vibration over the entire range of cable lengths tested.

The theoretical and experimental sensitivity curves for the ZV shaper are shown in Figure 42. The experimental results closely match those predicted by theory. There are more data points at lower normalized frequencies due to the nature of the experimental setup. To achieve higher natural frequencies the suspension cable must be shortened. Shortening this cable toward its minimum length makes it impossible for the vision system to track the system response because the payload swings out of the camera's field of view. No such problem exists for longer cable lengths, which result in frequencies lower than the shaper design frequency.

The experimental sensitivity curve for the ZVD shaper is shown in Figure 43. It too

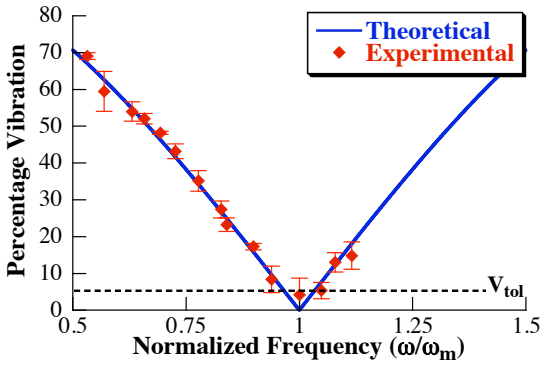

Figure 42: Experimental Sensitivity of ZV Shaper

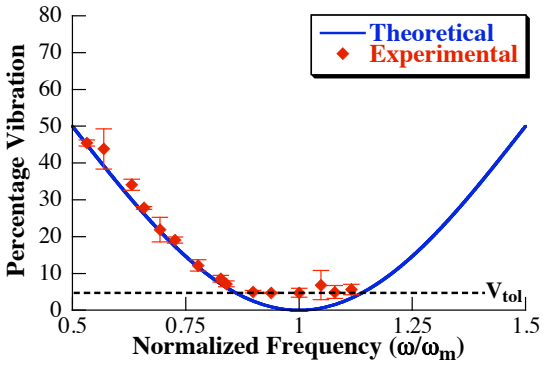

Figure 43: Experimental Sensitivity of ZVD Shaper

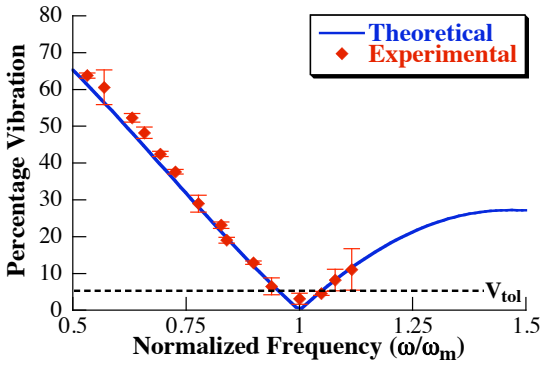

Figure 44: Experimental Sensitivity of a Four-Impulse MISZV Shaper

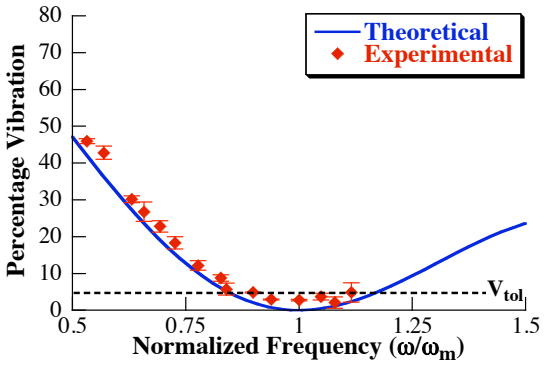

Figure 45: Experimental Sensitivity of 2×3 MISZVD Shaper

closely matches the predicted behavior; however, even at the modeled frequency the percentage residual vibration is very near the 5% V_{tol} level. This corresponds to the noise level in payload swing and camera measurements. This result is not very troubling because even 10% vibration is very small - after all, that is a 90% reduction in vibration from the unshaped case. It does, however, provide further support for the use of tolerable vibration methods discussed in Section 3.1.2, because zero vibration cannot be achieved in practice.

Figures 44 and 45 show the experimental and theoretical sensitivity curves for the Four-Impulse MISZV and 2 × 3-Impulse MISZVD shapers. For each, the experimental results closely follow the theoretical. As with the ZV and ZVD shapers, the vibration never reaches the theoretical minimum of zero. The 2 × 3-Impulse MISZVD, however, exhibits good robustness to modeling errors in natural frequency, remaining below the V_{tol} over a large

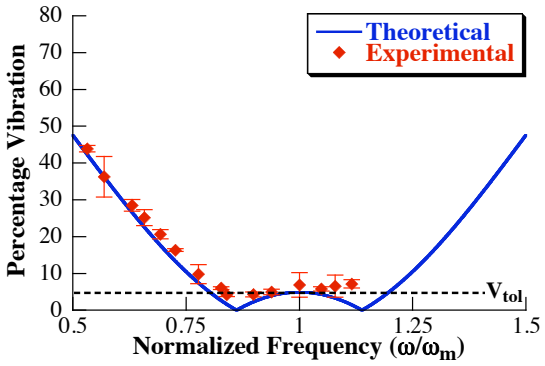

Figure 46: Experimental Sensitivity of EI Shaper

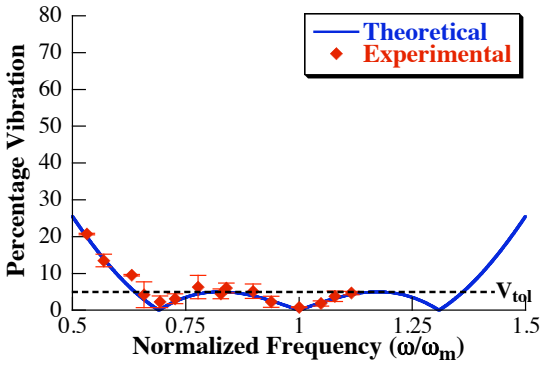

Figure 47: Experimental Sensitivity of Two-Hump EI Shaper

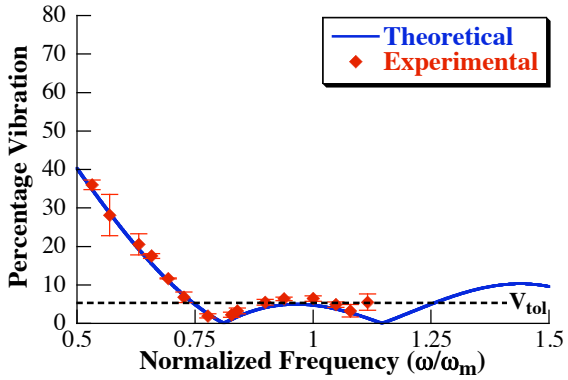

Figure 48: Experimental Sensitivity of SI [$I(5\%) = 0.5$] Shaper

range of cable lengths.

The results for the EI and Two-Hump EI shapers are shown in Figures 46 and 47, respectively. Again, the experimental behavior closely follows the theoretical predictions. The Two-Hump EI shaper provides great reduction in vibration levels over the entire range of cable lengths, remaining below or only slightly larger than V_{tol} over nearly the entire range. Note that the Two-Hump EI provides robustness over such a wide range that the experimental setup cannot be changed enough to cause any significant vibration.

The experimental sensitivity curve for an SI shaper designed for an $I(5\%) = 0.50$ is shown in Figure 48. Like the Two-Hump EI shaper, vibration is substantially reduced over nearly the entire range of cable lengths. For both the Two-Hump EI and SI shapers, only extreme changes in cable lengths resulted in vibration levels much greater than V_{tol}. For all

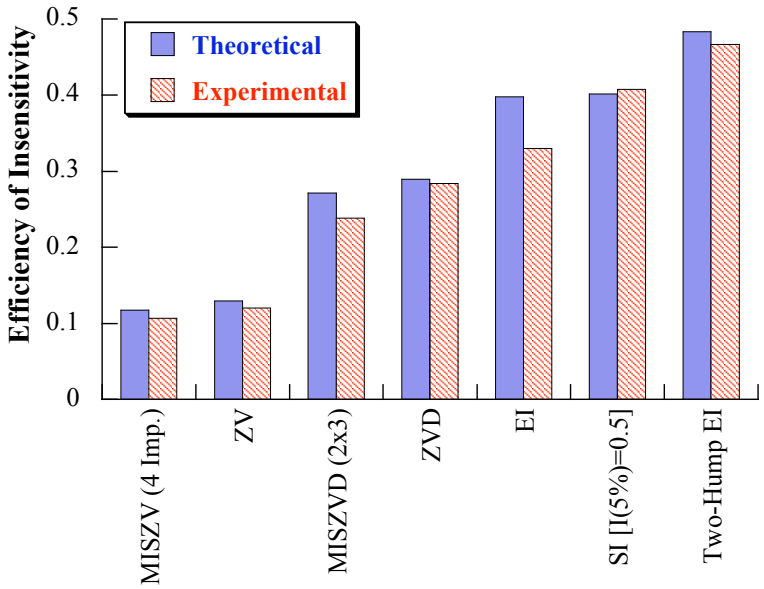

Figure 49: Theoretical and Experimental Efficiencies of Insensitivity for V_{tol} = 5%

shapers, it is important to note that deviation from theory usually occurs such that the actual percentage vibration is slightly larger than predicted by theory. This further reinforces the necessity of including robustness in the shaper design process and suggests that, where applicable, V_{tol} should be set slightly low during the shaper design process to ensure that actual system performance meets the desired vibration tolerances.

A bar graph containing the theoretical and experimental Efficiency of Insensitivity is shown in Figure 49. To calculate the experimental Efficiency of Insensitivity, points within the suppression range of the shaper, but slightly over the tolerable amount of vibration were still considered to be suppressed. For all cases, twice the width between the design frequency and the lowest frequency that was suppressed by the shaper was used as a measure of the Insensitivity. This practice is consistent with the common sense application of the Insensitivity criterion and with the accepted measurement of Insensitivity for experimental results. One can see that the experimentally measured Efficiency of Insensitivities closely match those predicted by the theory, but generally have slightly lower values. The close agreement is expected, considering how closely the experimental sensitivity curves

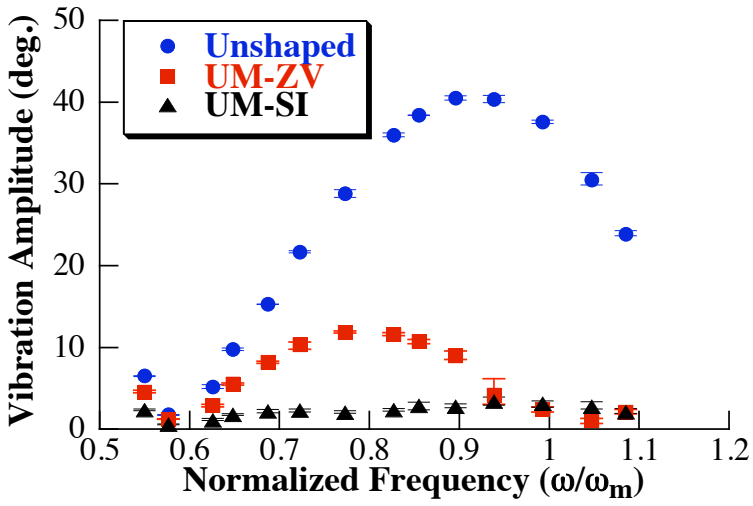

Figure 50: Vibration Amplitudes for Unshaped, UM-ZV, and UM-SI [I(5%) = 0.5] Shaped Motion

in Figures 42 - 48 matched the theoretical. It is also to be expected that the experimental values are slightly lower than the theoretical values. This is a function of the payload oscillation generally being slightly larger than predicted by theory, as seen in Figures 42 - 48.

3.8.2 Robust, Negative Shapers

To rigorously test the various robust, negative shaping methods, representative shapers from each method were experimentally evaluated using the portable bridge crane shown in Figure 40. Input shapers were again designed for a frequency of 0.74 Hz and zero damping. Eight shapers were evaluated using suspension cable lengths varying between 0.38m and 1.57m (15–62 in).

Figure 50 shows the vibration amplitudes for unshaped, UM-ZV shaped, and UM-SI (designed with I(5%) = 0.50) shaped motions. The horizontal axis represents the different natural frequencies resulting from varying the suspension cable length, normalized by the shaper design frequency. The experimental points are the average of three trials, with error bars indicating the minimum and maximum values of vibration for each set. Both the UM-SI and UM-ZV shapers excite much lower levels of vibration than the unshaped

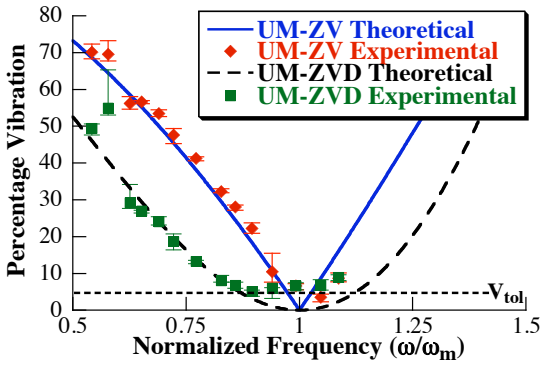

Figure 51: Experimental Sensitivities of UM-ZV and UM-ZVD Shapers

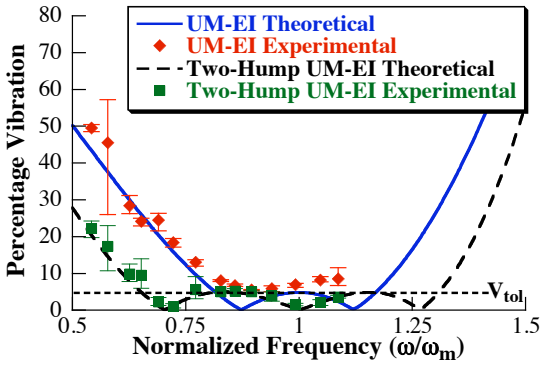

Figure 52: Experimental Sensitivities of UM-EI and Two-Hump UM-EI Shapers

command over the entire range of suspension cable lengths tested. The unshaped command does display a small level of vibration around a normalized frequency of 0.60. This results from the deceleration phase of the unshaped command inducing vibration that cancels the vibration caused by the acceleration phase. As a result, the largest deviation of experimental sensitivity curves from the theoretical and greatest variation in vibration between trials occurs in this region.

Figure 51 shows the theoretical and experimental sensitivity curves for the UM-ZV and UM-ZVD shapers. For both the UM-ZV and UM-ZVD shapers, the experimental results closely match those predicted by theory. Both of these shapers are designed to provide zero vibration at the design frequency. However, neither shaper achieves this theoretical minimum. Figure 52 shows the theoretical and experimental sensitivity curves for the UM-EI and Two-Hump UM-EI. The sensitivity curves for these two shapers also closely match the theoretical predictions.

Figures 53 - 56 show the theoretical and experimental sensitivity curves for a series of SNA-SI shapers, beginning with the UM-SI. Each shaper is designed for $I(5\%) = 0.50$ and the experimental results closely match the theoretical predictions.

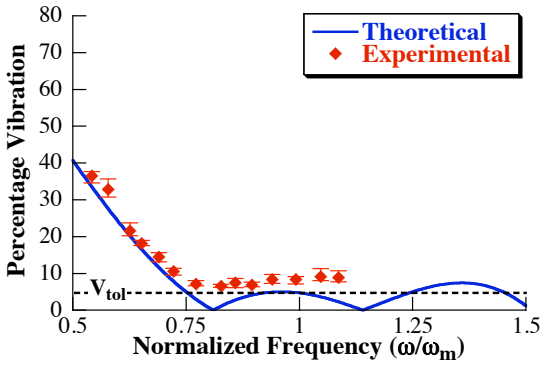

Figure 53: Experimental Sensitivity of UM-SI [$I(5\%) = 0.5$] Shaper

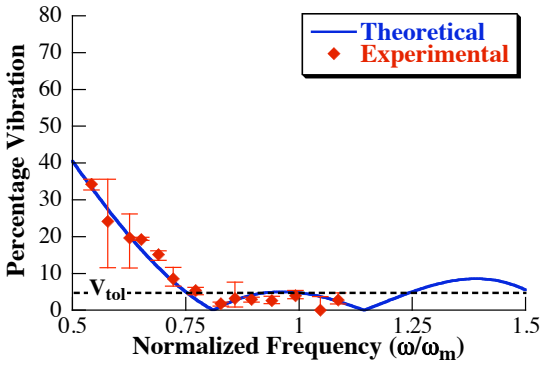

Figure 54: Experimental Sensitivity of SNA(0.25) [$I(5\%) = 0.5$] Shaper

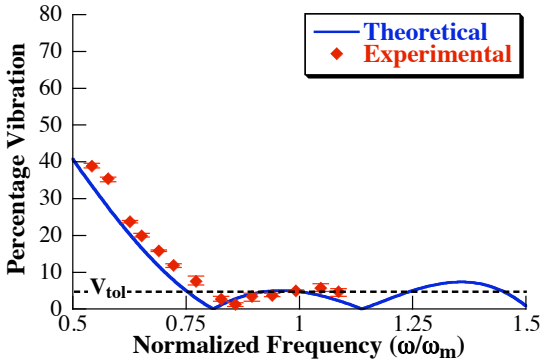

Figure 55: Experimental Sensitivity of SNA(0.50) [$I(5\%) = 0.5$] Shaper

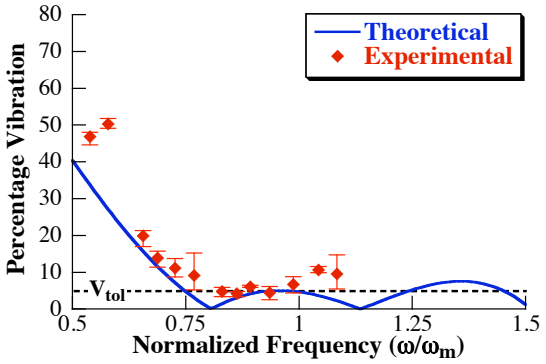

Figure 56: Experimental Sensitivity SNA(0.75) [$I(5\%) = 0.5$] Shaper

3.9 Conclusion

This chapter presented an extensive and thorough review of robust input-shaping techniques, highlighting the fundamental compromises in input shaper design. For all robust shaping methods, shaper duration (and as a result, command rise time) increases with robustness. However, this compromise is not consistent between shaping methods. Some robust shaping methods provide robustness more efficiently, in terms of shaper duration. To aid in the evaluation of this compromise, a new input-shaping performance measure was introduced, the Efficiency of Insensitivity. This measure showed that tolerable vibration methods (EI and SI) most efficiently provide robustness.

Allowing the input shaper to contain negative impulse amplitudes decreased shaper duration and further increased the Efficiency of Insensitivity. However, these improvements come at the cost of increased actuator demands and possible high-mode excitation. A new Specified Negative Amplitude–Specified Insensitivity (SNA–SI) shaper was introduced that provides a continuous spectrum of solutions for the compromise between shaper duration, robustness, and high-mode excitation. The Efficiency of Insensitivity performance measure showed that there are points within the SNA-SI solution space that negotiate the duration/robustness compromise most efficienctly. As such, the measure can be used as a tool during the input shaper design process. Experimental results from a portable bridge crane verified the theoretical predictions.

CHAPTER IV

COMPARISON OF COMMAND FILTERING METHODS FOR VIBRATION REDUCTION

CHAPTER SUMMARY: *This chapter presents a comparison of command filtering methods for vibration reduction in mechanical systems. The three methods compared are lowpass filtering, notch filtering, and input shaping. It is shown that due to larger constraint sets, the minimum duration filter resulting from either filtering method is that of an input shaper with identical stopband constraints. In addition to showing that input shapers are, at worst, equal in duration to a filter, it is shown that input shapers are easier to design and implement.*

As seen in the previous chapters, the command signals used to drive open- or closed-loop machines can have a substantial impact on performance. Digital filtering and input shaping are both well-known methods for shaping the reference commands for flexible systems. Since the introduction of robust input shaping [57], there has been substantial evidence that input shaping is superior to notch and lowpass filtering for applications involving flexible mechanical systems [57, 59]. Much of this evidence has been empirical comparisons between traditional notch filters (Chebychev, elliptical, Parks-McClellan, etc.) and robust input shapers, like those discussed in the previous chapter.

Like input shapers, digital filters are sequences of impulses that are convolved with a baseline command to produce a shaped command. This process is shown in Figure 57. Given that they are implemented in the same way, it is important to clearly understand what is different about the two approaches. The key difference lies in the constraint equations

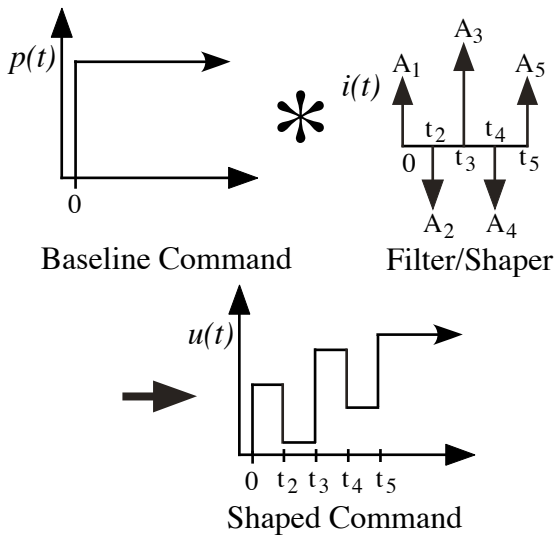

Figure 57: Shaping a Reference Command

that are used to design the impulse sequences.

Given the great number of filters and shapers, and the large number of design strategies and parameters, there is still some uncertainty as to which approach is better. In fact, numerous papers have indicated that notch or lowpass filters should be used for vibration suppression in mechanical systems [10, 14]. This chapter seeks to end this debate by proving that digital notch and lowpass filters are never better than input shapers for suppressing mechanical vibration via command filtering.

4.1 Command Filtering Overview

Notch filters pass certain frequencies with very little attenuation or amplification (passbands). They also suppress a range of frequencies (stopbands). These characterstics are shown graphically in Figure 58. The figure shows the magnitude of the notch filter's Laplace transform on the vertical axis and the frequency on the horizontal axis. The figure shows that at low frequencies, below ω_{P1}, and at high frequencies, above ω_{P2}, the filter maintains frequency amplitudes near one. That is, these frequencies are passed without significant amplitude modification. The height of the magnitude variation (shown as grey areas) determines how accurately the frequency amplitudes are passed through the filter.

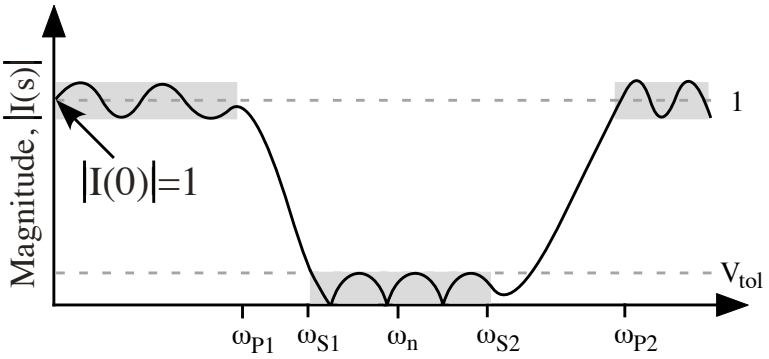

Figure 58: Notch Filter Design Constraints

In the stopband frequency range, between ω_{S1} and ω_{S2}, the filter is required to have a small magnitude Laplace transform. This requirement attenuates these frequencies when the filter is used to shape a command signal going into a flexible system [58, 6, 61]. The height of the stopband range determines how much these frequencies are suppressed. For mechanical systems, this height is the tolerable vibration limit, V_{tol}.

An additional condition is that the magnitude of the Laplace transform equals one at the zero frequency. This ensures that the steady-state gain of the filtering process equals one, forcing the shaped command signal to reach the same steady-state value as the baseline reference command that is being filtered. Note that this constraint is not explicitly stated in many filter design algorithms and is typically solved for in an iterative fashion [10]. In between the passbands and stopbands are transition bands. In these frequency ranges, no requirements are placed on the filter. If a filter can be constructed to meet the constraints shown in Figure 58, then when it is used to filter the baseline reference command, a system driven by the filtered command will have low vibration at frequencies in the stopband.

Lowpass filters are similar to notch filters in that they have a low-frequency passband, a transition band, and a stopband. However, they do not have a high-frequency passband. The stopband extends all the way out to the filter's Nyquist frequency. The design constraints for a lowpass filter are shown in Figure 59. When a lowpass filter is used to shape a baseline reference command, a system driven by the filtered command will have low vibration at frequencies above the cutoff frequency of the stopband and below the Nyquist frequency

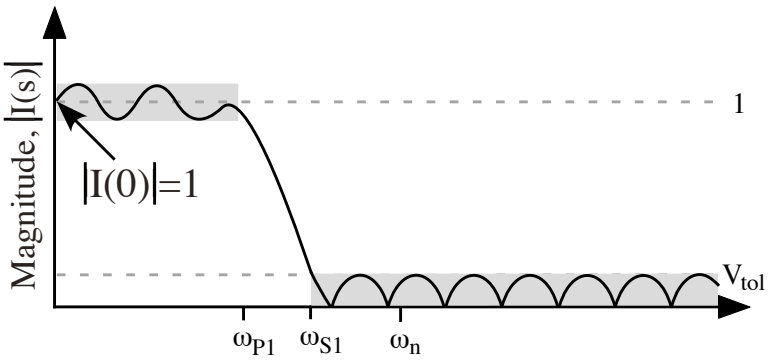

Figure 59: Lowpass Filter Design Constraints

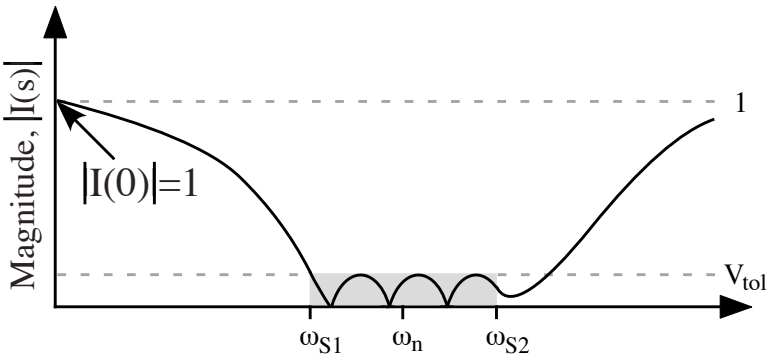

Figure 60: Input Shaper Design Constraints

of the filter.

Input shapers are designed by requiring them to suppress a range of frequencies (stopbands). These design constraints are shown graphically in Figure 60. While input shapers do not have passband requirements, they do have the requirement that the magnitude of the Laplace transform equal one at a frequency of zero. Note that this constraint is not explicitly enforced as a passband constraint, but rather is the result of the constraint that impulse amplitudes sum to one. When an input shaper is used to filter the baseline reference command, a system driven by the filtered command will have low vibration at frequencies in the stop band.

When designing filters or input shapers there are many performance measures that can be considered. For example, the wider the stopband, the more robust the command shaping will be to uncertainties in the vibration frequency that is being targeted for elimination.

However, as the stop band width is increased, the duration of the filter or shaper must increase (assuming all other constraints are held constant) [73, 86]. When the filter or shaper duration increases, this causes a corresponding increase in the command rise time, which in turn, slows down the system rise time.

If the tolerable vibration limit is lowered, then the command shaping will suppress the vibration to a greater extent. Of course on a real system, the limit can only be realistically lowered to the amplitude of the noise in the system [72]. Lowering the vibration limit will also increase the duration of the filter or shaper.

When implementing command shaping on real systems, especially those whose commands need to be shaped in real-time, the number of impulses becomes a concern. Real-time convolution of the baseline reference command with an impulse sequence is very easy; however, it requires one multiplication and one addition for each impulse. Therefore, command shaping with a few impulses incurs very little computational cost, but using hundreds of impulses can burden the control computer. Most robust input shapers contain 3-5 impulses, while filters can often contain 64, 128, or 256 impulses [10].

Given that performance requirements can vary from system to system, this chapter focuses on the two most important requirements: vibration suppression and rise time. These two requirements are naturally opposed to each other. Vibration can be lowered by simply moving the system slower. But, keeping the vibration low and moving faster obviously has its limits. This chapter will prove that for any given vibration suppression requirements, notch and lowpass filters can never be faster than input shapers. Although this evaluation concentrates on proving input shaper superiority in this fundamental design trade-off, it also shows that input shapers are easier to implement.

Section 4.2 describes the design criteria for filters and input shapers. It is then proven that filters cannot perform better than input shapers. Section 4.4 expands on the results of the proof by showing performance comparisons as a function of filter and shaper design parameters. Section 4.6 presents experimental evidence to support the key results.

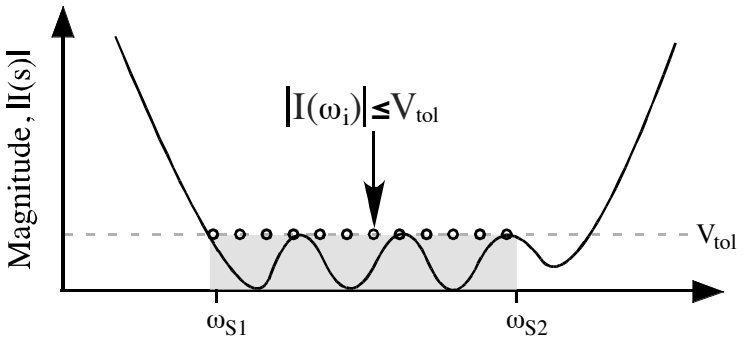

Figure 61: Discrete Frequency Stopband Constraints.

4.2 Filter Design Criteria

4.2.1 Notch Filter Constraints

Figure 58 shows the design requirements for a typical notch filter. There are numerous possible methods for designing a filter to meet the specifications [39, 46]. However, irrespective of the method, the filter must satisfy constraints on the passbands and on the stopband. These constraints can be visualized by placing constraints at numerous discrete frequencies, like the method used for SI, UM-SI, and SNA-SI shapers in Chapter 3. For example, Figure 61 shows the stopband with constraints indicated by circles at several frequencies. At each labeled frequency, the design constraints include a limitation on the magnitude. Given that the notch filter is a sequence of impulses, the normalized vibration amplitude it induces at a frequency ω_n, with an associated damping ratio of ζ, is given by [58]:

$$V(\omega_n, \zeta) = e^{-\zeta\omega_n t_n} \sqrt{[C(\omega_n, \zeta)]^2 + [S(\omega_n, \zeta)]^2} \tag{34}$$

where,

$$C(\omega_n, \zeta) = \sum_{i=1}^{n} A_i e^{\zeta\omega_n t_i} cos(\omega_d t_i) \tag{35}$$

$$S(\omega_n, \zeta) = \sum_{i=1}^{n} A_i e^{\zeta\omega_n t_i} sin(\omega_d t_i) \tag{36}$$

A_i and t_i are the amplitudes and time locations of the n impulses that compose the filter. Therefore, to suppress the vibration to below the tolerable level at a frequency of ω_n, the

notch filter impulses must satisfy the following equation:

$$V(\omega_n, \zeta) \leq V_{tol} \tag{37}$$

To suppress the vibration over the entire stopband range, the design constraints must include multiple versions of the above equation, each enforced at a different frequency. As the number of suppressed frequencies approaches infinity, the constraints ensure that every frequency within the stopband is suppressed. This theoretically-possible set of constraints on the stopband can be stated as:

$$SBT : V(\omega_i, \zeta) \leq V_{tol}, \quad i = 1, 2, \ldots, \infty \tag{38}$$

where the frequencies ω_i range from the low end of the stopband, ω_{S1}, to the high end, ω_{S2}. Of course an infinity of equations cannot actually be used, but it has been shown that just a few such constraints will effectively limit the vibration [73]. Therefore, the design constraints in the above equation can be replaced with the practical set of constraints given by:

$$SBP : V(\omega_i, \zeta) \leq V_{tol}, \quad i = 1, 2, \ldots, m \tag{39}$$

where m is finite.

The design constraints given above are only one way to enforce the stopband requirements. This approach is used to illustrate the idea of constraint equations because it is straightforward. Many other approaches exist and they can lower the number of constraints by, for example, limiting the vibration at only the peak values of the filter's Laplace magnitude plot within the stopband [73]. So, a more general statement of the stopband constraints is simply:

$$SB : V(\omega_i, \zeta) \leq V_{tol}, \quad \omega_{S1} \leq \omega_i \leq \omega_{S2} \tag{40}$$

The exact method for formulating and solving the constraints in (40) is not important for the purposes of this chapter. What is important to understand is that a set of constraint equations must be enforced to limit vibration in the stopband.

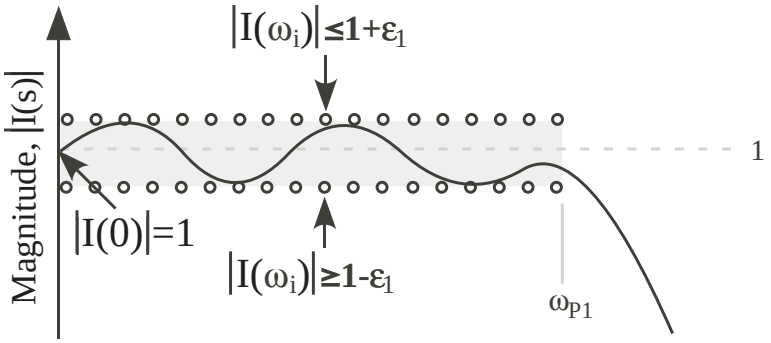

Figure 62: Discrete Frequency Passband Constraints.

The design requirements for the notch filter's passbands are more complicated. Figure 62 shows the requirements for the low-frequency passband that runs from 0 to ω_{P1}. Again, discrete constraints are used to illustrate the requirements. The passband has constraints that limit the maximum value of the magnitude, just as in the stopband. The constraints can be represented as a theoretically-possible, or a practical set of constraints, as was done in (38) and (39). However, the design constraints do not need to take those specific forms, so we represent the constraints on the upper level of the passband as:

$$PB1U : V(\omega_i, \zeta) \leq 1 + \epsilon_1, \quad 0 \leq \omega_i \leq \omega_{P1} \tag{41}$$

where ϵ_1 is some small value.

The passband also has constraints that require the magnitude of the Laplace transform to be above a certain level. Again, these constraints are shown at a finite number of frequencies in Figure 62. A general expression for the constraints on the lower value of the filter's Laplace magnitude is:

$$PB1L : V(\omega_i, \zeta) \geq 1 - \epsilon_1, \quad 0 \leq \omega_i \leq \omega_{P1} \tag{42}$$

The passband at the higher frequencies requires constraints similar to those at the lower frequencies:

$$PB2U : V(\omega_i, \zeta) \leq 1 + \epsilon_2, \quad \omega_{P2} \leq \omega_i \tag{43}$$

$$PB2L : V(\omega_i, \zeta) \geq 1 - \epsilon_2, \quad \omega_{P2} \leq \omega_i \tag{44}$$

To ensure unity gain of the filtering process, the Laplace transform magnitude at the zero frequency must equal one. This is equivalent to requiring the impulse amplitudes to sum to one:

$$SS1 : \sum A_i = 1 \tag{45}$$

Note again that this constraint is not explicitly included in many filter design methods, but must be enforced for mechanical systems to ensure the system is moved to the same final state as the unfiltered command. This is typically done as part of an iterative design process [10].

The entire set of constraints for a typical notch filter can now be stated as:

$$VIBNF : \{SB, PB1U, PB1L, PB2U, PB2L, SS1\} \tag{46}$$

Many filter design algorithms require the designer to choose the filter duration as part of the design parameters. Then, the deviation from the vibration constraints is minimized. When a solution is obtained, the vibration properties of the filter are then examined to see if they are satisfactory. If they are not, then the filter duration must be increased and the problem is resolved.

Note that the constraints illustrated in Figure 58 can be modified in numerous ways. For example, the magnitude in the passbands does not need to be symmetrical above and below 1, nor do the two passbands need to be equal in height. Furthermore, the passband and stopband areas do not need to be rectangular. Some of these more esoteric design constraints are illustrated in Figure 63. Any such deviations from the typical constraints would change only the details of the constraints, but not the fundamental nature of the constraint set. The constraints could still be represented by the set given in (46); however the individual passband and stopband constraints that compose the set would be modified accordingly.

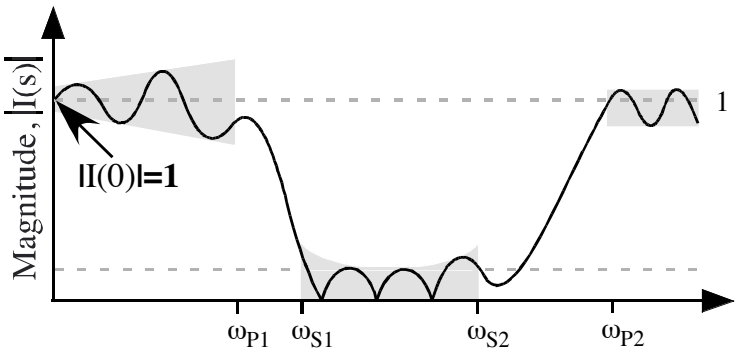

Figure 63: Examples of Esoteric Notch Filter Design Constraints

4.2.2 Lowpass Filter Constraints

Figure 59 shows the design requirements for a typical lowpass filter. The vibration constraints for a lowpass filter are similar to a notch filter, but they do not include a high-frequency passband constraint. Therefore, the low-frequency passband constraints are:

$$PB1U : V(\omega_i, \zeta) \leq 1 + \epsilon_1, \quad 0 \leq \omega_i \leq \omega_{P1} \tag{47}$$

and

$$PB1L : V(\omega_i, \zeta) \geq 1 - \epsilon_1, \quad 0 \leq \omega_i \leq \omega_{P1} \tag{48}$$

The stopband constraints are:

$$SBLP : V(\omega_i, \zeta) \leq V_{tol}, \quad \omega_{S1} \leq \omega_i \tag{49}$$

Note that the stopband constraints for a lowpass filter contain the stopband constraints for a notch filter, but also extend the constraints to all higher frequencies (below the Nyquist frequency of the filter). The filter must also satisfy the requirement of unity gain:

$$SS1 : \sum A_i = 1 \tag{50}$$

The entire set of constraints for a typical lowpass filter can now be stated as:

$$VIBLPF : \{SBLP, PB1U, PB1L, SS1\} \tag{51}$$

4.2.3 Input Shaper Constraints

The vibration constraints for an input shaper do not include passband constraints. The only design constraints are those on the stopband. For the common case of a constant vibration limit in the passband, these constraints are the same as for the notch filter passband:

$$SB : V(\omega_i, \zeta) \leq V_{tol}, \quad \omega_{S1} \leq \omega_i \leq \omega_{S2} \tag{52}$$

An input shaper must also satisfy the requirement of unity gain:

$$SS1 : \sum A_i = 1 \tag{53}$$

The entire set of vibration constraints for a typical input shaper can now be stated as:

$$VIBIS : \{SB, SS1\} \tag{54}$$

4.3 Proof of Input Shaper Superiority

Theorem: The space of lowpass filter solutions and the space of notch filter solutions are subsets of the space of input shaper solutions. Therefore, for a given set of vibration suppression constraints and selection of the minimum duration solution, a notch filter or a lowpass filter can never be shorter in duration than an input shaper.

Proof: For a notch filter, the vibration constraints are the set:

$$VIBNF : \{SB, PB1U, PB1L, PB2U, PB2L, SS1\} \tag{55}$$

For a lowpass filter the vibration constraints are the set:

$$VIBLPF : \{SBLP, PB1U, PB1L, SS1\} \tag{56}$$

For an input shaper, the vibration constraints are the set:

$$VIBIS : \{SB, SS1\} \tag{57}$$

Given that the constraint equations for an input shaper, (57), are a necessary subset of the constraints for a notch filter, (55), and a necessary subset of the constraints for a lowpass

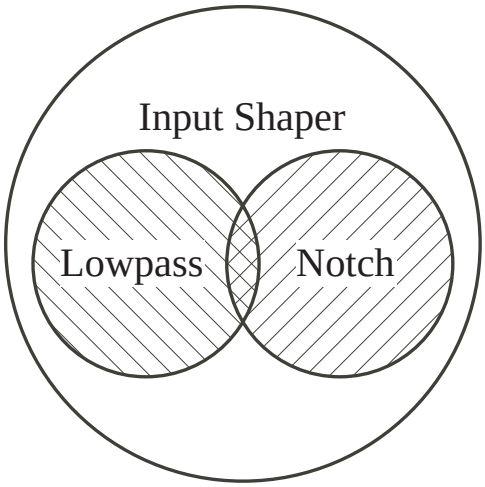

Figure 64: Graphical Representation of the Possible Solution Space

filter, (56), then any solution to the filter constraints is also a solution to the input-shaper constraints. However, the converse is not true. This means that the space of lowpass filter solutions and the space of notch filter solutions are subsets of the space of input shaping solutions. The set of possible solutions for the input-shaper constraints is therefore equal to or larger than the possible solution set for the filter constraints. This relationship is shown graphically in Figure 64.

Given that the filtered/shaped command duration will be increased by the duration of the filter or shaper used, the minimum duration solution should be selected. This selection process is captured by minimizing the time of the last impulse of the filter or shaper:

$$min(t_n) \tag{58}$$

Using this selection criteria, a notch filter or a lowpass filter can never be shorter in duration than an input shaper that satisfies the same vibration suppression constraints. QED.

Implications: While the proof guarantees that lowpass and notch filters cannot be shorter in duration than an input shaper with identical stopband and selection requirements, it is easy to see that input shapers have significantly fewer requirements to satisfy. Therefore, in any practical design scenario, the input shaper will be significantly shorter than the corresponding filter. In fact, the only way to get a notch filter that has performance close

to an input shaper is to shrink the passbands down to zero frequency width. But this, of course, means that we are designing an input shaper and not a notch filter. This effect of shrinking the passbands is demonstrated, along with other performance evaluations, in the next section.

A lowpass filter suppresses all frequencies higher than the lowest frequency in the stopband. Only in the limit of zero passband width and ideal selection of the sampling frequency does the duration of a lowpass filter approach the duration of an input shaper. However, this again means that we are designing an input shaper, not a lowpass filter. This effect is also demonstrated in the next section.

4.4 Filter Performance Comparison

The proof in the previous section demonstrated that filters can never provide vibration suppression faster than an input shaper. However, it does not indicate how much better input shapers perform. This section will present a performance comparison that documents the degree of input shaper superiority in terms of rise time, robustness, and ease of implementation. The comparison will be performed assuming that the nominal system frequency is 1 Hz.

4.4.1 Lowpass Filters

A series of lowpass filters were designed using an iterative algorithm similar to that found in [10] with a stop band beginning at $\omega_{S1} = 0.8$ Hz and $V_{tol} = 5\%$. The pass band was limited to be within ±5% of 1 ($\epsilon_1 = 0.05$). Figure 65 shows the filter duration as a function of lowpass edge frequency, ω_{P1}, at four different sampling rates, 10, 20, 50 and 100 Hz. Notice that the filters, despite being different order, are similar in duration. This suggests that while decreasing filter order by decreasing sampling rate may ease the computational burden of both filter solution and implementation, it does not significantly affect time duration of the filter. This is an important point, as any command shaped by the filter is lengthened by the filter duration. As a result, increasing filter duration slows system response.

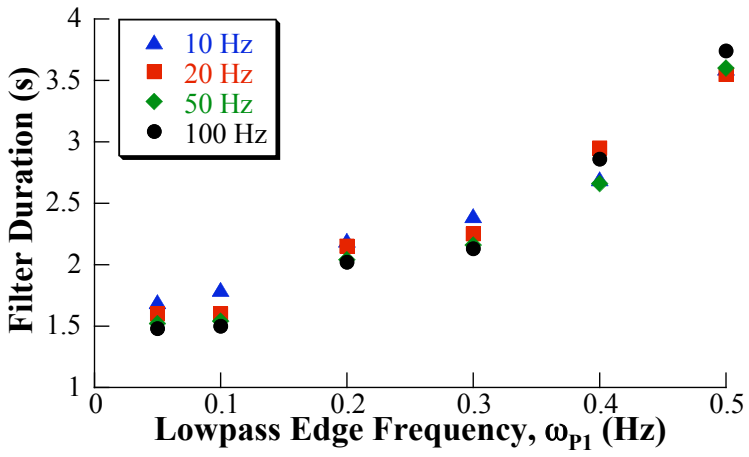

Figure 65: Lowpass Filter Duration as a Function of Passband Size and Sampling Rate ($\omega_{S1} = 0.8$Hz)

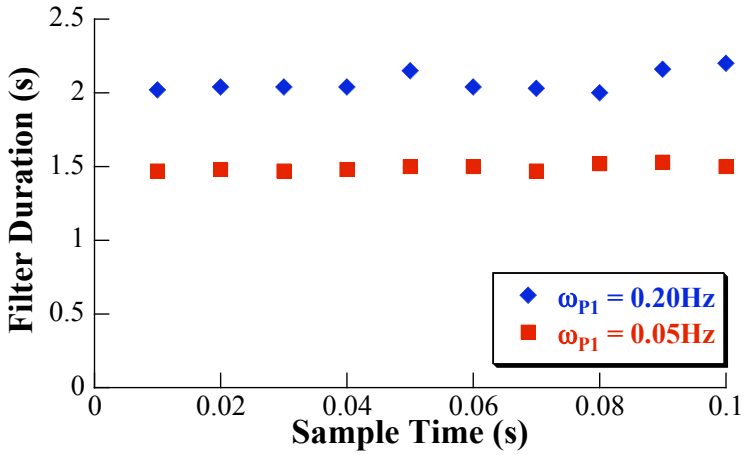

Figure 66: Lowpass Filter Duration as a Function of Sampling Frequency

The nearly constant filter duration (independent of sampling frequency) is demonstrated further in Figure 66. The plot shows filter duration as a function of the filter's sampling frequency (expressed as sample time in the figure to allow easier visualization). The plot shows the effect for two passband edge frequencies, $\omega_{P1} = 0.2$ Hz and $\omega_{P1} = 0.05$ Hz, with all design parameters identical to those above.

The low pass filters shown in Figures 65 and 66 are typical of filters that might be used to shape the commands of a system with a natural frequency of 1 Hz, providing robustness to a 20% decrease in frequency. An input shaper that provides the same level of robustness to frequency decreases is the EI shaper [72], which is significantly shorter in duration. Its

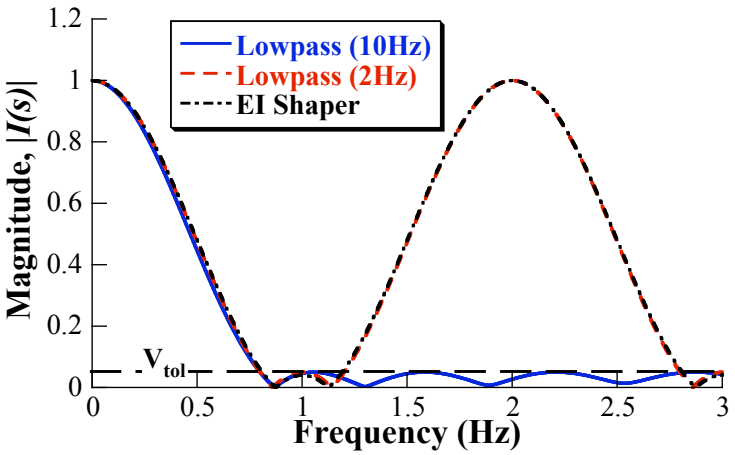

Figure 67: Comparison of Lowpass Filters and EI shaper

duration is only one second for a system with natural frequency of 1 Hz.

A comparison of the magnitude plots of the EI shaper and a lowpass filter designed as above with a sampling frequency of 10 Hz and passband edge at 0.05 Hz is shown in Figure 67. Notice that around 1 Hz both the filter and the EI shaper provide similar stopband performance. The two have nearly identical robustness to decreases in system natural frequency. However, the stopband constraints of the EI Shaper, SB, stop at 1.2 Hz., while the stopband constraints for the lowpass filter, $SBLP$, extend all the way to the Nyquist frequency. Therefore, the EI curve is free to assume any shape beyond the stopband. As a result of this freedom the EI Shaper can be much shorter. For example, the lowpass filter (with a 10 Hz sampling frequency) shown in Figure 67 is 50% longer than the EI shaper.

Even if the sampling frequency of the filter is lowered such that its magnitude curve more closely resembles that of the EI shaper, its duration is still approximately 50% longer. The magnitude curve of this filter is also shown in Figure 67. In this case, the stopband constraint width is actually smaller than the EI shaper (between 0.8 Hz and the 1 Hz Nyquist Frequency for the filter versus 0.8–1.2 Hz for the EI shaper). Even when the passband is narrow like in this example, the duration is longer than the EI shaper. As seen in Figure 65, increasing the passband size will increase the duration of the filters, further slowing

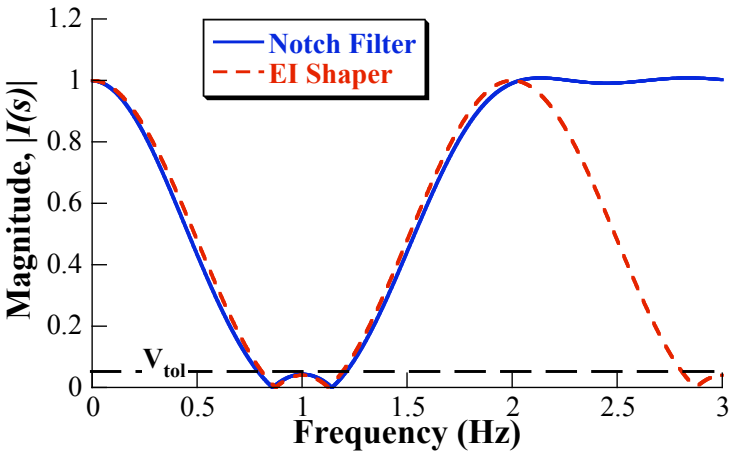

Figure 68: Comparison of Notch Filter and EI shaper

the filter in comparison to the EI shaper. Decreasing the passband width will, in the limit, create a lowpass filter identical in duration to the EI shaper. However, as the passband approaches zero, the result is, by definition, no longer designing a lowpass filter.

4.4.2 Notch Filters

The trends developed in the previous section will also generally hold for notch filters. The time duration of filters is typically not heavily dependent on the sampling frequency, but is dependent on the width of the pass and stop bands.

Figure 68 shows the magnitude plot of a notch filter designed with a low-passband edge of 0.05 Hz, a stopband between 0.8 and 1.2 Hz, a high-passband edge at 2 Hz, and a sampling frequency of 10 Hz. The tolerable level of vibration was 5% and the passband was constrained to be between 0.95 and 1.05 ($\epsilon_1 = \epsilon_2 = 0.05$). Also shown in this figure is an EI shaper designed to suppress vibration at 1 Hz. Despite its narrow low passband width and identical stop band constraints as the EI shaper, the notch filter is 122% longer than the EI shaper (2.22s for the Notch Filter vs. 1s for the EI shaper). The dramatically longer duration of the notch filter is due to the upper passband constraints of the notch filter, constraints that the EI shaper does not have to fulfill.

If the sampling frequency is decreased to 2 Hz, and the passband widths are forced to near zero, then the notch filter approaches the EI shaper in duration. In the limit, the

Table 5: Design Parameters for Shaping Methods

	Stopband	Low Passband	High Passband
Notch Filter	$\omega_{S1}, \omega_{S2}, V_{tol}$	ω_{P1}, ϵ_1	ω_{P2}, ϵ_2
Lowpass Filter	ω_{S1}, V_{tol}	ω_{P1}, ϵ_1	
Input Shaper	$\omega_{S1}, \omega_{S2}, V_{tol}$		

EI shaper and notch filter are identical because the notch filter does not need to pass any frequencies; it is an input shaper. However, the notch filter is never shorter in duration that the EI Shaper. This is an important distinction, as the design and implementation of the EI shaper is much easier. It is known in closed form and contains only three impulses. So, even if the duration and magnitude curves of the EI shaper and notch filter are identical, the EI shaper is the preferable solution. For sampling frequencies different than 2 Hz, notch filters with identical constraints as above are always longer than the EI shaper.

4.5 Ease of Implementation

Given that digital filters and input shapers are implemented in the same manner, it might seem that the ease of implementation would be similar. However, there are two important aspects to consider i) ease of generating the impulse sequence and ii) run-time computational burden.

Filters must satisfy the input shaper constraints equations, plus some additional constraints. Therefore, they must be more difficult to generate in a computational sense. In addition, an engineer designing a filter must also choose more design parameters than when designing an input shaper. This is illustrated by the size of the constraint sets in (55)–(57) and the list of design parameters for each command-shaping method shown in Table 5.

An additional benefit from the lower number of constraints is the ability to solve for impulse amplitudes and times in closed-form. In fact, there are closed-form solutions for many input shapers [58, 72, 86, 88], including some addressing additional constraints such as fuel use [64] and transient deflection [47]. No such closed-form solutions exist for digital filers [39].

Figure 69: Portable Bridge Crane

An additional consideration is the implementation of the filters on real machines. Filters designed using traditional filtering techniques, originally developed for signal processing, do not include any form of actuator constraints. As such, commands shaped with these filters may not be realizable on a given system. Input shapers do contain constraints that create realizable commands. For example, shaper impulses amplitudes are limited to be positive [86] or explicitly constrained to create commands within the bounds of the unshaped command [88].

4.6 Experimental Results

To experimentally compare lowpass filters, notch filters, and input shapers, the portable bridge crane in Figure 69 was used. Details of the crane can be found in Appendix A. For the experiments presented in this section, the command filters were designed for a suspension cable length of 0.76m (30in). To examine the robustness of the filters to changes in frequency, the cable length was varied between 0.38m (15in) and 1.52m (60in). The

The experimental results presented in Section 4.6 were completed with generous help from undergraduate researcher Anderson Smith.

Table 6: Parameters for Experimental Comparison

	Stopband	Low Passband	High Passband
Notch Filter 4.29s	$\omega_{S1} = 0.8\omega_n$ $\omega_{S2} = 1.2\omega_n$ $V_{tol} = 5\%$	$\omega_{P1} = 0.05\omega_n$ $\epsilon_1 = 0.05$	$\omega_{P2} = 2\omega_n$ $\epsilon_2 = 0.05$
Lowpass Filter 2.88s	$\omega_{S1} = 0.8\omega_n$ $V_{tol} = 5\%$	$\omega_{P1} = 0.05\omega_n$ $\epsilon_1 = 0.05$	
EI Shaper 1.82s	$w_{S1} = 0.8\omega_n$ $w_{S2} = 1.2\omega_n$ $V_{tol} = 5\%$		

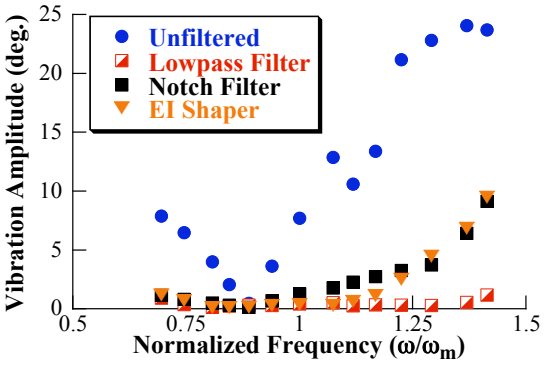

Figure 70: Experimental Vibration Amplitudes

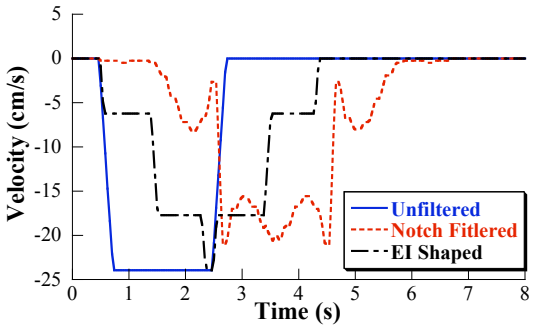

Figure 71: Unfiltered, Notch Filtered, and EI-shaped Commands

additional parameters used to design the lowpass and notch filters are shown in Table 6. The duration of each filter is also indicated in the table.

Figure 70 shows the amplitudes of payload oscillation excited by the unfiltered, lowpass filtered, notch filtered, and EI-shaped commands. The points are the average of three trials. The horizontal axis is normalized by the design frequency, ω_m. The unfiltered command, a 2.25s trapezoidal velocity profile shown in Figure 71, excited significant vibration over much of the range of cable lengths tested. All command filtering methods produced significantly lower payload oscillation.

The lowpass filter provided greater attenuation of payload oscillation at high frequencies, as expected. It also closely matched the theoretical prediction of magnitude, as shown in Figure 72. The error bars on this plot, and Figures 73 and 74, represent the minimum

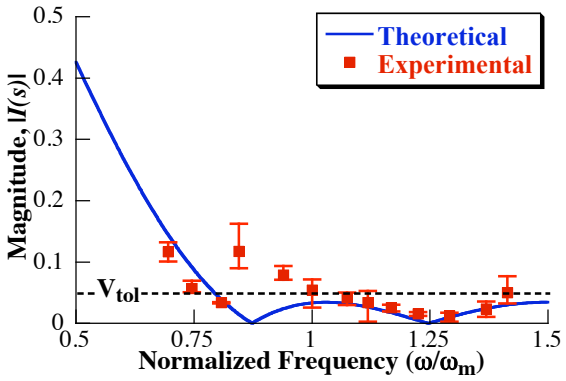

Figure 72: Lowpass Filter Magnitude Plot

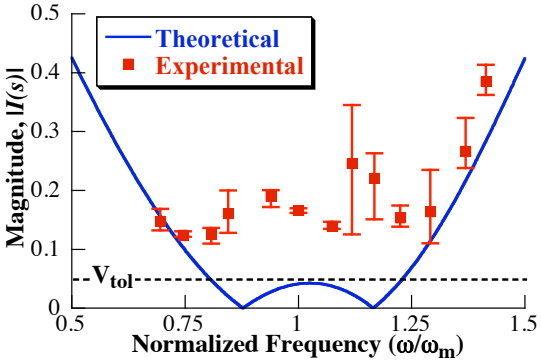

Figure 73: Notch Filter Magnitude Plot

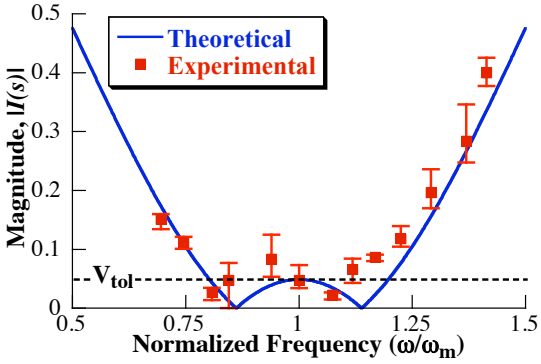

Figure 74: EI Shaper Magnitude Plot

and maximum vibration for each cable length in the data set. This vibration-supressing performance does not come without cost. The duration of the filter was 2.88s.

The theoretical and experimental magnitude curves of the notch filter are shown in Figure 73. The variance between experimental results and the theoretical prediction is greater than that seen for the lowpass filter. This is a result of the more aggressive nature of the notch filtered command, shown in Figure 71. This command is difficult to accurately track. This is further indicated by the larger range of vibration seen at each suspension cable length for the notch shaper, compared to the lowpass filtered and EI-shaped trials. The deviation from the theoretical is even more troubling when the duration of the filter is considered; it was 4.29s in duration.

Shown in Figure 74 are theoretical and experimental magnitude curves for the EI shaper. The experimental results more closely match the theoretical than the notch filter. The less

aggressive EI-shaped command, shown in Figure 71, is easier to track and excites less vibration than the notch filtered command, despite the similarity in theoretical values. It is also much shorter; the duration of the EI shaper used in the experiments was only 1.82s.

4.7 Conclusion

The constraints used to design lowpass filters, notch filters, and input shapers were outlined. It was shown that input shapers must satisfy fewer constraints than both lowpass and notch filters, allowing a larger solution space, that includes the solution spaces of the lowpass and notch filters. This proves that the filters can never be shorter in duration than input shapers. In addition, input shapers were shown to be easier to design, compute, and implement. Experimental results from a portable bridge crane verified the key theoretical predictions.

CHAPTER V

TOWER CRANE DYNAMICS

CHAPTER SUMMARY: *This chapter examines the dynamics of a mobile tower crane and a tower crane with double-pendulum payload dynamics. The analysis distills the essential properties of each, but does not seek to be a complete analysis. The models are presented as references for examples throughout this thesis. In addition, a precise mathematical model is not necessary for many of the techniques presented in this thesis. For many, a rough estimate of system natural frequencies and damping ratios is all that is needed.*

5.1 Mobile Tower Crane Model

A sketch of a mobile tower crane with an omni-directional base is shown Figure 75. In this model, the inputs are X and Y base translation, base rotation, ψ, jib rotation relative to the base, θ, the trolley position along the jib, r, and the cable length, l. Important outputs are the hook deflection angle in the radial direction, ϕ, and in the tangential direction, β. The model assumes that the crane is significantly more massive than the payload, such that the payload motion is unable to affect the motion of the crane itself. The model also assumes that the suspension cable is massless and inelastic and that the payload swing is undamped.

Using a commercial dynamics package, the equations of motion for this system were

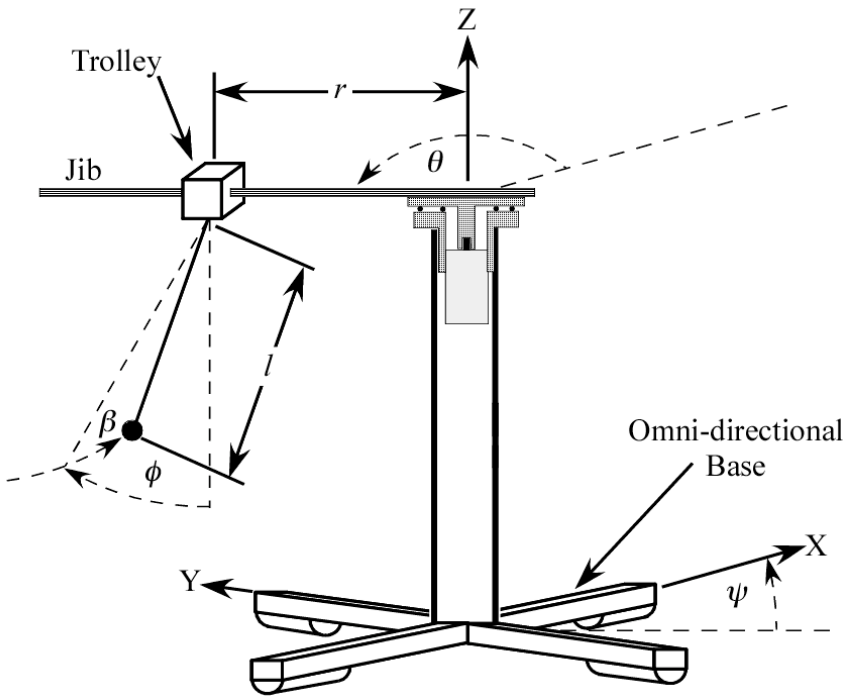

Figure 75: Model of a Mobile Tower Crane

developed. The equation of motion describing β is:

$$\ddot{\beta} = \frac{1}{l}\Big[(r(\dot{\psi}+\dot{\theta})^2 - \ddot{r})\sin\beta\sin\phi - 2\dot{l}((\dot{\psi}+\dot{\theta})\sin\phi + \dot{\beta}) - g\sin\beta\cos\phi - 2\dot{l}((\dot{\psi}+\dot{\theta})\sin\phi + \dot{\beta}) + \ldots \tag{59}$$

$$+ l\dot{\phi}\sin\beta((\dot{\psi}+\dot{\theta})\sin\beta\cos\phi - \dot{\phi}\cos\beta) - l((\dot{\psi}+\dot{\theta})\sin\phi + (\dot{\psi}+\dot{\theta})\dot{\phi}\cos\phi) + \ldots$$

$$+ \ddot{x}(\cos\psi(\sin\theta\cos\beta + \cos\theta\sin\beta\sin\phi) + \sin\psi(\cos\theta\cos\beta - \sin\theta\sin\beta\sin\phi)) + \ldots$$

$$- \ddot{y}(\cos\psi(\cos\theta\cos\beta - \sin\theta\sin\beta\sin\phi) - \sin\psi(\sin\theta\cos\beta + \cos\theta\sin\beta\sin\phi)) + \ldots$$

$$+ \cos\beta\Big(-l\cos\phi(\dot{\psi}+\dot{\theta})((\dot{\psi}+\dot{\theta})\sin\beta\cos\phi - \dot{\phi}\cos\beta) + 2\dot{r}(\dot{\psi}+\dot{\theta}) + r(\ddot{\psi}-\ddot{\theta})\Big)\Big]$$

and the equation describing ϕ is:

$$\ddot{\phi} = \frac{1}{l\cos\beta}\Big[(r(\dot{\psi}+\dot{\theta})^2 - \ddot{r})\cos\phi + 2\dot{l}((\dot{\psi}+\dot{\theta})\sin\beta\cos\phi - \dot{\phi}\cos\beta) - \ddot{x}\cos(\psi+\theta)\cos\phi + \ldots \tag{60}$$

$$- \ddot{y}\sin(\psi+\theta)\cos\phi + ((\dot{\psi}+\dot{\theta})\sin\phi + \dot{\beta})((\dot{\psi}+\dot{\theta})\cos\beta\cos\phi + \dot{\phi}\sin\beta) - g\sin\phi + \ldots$$

$$- l((\dot{\psi}+\dot{\theta})\dot{\phi}\sin\beta\sin\phi - (\ddot{\psi}+\ddot{\theta})\sin\beta\cos\phi - \dot{\beta}\dot{\phi}\sin\beta - (\dot{\psi}+\dot{\theta})\dot{\beta}\cos\beta\cos\phi)\Big]$$

Given the complexity of (59) and (60), examination of several special cases can provide confidence in their validity. Two cases are of particular interest, as they represent widely used cranes. In a case that mimicks bridge cranes, only base motion in the X and Y directions is allowed, and r, θ and ψ are set equal to zero. This reduces the equations to:

$$\ddot{\phi} = \frac{1}{l\cos\beta}\Big[2l\dot{\beta}\dot{\phi}\sin\beta - 2\dot{l}\dot{\phi}\cos\beta - \ddot{x}\cos\phi - g\sin\phi\Big], \tag{61}$$

and

$$\ddot{\beta} = \frac{1}{l}\Big[\ddot{x}\sin\beta\sin\phi - \ddot{y}\cos\beta - l\dot{\phi}^2\sin\beta\cos\beta - g\sin\beta\cos\phi - 2\dot{l}\dot{\beta}\Big]. \tag{62}$$

In the second case, no base motion is allowed. This represents a standard tower crane. Equations (60) and (59) reduce to:

$$\begin{aligned}\ddot{\phi} = \frac{1}{l\cos\beta}\Big[&(r\dot{\theta}^2 - \ddot{r})\cos\phi + 2\dot{l}(\dot{\theta}\sin\beta\cos\phi - \dot{\phi}\cos\beta) + \\ &+ l(\dot{\theta}\sin\phi + \dot{\beta})(\dot{\theta}\cos\beta\cos\phi + \dot{\phi}\sin\beta) - g\sin\phi + \\ &- l(\dot{\theta}\dot{\phi}\sin\beta\sin\phi - \dot{\theta}\sin\beta\cos\phi - \dot{\beta}\dot{\phi}\sin\beta - \dot{\theta}\dot{\beta}\cos\beta\cos\phi)\Big],\end{aligned} \tag{63}$$

and

$$\begin{aligned}\ddot{\beta} = \frac{1}{l}\Big[&l\dot{\phi}\sin\beta(\dot{\theta}\sin\beta\cos\phi - \dot{\phi}\cos\beta) - g\sin\beta\cos\phi + \\ &- (r\dot{\theta}^2 - \ddot{r})\sin\beta\sin\phi - 2\dot{l}(\dot{\theta}\sin\phi + \dot{\beta}) - l(\ddot{\theta}\sin\phi + \\ &+ \dot{\theta}\dot{\phi}\cos\phi) - \cos\beta(2\dot{r}\dot{\theta} + r\ddot{\theta} + l\dot{\theta}\cos\phi(\dot{\theta}\sin\beta\cos\phi - \dot{\phi}\cos\beta))\Big].\end{aligned} \tag{64}$$

5.1.1 Experimental Verification of Mobile Tower Crane Model

To test the validity of the equations of motion presented in the previous section, the mobile tower crane shown in Figure 76 was used. The tower portion of the crane, shown in Figure 76(a), is approximately 2m tall with a 1m jib arm. The jib is actuated by Siemens synchronous, AC servomotors and is capable of 340° slewing rotation. The trolley moves radially along the jib via a lead screw, and a hoisting motor controls the suspension cable

(a) Mobile, Portable Tower Crane **(b)** Mobile, Portable Tower Crane Base

Figure 76: A Mobile, Portable Tower Crane

length. A Siemens digital camera is mounted to the trolley and records the swing deflection of the payload [30]. In addition, the crane has teleoperation capabilities that allow it to be operated in real-time from anywhere in the world via the Internet [30, 23].

Base mobility is provided by DC Motors with omni-directional wheels attached to each support leg. The base is under PD feedback control using two HiBot[1] *TiTechSH2 Tiny Controllers*®, each controlling two motors. These SuperH™-2 based microcontrollers use feedback from motor shaft mounted encoders to generate PWM signals for each motor driver. The DC motors are each driven with a HiBot *1Axis DCMotor Module*®, each of which is capable of providing 10A nominal current. A close-up view of the mobile base is shown in Figure 76(b).

Table 7 summarizes the performance characteristics of the mobile crane. It should be noted that most of these limits are enforced via software and are not the physical limitations

[1] http://www.hibot.co.jp/

Table 7: Mobile Tower Crane Performace Limits

Parameter	Min	Max	Units
Cable Length, l	70	170	cm
Slew Velocity, $\dot{\theta}$	-0.35	0.35	$\frac{rad}{s}$
Slew Acceration, $\ddot{\theta}$	-0.7	0.7	$\frac{rad}{s^2}$
Radial Velocity, $\dot{r}$	-14	14	$\frac{cm}{s}$
Radial Acceleration, $\ddot{r}$	-120	120	$\frac{cm}{s^2}$
Base Velocity, $\dot{x}, \dot{y}$	-25	25	$\frac{cm}{s}$

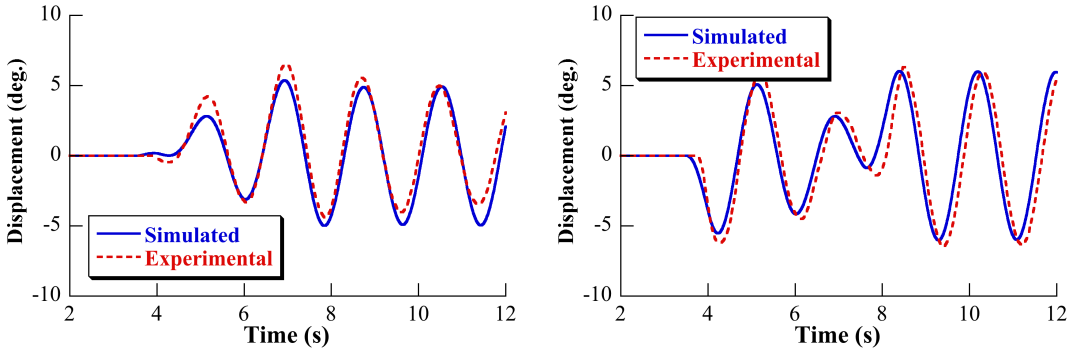

(a) ϕ (radial) Response **(b)** β (tangential) Response

Figure 77: Experimental Verification for 90° Jib Rotation

of the system. This was done to more closely match the operational parameters of full-sized tower cranes. More details of this mobile tower crane can be found in Appendix A.

Figures 77(b) and 77(a) show simulated and experimental responses of the crane to a 90° rotation in jib position using a trapezoidal velocity profile. The move begins at approximately $T = 3.5$s and has a duration of approximately 5.0s. The experimental responses match the simulation fairly well. The majority of the discrepancy can be attributed to damping in the real system that is not included in the model. This discrepancy is especially evident in Figure 77(a).

Figure 78 is a sketch outlining another one of the test cases, in which there is linear base motion, a rotational slew of the jib, and radial motion of the trolley. With a suspension cable length of 124.5cm, the base moved at a velocity of approximately 25cm/s for a distance of 30cm. During the same time, the jib rotated approximately 90° and the trolley moved

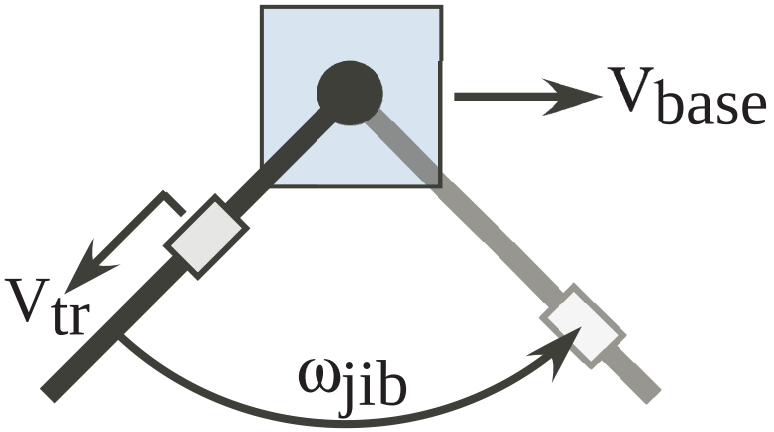

Figure 78: Sketch of Model Verification Commands

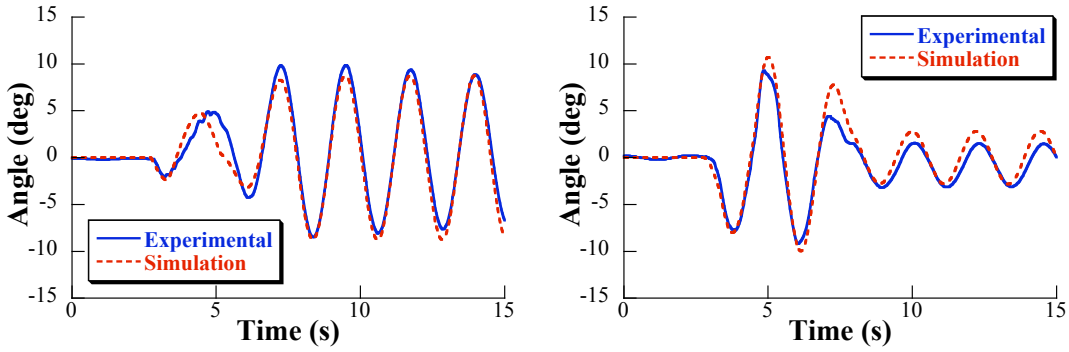

(a) ϕ (radial) Response **(b)** β (tangential) Response

Figure 79: Experimental Verification of a Mobile Tower Crane Model

along the jib at approximately 14cm/s for 30cm. The payload swing angle responses to these motions are shown in Figures 79(a) and 79(b). One can see from these figures that the experimental responses closely match the responses predicted by theory. The slight discrepancies between the predicted and actual responses can be attributed to imperfect tracking of reference commands, measurement error, structural flexibility not accounted for in the model, and/or other un-modeled system non-linearities.

5.1.2 Slewing Responses

This section will present a series of example simulation responses of the mobile tower crane model. These examples demonstrate the range of responses of the mobile tower

The work in Section 5.1.2 was completed in collaboration with undergraduate researcher Adrit Lath.

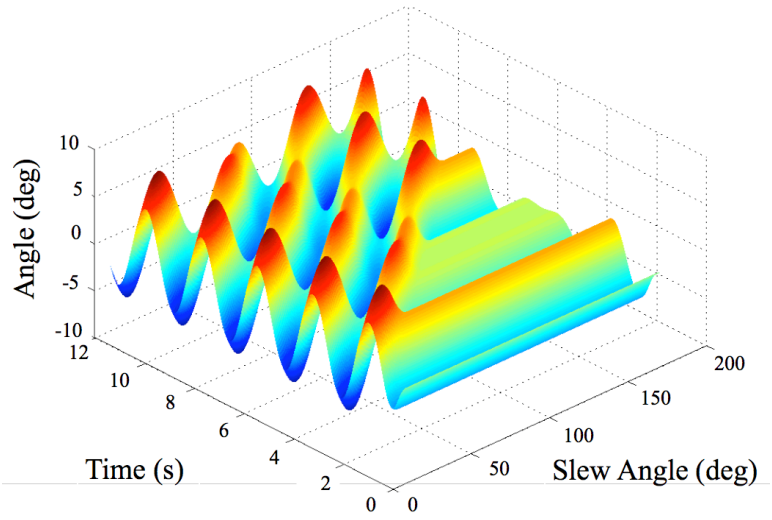

Figure 80: β (tangential) Responses for Various Slewing Angles

crane and identify maneuvers that cause maximum amounts of vibration.

Figure 80 shows a series of time responses of the β (tangential) direction of oscillation for a range of slewing commands. For these responses, parameters matching the mobile tower crane in Figure 76 were used. The "Slew Angle" axis represents slewing commands of varying duration. The slew angle is the change is the slew position, θ, from the beginning of the move to the end. For each command, the jib accelerated to, and decelerated from, its maximum slewing velocity at its maximum angular acceleration. The trolley position and suspension cable length were held constant at 0.7m and 1.245m, respectively. There was no base motion. For every slewing angle shown in the figure the residual vibration amplitude is greater than or equal to the transient. Figure 81 shows the ϕ (radial) oscillation from the same commands. The ampltide of vibration is much smaller in this direction for all slewing maneuvers shown.

Figure 82(a) shows the maximum and residual oscillation amplitudes from the responses shown in Figure 80. The maximum oscillation peaks at a vibration amplitude of approximately 15°, while the minimum shown is approximately 7°. The residual vibration amplitude also peaks near 15°, but reaches a much lower minimum of less than 1° at a slew angle of approximately 155°. The local minimums in Figure 82(a) are the result of

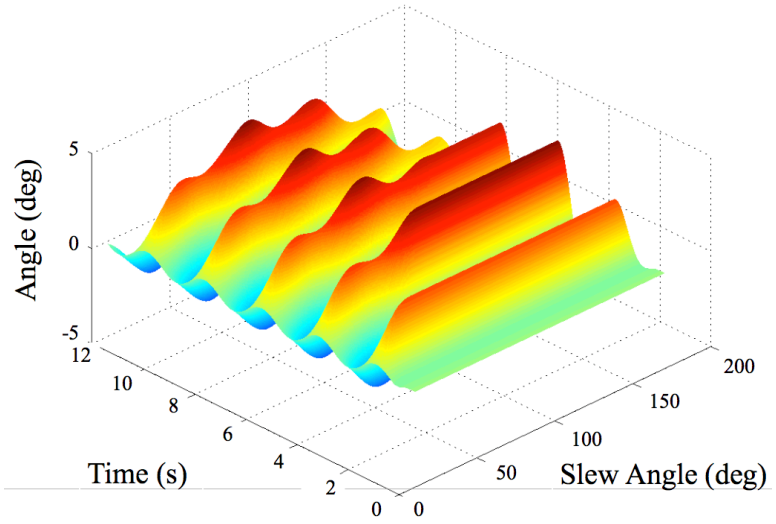

Figure 81: ϕ (radial) Responses for Various Slewing Angles

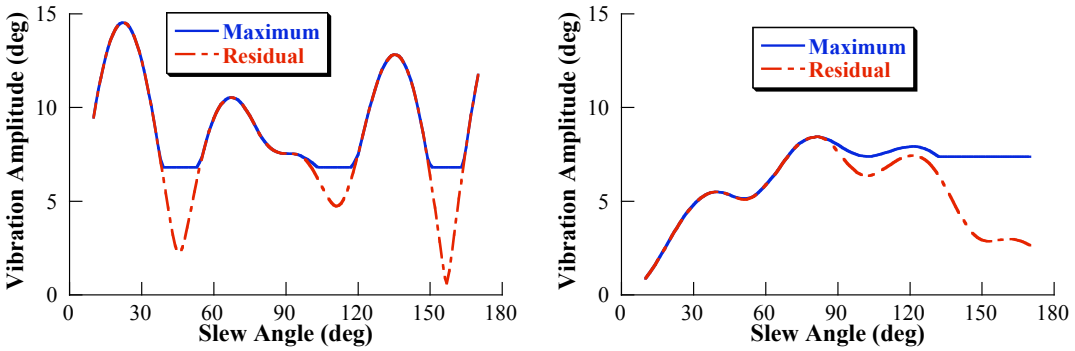

(a) β (tangential) **(b)** ϕ (radial)

Figure 82: Maximum and Residual Vibration as a Function of Slew Angle (r = 0.7m)

the acceleration and deceleration portions of the command being timed such the vibration caused by each destructively interferes with the other.

Figure 82(b) shows the maximum and residual oscillation amplitudes from the responses shown in Figure 81. The ϕ response peaks at a vibration amplitude of approximately 8° for a slewing angle of approximately 80°. For all slewing angles less than this maximum, the residual amount of ϕ oscillation is equal to the maximum value at that slew angle. Above this maximum, the residual oscillation is always less.

Figure 83 shows β responses for the same range of slewing angles as Figure 80, but with a ZV-shaped slewing profile. Over all the slewing angles in the plot, the amount of

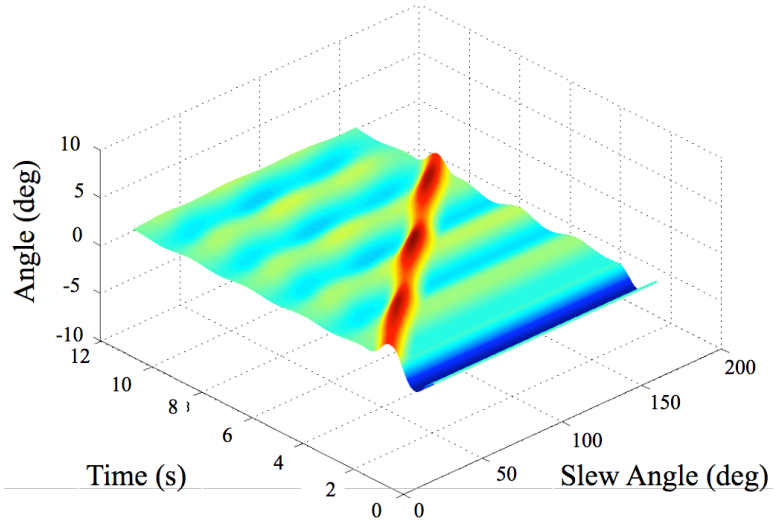

Figure 83: β (tangential) Responses for Various Slewing Angles with ZV-Shaped Commands

vibration is drastically reduced. The radial, ϕ, oscillation is also reduced over the majority of the operating range.

The maximum and residual oscillation from the ZV-shaped slewing commands is shown in Figure 85. For both the β and ϕ angles, the maximum and residual levels of vibration are much lower than for the unshaped case. The residual oscillation for both angles is less than 2° over the entire range of slewing commands.

This is a significant point, as the centripetal effects of the tower slewing have not caused significant vibration in the shaped case. The centripetal effects did prevent the ZV shaper tested from reaching its theoretical minimum of zero vibration, but it still provides a substantial improvement over the unshaped case. The realization that the primary dynamic nonlinearity present in tower cranes, at common of angular velocity values, does not dramatically reduce input shaper effectiveness, is important for the multi-input shapers developed in Chapter 6.

5.2 Model of a Tower Crane with a Double-Pendulum Payload

In certain configurations, a crane payload and rigging may introduce a second oscillatory mode to the system. This section will present a model of a tower crane with such a payload

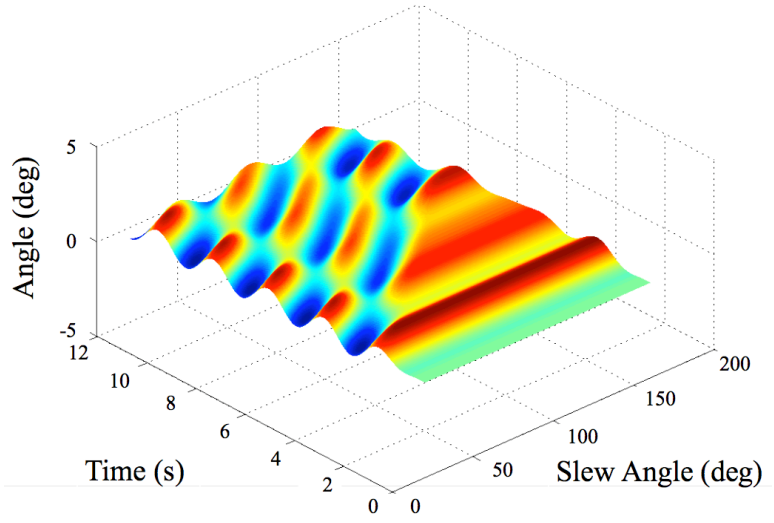

Figure 84: ϕ (radial) Responses for Various Slewing Angles with ZV-Shaped Commands

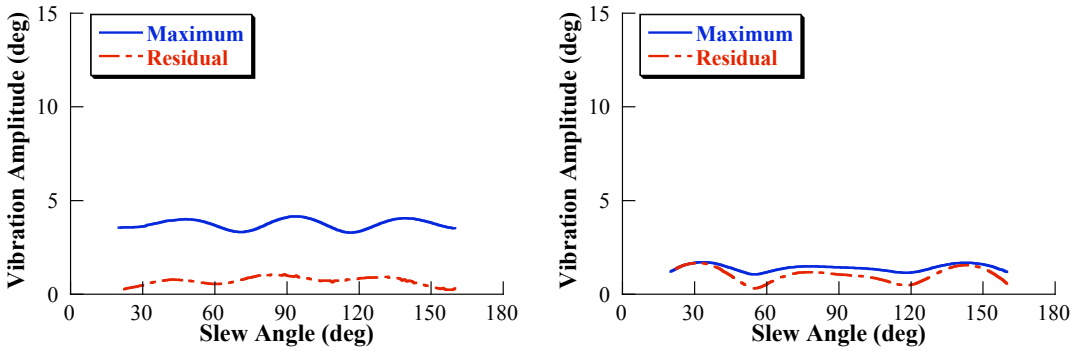

(a) β (tangential) **(b)** ϕ (radial)

Figure 85: Maximum and Residual Vibration as a Function of Slew Angle with ZV-shaped Commands (r = 0.7m)

configuration and an analysis of the influence of each mode of vibration to the system response.

Figure 86 shows a sketch of a tower crane with a double-pendulum payload configuration. The jib rotates by an angle θ around the vertical axis, Z, parallel to the tower column. The trolley moves radially along the jib; its position along the jib is described by r. The suspension cable length from the trolley to the hook is represented by an inflexible, massless link of variable length l_1. The payload is connected to the hook via an inflexible, massless link of length l_2. Both the hook and the payload are represented as point masses having masses m_h and m_p, respectively.

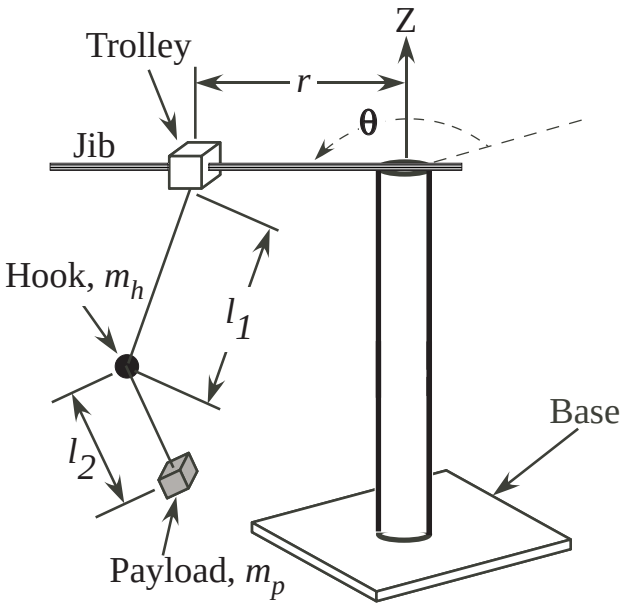

Figure 86: Sketch of Tower Crane with Double Pendulum

The angles describing the position of the hook are shown in Figure 87(a). The angle ϕ represents a deflection in the radial direction, along the jib. The angle χ represents a tangential deflection, perpendicular to the jib. In Figure 87(a), ϕ is in the plane of the page, and χ lies in a plane out of the page. The angles describing the payload position are shown in Figure 87(b). Notice that these angles are defined relative to a line from the trolley to the hook. If there is no deflection of the hook, then the angle γ describes radial deflections, along the jib, and the angle α represents deflections perpendicular to the jib, in the tangential direction. The equations of motion for this model were derived using a commercial dynamics package, but they are too complex to show here, as they are each over a page in length.

5.2.1 Experimental Verification of the Double-Pendulum Tower Model

The equations of motion were experimentally verified using several cases. Figure 88 shows two cases involving only radial motion at maximum velocity for a distance of 0.30m, with $l_2 = 0.45$m. The payload mass, m_p, for both cases was 0.15kg and the hook mass, m_h was approximately 0.105kg. The cases present two extremes of suspension cable lengths, l_1. In Figure 88(a), l_1 is 0.48m, close to the minimum length that can be measured by the

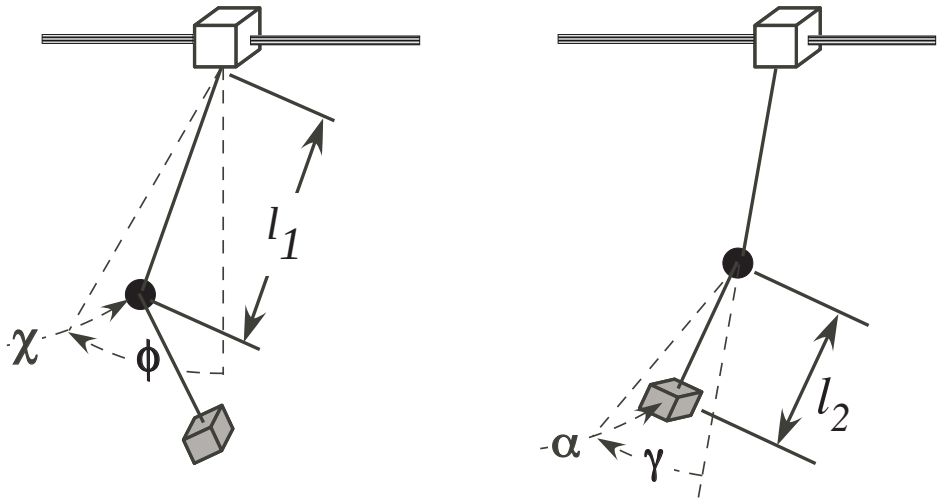

(a) Angles Describing Hook Motion **(b)** Angles Describing Payload Motion

Figure 87: Angles Describing Hook and Payload Motion

overhead camera. At this length, the double-pendulum effect is immediately noticable. One can see that the experimental and simulated responses closely match one another. In Figure 88(b), l_1 is 1.28m, near the maximum length available to keep the payload from hitting the ground. At this length, the second mode of oscillation has much less effect on the response. The model closely matches the experimental response for this case as well.

If the trolley position is held constant and the jib is rotated, then the rotational and centripetal accelerations cause oscillation in both the radial and tangential directions. This can be seen in Figures 89 and 90. In Figure 89 the trolley is held at a fixed position of $r = 0.75$m, while the jib is rotated 20°. This relatively small rotation only minimally excites oscillation in the radial direction, as shown in Figure 89(a). The vibratory dynamics are dominated by oscillations in the tangential direction, χ. The χ response is shown in Figure 89(b). If, however, a large angular displacement of the jib occurs, then significant oscillation will occur in both the radial and tangential directions, as shown in Figure 90. In this plot, the trolley was held at a fixed position of $r = 0.75$m and the jib was rotated approximately 90°. Figures 89 and 90 show that the experimental responses closely match

tb

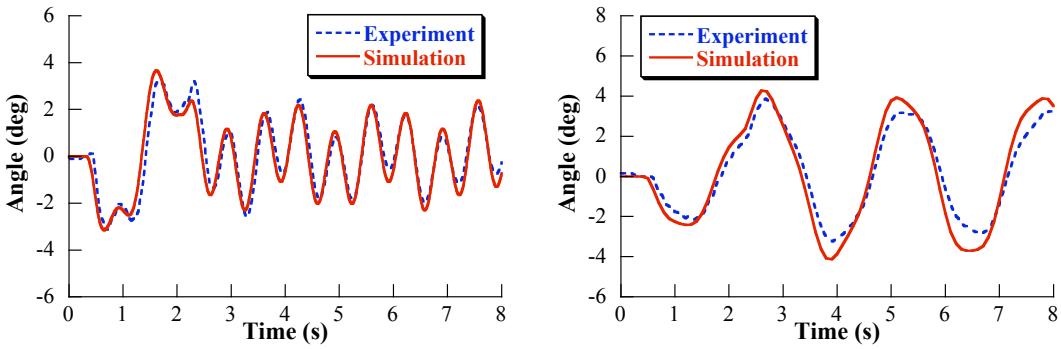

(a) Hook Responses (ϕ) for $l_1 = 0.48$m **(b)** Hook Responses (ϕ) for $l_1 = 1.28$m

Figure 88: Experimental and Simulated Reponses of Radial Motion

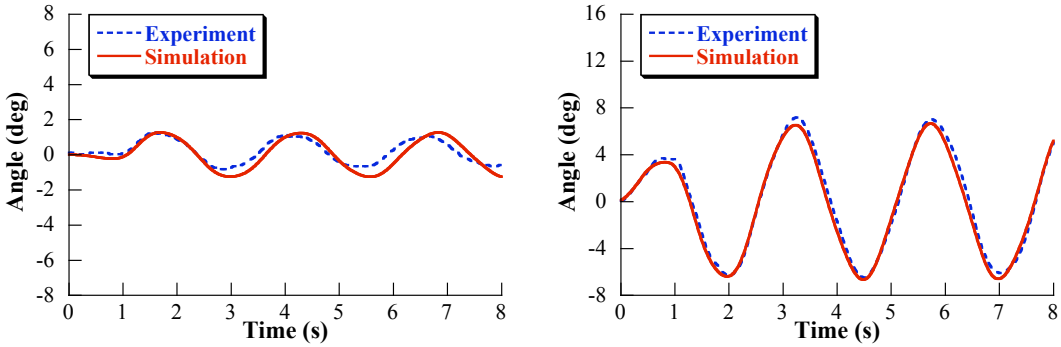

(a) ϕ (Radial) Response **(b)** χ (Tangential) Reponse

Figure 89: Hook Responses to 20° Jib Rotation

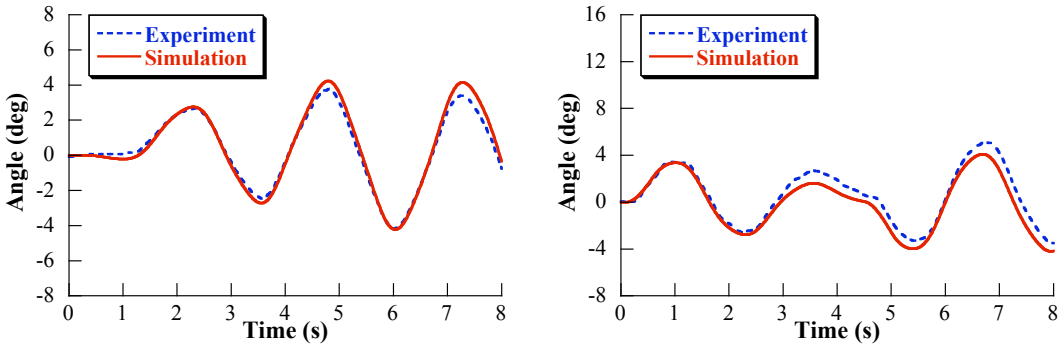

(a) ϕ (Radial) Response **(b)** χ (Tangential) Reponse

Figure 90: Hook Responses to 90° Jib Rotation

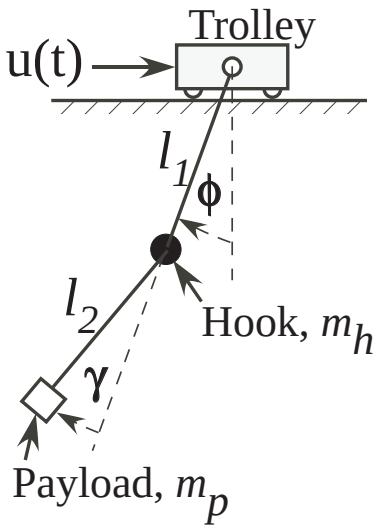

Figure 91: Planar Double–Pendulum Model

those predicted by the model for these rotational motions as well. Part of the deviation in Figure 90(b) can be attributed to the unevenness of the floor on which the crane sits. After the 90° jib rotation the hook and payload oscillate about a slightly different equilibrium point, as measured by the overhead camera.

5.2.2 Dynamic Analysis of Double-Pendulum Tower Crane

If the motion of the tower crane is limited to trolley motion, like the responses shown in Figure 88, then the model may be simplified to that in Figure 91, with variables corresponding to those defined above. This model simplifies the analysis of the system dynamics and allows estimates of the two natural frequencies of the double pendulum. These natural frequency estimates will be crucial to the development of input shapers for the double-pendulum tower crane.

The crane is moved by applying a force, $u(t)$, to the trolley. A cable of length l_1 hangs below the trolley and supports a hook, of mass m_h, to which the payload is attached using a rigging cable. The rigging and payload are modeled as a second cable, of length l_2, and point mass, m_p. Assuming that the cable and rigging lengths do not change during the

The work in Section 5.2.2 was completed in collaboration with NSF Fellow, Ms. Dooroo Kim.

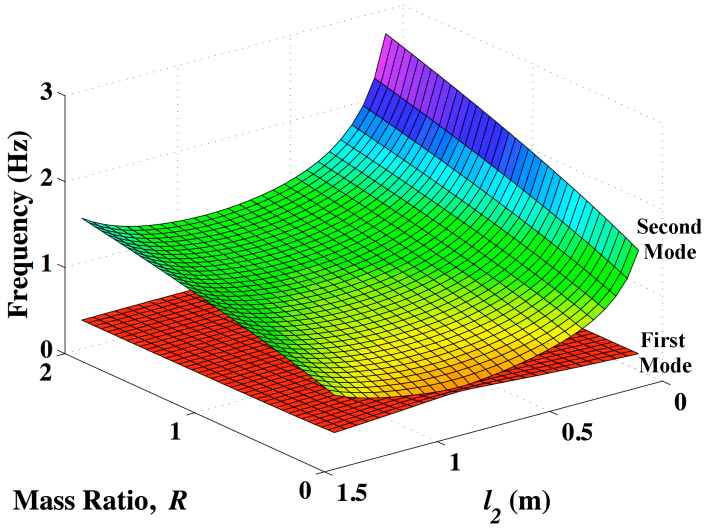

Figure 92: Variation of First and Second Mode Frequencies when $l_1 + l_2 = 1.8m$.

motion, the linearized equations of motion, assuming zero initial conditions, are:

$$\begin{aligned} \ddot{\phi}(t) &= -\left(\tfrac{g}{l_1}\right)\phi + \left(\tfrac{gR}{l_1}\right)\gamma + \tfrac{u(t)}{l_1} \\ \ddot{\gamma}(t) &= \left(\tfrac{g}{l_1}\right)\phi - \left(\tfrac{g}{l_2} + \tfrac{gR}{l_2} + \tfrac{gR}{l_1}\right)\gamma - \tfrac{u(t)}{l_1}, \end{aligned} \tag{65}$$

where ϕ and γ describe the angles of the two pendulums, R is the ratio of the payload mass to the hook mass, and g is the acceleration due to gravity.

The linearized frequencies of the double-pendulum dynamics modeled in (65) are [8]:

$$\omega_{1,2} = \sqrt{\frac{g}{2}}\sqrt{(1+R)\left(\frac{1}{l_1}+\frac{1}{l_2}\right) \mp \beta} \tag{66}$$

where,

$$\beta = \sqrt{(1+R)^2\left(\frac{1}{l_1}+\frac{1}{l_2}\right)^2 - 4\left(\frac{1+R}{l_1 l_2}\right)}. \tag{67}$$

Note that the frequencies depend on the two cable lengths and the mass ratio.

Figure 92 shows the two oscillation frequencies as a function of both the rigging length and the mass ratio when the total length (suspension length plus rigging length) is held constant at 1.8 m. The low frequency is maximized when the two cable lengths are equal.

Note that over the wide range of parameter values shown in Figure 92, the low frequency only varies ±10% from its median value of 0.42 Hz. In contrast, the second mode deviates ±34% over the same parameter range.

These results seem to indicate that an oscillation control scheme would need more robustness to variations in the second mode than in the first mode. However, if the amplitude of the second mode is very small compared to the amplitude of the first mode, then the controller does not need to address the second mode. The relative contribution of the two modes can be examined by breaking the overall dynamic response into components arising from ω_1 and ω_2.

Assuming small angles, the payload response from a series of impulses, A_j, can be expressed as [21]:

$$x(t) = C_1 \sin(\omega_1 + \psi_1) + C_2 \sin(\omega_2 + \psi_2) \tag{68}$$

where,

$$C_1 = \frac{\omega_1 L_1 \left(1 + \omega_2^2 \alpha (L_1 + L_2)\right)}{k} \sqrt{\left(\sum_{j=1}^{n} A_j \cos\left(\omega_1 t_j\right)\right)^2 + \left(\sum_{j=1}^{n} A_j \sin\left(\omega_1 t_j\right)\right)^2} \tag{69}$$

$$C_2 = \frac{\omega_2 L_1 \left(1 + \omega_1^2 \alpha (L_1 + L_2)\right)}{k} \sqrt{\left(\sum_{j=1}^{n} A_j \cos\left(\omega_2 t_j\right)\right)^2 + \left(\sum_{j=1}^{n} A_j \sin\left(\omega_2 t_j\right)\right)^2} \tag{70}$$

$$\alpha = \frac{-g(1+R)}{\omega_1^2 \omega_2^2 L_1 L_2}, \quad \textit{and} \quad k = \chi L_1 g \tag{71}$$

Given $\omega_1 \neq \omega_2$, the maximum amplitude is found by adding the maximum amplitudes due to each frequency [21]:

$$V_{max} = |C_1| + |C_2|, \tag{72}$$

where the coefficients, C_1 and C_2, indicate the contributions of each mode to the overall response. Using this decomposition, the contribution of the second mode to the overall vibration becomes apparent and indicates when single-mode input shaping might be an insufficient solution. Figure 93 shows the ratio of the high-mode contribution to the low-mode contribution for a large range of length and mass ratios, again assuming an overall

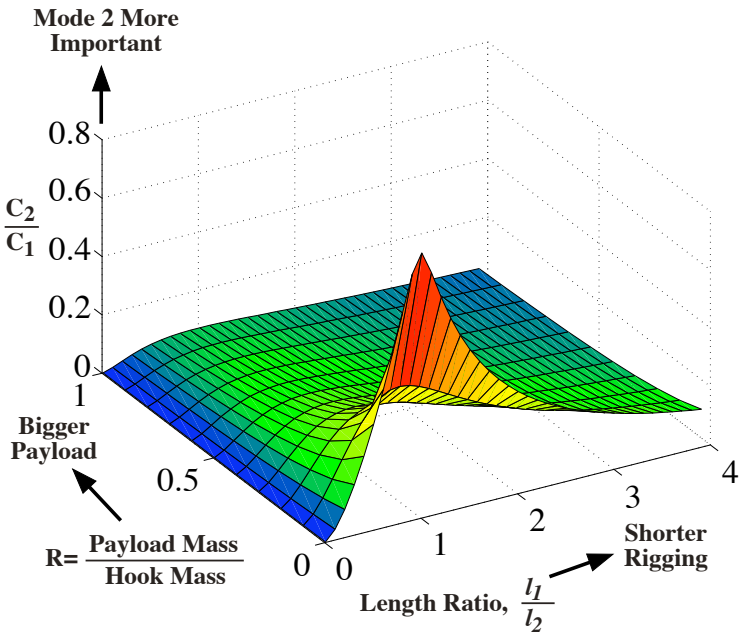

Figure 93: Ratio of High-Mode Amplitude to Low-Mode Amplitude when $l_1 + l_2 = 1.8m$

length of 1.8m. The surface indicates that double-pendulum input shaping will be necessary for systems with low payload-to-hook mass ratios. The second mode contribution is particularly large when the suspension and rigging lengths are approximately equal.

5.3 Conclusion

This chapter presented models for a mobile tower crane and for a tower crane with a double-pendulum payload configuration. Each model was experimentally verified using a portable, mobile tower crane. Only key dynamic characteristics of each were presented. Both models will be used in later chapters of this thesis to test the effectiveness of proposed control methods.

CHAPTER VI

SHAPING MULTI-INPUT COMMANDS TO IMPROVE SYSTEM PERFORMANCE

CHAPTER SUMMARY: *This chapter introduces several design methods for multi-input shapers, one of the major contributions of this thesis. Each procedure relies heavily on knowledge of traditional, single input shaping methods. Multi-input shaping design procedures are introduced that result in shapers that use secondary actuators to reduce vibration, increase robustness, and speed system motion. Simulations from the full, nonlinear mobile tower crane model introduced in Chapter 5 are used as examples for multi-input shaper design. Experiments from a mobile tower crane are also presented.*

A crane with added base mobility presents significant control challenges. Base motion, from ground disturbances and/or purposeful motion, will excite payload oscillation. However, there are also additional opportunities for control. The crane is redundantly actuated (overactuated); multiple combinations of actuation can move the payload from one location to another. This presents the opportunity to use a combination of actuation to provide both rapid motion and low payload oscillation. Multi-input shaping presents one method to determine effective combinations of actuation.

Relatively few researchers have investigated the extension of input shaping to the multi-input domain. The first published methods for multi-input shaping relied on a zero-placement method to solve for the mutliple impulse sequences [42, 40]. Later works presented improvements on this intial algorithm [3, 9]. These methods proposed improving the performance of a multi-input system by using more information from the system than is typically

needed to generate input shapers for single input systems. The original method, and the subsequent improvements, need some information, and in most cases somewhat accurate information, about influence of each input over the vibratory modes of the system.

The first improvement to this algorithm removed the impulse amplitude constraints from the original solution procedure, then scaled the resulting solution according to rigid body constraints [9]. This method generated marginally faster shapers than the original approach. An alternative improvement included additional robustness constraints, mentioned in the original work, but not implemented [3]. This work also proposed an adaptive multi-input shaping routine to account for situations when one or more input becomes zero. Problems with this approach included possible actuator saturation and the ability to find (and even the existence of) a solution that meets both vibration and impulse amplitude requirements.

Other researchers have approached the problem by reformulating the problem as a quasi-convex optimization [4, 5, 32]. In each of these cases, the problem is transfered to the digital domain. Once in the digital domain, constraints on vibration and impulse amplitudes are created to form the optimization problem. Additional constraints can be added to the formulation to increase robustness and/or satisfy transient response requirements [32]. Only one previous paper has presented experimental results [32].

The methods published thus far present several difficulties for practical implementation. The first is that the majority of the methods do not account for situations where one, or more, of the inputs is not used; the solutions require all actuators to be acting at all times. A second limitation is the requirement that each input utlize an equal number of impulses, spaced equally in time. This severely limits the solution space. Finally, there is no explicit consideration of actuator limits in the methods published to date.

This chapter presents multi-input shaping methods that address these issues. Multi-input shapers are generated using techniques similar to those used for single input shaper design. However, the fundamental principle driving the use of multi-input shapers is to use

multiple inputs to achieve performance that is not possible with a single input. This chapter will examine several classes of such multi-input shapers. The first case is using secondary, compensating inputs to overcome the structural limitations of one primary input. Sections 6.1-6.3 outline the methods of this class of multi-input shpaers. The second class of multi-input shapers, introduced in Section 6.4, use additional actuators to improve the robustness of the control system. The final category of multi-input shapers utilize multiple inputs to improve the rise time of the system, while maintaining low levels of vibration. These are detailed in Section 6.5.

A mobile crane is used as the primary application example of multi-input shaping. However, the methods can be applied to other mutli-input systems and be particularly well suited to overactuated systems, such as mutli-stage positioning stages or hard disk drives. However, the methods presented in this chapter assume a linear (or near linear) system. Extensions of the methods to systems that are highly nonlinear or non-stationary may require additional modifications.

6.1 Multi-Input Shaping Development

To demostrate the input-shaping principles applied to multi-input cases, the two-mass-spring-damper model in Figure 94 is utilized. The inputs are u_1 and u_2 and the outputs are the positions of M_1 and M_2, x_1 and x_2, respectively. The two masses are connected via a spring with spring constant k and damper with damping coefficient c. It is easy to see that the inputs affect the outputs identically. This eliminates the problem of scaling between

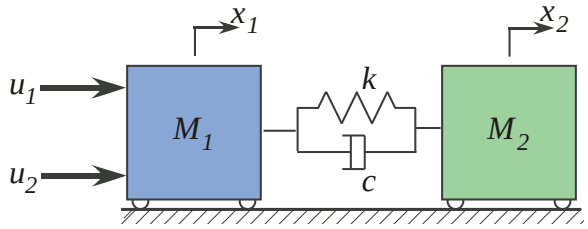

Figure 94: Simple Multi-Input Multi-Output Model

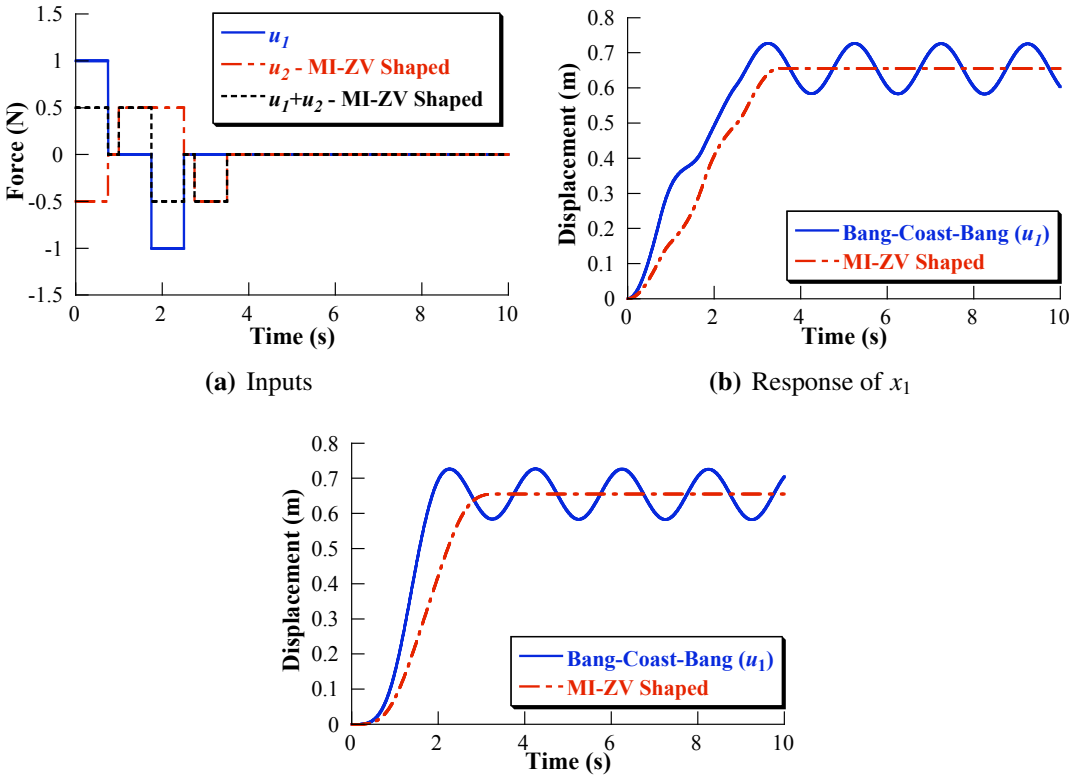

(a) Inputs

(b) Response of x_1

(c) Response of x_2

Figure 95: Responses to Unshaped and MI-ZV Commands

inputs and makes identification of key input parameters straightforward. The general principle utilized here is that the two inputs, u_1 and u_2, can be used together to create a properly shaped input for the system.

A bang-coast-bang input from u_1 with $u_2 = 0$, shown as a solid line in Figure 95(a), will excite significant vibration in the system. This can been seen in the responses of x_1 and x_2 as shown by solid lines in Figures 95(b) and 95(c), respectively. It has been shown that ZV input shaping can drastically reduce the amount of system vibration. However, suppose that u_1 is unable to produce a shaped input. This could result from actuator limitations or limitations on timing resolution. The second input, u_2 can then be chosen to compensate for the limitations of u_1, such that the sum, $u_1 + u_2$, is a properly shaped input. The u_2 function needed to create a ZV shaped sum can be seen in Figure 95(a), in addition to the summed input, $u_1 + u_2$. The responses shown as dashed lines in Figures 95(b) and 95(c)

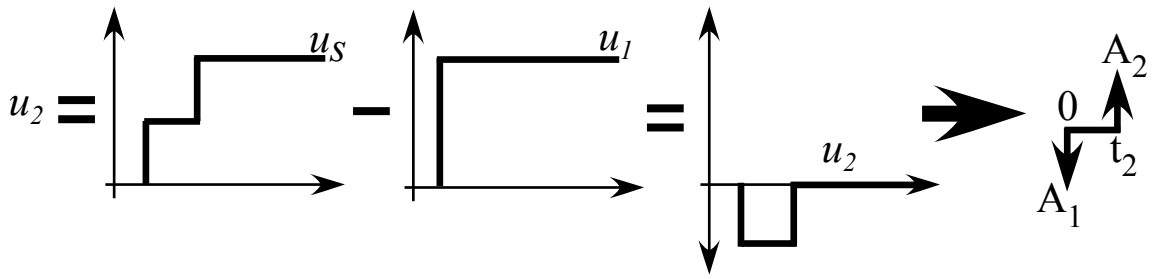

Figure 96: Multi-Input ZV Shaper Development Example

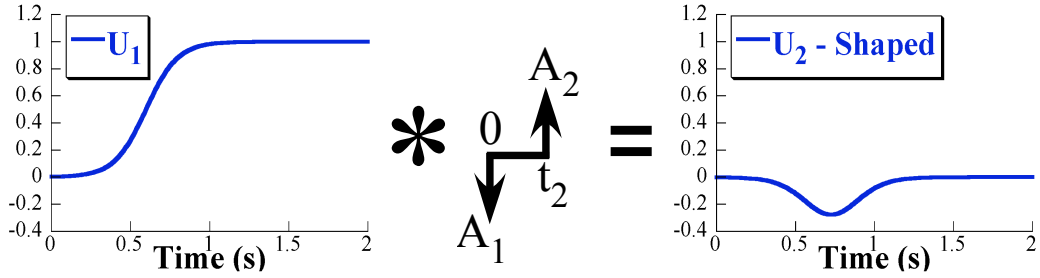

Figure 97: Multi-Input ZV Shaper Application

show the effectiveness of this new Multi-Input ZV (MI-ZV) shaped command. Any input shaper utilizing multiple actuators will be qualified with MI to indicate it is a multi-input shaped command. The shaped command that the sum of inputs is designed to create will be included after the MI designation. For example, if multiple actuators are combined to create a ZVD shaped command, it will be labeled MI-ZVD.

The methodology used to determine the necessary input u_2 to compensate for the inability to generate a shaped u_1 command is shown in Figure 96. Suppose the ZV-shaped command, u_s, is a two-step staircase command and u_1 can only produce a step function. To determine the proper shape of u_2, u_1 is simply subtracted from the desired shaped command, u_s. To find a compensating actuator effort for any u_1, the resulting command can be deconvolved into a step and an impulse sequence. The resulting impulse sequence is convolved with ay u_1, and the resulting command is applied to u_2. This process is shown in Figure 97.

This method has several drawbacks. The first is that this method does not account for the influence of each actuator on the vibratory dynamics of the system; each is assumed to

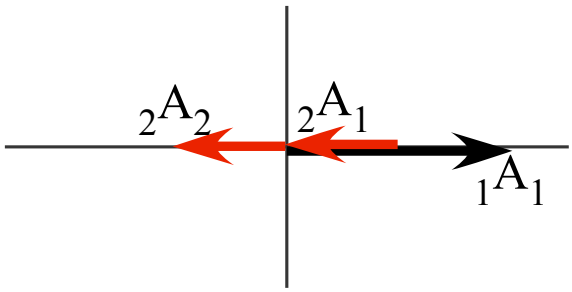

Figure 98: Multi-Input Vector Diagram

affect the oscillatory modes identically. This is often not the case. The second drawback is that actuator limits are not addressed, meaning that the multi-input commands generated may not be realizable on a given system. The next several sections propose solutions to each of these problems.

6.2 Multi-Input Vector Diagrams

The multi-input commands from the previous section can also be constructed using a vector diagram, a tool that predicts the amount of vibration that an impulse sequence will produce. For a review of vector diagrams see Section 2.3.2.1. For clarity on multi-input vector diagrams, vectors must not only be designated according to their place in the impulse sequence, but also according to the input they are used to shape. Vectors are labeled ${}_kA_i$, where k represents the input they apply to and i represents their place in the impulse sequence for that input.

Figure 98 shows the vector diagram for the commands developed in the previous section. In the examples from the previous section, the first input, u_1, was applied to the system without any modification. As a result it can be represented on the vector diagram as a unity magnitude vector at time zero. This impulse was plotted on the diagram as ${}_1A_1$. To form a MI-ZV shaper, vectors ${}_2A_1$ and ${}_2A_2$ were added to the diagram. The sum of ${}_1A_1$, ${}_2A_1$, and ${}_2A_2$ is a resultant vector of zero length, indicating that the sum of these two impulse sequences will result in zero vibration.

The vectors in Figure 98 were chosen to mimic the effect of a ZV shaper. However,

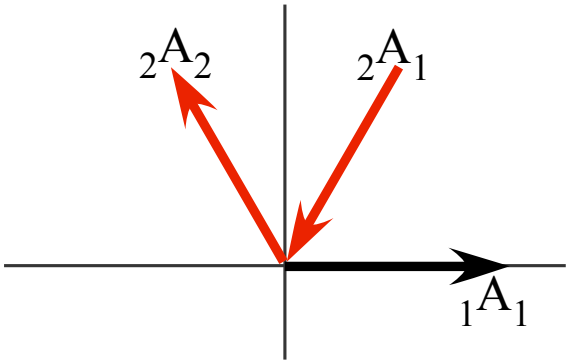

Figure 99: Multi-Input Vector Diagram – Unity Magnitude Impulse Constraints

just as with a single input vector diagram, there are an infinite number of choices to create impulse sequences that result in low levels of vibration. Figure 99 shows another such choice. In this case, the vectors were all chosen to be unity magnitude, and the sequence was chosen to match a UM-ZV shaper.

Due to the large number of possible solutions conceived using vector diagrams, it makes an excellent tool to develop multi-input shapers that account for the problems discussed in the previous section. It provides a graphical representation of the ability to change impulse amplitudes and time locations to match physical system requirements.

It should be noted that multi-input vector diagrams assume that each impulse sequence is shaping the same reference command. While this appears to be a siginificant limitation of the tool, in practice, it is only a minor inconvenience. Proper scaling of the vector solutions and inclusion of additional vectors allows a wide variety of commands to be created.

6.3 Design Using Multi-Input Vector Diagrams

This section will present design methods utilizing the multi-input vector diagram that can be used to develop multi-input shapers for a wide variety of cases. The methods also provide the necessary tools to create shapers that are able to meet actuator requirements, account for varying contributions between inputs, and result in low vibration commands. A two-input, single-vibratory-mode system will be used to demonstrate the use of the multi-input vector diagram. Examples from full, nonlinear mobile tower crane model presented

in Chapter 5 are also presented. The techniques developed, however, scale to systems with greater numbers of inputs and additional modes of vibration.

6.3.1 Compensating Inputs

One category of multi-input shapers is the class of shapers where a second input is primarily used to eliminate the vibration caused by the first. This method is particularly applicable to systems that are redundantly actuated, such as mobile cranes. For example, one primary actuator may be used to position the system, while the secondary input(s) compensate for the vibration caused by the first. Many of the examples presented in this chapter follow this form. However, the multi-input vector diagram may be used to design multi-input shapers for more general cases.

6.3.2 Scaling for Input Contributions

Thus far, the system used to develop and demonstrate multi-input techniques has contained two inputs that equally affect the output. This will often not be the case. This section will present a method to scale vector diagram solutions to create impulse sequences that account for this effect. This procedure is first demonstrated on an example system. Then, the general method is outlined.

To begin the investigation, the model Figure 100 was chosen. It consists of a translational input, x_1, attached to a massless beam of length, L. The second input to the system is the rotation of this beam, θ. A spring of stiffness k is attached to the end of the massless beam. The other side of the spring is attached to a mass, m, only capable of translational motion, x_3. This model is very similar to a mobile tower crane in which the centripetal effects of jib rotation are ignored.

The state-space form of the linearized equations of motion for the system is:

$$\dot{\bar{x}} = A\bar{x} + B\bar{u} \tag{73}$$

$$\dot{\bar{x}} = \begin{bmatrix} 0 & 1 \\ -\frac{k}{m} & 0 \end{bmatrix} \bar{x} + \begin{bmatrix} 0 & 0 \\ \frac{k}{m} & -\frac{k}{m}L \end{bmatrix} \begin{bmatrix} x_1 \\ \theta \end{bmatrix} \tag{74}$$

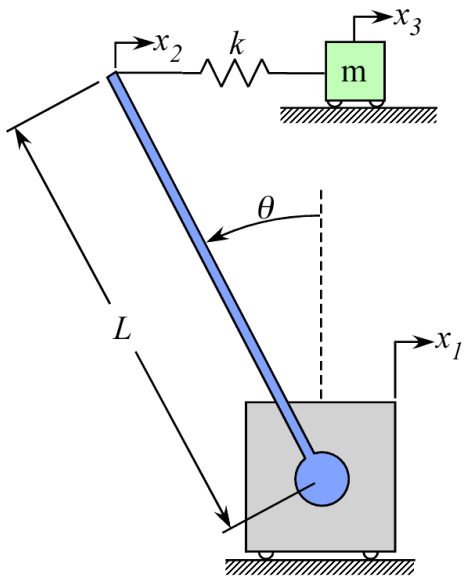

Figure 100: Simple Rotational Model

The model has two inputs, x_1 and θ, that do not equally affect the vibratory response of the system. The coefficients of the B matrix provide insight into how each does affect the system. As a result, they also provide insight into how multi-input shaper impulse sequences should be scaled.

To design a multi-input shaper for this system, begin with the multi-input vector diagram. One choice of impulses was shown in Figure 98. For this system, the two sequences of impulses from this vector diagram are:

$$x_1 : \begin{bmatrix} A_i \\ t_i \end{bmatrix} = \begin{bmatrix} 1 \\ 0 \end{bmatrix} \tag{75}$$

$$\theta : \begin{bmatrix} A_i \\ t_i \end{bmatrix} = \begin{bmatrix} -0.5 & 0.5 \\ 0 & \frac{\pi}{\sqrt{\frac{k}{m}}} \end{bmatrix} \tag{76}$$

If these sequences are used directly on the system, without scaling, then the multi-input shaped case actually excites more vibration than the unshaped, as seen in Figure 101. To properly scale the impulse sequences to account for each input's influence on the output,

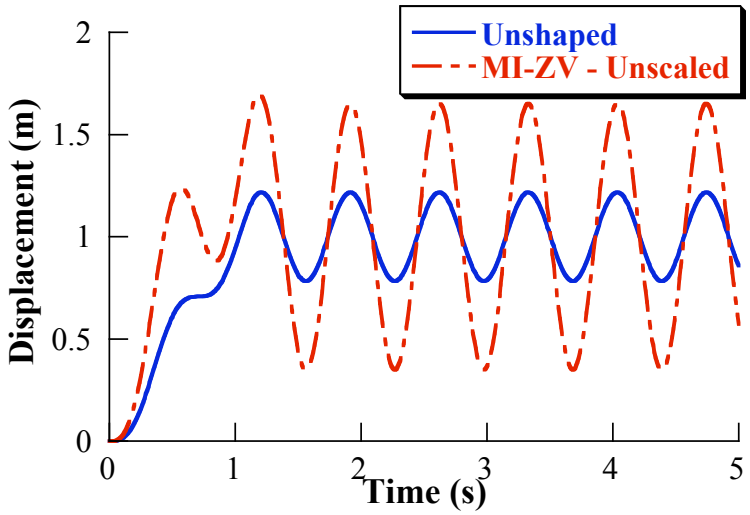

Figure 101: Mutli-Input Shaping without Proper Impulse Scaling

the impulse amplitudes of each sequence can be scaled according to the inverse of its corresponding entry in the B matrix. When this scaling is performed, the sequences become:

$$x_1 : \begin{bmatrix} A_i \\ t_i \end{bmatrix} = \begin{bmatrix} \frac{m}{k} \\ 0 \end{bmatrix} \tag{77}$$

$$\theta : \begin{bmatrix} A_i \\ t_i \end{bmatrix} = \begin{bmatrix} 0.5\frac{m}{kL} & -0.5\frac{m}{kL} \\ 0 & \frac{\pi}{\sqrt{\frac{k}{m}}} \end{bmatrix} \tag{78}$$

The sequences now properly account for the influence of each input on the vibratory dynamics of the system. However, the impulse amplitudes no longer sum to one. To correct this, for this case, each impulse is multiplied by $\frac{k}{m}$. The final, correct impulse sequences become:

$$x_1 : \begin{bmatrix} A_i \\ t_i \end{bmatrix} = \begin{bmatrix} 1 \\ 0 \end{bmatrix} \tag{79}$$

$$\theta : \begin{bmatrix} A_i \\ t_i \end{bmatrix} = \begin{bmatrix} 0.5\frac{1}{L} & -0.5\frac{1}{L} \\ 0 & \frac{\pi}{\sqrt{\frac{k}{m}}} \end{bmatrix} \tag{80}$$

The response of the system, using these two impulse sequences is shown in Figure 102. The multi-input shaped response now exhibits no residual oscillation.

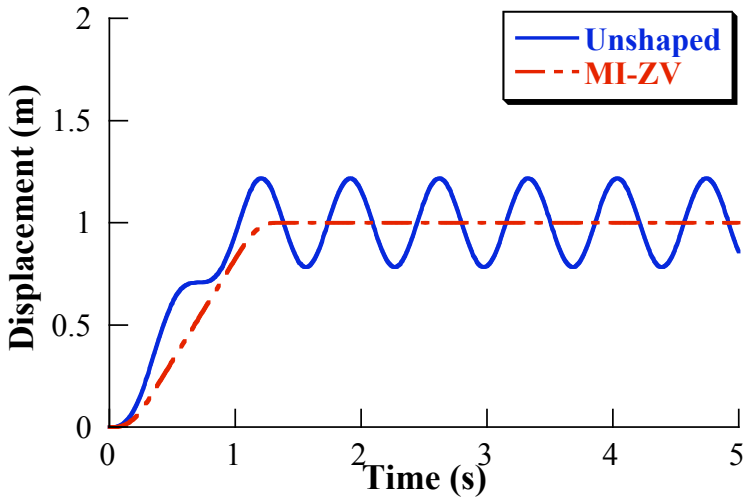

Figure 102: Mutli-Input Shaping with Proper Impulse Scaling

For systems with two inputs, this process is easily completed by scaling one of the impulse sequences by the ratio of coefficients from the B matrix. For this example, the θ impulse sequence could be scaled by:

$$\frac{B(2,1)}{B(2,2)} = \frac{\frac{k}{m}}{-\frac{kL}{m}} = -\frac{1}{L} \tag{81}$$

To generally apply the methods described above, the the system must be represented in block diagonal form:

$$\begin{aligned} \dot{\bar{x}} &= A\bar{x} + B\bar{u} \\ \bar{y} &= C\bar{x} \end{aligned} \tag{82}$$

where

$$\begin{aligned} A &= \text{blockdiag}[A_l] = \text{blockdiag}\begin{bmatrix} 0 & 1 \\ -\omega_l^2 & -2\zeta\omega_l \end{bmatrix} \\ B &= \text{blockcol}\begin{bmatrix} 0 & 0 & \dots & 0 \\ b_1^l & b_2^l & \dots & b_k^l \end{bmatrix}, \quad l = 0, 1, \dots, p \end{aligned} \tag{83}$$

where there are k inputs to the system, p is the number of modes, and ω_l and ζ_l represent the frequency and damping ratio of the l^{th} mode, respectively. Placing the system in this form

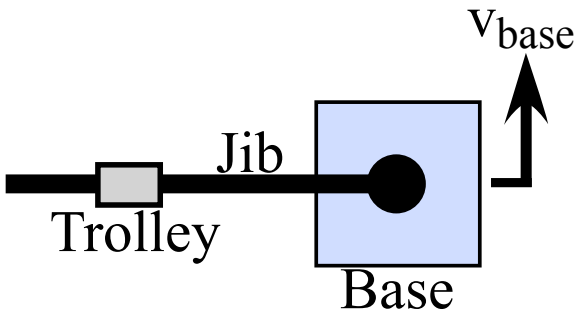

Figure 103: Mutli-Input Shaping Example Configuration

allows the influence of each input on each vibratory mode to be determined. To eliminate vibration for multiple modes of vibration, vector diagrams representing each mode must be solved simultaneously.

Using this method, multi-input commands were generated for the full, nonlinear mobile tower crane model presented in Chapter 5, using a combination of base motion and jib rotation. To establish a baseline, unshaped command and response, only base motion was used with the jib held perpendicular to the base velocity, as shown in Figure 103. For the MI-ZV shaped case, the same base command was used, but the jib was rotated to eliminate the vibration caused by the base motion. For both cases, the suspension cable length, l, was set to 1.245m and the trolley position, r, at 0.8m. Both cable length and trolley position were held constant during the simulations. A system natural frequency of approximately 0.22Hz results from this configuration. The base and slewing (θ) commands are shown in Figure 104.

The unshaped and MI-ZV shaped payload responses are shown in Figure 105. The unshaped base motion alone causes significant vibration in the β-direction, tangential to the jib, as seen in Figure 105(a). Because the base motion is exactly perpendicular to the jib, no radial vibration is excited. The MI-ZV shaped case, utilizing jib slewing, is shown in Figure 105(b). The vibration in the β-direction, excited by the base motion, is eliminated. However, the centripetal effects of rotating the jib have excited a small level vibration in the radial direction. Despite this, the total amount of vibration is dramatically reduced.

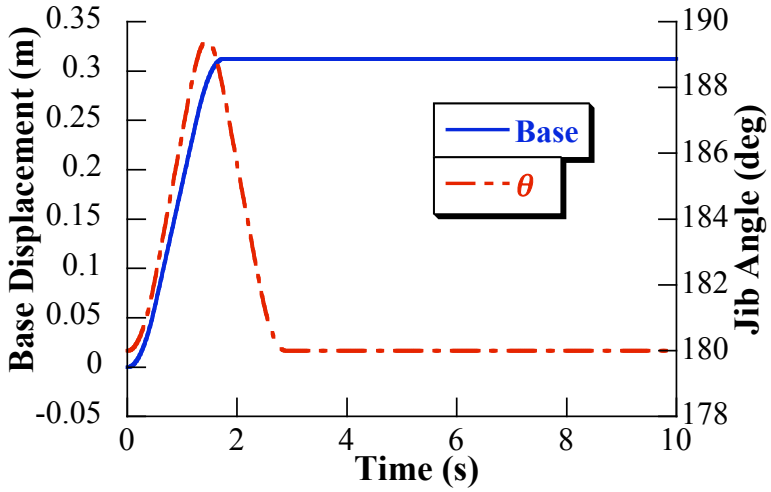

Figure 104: Mutli-Input Shaping Commands for Full Tower Model

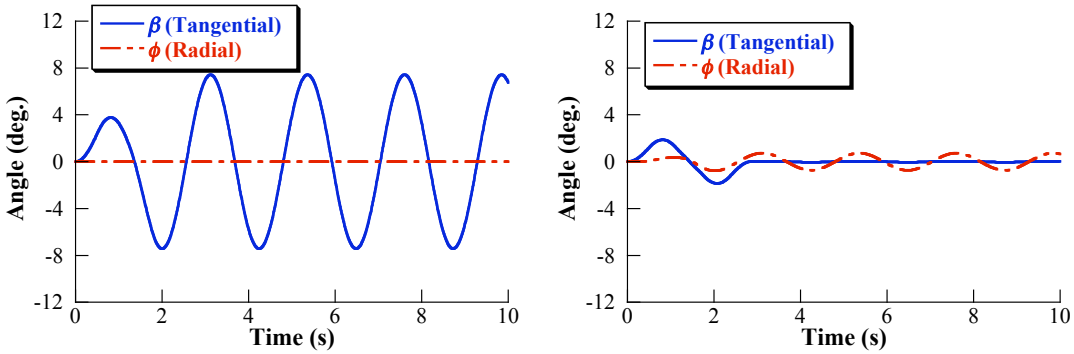

(a) Unshaped **(b)** MI-ZV Shaped

Figure 105: Full Tower Model Responses to Unshaped and MI-ZV Commands

Under certain conditions, even the radial component of oscillation can be reduced using only base motion and jib slewing. Figures 106 shows one such case. The configuration is nearly identical to the previous example. The difference is that the initial angle of the jib is not perpendicular to the direction of base motion. It is 5° forward of perpendicular (using Figure 103 as a guide). Because the jib is no longer exactly perpendicular to the base motion, the unshaped base command now excites vibration in both the β (tangential) and ϕ (radial) directions, as seen in Figure 106(a). For the MI-ZV shaped case, shown in Figure 106(b), both the β and ϕ responses have nearly zero residual vibration.

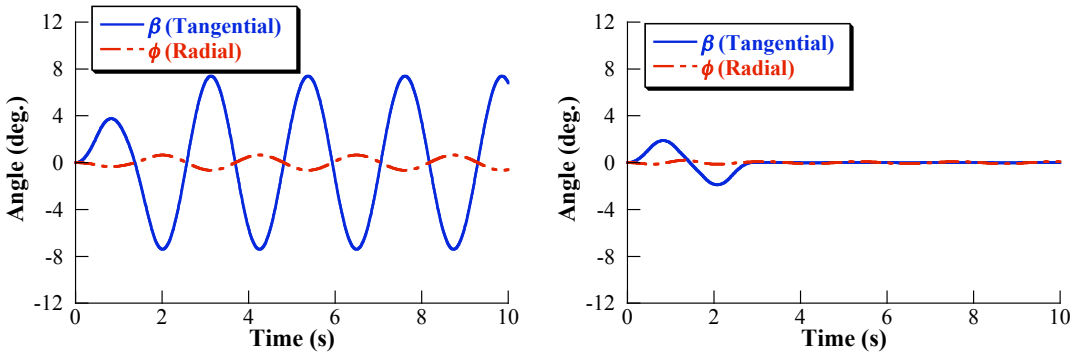

(a) Unshaped **(b)** MI-ZV Shaped

Figure 106: Full Tower Model Responses to Unshaped and MI-ZV Commands - Jib 5° Forward of Perpendicular to Base Motion)

The vector diagram presents a tool to visualize the vibration cause by an impulse sequence. It, however, presents only one methods to satisfy the vibration constraints. A more general method, for example, may do so via an optimization routine. To summarize, the generalized algorithm for the procedure detailed in this section is:

1. Model the system in block diagonal form
2. Simultaneously solve for impulse sequences to satisfy vibration constraints for each vibratory mode
3. Scale resulting impulses according to the inverse of corresponding B-matrix entries
4. Check for impulse summation to one
5. If impulses do not sum to one, then apply uniform scaling to achieve unity sum

6.3.3 Accounting for Actuator Limits

The vector diagram multi-input shaper design method developed in the previous section assumes that each actuator is able to produce the desired commands. This may not always be the case. In particular, the method requires the impulse sequences for each input to be convolved with identical reference commands. This can result in exceeding the limits of one or more actuators, while underutilizing others. In addition, the scaling to account

for each input's influence on the vibratory dynamics of the system may force an input to exceed its limits. To prevent this, the vectors on the vector diagram can be limited based upon the limits of each input.

Because the vector diagram methods require each impulse sequence to convolved with an identical reference command, the relationship between the input limits can be used to scale the vectors on the vector diagram. The common reference command can be scaled according to limit of one input. Then, the scaling of the impulse sequence (and corresponding vectors) can be used to account for the differences in actuator limits (and units).

The technique will be illustrated using a two-input system, in which both inputs equally affect the system, like that shown in Figure 94. The maximum actuator effort of the first input, u_1, is u_{1max}. The maximum effort of the second input, u_2, is u_{2max}. If the reference command is chosen such the the limits of the first input are not exceeded, then limiting the vectors representing the impulse sequence for the second input will ensure that the limits of the second input are not exceeded as well. The impulse amplitudes are limited according to:

$$\sum_{i}^{n} |_2A_i| \leq \left| \frac{u_{2max}}{u_{1max}} \right| \tag{84}$$

where n is the number of impulses in the impulse sequence for the second input[81]. This limit ensures that the shaped command will remain bounded by the actuator limit for all reference commands that are also bounded by the actuator limits. If the inputs do not equally affect the output, as seen in the previous section, then the impulse sequence must be scaled to account for the differences. To account for this impulse scaling, the limit on the impulse amplitudes should be further limited to compensate. For example, for the two input system, the maximum vector magnitude for second input is limited to be:

$$\sum_{i}^{n} |_2A_i| \leq \left| \frac{u_{2max}}{u_{1max}} \frac{B(2,2)}{B(2,1)} \right| \tag{85}$$

The constraints in (84) and (85) may be too severe for many cases. They were formed using worst case scenario, in which the absolute maximum actuator effort from a impulse

sequence is limited. For many cases, the constraint may be relaxed. This has been done successfully for traditional, single input shapers. The unity magnitude shapers presented in Section 3.4 are prime examples.

A more practical constraint may be to limit individual impulse amplitudes, rather than their sum. This is again analogous to the procedure used for unity magnitude shapers. This constraint is:

$$|_2A_i| \leq \left|\frac{u_{2max}}{u_{1max}}\right|, \quad i = 1, \ldots, n \tag{86}$$

This type of actuator scaling has already been demonstrated in this chapter. Figure 95(a) showed the commands generated from a MI-ZV shaper. The impulse amplitudes for the second input, u_2 impulse sequence where -0.5 and 0.5. These impulse amplitudes limited the input of the second command to half that of the unshaped, first input, u_1.

The general algorithm slightly modifies the algorithm presented in the previous section, as seen below:

1. Model system in block diagonal form
2. Determine impulse amplitude constraints for each input
3. Simultaneously solve for impulse sequences, which satisfy amplitude requirement from above, to satisfy vibration constraints for each vibratory mode
4. Scale resulting impulses according to corresponding B-matrix entries
5. Check for impulse summation to one
6. If impulses do not sum to one, then apply uniform scaling to achieve unity sum while satisfying impulse amplitude requirement

6.4 Adding Robustness via Secondary Actuation

In addition to combining inputs to create low vibration commands, multi-input shapers can also be used to increase the robustness of shaped commands. The illustration of these

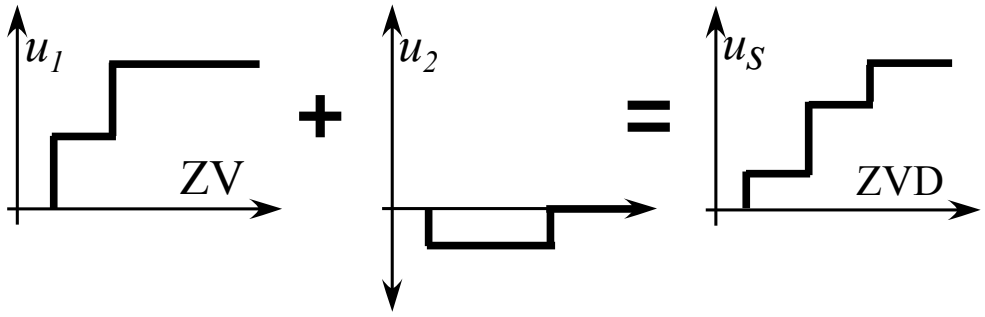

Figure 107: Compensation for Non-Robust Commands Utilizing Redundant Actuation

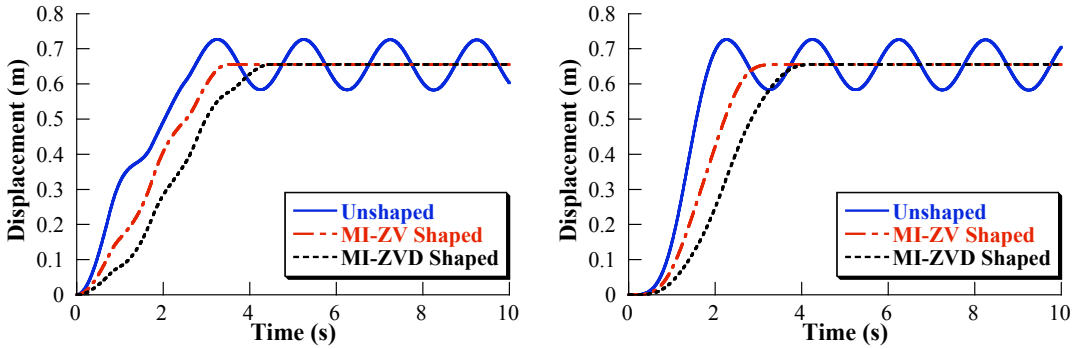

(a) Response of x_1 **(b)** Response of x_2

Figure 108: Responses to Unshaped, Base ZV-Shaped, and MI-ZVD commands

methods will utilize the two-mass spring damper system shown in Figure 94. Suppose that the first input, u_1, is only capable of the non-robust ZV shaped command. This scenario could result from a number of issues, namely a limited number of possible actuation states or other actuator limitations. In this case, the second input, u_2, can be designed such that the non-robust ZV command of u_1 is augmented by the secondary input, u_2, to create a more robust command. This process is shown in Figure 107 for an intial ZV-shaped command that is converted to a robust ZVD command, u_s, by the addition of a pulse in u_2.

The vibration at the design frequency will still reach a theoretical minimum of zero, as seen in Figures 108(a) and 108(b), but the command signal is more robust to errors in natural frequency. The additional robustness gained from this approach is evident in Figure 109. The horizontal axis on this plot is normalized frequency, the actual frequency of the system divided by the frequency used to design the input shaper. The vertical axis

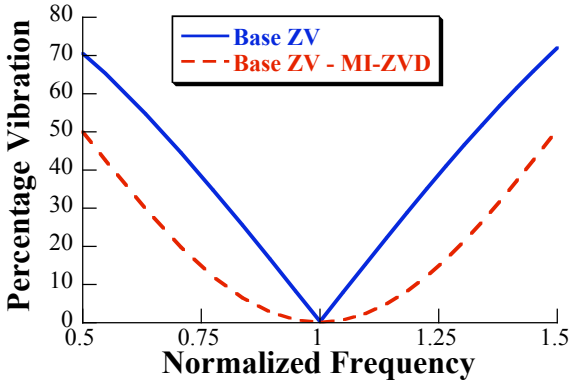

Figure 109: Sensitivity Curves for Base ZV Shaped and Multi-Input ZVD Shaped Commands

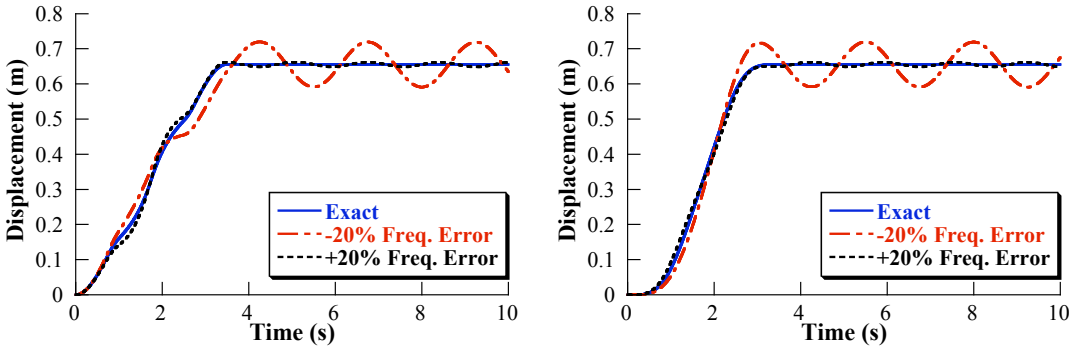

(a) x_1 Response **(b)** x_2 Response

Figure 110: Responses to MI-ZV Shaped Commands with ±20% Frequency Error

represents a measure of the reduction in system vibration. It is the ratio of vibration excited by a shaped command to that excited by an unshaped command, expressed as a percentage. The price of this increase in robustness is an increase in system rise time, also seen in Figures 108(a) and 108(b).

The benefit of the added robustness is shown in Figures 110 and 111. Figure 110 shows the responses of two masses from the model introduced in Section 6.1 to a MI-ZV shaped commands with ±20% modeling error in frequency. The vibration reducing qualities of the MI-ZV shaper are greatly reduced due to this error. Figure 111 shows the responses of the two masses to a MI-ZVD shaped commands in the presence of the same error. The vibration for both masses remains well below that of the MI-ZV shaped case, illustrating

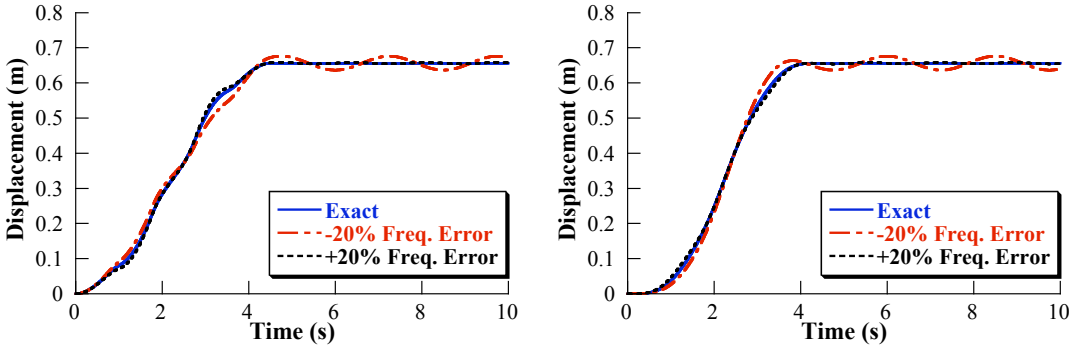

(a) x_1 Response **(b)** x_2 Response

Figure 111: Responses to MI-ZVD Shaped Commands with ±20% Frequency Error

that it is more robust to errors in frequency, as Figure 109 predicted.

This method of multi-input commands that increase robustness followed the orignial method for developing multi-input commands from Section 6.1. Like the original method, these methods may be generalized, including accounting for scaling between inputs and actuator limits as was done in Section 6.3.

6.5 Using Multi-Input Shapers to Reduce Perceived Lag

Another area in which multiple inputs can be utilized is in speeding system motion, while maintaining low levels of vibration. Input shaping provides a method to dramatically reduce motion-induced oscillation, but introduces a lag to the command. While necessary to limit vibration, this lag may be perceived by human operators as causing the system to behave more sluggishly. The multi-input shaping methods discussed to this point have leveraged heavily from single input shaper forms, using multiple inputs to mimic the form of traditional single input shapers. As such, the system, under these multi-input shaped commands, may also appear to behave more sluggishly than without input shaping. This section presents a method to reduce the perceived lag caused by these commands.

While the idea of minimizing shaper duration is common, the explicit consideration of the perception of system's performance during input shaper design has received relatively

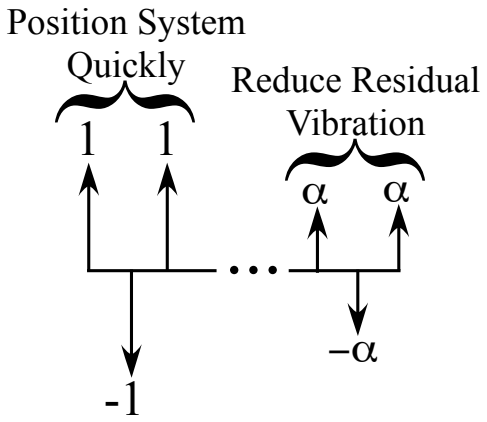

Figure 112: Reduced-Perceived-Lag (RPL) Input Shaper Form

little attention. Grosser and Singhose presented one method that essentially partitions the impulse sequence into positioning and vibration reduction segments [16]. A Reduced-Perceived-Lag (RPL) input shaper similar to what their method might produce is shown in Figure 112.

In this case, the initial, unity magnitude impulses position the system quickly, with a relatively low level of vibration (Grosser and Singhose recommended 10-15% of the unshaped level). Then, the second series of impulses reduces the level of vibration to the tolerable level, typically 5% of the unshaped. In addition, the second series of impulses is usually constrained to be smaller in amplitude than the first. This serves to limit the deviation of the system from the desired position established by the positioning portion of the impulse sequence. This fact also makes this method easily extended to multi-input systems where secondary actuators could have much lower actuator limits than the main positioning inputs, such as multi-stage positioning systems or micro/macro manipulators.

While this method does decrease the rise time of the system, reducing the perceived input shaper lag, it does increase the duration of the shaper. As such, the time at which vibration is limited to below the tolerable level is increased. Utilizing a multi-input shaper can reduce the perceived input shaper lag, while achieving the tolerable level of vibration in a timeframe equivalent to a standard input shaper.

To do so, some actuators are assigned to be primarily responsible for positioning the

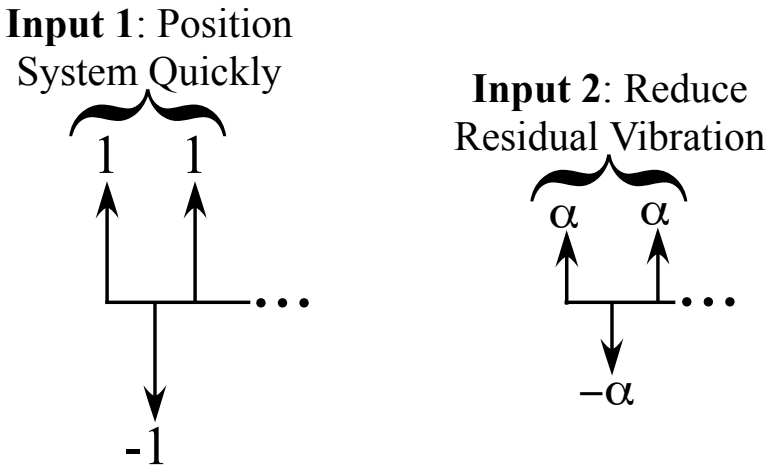

Figure 113: Multi-Input Reduced-Perceived-Lag (MI-RPL) Input Shaper Form

system, while others are made primarily responsible for reducing vibration to a tolerable level. The RPL shaper from Figure 112 is essentially divided among the inputs, as shown in Figure 113.

The solution procedure for Multi-Input Reduced-Perceived-Lag (MI-RPL) shapers reduces to solving for the two sequences. To generate the first, positioning sequence, SNA-SI methods are most generally applicable. By increasing the tolerable level of vibration at a constant Insensitivity, the duration of the shaper generated will decrease [86]. The second, vibration-reduction sequence, must reduce the vibration induced by the positioning sequence to the tolerable level.

This can be visualized using multi-input vector diagrams like that shown in Figure 114. The vector diagram in Figure 114(a) shows the positioning sequence, which results in some amount of vibration proportional to ${}_1A_R$. The vibration-reducing sequence must then sum with this vector such that the total is a vector of small amplitude, meaning that the resulting vibration will also be low amplitude. This is shown in Figure 114(b) where the resultant vector from vibration-reduction sequence, ${}_2A_R$, is opposite ${}_1A_R$. This MI-RPL shaper will result in zero residual vibration at the design frequency.

In practice, the solutions to both sequences can be determined by a single optimization routine. This solution procedure is also advantageous, as the optimal solution is sometimes

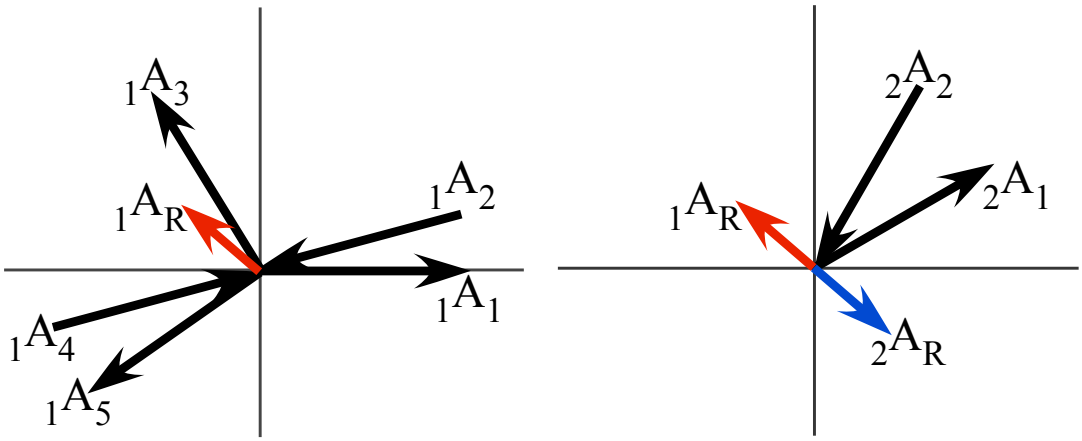

(a) Positioning Sequence **(b)** Vibration-Reduction Sequence

Figure 114: MI-RPL Vector Diagrams

Table 8: Parameters Used for MI-RPL Design

Parameter	Value
V_{tol}^{Pos}	20% (0.20)
V_{tol}	5% (0.05)
Insensitivity, I(5%)	0.20
α	0.15

difficult to determine using a vector diagram alone, especially as the number of impulses increases.

To illustrate the time saving from MI-RPL shapers, the two-mass spring model from Figure 94 is used. To design MI-RPL shapers several design parameters must be set. These include the tolerable level of vibration from the positioning portion of the command, V_{tol}^{Pos}, and the Insensitivity and tolerable amount of vibration of total command, V_{tol}. In addition, the amplitude of the impulses of the vibration-reducing impulse sequence, α, must be set. The design parameters used for the MI-RPL shaper for this example are shown in Table 8. For comparison, a UM-SI shaper was also designed with identical Insensitivity to the MI-RPL shaper. The UM-SI shaped case only utilized the first input, u_1.

Figure 115 compares the responses to unshaped, UM-SI shaped, and MI-RPL shaped

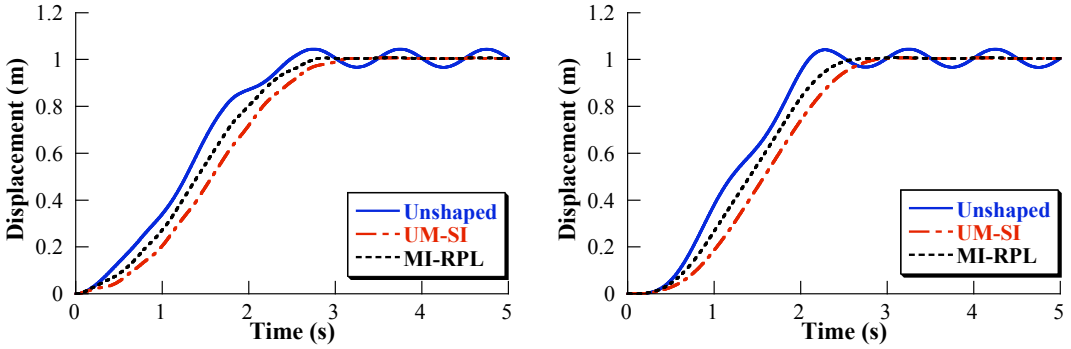

(a) x_1 Response **(b)** x_2 Response

Figure 115: Responses to Unshaped, UM-SI Shaped, and MI-RPL Shaped Commands

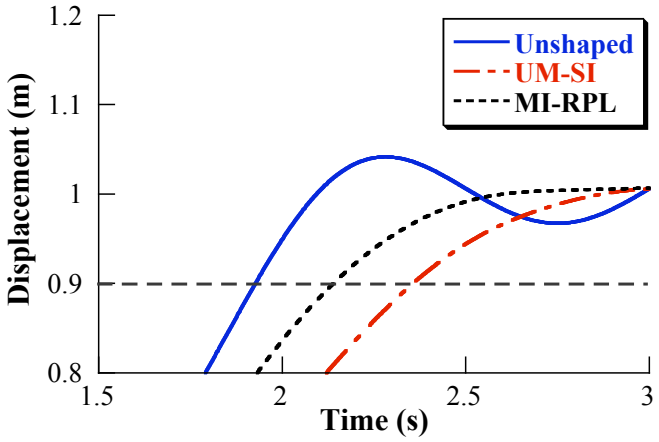

Figure 116: Close View of Time Savings from MI-RPL Shaping

commands. Both the UM-SI and MI-RPL commands excite less vibration than the unshaped case. The MI-RPL command does so, however, with a much shorter rise time than the UM-SI case. For this case, the MI-RPL provides an approximate 10% reduction in rise time of x_2 from the UM-SI shaped case, as seen in the closer view of the x_2 response shown in Figure 116. This is particularly significant, as the UM-SI shaper is the shortest duration shaper for a given Insensitivity [87, 88].

While the development of the MI-RPL shapers has used the simple model, the technique can be combined with the methods to scale for input contributions or actuator limits, presented in the previous sections. This is demonstrated by the responses in Figure 117, which shows the payload position for unshaped, UM-SI, and MI-RPL commands, using

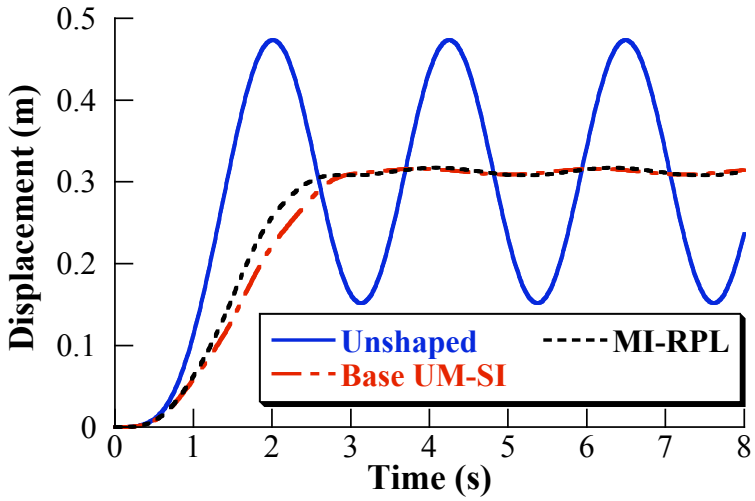

Figure 117: Payload Response for Unshaped, Base UM-SI, and MI-RPL Shaped Commands

Table 9: Parameters Used for UM-SI and MI-RPL Design on Full Model

Parameter	Value
Cable Length, l	1.245m
ω_n	0.22 Hz
ζ	0.0
Trolley Position, r	0.80m
V_{tol}^{Pos}	20% (0.20)
V_{tol}	5% (0.05)
Insensitivity, I(5%)	0.20
α	0.15

the full, nonlinear tower crane model. The initial configuration was again with the jib perpendicular to the direction of base motion, shown in Figure 103. UM-SI and MI-RPL shapers were designed using the parameters shown in Table 9. For the UM-SI shaped case, only the base was shaped with the UM-SI command. For the MI-RPL shaped case, the base was shaped using the unity magnitude, positioning portion of the MI-RPL command. The slewing motion was shaped with the vibration-reducing portion of the MI-RPL command.

The cost of the improved rise time is a small excitation in the ϕ (radial) direction and slightly higher amplitude β (tangential) vibration, both in transient and residual, as seen by comparing Figures 118(a) and 118(b).

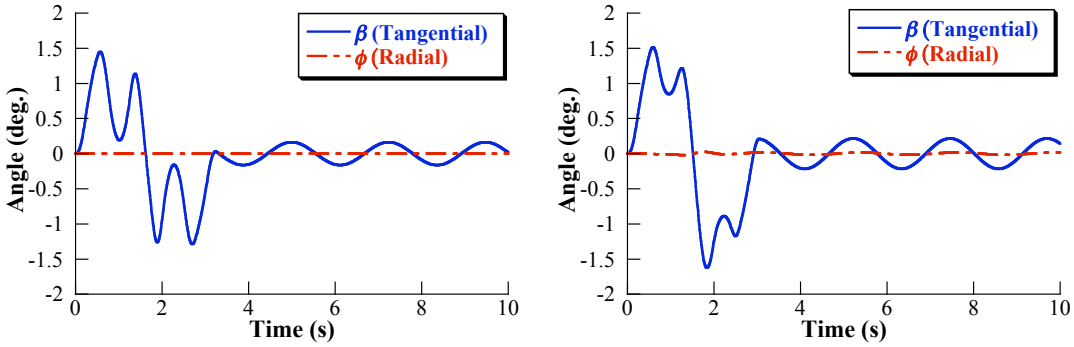

(a) UM-SI [I(5%) = 0.20] Shaped Responses **(b)** MI-RPL [I(5%) = 0.20] Shaped Responses

Figure 118: Payload Angle Responses to UM-SI Shaped and MI-RPL Shaped Commands

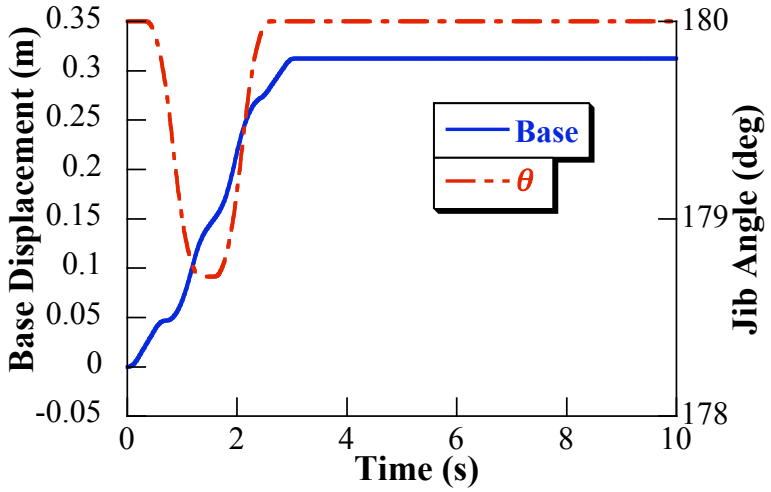

Figure 119: MI-RPL [I(5%)= 0.20] Shaped Commands

Remember that the vibration-reducing portion of the MI-RPL commands are typically constrained to be much smaller in amplitude than the positioning sequence impulses (α = 0.15 for this case). These smaller impulses lead to smaller amplitude slewing commands, as shown in Figure 119, along with the base command. The amplitude of the MI-RPL slewing command is approximately 10% of the MI-ZV command shown previously in Figure 104. The smaller amplitude slewing command reduces the influence of the centripetal effects on payload oscillation. This leads to a ϕ excitation that has much smaller amplitude than was excited by the MI-ZV command, as seen by comparing Figures 105 and 118(b).

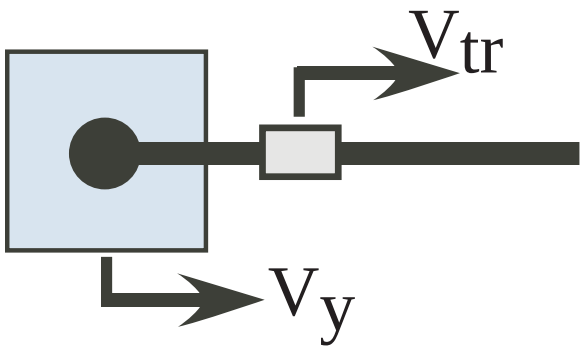

Figure 120: Trolley Motion Parallel to Base Motion

6.6 Experimental Verification of Multi-Input Shaping

While the system posed in Figure 94 can be considered simplistic, it does represent one possible operating condition of mobile cranes. This condition occurs when the jib is aligned with the direction of base motion, and base and trolley motions are combined, as shown in Figure 120. This case was tested on the mobile tower crane shown in Figure 121. Details of this experimental setup can be found in Appendix A.

The payload response to a step command in base position is shown as a solid line in Figure 122. One can see that this unshaped command excited significant payload oscillation. The response of the payload to a base command shaped via a ZV shaper is also shown in Figure 122. In theory, the ZV shaper should result in zero vibration. However, the tower contains un-modeled dynamics, primarily base rocking due to floor irregularities. In addition, the control of the base motion is relatively course, making tracking a shaped command profile difficult. As a result, the ZV shaped command results in a much lower vibration than the unshaped case, but not the theoretical minimum. If a multi-input ZV (MI-ZV) shaper is applied, a lower amount of vibration results, also seen in Figure 122. In theory, this shaper should have the same amount of vibration as the single input ZV. Again, however, the shaper's effectiveness depends upon the linearity of the system. Un-modeled dynamics can account for the differences between the different shapers and differences between the theory and experiments. Also, the trolley is capable of much finer motion than

(a) Mobile, Portable Tower Crane **(b)** Mobile, Portable Tower Crane Base

Figure 121: A Mobile, Portable Tower Crane

the base, enabling it to more accurately track a shaped command profile.

This phenomenon is also seen if the amplitude of vibration for the unshaped, ZV shaped, and MI-ZV shaped commands for varying suspensino cable lengths is examined. Figure 123 shows the vibration amplitude of each command as a function of normalized frequency. The normalized frequency is the actual system frequency (changed by varying the suspension cable length) divided by the frequency used for the input shaper design. Using the methods for creating robust multi-input shapers presented in Section 6.4 would increase the robustness of the multi-input command to frequency changes.

6.7 Conclusion

This chapter presented methods to design multi-input shapers that utilize design techniques similar to those for single input shapers. The multi-input vector diagram was introduced and used to design multi-input shapers. In addition, methods of scaling these multi-input

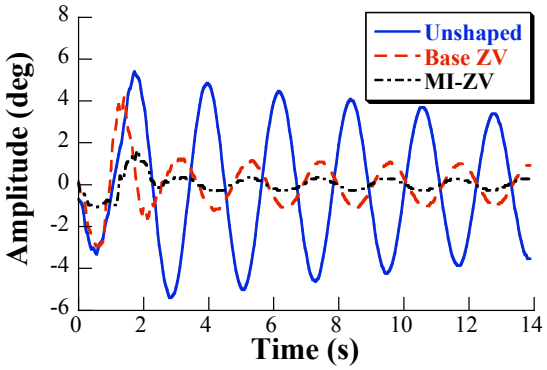

Figure 122: Payload Response to Unshaped, ZV, and MI-ZV Shaped Commands

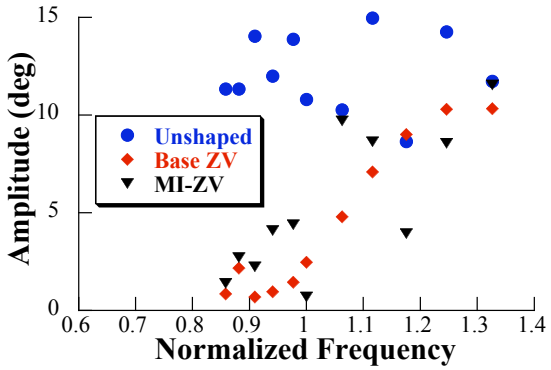

Figure 123: Vibration Amplitude for Varying Cable Lengths

vector diagram solutions to account for the influence of each input on the vibratory dynamics were shown. A technique that explicitly considers actuator limits during the mutli-input vector diagram design process was also demonstrated. In addition to creating multi-input shaped commands, a method was introduced that uses secondary actuators to increase the robustness of a single input shaped command. Finally, a Multi-input Reduced Perceived Lag input (MI-RPL) shaper was presented that improves system rise time beyond that capable with traditional single input shaped commands.

CHAPTER VII

INPUT SHAPERS FOR REDUCING OVERSHOOT IN HUMAN-OPERATED SYSTEMS

CHAPTER SUMMARY: *This chapter presents a new class of Zero Overshoot (ZO) input shapers that are designed to reduce shaper induced overtravel from human operator commands. During the development of these new shapers, an expression for shaper induced overtravel is introduced. This expression is used as an additional constraint in the input shaper solution process to generate the ZO shapers. Experiments from a portable bridge crane verify the theoretical predictions.*

Input shaping has been shown to drastically reduce motion-induced oscillation. The compromise between shaper duration and robustness has also been thoroughly discussed. This chapter will focus on one of the detrimental effects of longer shaper duration: overtravel and overshoot.

Preprogrammed, input shaped commands will reach the same setpoint as unshaped by traveling for a short time duration after the unshaped command has stopped, as shown in Figure 124. When used with human operators, input shaping will also cause some system motion after the user has commanded the system to stop. This continued motion, which occurs in a timeframe equal to the duration of the shaper, is needed to suppress the system vibration excited during the deceleration portion of the command. However, to accurately position the system, the human operator must estimate this travel time. This effect may make precise positioning of the system difficult, especially for inexperienced operators.

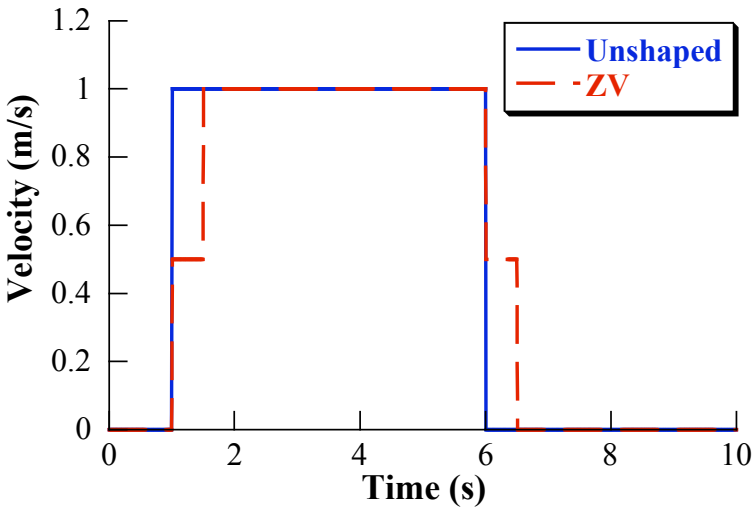

Figure 124: Unshaped and ZV-shaped commands

This chapter will present a new class of input shapers designed to explicitly consider the stopping portion of command from human operators. Final positioning error will be a primary consideration for these commands. A new constraint on input shaper overshoot is introduced and used to generate shapers that provide zero overshoot beyond the unshaped case. During the formulation of these new shapers, commands are assumed to be velocity commands. This is consistent with the way that many machines, including cranes, are controlled by human operators.

7.1 Overtravel and Overshoot

Figure 124 showed that a ZV-shaped pulse command is longer than the unshaped reference command. In the figure, an ideal pulse in velocity was shown. However, such ideal velocity profiles do not exist. Instead, the velocity command will likely be trapezoidal in shape, like that shown in Figure 125. The trapezoidal profile can be categorized by its ramp time, the time the systems take to accelerate to (and decelerate from) maximum velocity. When the rate-limited velocity commands are used in conjuction with a human operator, even the unshaped command will move the system beyond where the user issues the "Stop Now" command. This is shown in Figure 126, where the ramp to zero velocity takes a finite

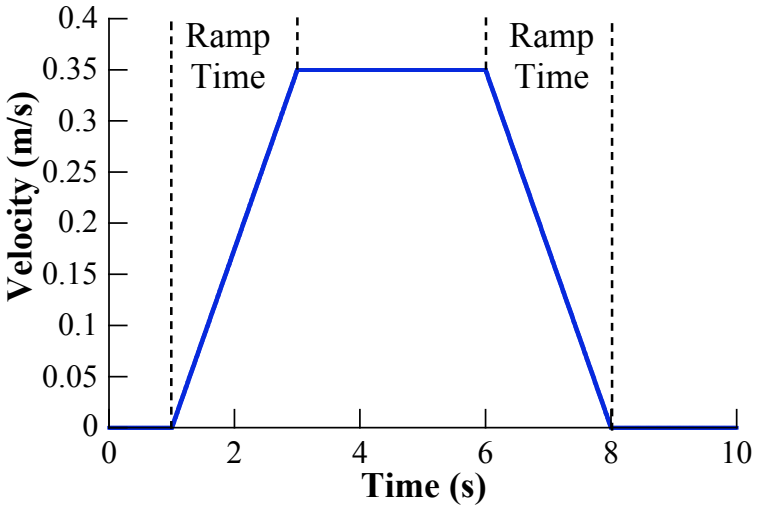

Figure 125: A Trapezoidal Velocity Profile

amount of time. During this time the system will continue to move. The distance it moves is equal to the hatched region in Figure 126. As a result, all commands will have some amount of overshoot beyond the operator's intentions.

Also shown in Figure 126 is the ZV-shaped version of the same velocity profile. It is immediately obvious that the ZV-shaped command takes longer to reach zero velocity. The distance that the system will move after the "Stop Now" command, when ZV shaping is enabled, is the sum of the hatched and shaded regions in the figure. In addition, the overtravel caused solely by the increase in command duration by the input shaper is equal to the shaded region. It will soon be shown that the area of this region is easily described using only the impulse amplitudes and times of the input shaper. Furthermore, it will be shown to be independent of the form of the original unshaped command (provided the unshaped command meets certain criteria).

If the commands in Figure 126 are issued to a bridge crane, then the trolley responses shown in Figure 127 result. Notice both the unshaped and ZV-shaped cases result in some trolley overtravel. For the ZV-shaped case, the final positioning error is much larger.

The payload responses to the same commands are shown in Figure 128. Notice that the unshaped command exhibits significant oscillation, resulting in a maximum deviation

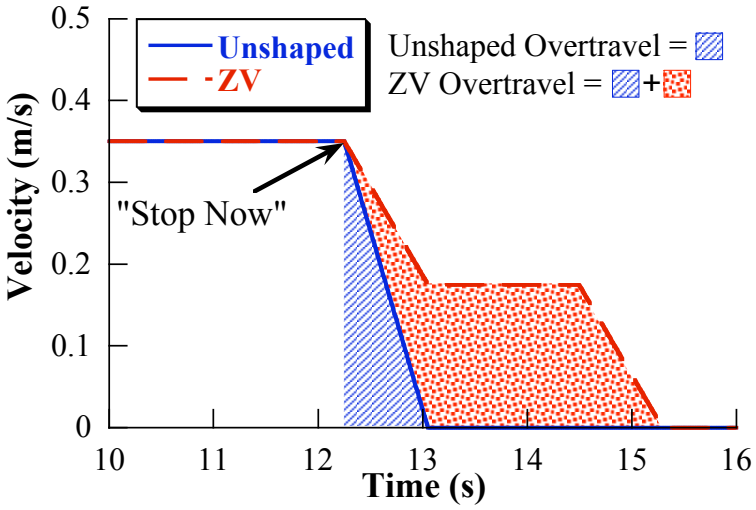

Figure 126: Overtravel

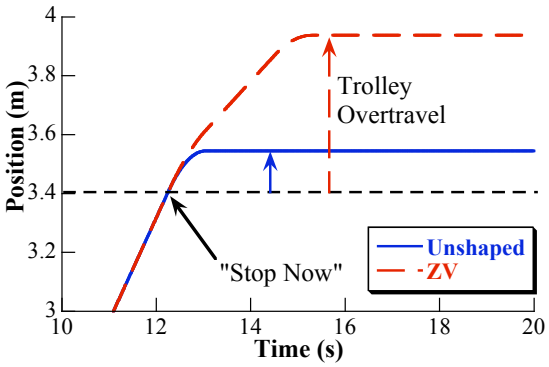

Figure 127: Example of Unshaped and ZV-shaped Overtravel

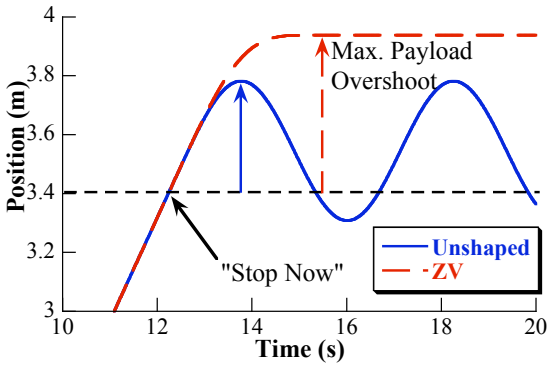

Figure 128: Example Unshaped and ZV-shaped Maximum Overshoot

from the desired position that is much greater than the trolley positioning error. However, for the ZV-shaped command, the payload response exhibits no oscillation and the payload deviation from the desired position is equal to the trolley's overtravel.

The difference between the trolley overtravel and the maximum overshoot of the payload from desired position indicates the need for some additional terminology. For the remainder of this chapter, the trolley's deviation from the desired position will be called *overtravel*. The maximum deviation of the payload from the desired position will be called *overshoot*. The difference between trolley overtravel and payload overshoot is shown schematically in Figure 129.

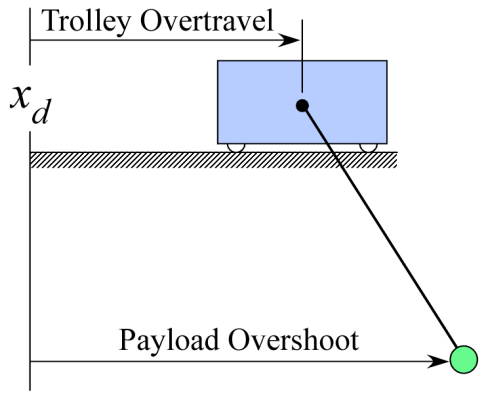

Figure 129: Diagram of Trolley Overtravel and Payload Overshoot

7.2 Input Shaper Overtravel and Overshoot

Knowing that input shapers cause overtravel and overshoot, having an expression that describes each independent of the reference command would be useful. In Figure 130, the distance that an input shaped command travels over the unshaped case is described by the shaded region in each subfigure. As additional impulses are added, from the ZV shaper in Figure 130(a) to the ZVDDD shown in Figure 130(c), it becomes apparent that this area can be represented in terms of shaper impulse times and amplitudes. The area is essentially a course integration of the velocity command, using the shaper impulse times as the integration step size.

The equation to describe the area is:

$$x(t_n + t_f) - x(t_f) = V_{stop} \sum_{m=1}^{n-1} \left[(1 - \sum_{i=1}^{m} A_i)(t_{m+1} - t_m) \right] \tag{87}$$

where n is the number of impulses in the shaper, t_f is "stopping" time, V_{stop} is the velocity when the deceleration portion of the command begins, and A_i and t_i are i^{th} impulse amplitude and time location, respectively. This conveniently simplifies to:

$$x(t_n + t_f) - x(t_f) = V_{stop} \sum_{i=2}^{n} A_i t_i \tag{88}$$

It is useful to describe the overtravel independent of the reference command and system parameters. To do so, Equation (88), can be normalized by multiplying by $(V_{stop}\tau)^{-1}$, where

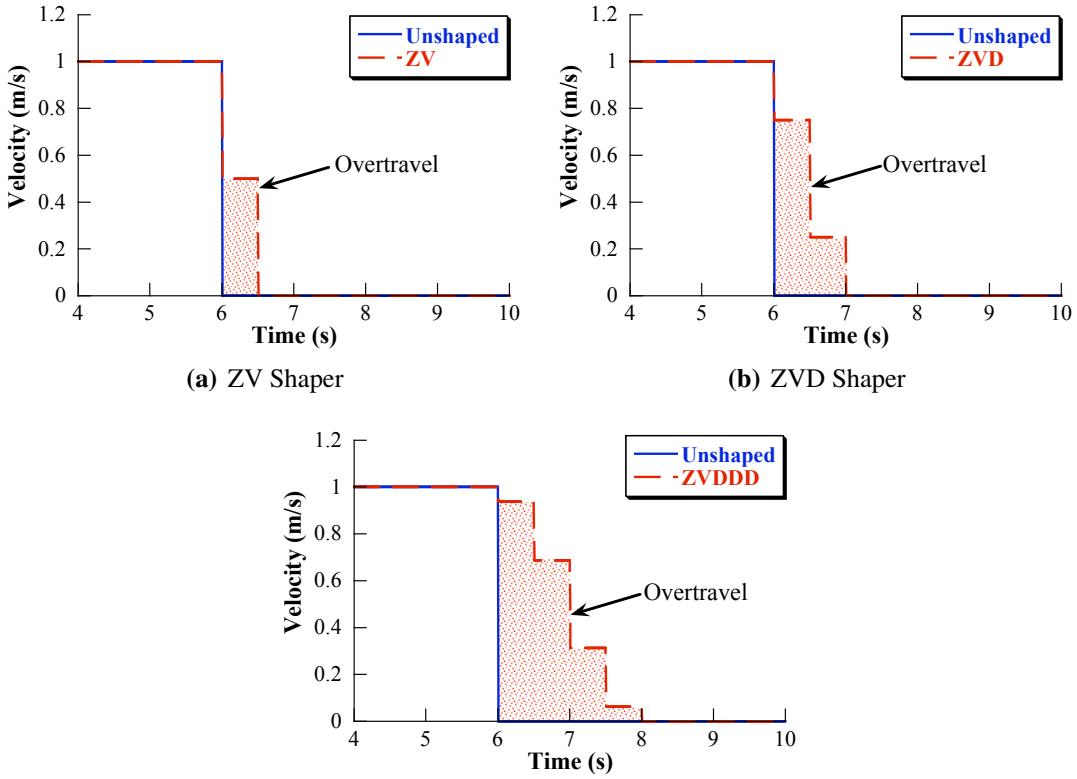

(a) ZV Shaper

(b) ZVD Shaper

(c) ZVDDD Shaper

Figure 130: Shaper Overtravel Beyond the Unshaped Command

τ is the vibration period the shaper was designed for:

$$x^{+} \equiv \bar{x}(t_n + t_f) - \bar{x}(t_f) = \frac{1}{\tau} \sum_{i=2}^{n} A_i t_i \tag{89}$$

where x^{+} is the overtravel caused solely by the input shaper. Equation (89) provides a measure of the overtravel induced by an input shaper, independent system parameters. It represents the overtravel of the shaped command beyond that present in the original reference command. The equation will hold true for all command types given that the command meets one primary certain criteria, that the unshaped and shaped commands begin decelerating from the same velocity and decelerate to zero velocity.

The normalized overtravel of several, common input shapers is shown Figure 131. To the left of the vertical line are all positive shapers. Notice that, as expected, the longer duration shapers display larger amounts of normalized overtravel. To the right of the vertical line are several, common unity magnitude shapers. Again, longer duration shapers display

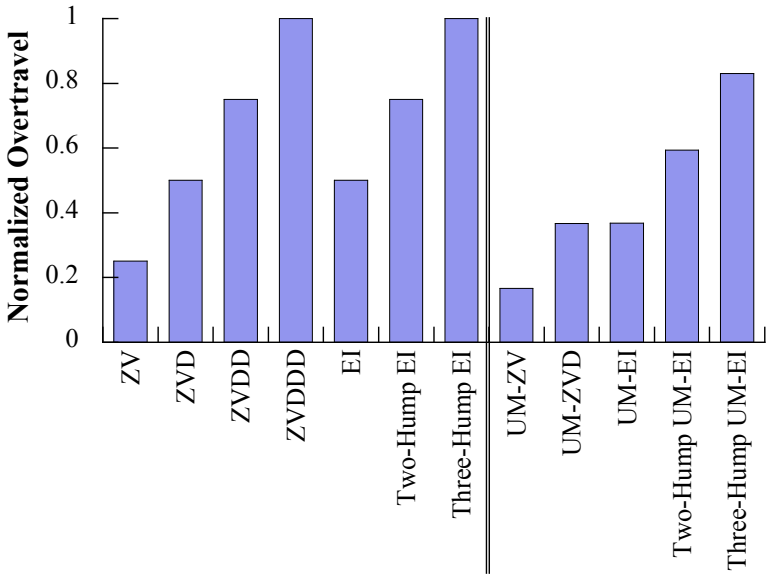

Figure 131: Normalized Overtravel

larger amounts of overtravel. Notice, however, that the unity magnitude shapers overtravel less than their positive counterparts. This also is expected, as the unity magnitude equivalent shapers are shorter in duration.

Figure 132 shows the normalized overtravel of several SNA-SI shapers as a function of maximum negative amplitude. The three SNA-SI shapers were designed with Insensitivities at $V_{tol} = 5\%$ of 0.25, 0.50 and 0.75. The normalized overtravel decreases as higher amplitude negative impulses are allowed and as the Insensitivity is decreased. Both of these changes have the effect of decreasing shaper duration, allowing lower overtravel.

To better understand what these values of normalized overshoot mean, simulations of a typical industrial bridge crane, like the one shown in Figure 133 were used. It has a maximum velocity of approximately $0.35\frac{m}{s}$. In the simulations, the suspension cable length was set to 5m in length. The crane has a ramp-time of approximately 0.8s, meaning it takes 0.8s to accelerate to (and decelerate from) maximum velocity. However, to test a range of ramp-times, simulations were conducted over ramp-times ranging from 0.0s to 3.0s. For all cases, the command time was chosen to be long enough that the trolley reached its maximum velocity before deceleration began.

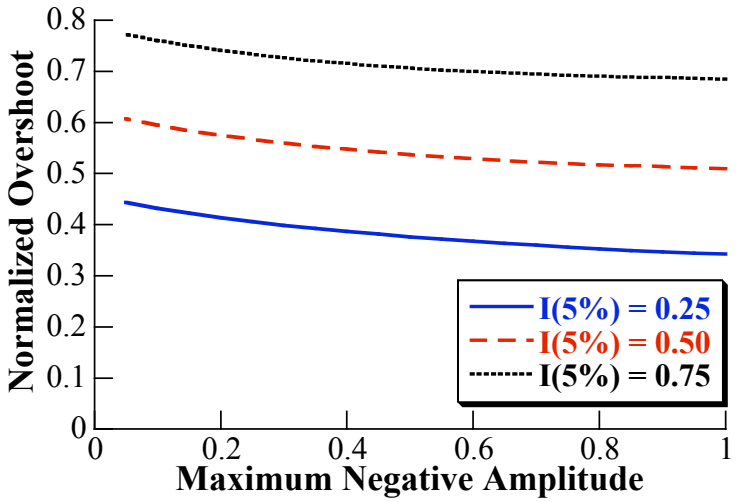

Figure 132: Normalized Overshoot for Several SNA-SI Shapers

Figure 133: 10-ton Bridge Crane

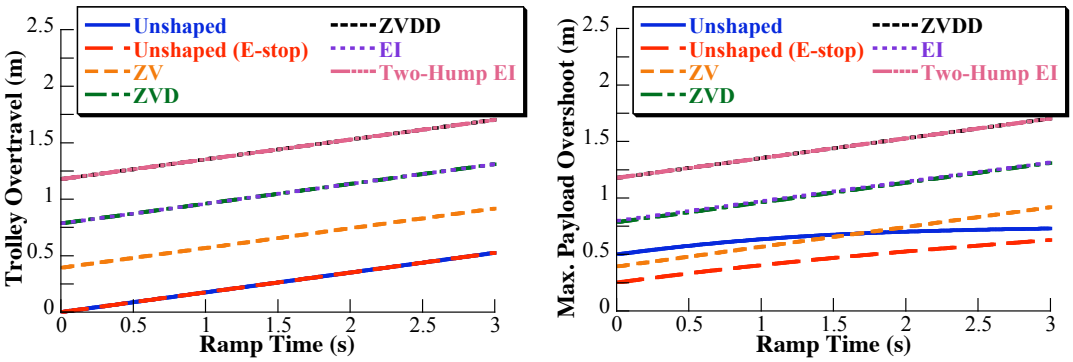

(a) Trolley Overtravel

(b) Maximum Payload Overshoot

Figure 134: Overtravel and Overshoot as a Function of Ramp Time for Positive Shapers

Figure 134(a) shows the trolley overtravel as a function of ramp-time for two unshaped commands and several positive input shapers. In the first unshaped case, the command is completely unshaped; the acceleration and deceleration portions of the command both caused payload oscillation. In the second case, labeled *Unshaped (E-stop)*, the acceleration portion of the command was assumed to have excited no vibration. This would be analogous to using a ZV input shaper on the acceleration portion of the command to reach maximum velocity without any payload oscillation. For the deceleration portion, input shaping was not used. This might be similar to an "E-stop" condition, where the crane would be forced to stop as quickly as possible.

All of the input shaped commands display larger amounts of trolley overtravel than the unshaped cases, at all values of ramp time. Longer, more robust shapers display larger amounts of overtravel than shorter, less robust shapers. This is expected given the results shown in Figure 131. It is also important to note that the overtravel of the shaped commands increases at the same rate as the unshaped commands as ramp time increases (*i.e.*, the slopes are the same). The overtravel caused solely by input shaping remains constant. This confirms the prediction given in (89).

Figure 134(b) shows the maximum payload overshoot for the same commands that were shown in Figure 134(a). There are several important points to see here. The first is that both unshaped cases exhibit much more payload overshoot than trolley overtravel.

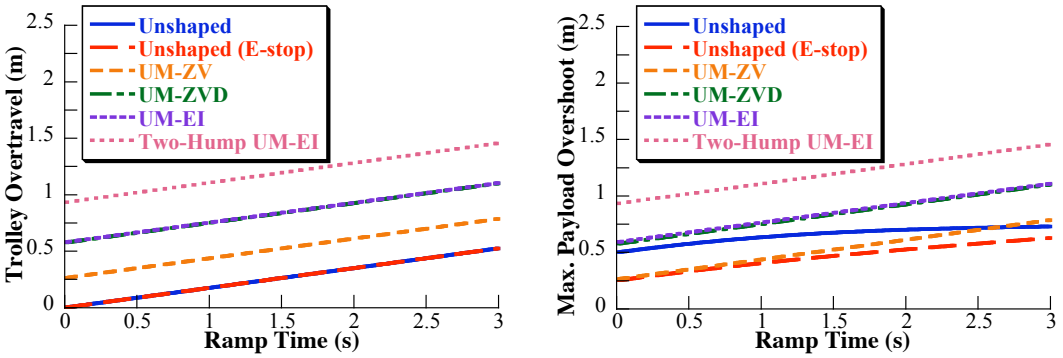

(a) Trolley Overtravel **(b)** Maximum Payload Overshoot

Figure 135: Overtravel and Overshoot as a Function of Ramp Time for Unity Magnitude Shapers

Another point to notice is that the maximum payload overshoot and trolley overtravel are equal for the all shaped commands shown but the EI. This is because each shaped command excited zero vibration at the modeled frequency. The EI shaper is designed with a V_{tol} of 5%, so the maximum payload overshoot is slightly greater than trolley overtravel. The final point to notice is that for ramp times below 1.5s, the maximum payload overshoot for the ZV shaped command is less than that of the unshaped command. This is an important point; even if the trolley overtravels farther than the unshaped case, the payload does not.

Figure 135(a) shows the trolley overtravel for the unity magnitude analogies of the shapers shown in Figure 134(a). The same general trends hold true. Robust, longer duration shapers exhibit higher levels of overtravel. However, when compared to their positive counterparts, the unity magnitude shapers overtravel less. Figure 135(b) shows the maximum payload overshoot for these shapers. There is again little or no difference between the trolley overtravel and payload overshoot for the shaped cases. The UM-ZV shaper has less maximum payload overshoot than the unshaped case for ramp times up to 2.5s. In addition, the UM-ZVD and UM-EI shapers approach the maximum payload overshoot of the unshaped case for low ramp times, despite having much higher trolley overtravel values.

7.3 Zero Overtravel (ZO) Shapers

The normalized overshoot equation, (89), leads to a new constraint on the shaper-induced overtravel. It can be expressed as:

$$x^+ \equiv \frac{1}{\tau} \sum_{i=2}^{n} A_i t_i \leq \Delta x^+_{des}, \tag{90}$$

where x^+_{des} is the desired amount of shaper-induced overshoot. This constraint can be applied in addition to any desired vibration constraints. It is important to note, however, that to reduce the amount of shaper-induced overtravel, negative impulses must be allowed. The following sections will present several classes of input shapers developed using this constraint.

7.3.1 Zero Vibration–Zero Overtravel (ZV-ZO) Shapers

Zero Vibration–Zero Overtravel (ZV-ZO) shapers seek to limit both residual vibration and shaper-induced overshoot to zero. The residual vibration constraints were summarized in Section 4.2.3. The zero overshoot constraint can be expressed as:

$$\frac{1}{\tau} \sum_{i=2}^{n} A_i t_i = 0 \tag{91}$$

In addition to the zero vibration and zero overtravel constraints, there are several impulse amplitude constraints. Impulses are constrained to be between negative one and one, which can be expressed as:

$$-1 \leq A_i \leq 1, \quad i = 1, \ldots, n \tag{92}$$

One difference between this constraint and the unity magnitude and specified negative amplitude impulse amplitude constraints is that the sign of the impulses is not forced to alternate. This is an important point for low overshoot shapers and necessary to limit overshoot. Impulse amplitudes are still constrained to sum to one.

Given the nonlinearity of the constraint set for the ZV-ZO shapers, impulse amplitudes and times must be solved using an optimization routine or numerical solver. The form of

Table 10: ZV-ZO Shapers for Damped Systems

$$t_i = (M_0 + M_1\zeta + M_2\zeta^2)\tau, \quad \tau = \frac{2\pi}{\omega}$$

$$A_i = M_0 + M_1\zeta + M_2\zeta^2$$

	M_0	M_1	M_2
A_1	0.8170	0.6871	-0.7456
A_2	1.0000	0.0000	0.0000
A_3 (= -A_1)	-0.8170	-0.6871	0.7456
t_2	0.6457	0.3982	0.2244
t_3	0.7898	-0.1504	0.8577

the ZV-ZO shaper for undamped systems is:

$$\begin{bmatrix} A_i \\ t_i \end{bmatrix} = \begin{bmatrix} 0.8164 & 1.000 & -0.8164 \\ 0 & 0.6451\tau & 0.7902\tau \end{bmatrix} \tag{93}$$

For systems with viscous damping, the amplitudes and times become functions of the damping ratio, as shown in Table 10. The shapers described in Table 10 are the result of curve fits for a series of solutions over the range $0 \leq \zeta \leq 0.3$. The maximum error of the fit for any impulse time or amplitude is less that 0.05% in the range.

The command resulting from shaping a velocity pulse with a ZV-ZO shaper is shown in Figure 136. Note that a ZV shaper was used to shape the acceleration portion of the command. The ZV-ZO shaper was only used on the deceleration portion of the command.

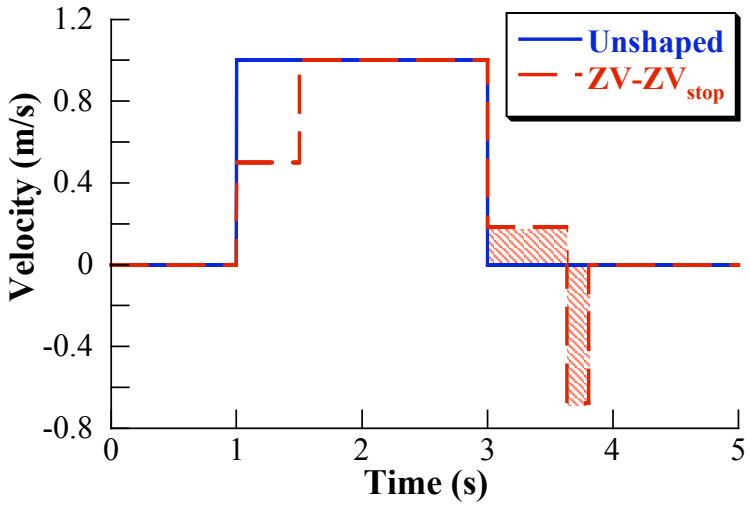

Figure 136: Unshaped and ZV-ZO Commands

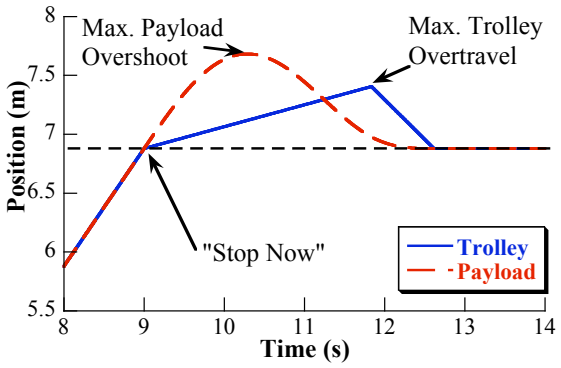

Figure 137: Response to ZV-ZO Commands

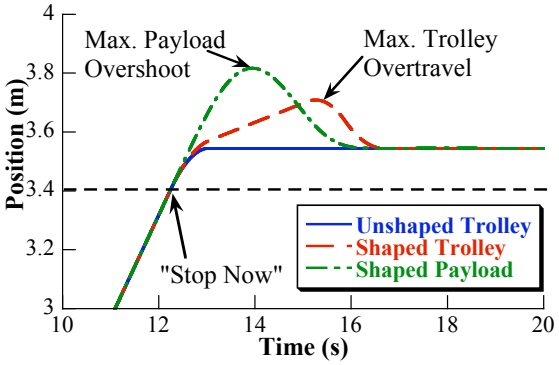

Figure 138: Responses to Unshaped and ZV-ZO Trapezoidal Velocity Profiles

Using a ZV-ZO shaper on the acceleration portion of the impulse would create a command with a higher maximum velocity than the unshaped command, possibly saturating actuators and resulting in vibration. Notice that the shaped command has a region of negative velocity. This region is what allows the zero overshoot constraint to be achieved; the negative velocity portion of the command returns the trolley to the position at which the "Stop Now" command was given (For example, in Figure 136 the "Stop Now" command was issued at 3s.).

The response of the bridge crane to the velocity pulse commands is shown in Figure 137. Both the trolley and payload return to the same position at which the "Stop Now" command was issued. However, both have a brief period of travel beyond the desired position. This leads to an important distinction for Zero-Overtravel input shapers. The maximum trolley overtravel and maximum payload overshoot will be different than the final, steady-state values.

Figure 138 shows the response of the bridge crane to realistic unshaped and shaped trapezoidal velocity profiles. The trolley and payload responses to the ZV-ZO command both have brief periods of travel beyond the desired final position. However, because the constraint on overshoot given in (91) represents the travel of a shaped command beyond an unshaped command, the trolley and payload do not return to the desired final position. Instead, they return to the final position of the unshaped command.

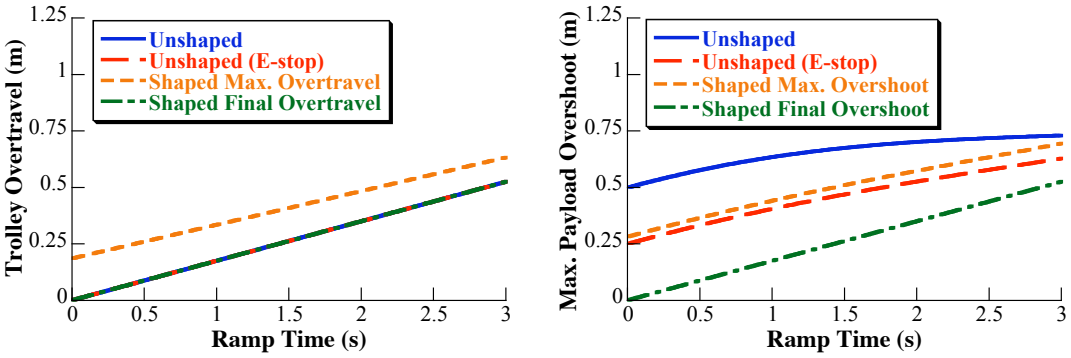

(a) Trolley Overtravel

(b) Payload Overshoot

Figure 139: Overtravel and Overshoot as a Function of Ramp Time for Unshaped and ZV-ZO Shaped Commands

Figures 139(a) and 139(b) show the trolley overtravel and payload overshoot, respectively, of the ZV-ZO shaper over a range of ramp times. For all ramp times shown, the final overtravel of the trolley using the ZV-ZO shaped command is identical to that of the unshaped command. This is the same final value of payload overshoot shown in Figure 139(b); the payload reaches the same final position as the trolley, with no vibration. Also shown in Figure 139(b) is the maximum payload overshoot for the ZV-ZO shaper. This value remains below the unshaped overshoot for all values shown. The ZV-ZO shaper not only returns the trolley and payload to the same position as the unshaped command, it does so with less maximum deviation from its final position.

The sensitivity curve for the ZV-ZO shaper is shown in Figure 140. The price for the zero overshoot constraint is shown in the plot; the shaper's Insensitivity is much less than the standard ZV shaper. The low Insensitivity has increased significance for the ZV-ZO shaper. The payload overshoot relies upon the shaped command having little residual vibration. If vibration does occur, then the payload will deviate from the zero-overtravel final position of the trolley. This is demonstrated in Figure 141, which shows the final payload overshoot for the ZV-ZO shaper for cases of ±20% modeling error in frequency. Only the case in which the frequency is known exactly results in zero final payload overshoot beyond the unshaped case.

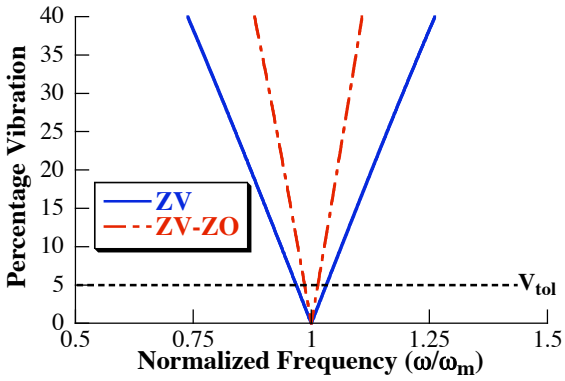

Figure 140: ZV-ZO Shaper Sensitivity Curve

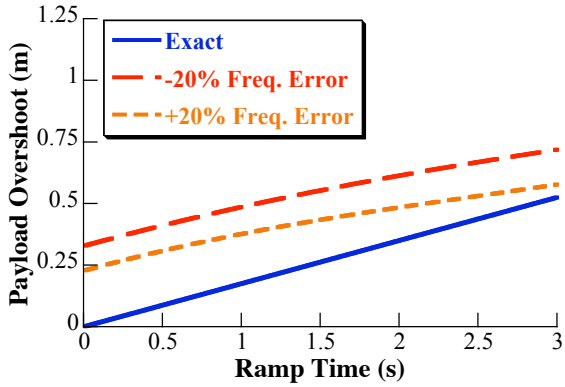

Figure 141: ZV-ZO Final Payload Overshoot with Frequency Modeling Error

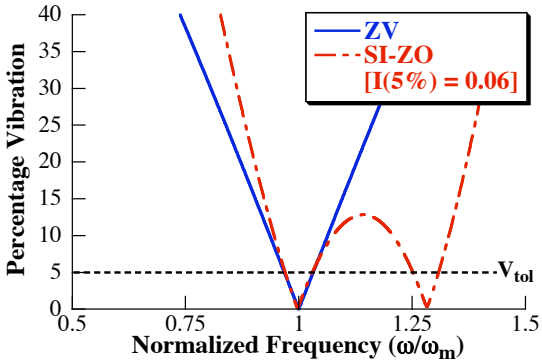

Figure 142: Sensitivity Curve of SI-ZO shaper with I(5%)=0.06

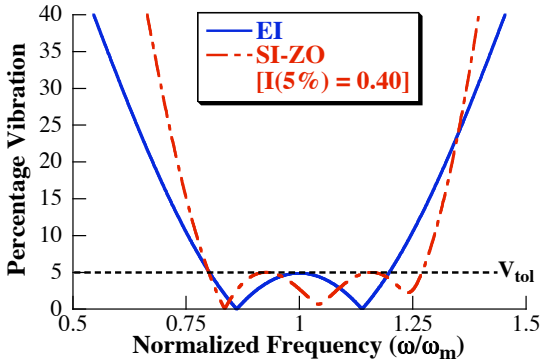

Figure 143: Sensitivity Curve of SI-ZO shaper with I(5%)=0.40

7.3.2 Specified Insensitivity–Zero Overtravel (SI-ZO) Shapers

Given the low robustness of the ZV-ZO shaper, it is clear that more robust zero overshoot shapers are necessary. If the zero overtravel constraint from (91) and the impulse amplitude constraints from Section 7.3.1 are combined with SI vibration constraints (see Section 3.1.2.2), then Specified Insensitivity–Zero Overtravel (SI-ZO) shapers result. These shapers allow the desired level of Insensitivity to be tailored to any given system, while maintaining zero final overshoot.

For example, the sensitivity curve of an SI-ZO shaper designed to have the same 5% Insensitivity as a standard ZV shaper is shown in Figure 142. This SI-ZO shaper is:

$$\begin{bmatrix} A_i \\ t_i \end{bmatrix} = \begin{bmatrix} 0.5487 & 0.7575 & -0.1007 & 0.3746 & -0.5801 \\ 0 & 0.4601\tau & 0.6653\tau & 1.1464\tau & 1.2257\tau \end{bmatrix} \tag{94}$$

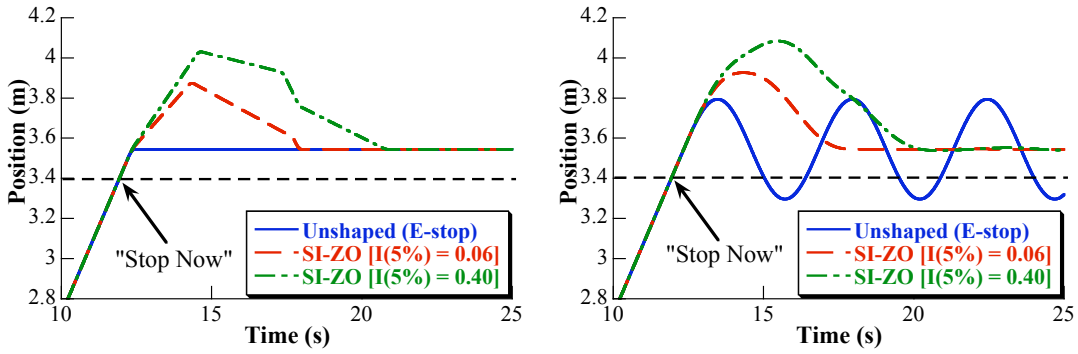

(a) Trolley **(b)** Payload

Figure 144: Responses to SI-ZO Commands

There are several penalties for achieving robust zero overtravel. The first is that the shaper contains a larger number of impulses and is significantly longer in duration than the ZV-ZO. The second is that, because negative impulses are needed to achieve zero overtravel, higher amounts of high mode excitation can occur. More robust SI-ZO shapers are also possible. For example, Figure 143 shows the sensitivity curve of a SI-ZO with the same 5% Insensitivity as an EI shaper, I(5%) = 0.40.

There is an additional penalty for the increase in robustness afforded by SI-ZO shapers, the maximum amount of overtravel and overshoot increases with robustness. Figure 144(a) shows the trolley responses of the SI-ZO shapers whose sensitivity curves were shown in Figures 142 and 143. Notice that maximum trolley overtravel for the longer duration SI-ZO [I(5%) = 0.40], designed to match the robustness of an EI shaper, is much larger than the SI-ZO [I(5%) = 0.06] shaper. The more robust shaper also takes much longer to reach the final value of zero overtravel beyond the unshaped command. The payload responses follow similar trends, as shown in Figure 144(b).

The benefit of the robustness is seen by comparing Figures 145(a) and 145(b). The plots show the final payload overshoot for the SI-ZO [I(5%)=0.06] and SI-ZO [I(5%)=0.40] shapers with ±20% error in frequency. Due to the relatively low robustness of the SI-ZO [I(5%)=0.06], this amount of error in frequency results in vibration at the completion of the command. This increases the value of the final payload overshoot, as seen in Figure

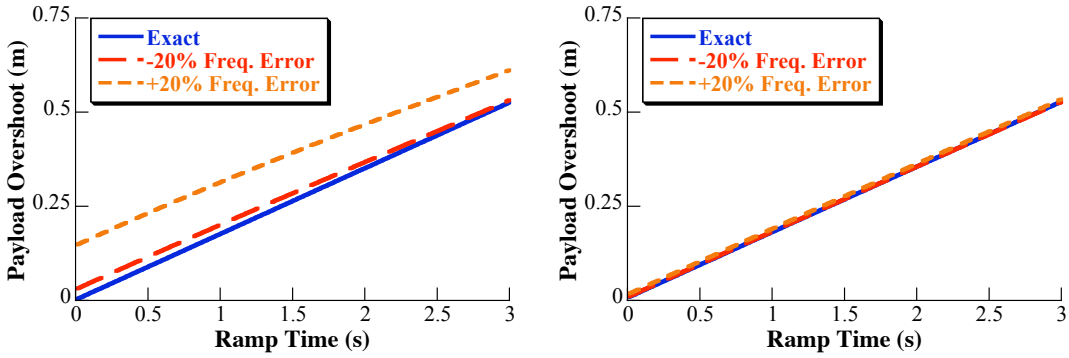

(a) SI-ZO [I(5%) = 0.06] **(b)** SI-ZO [I(5%) = 0.40]

Figure 145: Final Payload Overshoot with Modeling Error

145(a). The SI-ZO [I(5%)=0.40] shaper was designed to maintain low amounts of vibration for frequency variations of ±20%. The vibration remains below $V_{tol} = 0.05$ for all frequencies within this range. As a result, the final payload overshoot also exhibits robustness to frequency changes in this range, as seen in Figure 145(b).

7.4 "True" Zero Overtravel Shapers

In the previous sections, shapers were developed to limit the overtravel caused by an input shaped command to that of the unshaped reference command. This was accomplished by adding an additional zero-overshoot constraint, (91), to the input shaper design constraints. If, instead, the desired overshoot is set to some negative value, then the shaped command can return the system to a position with less overshoot than the original, unshaped command. If the unshaped, reference command is well known, then a shaper can be generated that results in zero (or near-zero) final overshoot.

For example, if the command is known to be a trapezoidal velocity profile, then the overtravel of the unshaped command is easily described by:

$$x^{+}_{unshp} = \frac{1}{2} V_{stop} t_r \tag{95}$$

where t_r is the ramp time of the velocity command. The shaper overshoot constraint can be

designed to eliminate this overtravel by setting:

$$x_{des}^{+} = -\frac{1}{2} V_{stop} t_r \tag{96}$$

Shapers formed using this constraint will return the system to the exact position at which the "Stop Now" command was issued by the user.

7.5 Experimental Verification of Zero Overshoot Input Shapers

To test the validity of the equations for predicting shaper overshoot and the effectiveness of the zero overshoot shapers on a real machine, experiments were conducted on the portable bridge crane shown in Figure 146. Detailed specifications for the crane can be found in Appendix A.

Commands were constructed that resulted in a trolley move distance of approximately 0.38m, if no overtravel or overshoot occured. Deceleration ramp times were varied between 0.2s and 1.2s, at intervals of 0.2s. However, to accommodate the small workspace of the portable bridge crane, the acceleration ramp time was held constant at 0.2s. In addition, for

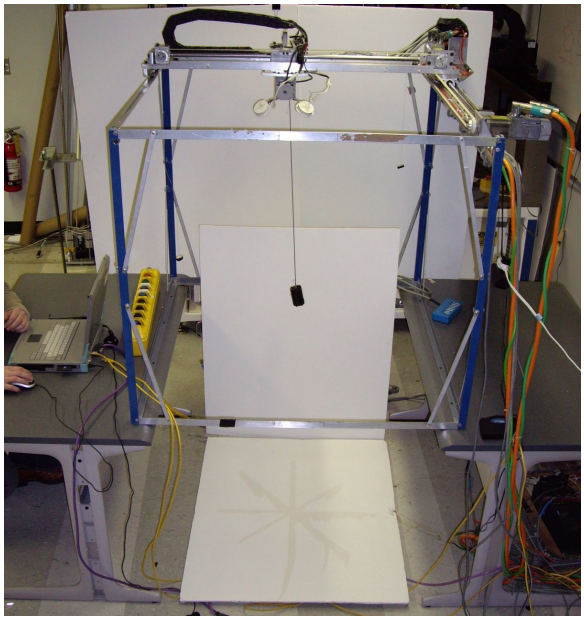

Figure 146: Portable Bridge Crane

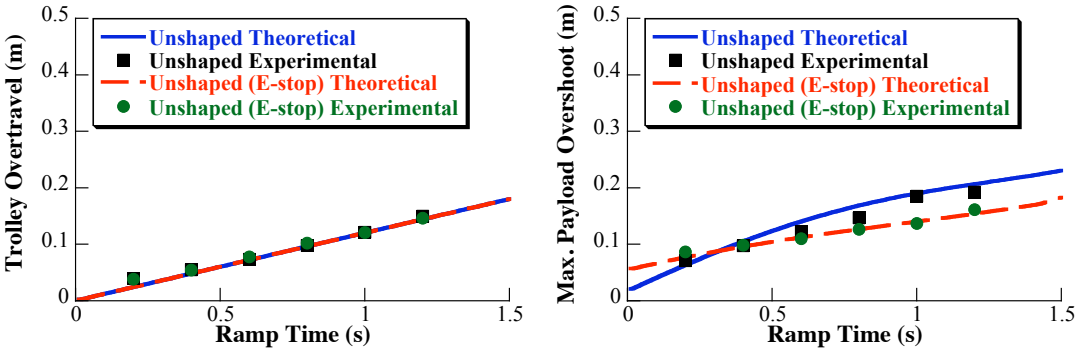

(a) Trolley Overtravel **(b)** Payload Overshoot

Figure 147: Experimental Overtravel and Overshoot for Unshaped Commands

all cases but the unshaped, the acceleration portion of the command was shaped with a ZV shaper, resulting in very little vibration from the completion of the acceleration portion of the command to the beginning of the deceleration phase.

Figure 147(a) shows the theoretical and experimentally measured trolley overtravel for the unshaped command. The theoretical results very closely match those predicted by theory. Also shown on Figure 147(a) are the theoretical and experimental results for the "Unshaped (E-stop)" command. Remember that this command has a shaped acceleration but unshaped deceleration phase. This command would occur during an Emergency-stop (E-stop) condition. Because the deceleration phase of the unshaped and "Unshaped (E-stop)" commands are identical, the trolley overtravel is equal for the two.

Figure 147(b) shows the maximum payload overshoot for the unshaped and "Unshaped (E-stop)" commands. The theoretical predictions of payload overshoot closely match the theoretical. Notice that in each case the maximum payload overshoot is greater than the trolley overshoot. This matches the prediction from the 10-ton crane simulations in Section 7.2.

Figure 148(a) shows the theoretical and experimental trolley overtravel for ZV-shaped and EI-shaped commands. The experimental results for both agree with the theoretical predictions. In addition, the increase of overtravel for the shaped cases over the unshaped is constant, regardless of the ramp time of the baseline trapezoidal velocity command.

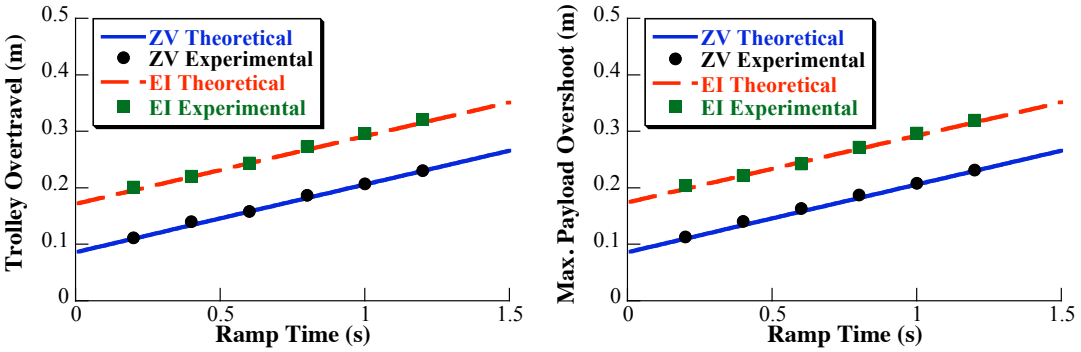

(a) Trolley Overtravel **(b)** Payload Overshoot

Figure 148: Experimental Overtravel and Overshoot for ZV and EI-Shaped Commands

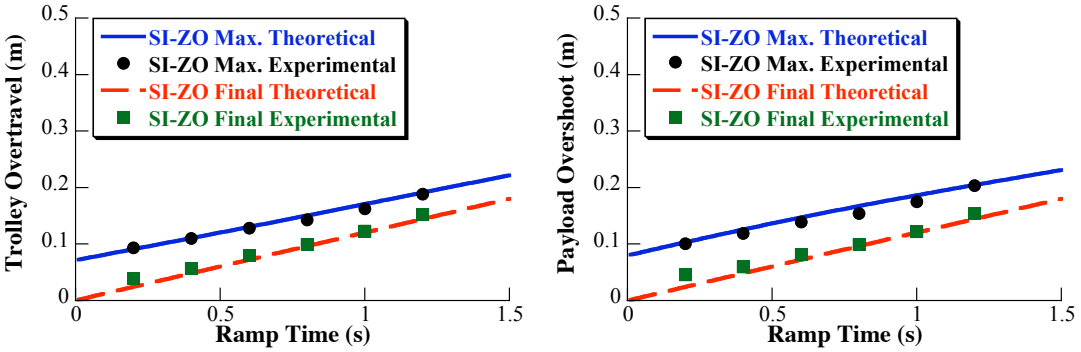

(a) Trolley Overtravel **(b)** Payload Overshoot

Figure 149: Experimental Overtravel and Overshoot for SI-ZO [I(5%) =0.06] Shaped Commands

This further confirms the prediction of overtravel given in (89). Figure 148(b) shows the maximum payload overshoot for the ZV-shaped and EI-shaped commands. In each case, the low payload oscillation provided by using input shaping results in a maximum payload overshoot nearly equal to the trolley overtravel.

The theoretical and experimental trolley overtravel for the SI-ZO shaper with I(5%)=0.06 from Figure 142 is shown in Figure 149(a). In the figure, the maximum and final trolley overtravel is presented. For both, the experimental results closely align with the theoretical. The final overtravel is also equivalent to that of the unshaped cases shown in Figure 147(a), indicating the the zero-overshoot constraint is satisfied.

The payload overshoot for the SI-ZO shaper is shown in Figure 149(b). The theoretical

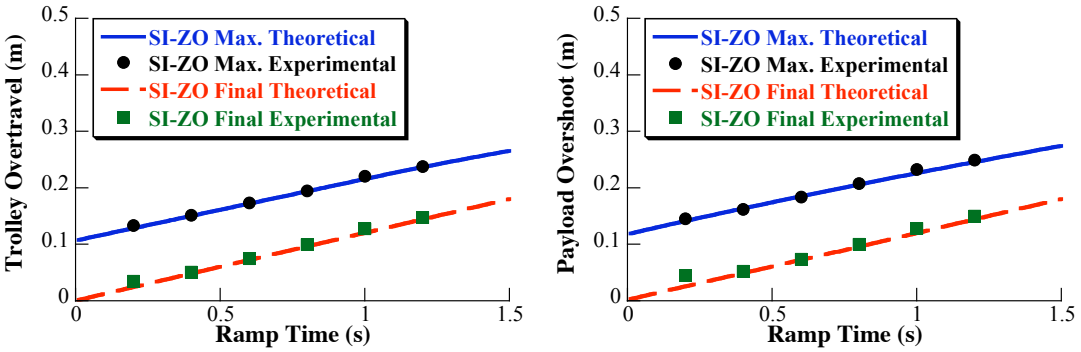

(a) Trolley Overtravel **(b)** Payload Overshoot

Figure 150: Experimental Overtravel and Overshoot for SI-ZO [I(5%) =0.40] Shaped Commands

final payload overshoot is equivalent to the unshaped case. The experimental results closely match the theoretical prediction, providing less final payload overshoot than the unshaped cases for all ramp times. The maximum payload overshoot is also shown on the plot. Above ramp times of 0.6s, this value closely matched the maximum payload overshoot of the unshaped case. In addition, the maximum trolley overtravel and maximum payload overshoot are less than the ZV-shaped case shown in Figure 148(a).

Similar plots are shown for the SI-ZO shaper with I(5%)=0.40 in Figures 150(a) and 150(b). For both, the experimental results closely match those predicted by the theory. Also, the final trolley overtravel and final payload overshoot match the SI-ZO [I(5%)=0.06] shaper, fulfilling the zero overshoot constraint. Notice, however, that the maximum trolley overtravel and maximum payload overshoot is greater than the SI-ZO [I(5%)=0.06] case. This is the price for the increase in robustness. However, these values are still less than the maximum overtravel and overshoot of EI-shaped case, which has similar robustness.

7.6 Conclusion

This chapter provided an analysis of trolley overtravel and payload overshoot when input shaping is used on human-operated systems. Using a simulation of a 10-ton industrial bridge crane, the overtravel and overshoot was presented for several common input shapers

and unshaped commands. In addition, an equation describing the amount of overshoot, beyond the unshaped command, caused by an input shaper was determined. This equation led to an additional constraint that can be included in input shaper design. The inclusion of this constraint led to two new classes of Zero Overshoot (ZO) shapers that provide the same overtravel as with unshaped commands. In addition, due to the low vibration properties of the input shapers, the final payload overshoot was less than the unshaped case. Experimental results from a portable bridge crane verified the theoretical predictions.

CHAPTER VIII

TELEOPERATION OF FLEXIBLE SYSTEMS

CHAPTER SUMMARY: *This chapter presents a series of crane operator studies. The primary goal of these studies is to examine the application of input shaping on teleoperated systems and the factors that influence operator performance on teleoperated flexible systems with input shaping. Input shaping is shown to improve operator performance when the crane is operated both locally and remotely. In addition, the results from studies that examine the effect of input shaper duration and communication delay on crane operator performance are presented.*

The improvement of crane functionality in the role of aiding first responders at disaster scenes also enables crane functionality in other harsh environments. Teleoperated mobile cranes could be driven into environments that are unsafe for human operators and could also extend the reach of humans. For example, cranes erected on the moon could be controlled by operators on Earth, lowering the construction costs for colonization of the moon. The distant nature of such cranes, and resulting expense of deploying a manned crew to move them, also further reinforces the advantages of base mobility.

This chapter begins with a brief review of teleoperation terminology and past research. Then, a series of crane operator studies will be presented. In the first study, in Section 8.2, operators were asked to complete point-to-point maneuvers using a remotely operated

The work in Sections 8.2–8.4 was completed in collaboration with undergraduate researchers Aayush Daftari and Adrit Lath. The work in Section 8.5 was completed in collaboration with NSF Fellow Dooroo Kim.

tower crane. The results from this study motivate the investigation into the influence of input-shaper and communication-induced delays in remotely operated, flexible systems. Section 8.3 presents a study to examine the effects of shaper duration on the performance of crane operators. A similar study is presented in Section 8.4, which attempts to isolate the effects of the communication delay in teleoperated systems. Finally, Section 8.5 demonstrates the effectiveness of input shaping in improving the performance of tower crane operators when moving double-pendulum payloads, both locally and remotely.

8.1 Teleoperation Review

For a thorough review of the history of teleoperation the reader is pointed to three surveys by Sheridan and the references contained within [53, 55, 54]. Other surveys of the field are presented by Niemeyer [36], who primarily reviews the use of wave variables to ensure stability of bilateral teleoperated systems, and Hokayem [18], who focuses on the history of bilateral teleoperation.

To date, a large percentage of the research work into teleoperation has been toward effectively mitigating the stability and other performance issues caused by communication delays in bilateral (force-feedback) systems. Primary works include those by Niemeyer and Slotine, who first presented the wave variable approach that results in stable, bilateral systems in spite of time delays of any length [35]. This presented a large advancement from the first studies of Ferrell, who first showed that human operators would adopt a "move-and-wait" strategy to avoid instability [11]. Ferrell also showed that teleoperation task performance is a function of the delay time. The results from one study suggested that not only is task performance a function of the delay time, but the variance between repeated operations is as well (task completion time and variance increased as delay time increased) [2].

Teleoperation via the Internet has been a topic of much of the recent research [12, 31, 34, 37, 48, 50, 51, 77, 89, 91]. The Internet provides a cheap, readily available medium

for teleoperation, but its packet based nature presents additional challenges, namely that the delay time can change greatly and rapidly and that packets may be lost. Despite this fact, numerous systems have been successfully controlled via the Internet, including several cranes [19, 24, 30].

The work presented in this chapter presents a fundamentally different approach to teleoperation. The vast majority of the research into teleoperation has been conducted on systems where the communication path between the user and the remote system is part of the system's feedback control system. A large portion of this research has been toward addressing the stability issues that having the communication time delay in the feedback loop can cause. This chapter presets several operator studies that represent an investigation into the teleoperation of systems for which bilateral operation does not suit the system, such as teleoperated cranes. The approach presented here seeks to improve teleoperated systems by reducing their dynamic complexity, namely drastically reducing the vibration of the remote system. This approach avoids the stability concerns of the force-feedback methods prevalent in the literature.

The method used to reduce the dynamic complexity of the remotely operated system is input shaping. Studies have been conducted that indicate input shaping improves the performance of crane operators [22, 23]. This chapter will investigate the application of input shaping on teleoperated systems and the factors that influence operator performance on teleoperated flexible systems with input shaping.

8.2 A Remotely Operated Tower Crane Study

Eight operators were asked to complete a point-to-point positioning maneuver using the portable tower crane shown in Figure 151. More detailed specifications for the tower crane can be found in Appendix A. An overhead view of the task is shown in Figure 152. The position of the start and end locations were selected such that users were required to utilize two degrees of actuation, both the rotational, slewing motion of the jib and the motion of

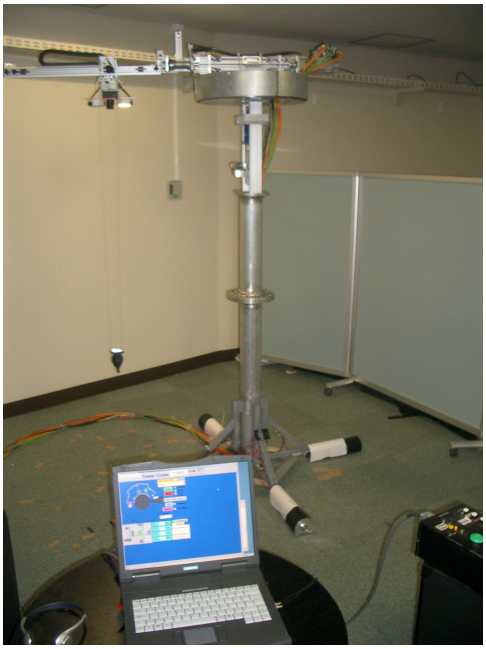

Figure 151: Remotely Controlled Portable Tower Crane

the trolley along the jib.

The operators controlled the crane remotely using the Graphical User Interface (GUI) shown in Figure 153. The upper left portion of the screen shows a real-time display of the crane from an overhead view using the camera and encoder data. The square is the trolley position and the circle is the payload position. The current configuration is also numerically displayed under the animation (slew angle, trolley position, etc.). The crane can be manually driven using the directional arrows at the bottom left of the screen.

The GUI was accessed using a VNC connection over the Internet. Because the Internet was used as a communication medium, the communication delay was unknown and likely varied between trials. The crane was located at the Tokyo Institute of Technology, while users were at the Georgia Institute of Technology in Atlanta. Each user completed the task without input shaping enabled and with ZV and EI shapers. The completion time was measured for each, with the time at which the payload settled to, and remained within, the "End" region marking the end of the trial.

The completion times for each operator are shown in Figure 154. All operators were

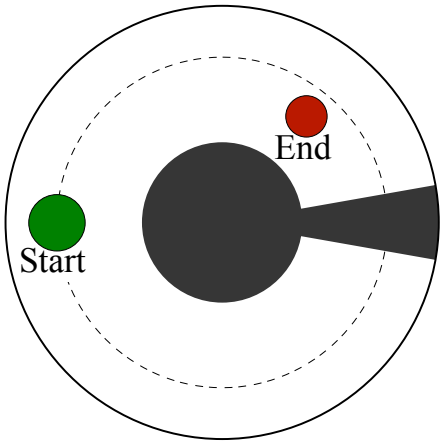

Figure 152: Task Overview for Remote Operation of the Tower Crane

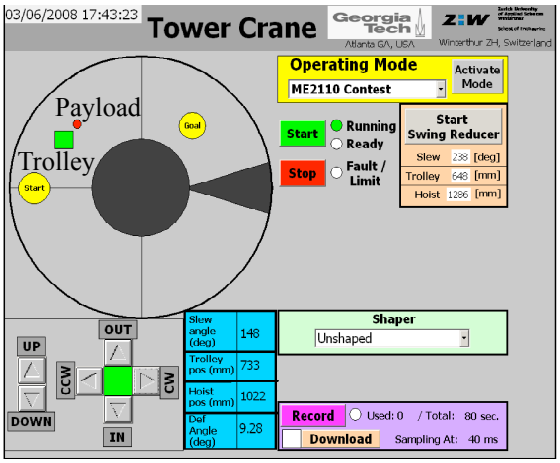

Figure 153: Tower Crane GUI

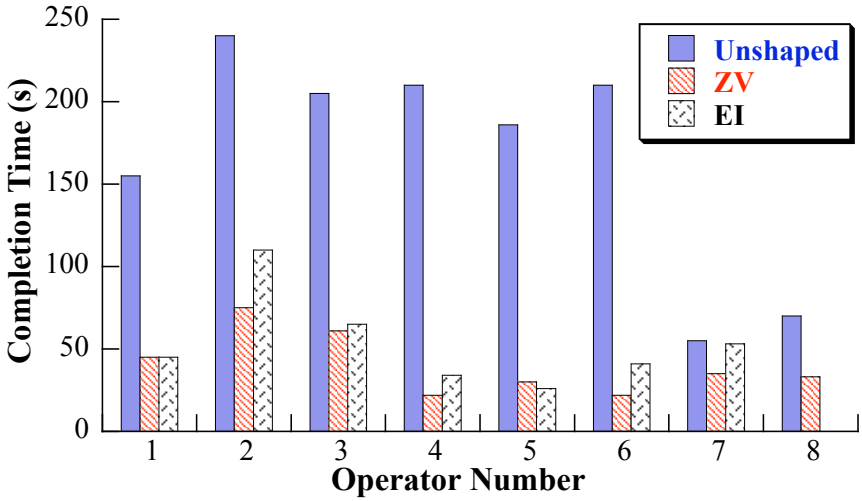

Figure 154: Completion Times for Remote Operation of the Tower Crane

able to complete the task more quickly with input shaping enabled. The average completion time without input shaping enabled was approximately 166s. When utilizing a ZV shaper, this completion time dropped 76% to approximately 40s. The average EI shaped completion time was approximately 53s, or a 68% decrease from the unshaped time. Note that the ZV shaper provided faster times than the EI shaper. This is likely due to the fact that the frequency of the system was well known, preventing the robustness advantage of the EI shaper from influencing the results.

These results suggest that utilizing input shaping on remotely operated, flexible systems can lead to drastic improvements in operator performance. The following sections present studies that investigated this idea further, including an examination of the influence of shaper duration on operator performance (The difference between the ZV and EI shapers in Figure 154, for example.). In addition, a study of the effect of the communication delay on the improvements in human operator performance when utilizing input shaping is presented.

8.3 The Influence of Shaper Duration on Bridge Crane Operators

This section will examine the effects of input-shaper duration on crane operator performance using a 10-ton bridge crane located at Georgia Tech. It is well known that input shaping increases the duration of a reference command by the duration of the input shaper. This increase in duration is necessary to limit the oscillatory dynamics of the system. There are two primary consequences of this lag in systems that are human-operated. The first is that the system may appear to move more sluggishly; it takes longer for commands to reach a maximum value or final setpoint. The second, discussed in detail in Chapter 7, is the lag increases the amount the system will move beyond the user's intentions.

In order to study the effects of input shaper duration on operator performance, input shapers with various durations must be used. However, there exists a fundamental compromise in input shaping between input shaper robustness and shaper duration; more robust shapers have longer durations [73, 86]. This presents a difficulty in isolating the effects of shaper duration, because longer shapers used in practice are more robust than shorter ones.

8.3.1 Long-Duration Zero Vibration Shapers

To mitigate the effects of this robustness/duration compromise, shapers were designed only using the zero residual vibration constraint introduced in Section 2.3.1. To review, for second-order underdamped systems, this constraint is:

$$0 = V(\omega, \zeta) = e^{-\zeta\omega t_n} \sqrt{[C(\omega, \zeta)]^2 + [S(\omega, \zeta)]^2} \tag{97}$$

where,

$$C(\omega,\zeta) = \sum_{i=1}^{n} A_i e^{\zeta\omega t_i} \cos(\omega t_i \sqrt{1-\zeta^2}) \quad (98)$$

$$S(\omega,\zeta) = \sum_{i=1}^{n} A_i e^{\zeta\omega t_i} \sin(\omega t_i \sqrt{1-\zeta^2}) \quad (99)$$

and n is the number of shaper impulses, ω represents the system's natural frequency, ζ is the damping ratio, and A_i and t_i represent the amplitude and time location of the i^{th} impulse, respectively. The shortest input shaper that satisfies (97), using only positive impulses, is the ZV shaper [80, 79]. It has a duration of 0.5τ, where τ is the vibration period.

Using the constraint in (97), along with constraints on impulse amplitudes, long-duration ZV shapers were designed that have durations of 0.75τ, 1.00τ, 1.25τ. In the remainder of this chapter, the duration of long ZV shapers will be indicated in parenthesis. For example, the long ZV shaper with a duration of 0.75τ is represented by ZV(0.75τ). The input shapers used in this study are shown in Table 11. The sensitivity curves for the long ZV shapers and the standard ZV shaper are shown in Figure 155. The figure shows that, near the design frequency, the sensitivity curves of the ZV shaper and all long ZV shapers, except the ZV(1.00τ), are similar. This indicates similar robustness to errors in natural frequency. The sensitivity curve of the ZV(1.00τ) shaper is identical to that of the ZVD shaper [58]. This is the result of the ZV(1.00τ) solution converging to that of the ZVD shaper. It is more robust to changes in frequency than the other shapers shown in the figure.

Table 11: Input Shapers Used in Shaper-Duration Operator Study

ZV	A_i	0.50	0.50	
	t_i	0	0.50τ	
ZV(0.75τ)	A_i	0.36	0.42	0.22
	t_i	0	0.41τ	0.75τ
ZV(1.00τ)	A_i	0.25	0.50	0.25
	t_i	0	0.50τ	1.00τ
ZV(1.25τ)	A_i	0.36	0.42	0.22
	t_i	0	0.59τ	1.25τ

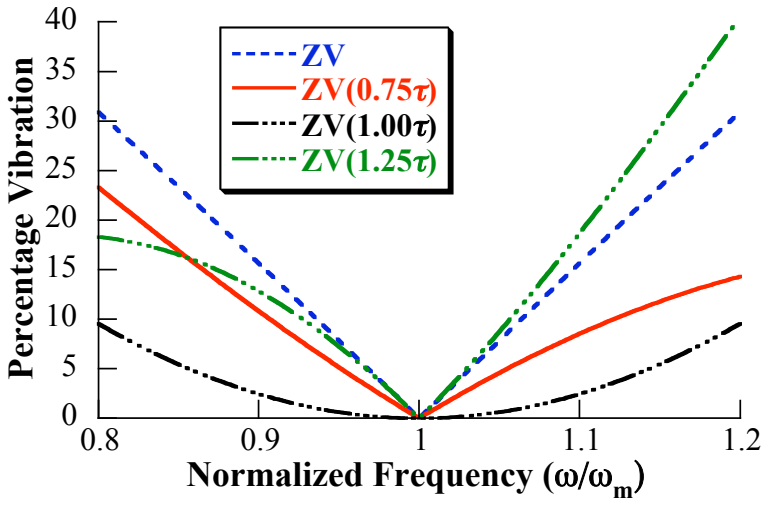

Figure 155: Sensitivity Curves of Shapers Used in Study

8.3.2 Experimental Protocol

Eight operators drove the 10-ton industrial bridge crane shown in Figure 156 through two different manipulation tasks. Each task was completed without input shaping and with each of the ZV shapers discussed in the previous section. The crane has a workspace that is 6 meters high, 5 meters wide and 42 meters long. It is controlled using a Siemens programmable logic controller (PLC), which receives operator commands from the control pendant. Commands from the PLC are sent to Siemens Masterdrives Series AC-AC inverters, which ensure accurate execution of the commands. To measure payload response, the crane is also equipped with a Siemens vision system. More detailed specifications of the crane can be found in Appendix A.

The two manipulation tasks are shown schematically in Figure 157. The first, simple task consists of a point-to-point move from the 0.5m square start-zone to the 0.75m diameter, circular end-zone 2.0m away. This first task is represented in the figure by the dashed arrow labeled “Nominal Path 1”. For the second, more difficult task, an obstacle was placed between the start and end-zones. This required the operators to navigate around the obstacle. This task is represented in the figure by “Nominal Path 2”.

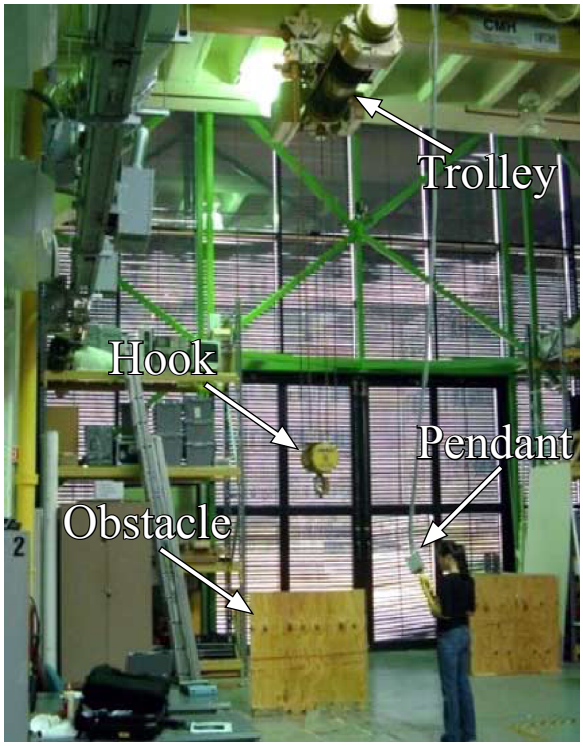

Figure 156: 10-ton Industrial Bridge Crane at Georgia Tech

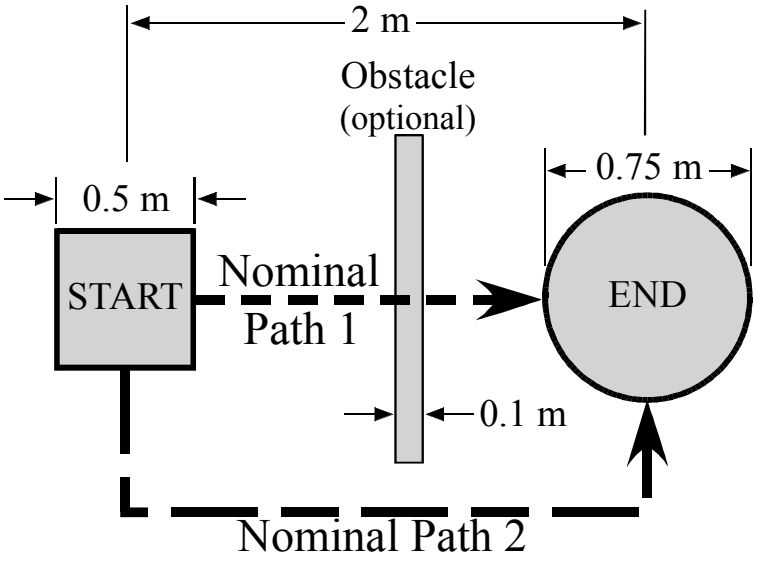

Figure 157: The Courses Used for Operator Study

For each test, the crane suspension cable length was set to 5.88m. This leads to a payload oscillation frequency of approximately 0.205Hz (τ=4.88s). With an oscillation period this long, the differences in the durations of the various ZV shapers are significant, with a variation of 3.66s between the ZV shaper (2.44s duration) and the ZV(1.25τ) shaper (6.10s duration).

For each trial, the completion time, number of pendant button pushes, and obstacle collisions were recorded. The completion time was measured from when the trial began to the time when the payload settled in, and remained within, the circular end-zone.

8.3.3 Experimental Results

8.3.3.1 Straight Line Motion

Figure 158 shows an example response from an operator performing the first (straight line) manipulation task. Notice that even after the trolley reaches the desired location, there is significant oscillation, such that the payload does not remain within the end-zone. The same operator's attempt with ZV shaping enabled is shown in Figure 159. The payload now reached and settled to within the goal region at the same time as the overhead trolley. Note that the time scale is different between Figures 158 and 159; the task is completed

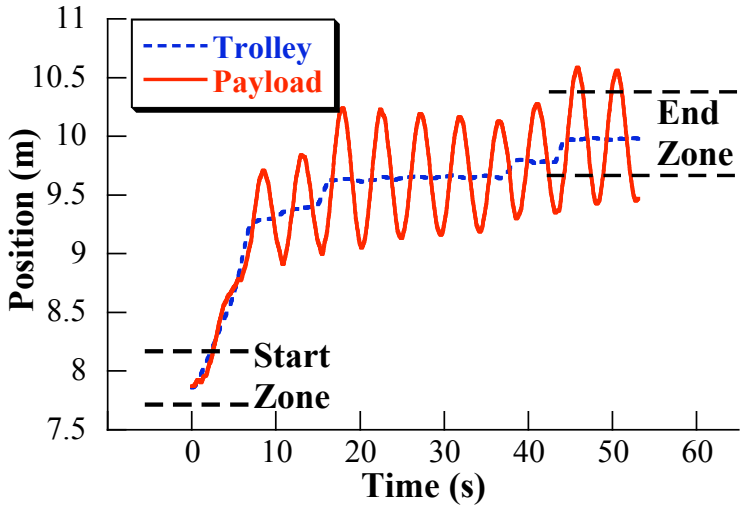

Figure 158: Example of Unshaped Trial on Straight Course

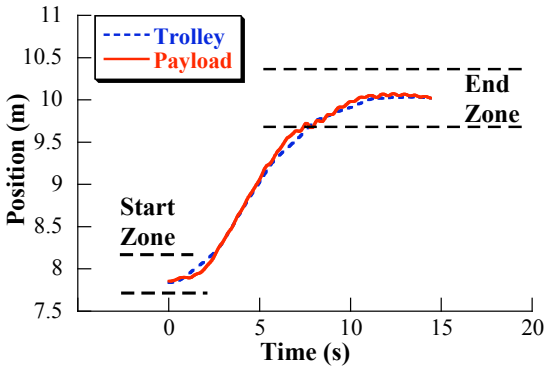

Figure 159: Example of ZV Shaped Trial on Straight Course

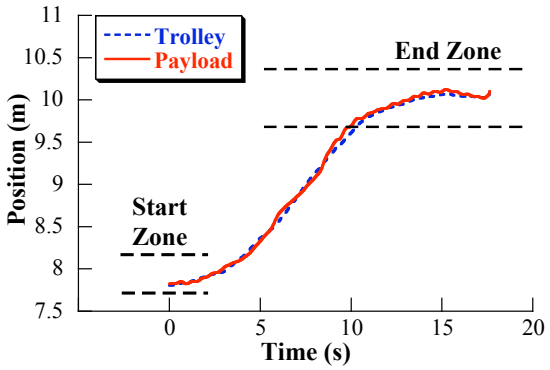

Figure 160: Example of ZV(1.25τ) Shaped Trial on Straight Course

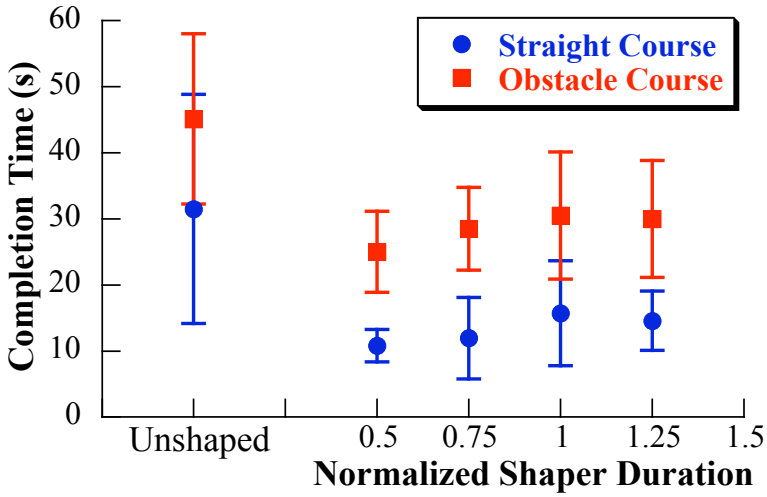

Figure 161: Completion Times

much faster with the ZV shaper enabled. Figure 160 shows the same operator using a long ZV(1.25τ) shaper. The payload still exhibits very little oscillation and again settles to within the end-zone when the trolley does. Notice, however, that the edges of the response are smoother, due to the longer duration of the ZV(1.25τ) shaper. In addition, the completion time is slightly longer than the ZV-shaped case shown in Figure 159.

The average completion times for all eight operators for the unshaped and input-shaped cases, as a function of normalized shaper duration, are shown in Figure 161. The error bars indicate one standard deviation above and below the mean. Note that the results from the obstacle avoidance trials are also included on this plot and are discussed in the next

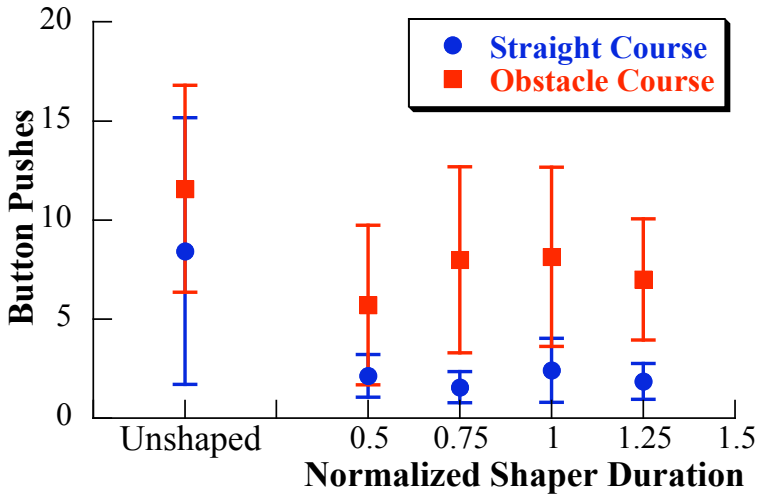

Figure 162: Operator Effort as Measured by Button Pushes

section. The ZV shaper provided the lowest completion times of the input shapers used. It provided an approximate 65% reduction in completion time compared to the average unshaped completion time of 31.5s. As shaper duration increased, there was an increase in completion time. However, even the longest duration shaper provided average completion times that were only 50% of the average unshaped completion time for straight line motion.

Figure 162 shows the average number of button pushes the operators used to complete the tasks. Button pushes are used as an indication of operator effort, as a higher number of pushes indicates that a greater number of control actions was needed. For each input shaper, the average number of button pushes was substantially lower than without shaping. For the straight line motion, there appeared to be no trend in button pushes as shaper duration increased.

8.3.3.2 Obstacle Avoidance

Figure 163 shows one operator's attempt to navigate around the obstacle during the second manipulation task. The payload oscillation makes efficient completion of this task very difficult. In addition, once the trolley has reached the goal region, the payload exhibits significant oscillation. Figure 164 shows the same operator's attempt to navigate the obstacle course with ZV shaping enabled. As with the straight line motion, the operator is able

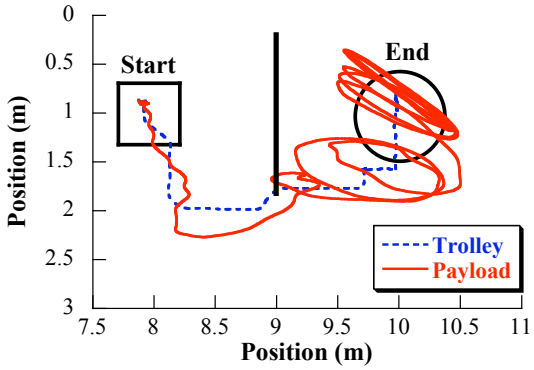

Figure 163: Example of Unshaped Trial on Obstacle Course

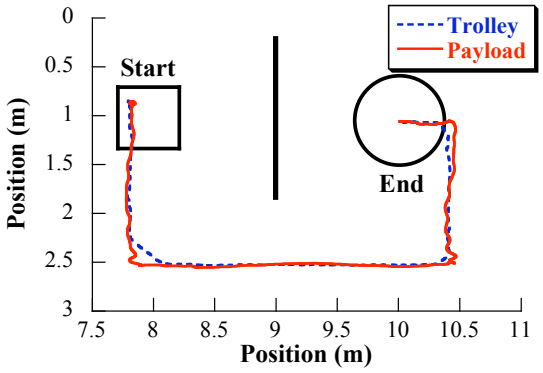

Figure 164: Example of ZV Shaped Trial on Obstacle Course

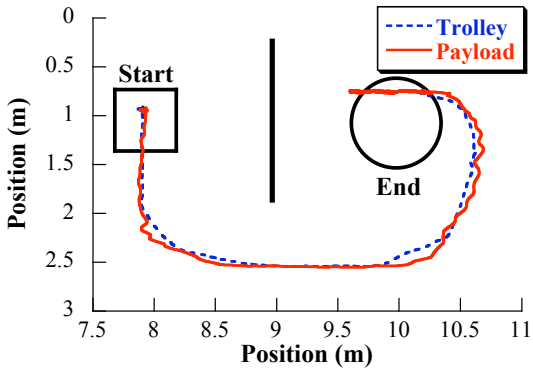

Figure 165: Example of ZV(1.25τ) Shaped Trial on Obstacle Course

to navigate the course very easily due to the significantly reduced payload oscillation. The operator's attempt to navigate the course with the ZV(1.25τ) shaper is shown in Figure 165. Notice that the corners of the move are more rounded and the operator slightly overshoots the end-zone. Both these effects are caused by the increased duration of the ZV(1.25τ) shaper and may increase completion time or cause collisions if the effect becomes excessive.

The average completion times for the obstacle course were also shown in Figure 161. The trends are similar to those for the straight line motion. The ZV shaper was again the fastest input shaper of those tested; using the ZV shaper, operators drove the crane twice as fast as without shaping. Average completion time again increased with shaper duration, but still remained well below the unshaped average.

The average number of button pushes used to navigate the obstacle course were shown in Figure 162. As with straight line motion, the average number of button pushes for each of the input shaped cases was lower than the unshaped case. For the obstacle course, however, there is a slight increase in the number of button pushes as shaper duration increases.

It should be noted that only one operator collided with the obstacle during the trials. This occurred during an unshaped trial.

8.4 The Influence of Communication Delay on Bridge Crane Operators

The previous section presented a study of the influence of input shaper duration on bridge crane operator performance. This section will present a similar study of the influence of pure time delays on operator performance. This study attempts to isolate the effects of the communication delay present in teleoperated systems.

8.4.1 Experimental Protocol

Four operators navigated the obstacle course shown in Figure 157. The operators only completed the course with the obstacle in the path; straight-line, point-to-point maneuvers were not performed. Each operator completed the course thirteen times. The course was completed three times without input shaping, with time delays of 0s, 2s, and 4s. Each operator completed the course ten times with input shaping enabled. They used both ZV and EI shaped commands. For both shapers, time delays of 0 – 4s, at 1s intervals were used. The time delays were enforced as pure time delays of the operator's command. For example, for a 2s delay time, every operator command (or shaped operator command) was delayed for 2s, without other modification, before it was passed to the crane's motor drives. For each trial, the task completion time, number of button pushes, and number of collisions were recorded.

8.4.2 Experimental Results

Figure 166 shows the average completion times as a function of delay time for unshaped, ZV shaped, and EI shaped cases. The error bars indicate the minimum and maximum

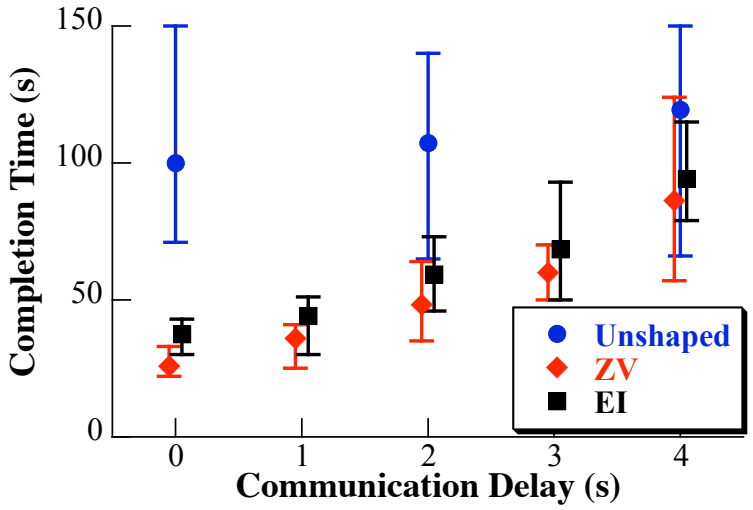

Figure 166: Average Competition Time as a Function of Communication Delay

completion times for a given communication delay. For all values of communication delay, the average completion times for the shaped cases were less than the unshaped case. The average completion time of the ZV shaped case was also slightly lower than the EI shaped case over the range of communication delays tested. Completion times also increase with communication delay for all three cases of control. However, the degree of this dependence was much lower for the unshaped case. The average completion times for the shaped cases tended toward that of the unshaped as communication delay was increased. This suggests that the operator performance improvements provided by input shaping may disappear in the presence of long communication delays.

The average number of button pushes needed to complete the manuevers is shown in Figure 167. For low communication delay times, the number of button pushes needed with input shaping enabled was dramatically less than without shaping. As communication delay time increased, however, the number of button pushes needed with input shaping enabled approached that of the unshaped case. In fact, the average number of button pushes for the unshaped case for a communication delay time of 4s was actually slightly lower than either shaped case. Over the range of parameters tested, there is a fairly linear relationship between the number of button pushes and communication delay time for the two shapers

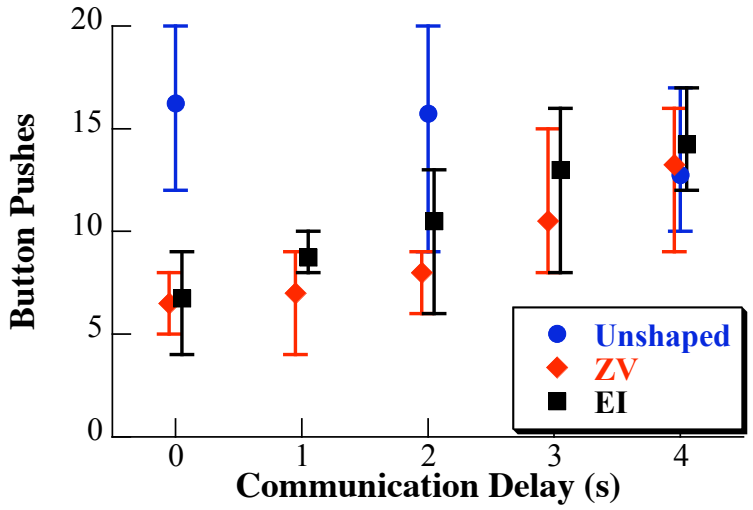

Figure 167: Average Number of Button Pushes as a Function of Communication Delay

tested.

The average number of obstacle collisions as a function of communication delay time is shown in Figure 168. For nearly all trials the number of collisions was fairly low. Only the unshaped case with no communication delay resulted in a significant number of obstacle collisions.

8.5 A Tower Crane Operator Study – Double Pendulum Dynamics

This section will present a study of operators utilizing the portable tower crane with a double pendulum payload configuration, shown in Figure 169.

The double pendulum payload configuration creates two modes of vibration, necessitating the use of a two-mode input shaper. The development of this shaper is also discussed in this section. In addition, the operators completed an identical series of tasks both locally and remotely. This allows a comparison between local and remote crane operator performance.

8.5.1 Multi-Mode Specified Insensitivity Input Shapers

When the second mode causes the payload oscillation to exceed tolerable levels, it must be taken into account when designing an input shaper. There are a number of methods

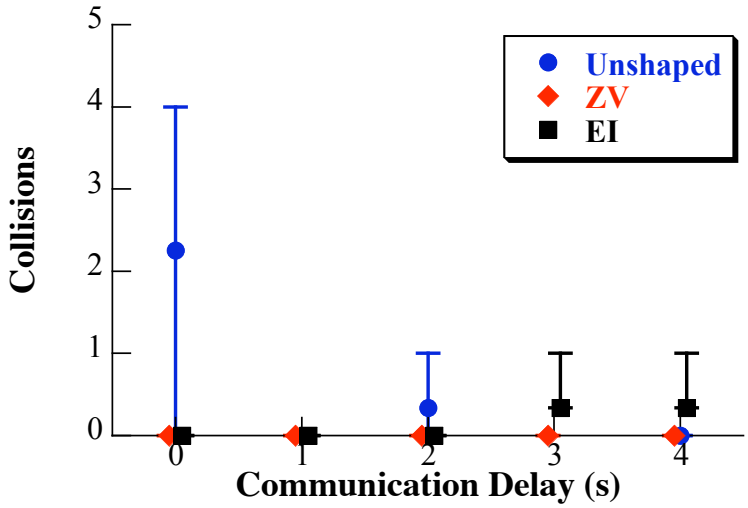

Figure 168: Average Number of Obstacle Collisions as a Function of Communication Delay

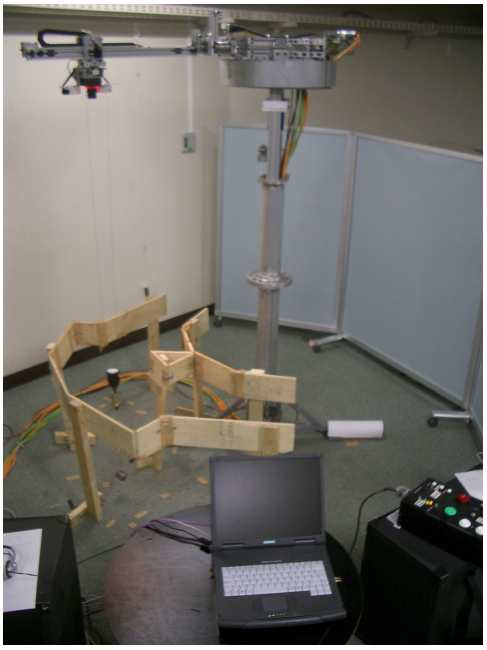

Figure 169: Tower Crane with Double Pendulum Payload

for designing multi-mode input shapers [20, 65, 60, 23]. In this section, a technique is developed to suppress the two frequencies of a double-pendulum crane. Furthermore, the technique is made robust to any expected variation in the two modes.

One method to design a multi-mode input shaper is to limit residual vibration at each frequency of oscillation. To do so, the residual vibration expression of (3) is used twice to limit the vibration at a single set of frequencies (ω_1 and ω_2). This is accomplished by requiring the residual vibration, (3), at each frequency to be below some tolerable level, V_{tol} (see Section 2.3.1 for a detailed discussion of vibration constraints):

$$V(\omega_1, \zeta_1) \leq V_{tol} \quad \text{and} \quad V(\omega_2, \zeta_2) \leq V_{tol} \tag{100}$$

If the actual crane frequencies coincide with those used in (100) to design the shaper, then the oscillation will be attenuated. However, to ensure robustness to modeling errors and parameter variations, the oscillation must remain small over a range of frequencies.

Robustness can be ensured by suppressing vibration at several points near the modeling frequencies. This method results in the Specified Insensitivity (SI) shapers discussed in Section 3.1.2.2. The process is demonstrated in Figure 170(a) for a single-mode system. In this case, the vibration has been limited at six frequencies near the model frequency, ω_m. Given a double-pendulum crane, the single-mode SI method can be extended by placing vibration constraints over frequency ranges near both of the expected frequencies [23]. This approach is illustrated in Figure 170(b) for a case where modes near 1 Hz and 2.8 Hz are suppressed.

8.5.2 Solution Procedure

Due to the transcendental nature of the residual oscillation equations, there are an infinite number of solutions. For the shapers discussed in this chapter, impulse amplitudes were constrained to be positive. To ensure that the system reaches the desired final state, impulse amplitudes are also constrained to sum to one. Even with these additional constraints there is still an infinite number of solutions. To select among these solutions and ensure that

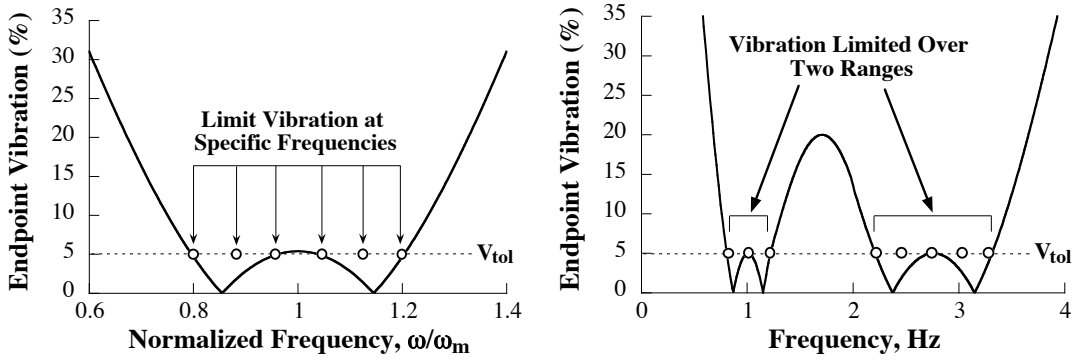

(a) Frequency Sampling Over One Range **(b)** Frequency Sampling Over Two Ranges

Figure 170: Frequency Sampling to Ensure Robustness

the rise time is as fast as possible, the shaper duration must be made as short as possible. Therefore, the final necessary design constraint minimizes the time of the final input shaper impulse.

To summarize, two-mode specified-insensitivity input shapers are designed by minimizing the shaper duration while enforcing (100) over two frequency ranges that contain the expected frequencies and limiting impulses to be positive and sum to one. The input shapers designed for this chaper were obtained using the MATLAB Optimization Toolbox.

8.5.3 Implementation of Two-Mode SI Shapers on Tower Cranes

The parameters need to design a two-mode shaper are shown in Figure 171. The suspension cable length from the trolley to the hook is represented by an inflexible, massless link of variable length l_1. The payload is connected to the hook via an inflexible, massless link of length l_2. The hook and the payload are point masses of mass m_h and m_p, respectively. The mass ratio, R, is defined as the ratio of the payload mass to the hook mass, $R = \frac{m_p}{m_h}$. More details of this model and its dynamics can be found in Section 5.2.

Using the method introduced in the previous section, a two-mode SI shaper was designed to suppress double-pendulum payload oscillations on the tower crane shown in Figure 169. The shaper was designed to suppress vibration to below five percent of the unshaped case for two frequency ranges. The lower range was 0.3 – 0.45 Hz. The upper

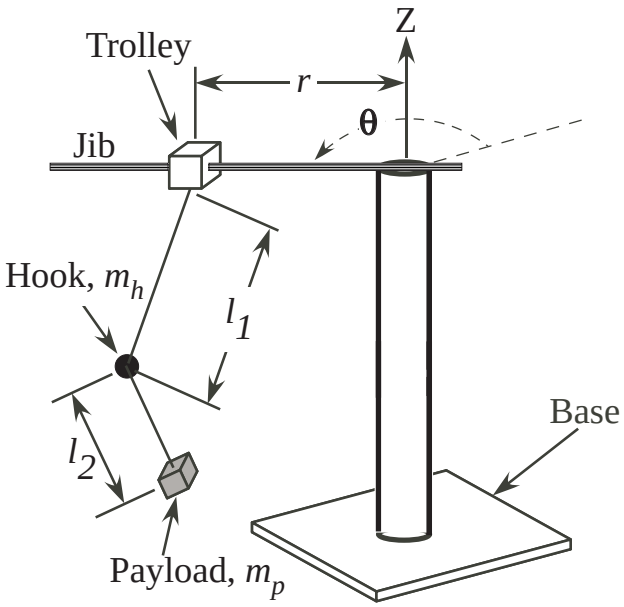

Figure 171: Sketch of Tower Crane with Double Pendulum

range was 1.0 – 1.4 Hz. The center of these frequency ranges represent the two modes of vibration for the tower crane with l_1 = 1.28m, l_2 = 0.45m, and the mass ratio, R, equal to 1.43. The resulting shaper is:

$$\begin{bmatrix} A_i \\ t_i \end{bmatrix} = \begin{bmatrix} 0.1474 & 0.1152 & 0.2374 & 0.2374 & 0.1152 & 0.1474 \\ 0 & 0.3680 & 1.2922 & 1.6749 & 2.5990 & 2.9670 \end{bmatrix}, \quad i = 1, \ldots, 6 \quad (101)$$

where A_i and t_i represent the i^{th} impulse amplitude and time, respectively. The sensitivity curve for this shaper is shown in Figure 172. The two suppression regions, I_1 and I_2, are easily seen.

Figure 173(a) shows the response of the tower crane to unshaped and shaped trolley motion of 0.30m. For this experiment, the suspension cable length, l_1, was 1.28m and the rigging length, l_2 was 0.45m. The hook mass was approximately 0.105kg and the payload mass was approximately 0.15kg, resulting in a mass ratio, R, of 1.43. One can see that the unshaped case results in large amounts of payload oscillation. Input shaping, however, provides a dramatic oscillation reduction. Figure 173(b) presents another example, where the suspension cable length, l_1, was reduced to 0.48m. All other parameters remained

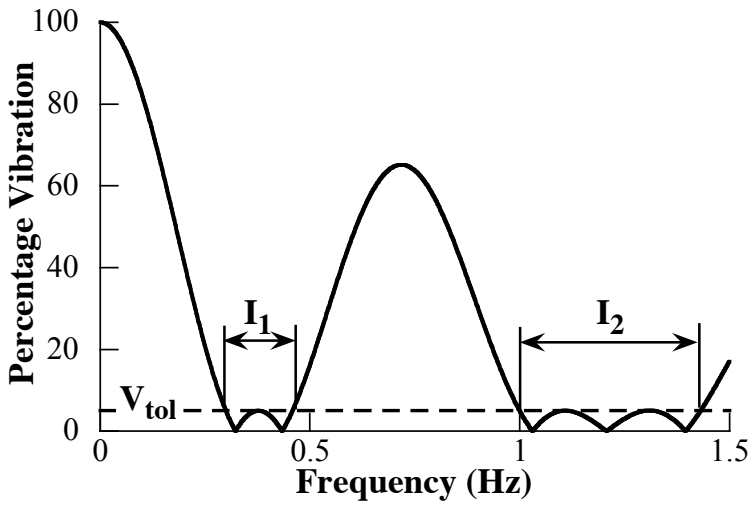

Figure 172: Sensitivity Curve of Multi-Mode SI Shaper Designed for the Tower Crane

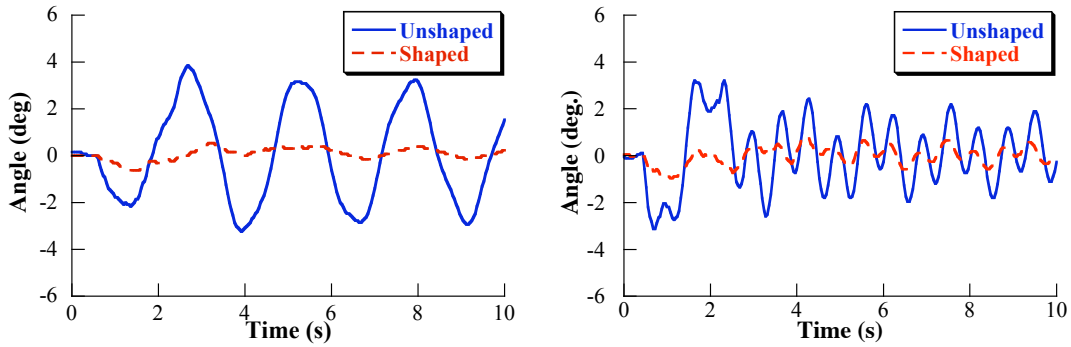

(a) Hook Responses (ϕ) for $l_1 = 1.28m$ **(b)** Hook Responses (ϕ) for $l_1 = 0.48m$

Figure 173: Shaped and Unshaped Responses to Trolley Motion

identical to those presented in the first case. This change produces a significant change in system dynamics. It gives a 37% change in the frequency of the low mode and a 18% change in the high mode frequency. However, as seen in Figure 173(b), the shaper in (101) still provides a substantial reduction in payload oscillation.

8.5.4 Robustness to Changes in Suspension Cable Length

To further analyze the robustness of the shaper over the range of possible suspension cable lengths, l_1 was varied from 0.48m to 1.28m, in approximately 0.05m increments. The residual vibration amplitudes over this range of suspension cable lengths are shown in Figure 174(a). For all lengths, the residual vibration resulting from the shaped command is

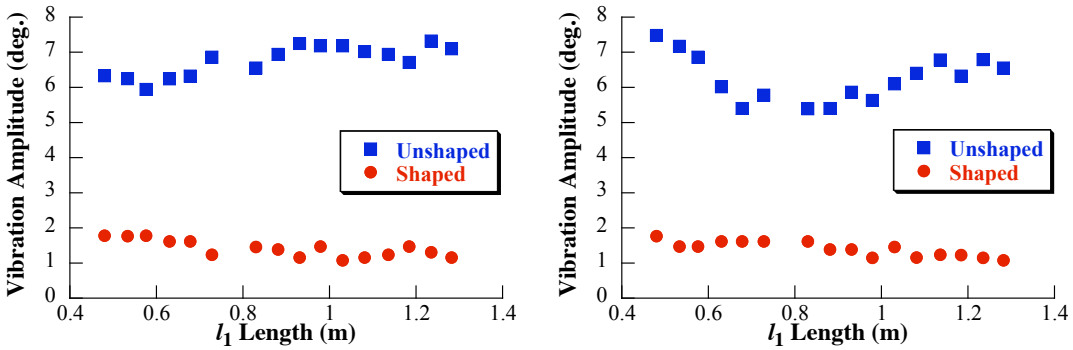

(a) Hook Vibration Amplitudes (ϕ) for $R = 1.43$ **(b)** Hook Vibration Amplitudes (ϕ) for $R = 0.76$

Figure 174: Residual Vibration for Varying Suspension Cable Lengths and Two Mass Ratios

substantially less than the unshaped case. The oscillation amplitude with shaping averaged only 21% of the amount without shaping. The sensitivity of this shaper to changes in suspension cable length was also examined for a mass ratio of 0.76, by repeating the trials with a lighter payload mass. Figure 174(b) shows that the oscillation amplitude with shaping averaged only 22% of the amount without shaping.

8.5.5 Robustness to Dynamic Nonlinearities – Tower Slewing

Input shaping theory is based upon an assumption of system linearity. However, all real systems contain some form of nonlinearity. For nonlinearities with relatively small influence on the total system dynamics, input shaping has been shown to work well. The experimental results in the previous section illustrate this fact. However, if the tower crane undergoes rotational motion (slewing), instead of only radial motion, then the nonlinear dynamics of the tower crane contribute more significantly to the total response. This section will provide an analysis of the shaper robustness to these dynamic nonlinearities.

Tower crane slewing will excite oscillations in both the radial and tangential directions, as seen previously in Section 5.2. Upon the completion of a slew command, these oscillations will result in hook and payload oscillations enclosed in ellipses. An example of this phenomenon for a 45° slew is shown by the simulation response in Figure 175. To capture both radial and tangential oscillations in a single measure, the principle radius of

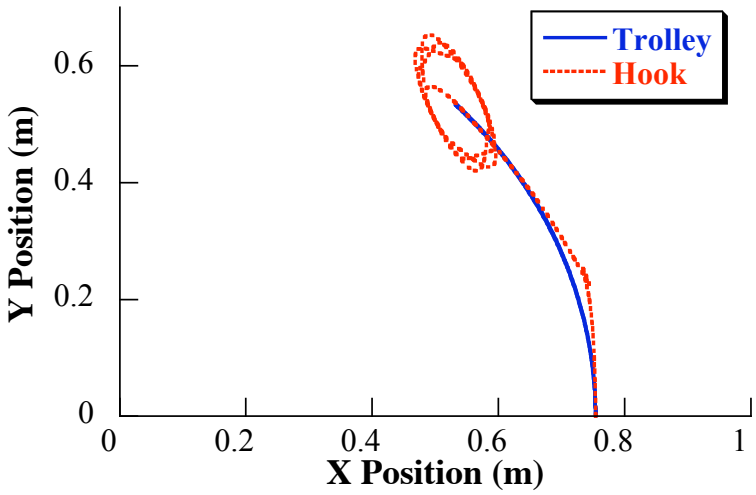

Figure 175: 45° Slew Viewed from Above

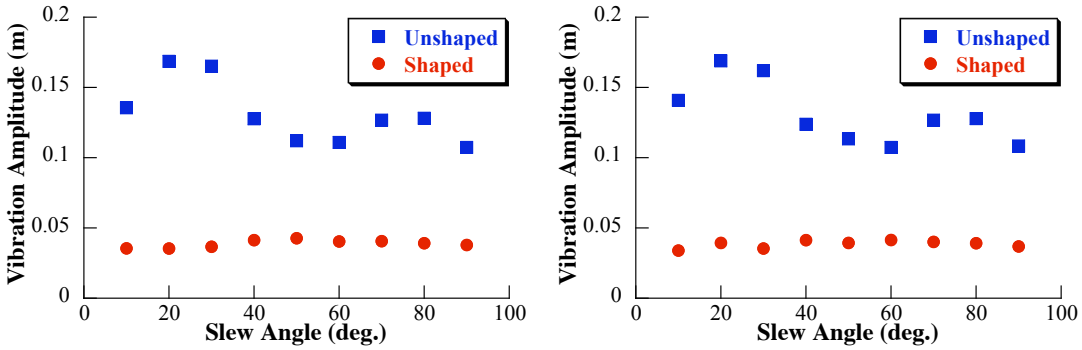

(a) Vibration Amplitude for $R = 1.43$ **(b)** Vibration Amplitude for $R = 0.76$

Figure 176: Residual Vibration Amplitude for Slewing Motion

this ellipse can be used as a measure of payload oscillation.

To examine the effect of tower crane dynamic nonlinearities on the effectiveness of the developed input shaper, a series of slewing commands were issued and the resulting oscillation was measured. Commands were generated to rotate the jib through angles from ten to ninety degrees. Figure 176 shows the resulting hook vibration amplitudes (as measured by ellipse diameter) for two different mass ratios. For both mass ratios and for all slew angles, the input-shaped command resulted in much lower levels of payload oscillation than the unshaped case, remaining below 0.05m for all cases. It should also be noted that

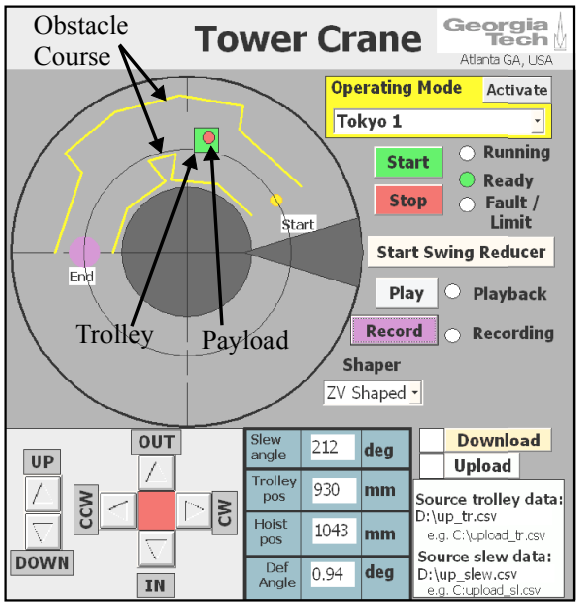

Figure 177: Tower Crane GUI for Double-Pendulum Study

the shaped command produced nearly constant vibration amplitudes across all slew angles. This indicates good robustness to the nonlinearities resulting from the slewing motion of the tower crane.

8.5.6 Human Operator Performance Using Two-Mode SI Shapers

The ability of input shaping to reduce double-pendulum oscillations in tower cranes was demonstrated in the previous sections. However, input shaping introduces a slight lengthening of the reference command; the long duration of the two-mode input shapers increases this lengthening. There have been studies indicating that the advantages of input shaping outweigh the negative impact of this delay [22, 23]. In addition, these studies were conducted on bridge cranes, rather than the tower cranes discussed in this chapter.

This section will present a study using the tower crane shown in Figure 169 and described in detail in Appendix A. The operators used the GUI shown in Figure 177 to control the crane. Operators navigated two obstacle courses, shown in Figure 178. The first, simple obstacle consists of a point-to-point manuever, while avoiding workspace boundaries; this course is shown in Figure 178(a). A second, more difficult course is shown in Figure

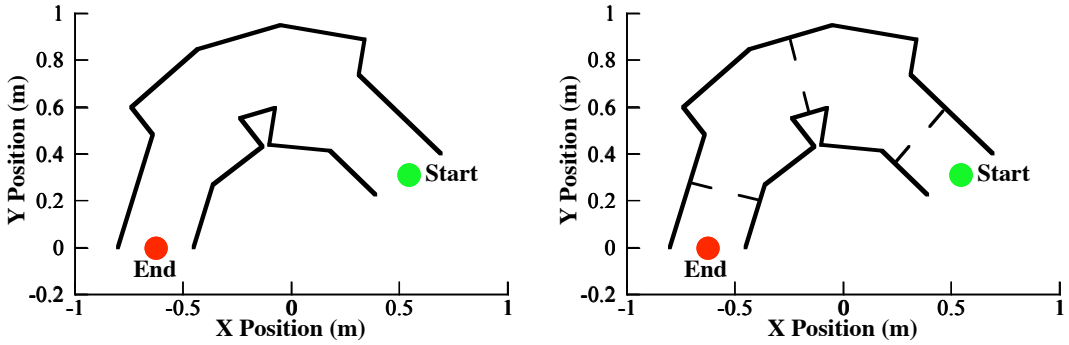

(a) Simple Obstacle Course **(b)** Difficult Obstacle Course

Figure 178: Tower Crane Obstacle Courses

178(b). The course is more difficult due to additional obstacles, placed perpendicular to the workspace boundary, narrowing the passage between the start and end zones.

For each time through the obstacle course, the total completion time and the number of obstacle collisions were recorded. The task was considered to be complete once the payload settled to within a 0.175m diameter, circular goal ("End") region. If the payload was still outside the goal region after 2.5 minutes, then the run was also considered finished. This was done primarily due to the extremely light damping of the crane; the response will take a long time to decay to within the goal region, even if the trolley is properly positioned. For example, the minimum deflection angle to remain within the goal region is approximately four degrees. Given the approximate 0.014 damping ratio of the crane, a deflection angle of five degrees will take nearly one minute to decay to within the goal region. Further details of each group of tests are presented in the following two subsections.

8.5.6.1 Simple Obstacle Course

One group of five operators navigated a simple obstacle course, shown in Figure 178(a), with and without input shaping for several cases. Operators first navigated the course with two different payloads locally. Then, the tests were repeated with the operators controlling the crane remotely, via teleoperation over the Internet.

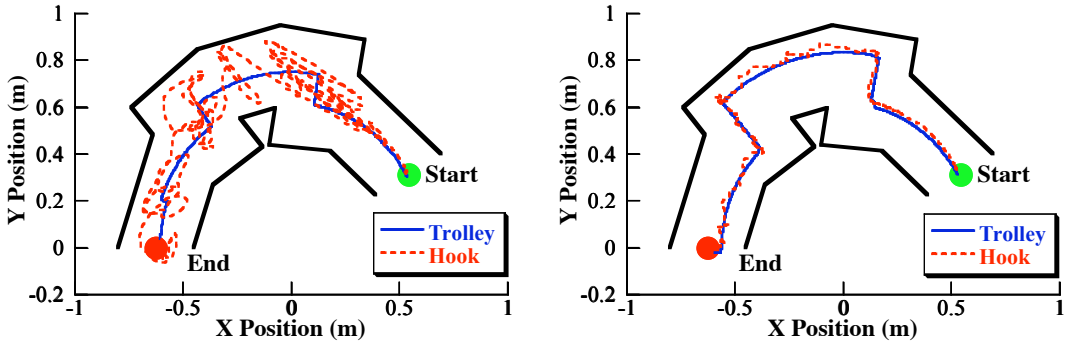

(a) Without Input Shaping **(b)** With Input Shaping

Figure 179: Navigating the Simple Obstacle Course Locally

Table 12: Local Operator Performance for Simple Obstacle Course

Control	Payload Mass Ratio, *R*	Average Completion Time (s)	Average Number of Collisions
Unshaped	1.43	98.3	3.4
Unshaped	0.76	130.2	3.4
Shaped	1.43	42.3	0.8
Shaped	0.76	44.4	0.2

Figure 179(a) shows one operator's attempt to navigate the simple obstacle course locally without input shaping. Even though the trolley position, shown as a solid line, tracks a safe trajectory through the obstacle course, the hook, shown as a dashed line, exhibits large oscillations making navigating the course difficult. Figure 179(b) shows the same operator's attempt to navigate the obstacle course with input shaping enabled. The reduction in payload oscillation makes navigating the course much easier.

Table 12 summarizes the performance of the operators with and without input shaping, when the crane was controlled locally. For both payloads, the operators completed the obstacle course much more quickly and with fewer collisions when input shaping was utilized. It should be noted that the 2.5 minute time constraint was enforced for five of the unshaped runs, but for none of the shaped runs. If this constraint had not been enforced, then the improvement in completion time with input shaping would be even more dramatic.

If the tower crane is operated remotely, then the combination of communication delay

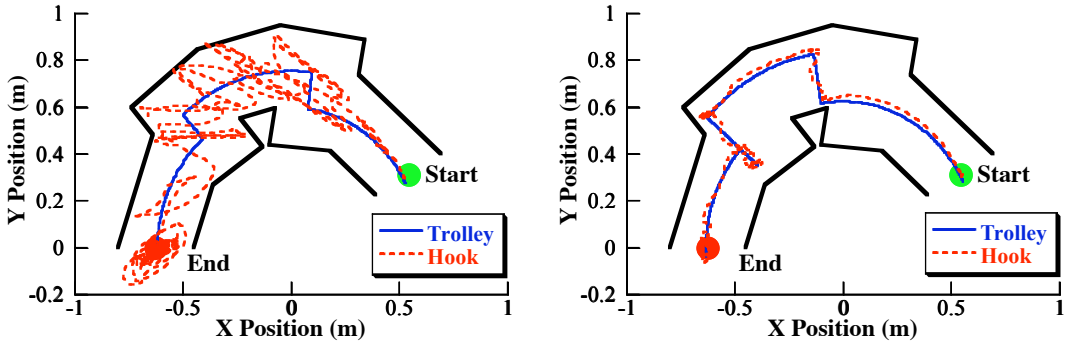

(a) Without Input Shaping **(b)** With Input Shaping

Figure 180: Navigating the Simple Obstacle Course Remotely

Table 13: Remote Operator Performance for Simple Obstacle Course

Control	Payload Mass Ratio, R	Average Completion Time (s)	Average Number of Collisions
Unshaped	1.43	72.3	7.0
Unshaped	0.76	129.0	5.4
Shaped	1.43	58.7	2.6
Shaped	0.76	38.4	0.4

and oscillatory dynamics makes navigating the course even more difficult. Figure 180(a) shows one user's attempt to navigate the course remotely, without input shaping. This particular attempt resulted in ten collisions with the obstacle course. However, limiting the oscillatory dynamics with input shaping again improved the ability of the operator to navigate the course. This is shown in Figure 180(b), an attempt of the same operator to navigate the obstacle course remotely, with input shaping enabled. With input shaping, the operator did not collide with the obstacles and completed the course more quickly. This result occured across all operators. Table 13 summarizes the operator performance when operating the tower crane remotely. The improvements in performance when utlizing input shaping are immediately evident, in terms of both completion time and number of collisions. It should again be noted that the 2.5 minute time constraint was enforced for four unshaped runs and for one shaped attempt. If this constraint had not been in place, a more dramatic improvement in completion time would be seen.

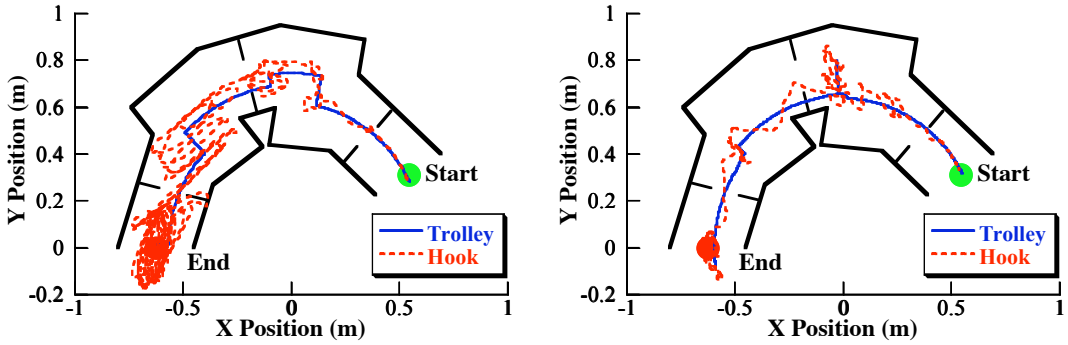

(a) Without Input Shaping **(b)** With Input Shaping

Figure 181: Navigating the Difficult Obstacle Course Locally

8.5.6.2 Difficult Obstacle Course

The obstacle course presented in the previous section was made more difficult by adding obstacles perpendicular to the course boundary, as shown in Figure 178(b). These additional obstacles narrow the path from the start-zone to the end-zone. Five operators were asked to navigate this obstacle course both locally and remotely. Only one payload was tested.

Figure 181 shows an operator's attempt to navigate the difficult obstacle course with and without shaping. As seen in Figure 181(a), the unshaped case results in significant payload oscillation, making navigating the course virtually impossible. This particular run contained eleven collisions. Figure 181(b) is the same operator's attempt to navigate the course with input shaping enabled. While there is much less payload oscillation than the unshaped case, there is a significant amount of vibration. This vibration was the result of a collision with the obstacle course early in the run. Input shaping does not utilize feedback, so it does not eliminate oscillations from disturbances, only those caused by commanded motion. Even with this one collision, the only of the run, the operator more easily and quickly navigated to the target. Collisions very rarely occured when input shaping was enabled, so the results of Figure 181(b) represent the worst case result with shaping. Overall, operator performance was greatly improved with input shaping, as summarized in Table 14. With input shaping enabled, operators were able to complete the course in less than

Table 14: Operator Performance for Difficult Obstacle Course

Control	Location	Average Completion Time (s)	Average Number of Collisions
Unshaped	Local	126.0	4.8
Unshaped	Remote	150.0	10.4
Shaped	Local	59.2	1.4
Shaped	Remote	47.4	0.2

half the time and with an order of magnitude less collisions, on average.

Remote operation increases the difficulty of completing the obstacle course. One such case is shown in Figure 182(a). This attempt of tele-operated navigation through the difficult obstacle course resulted in eleven collisions. The same operator, with input shaping enabled, successfully navigated the obstacle course with no collisions, as shown in Figure 182(b). Of all the tests conducted, the improvements in completion time and number of collisions were most dramatic for the remote control navigation of the difficult obstacle course. These improvements are summarized in Table 14. Notice that the average completion time without input shaping is 150 seconds, the maximum allowed by the testing procedure. No remote operator completed the difficult obstacle course in under 2.5 minutes without input shaping enabled, while averaging over ten collisions. Input shaping reduced the average number of collisions to nearly zero, while drastically reducing completion time. Again, without the 2.5 minute time constraint, the improvement of completion time with input shaping would have been more dramatic.

8.5.7 Analysis of Variance

To test the significance of the results presented in the previous sections, an Analysis of Variance (ANOVA) test was performed. For each testing condition, the differences between the shaped and unshaped cases were examined. For all but one set, the difference was found to be significant to a 0.05 confidence level ($p < 0.05$), with several sets exhibiting an improvement in input shaping to much higher probabilities ($p < 0.001$). Only the case of remote control of a heavy payload ($R = 1.43$) through the simple obstacle course did not

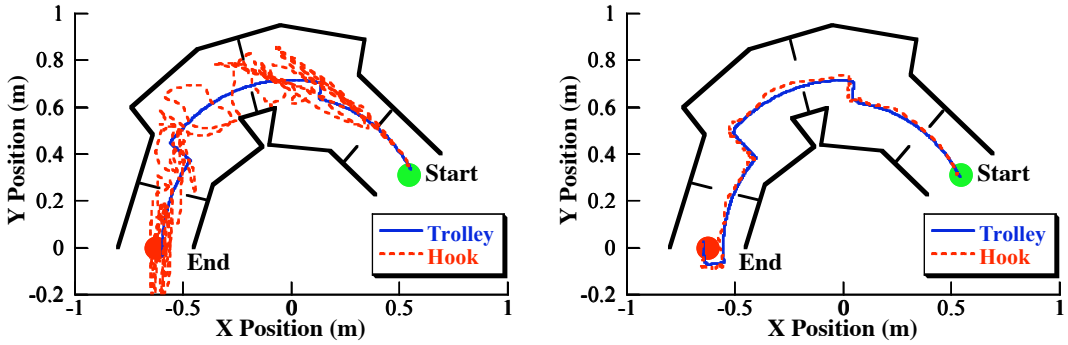

(a) Without Input Shaping **(b)** With Input Shaping

Figure 182: Navigating the Difficult Obstacle Course Remotely

show significant difference ($p = 0.697$) between the shaped and unshaped control. Looking at the data from this trial, one user collided with the obstacle course when using input shaping. This was the only trial within that subset of data that resulted in the input-shaped having a longer completion time than the unshaped case. The relatively small sample size allows this one trial to influence the significance of the results. Particularly significant results ($p < 0.0002$) were seen in the remote control of the light payload through the simple obstacle course and for the remote control through the difficult obstacle course.

8.6 Conclusion

This chapter presented several studies that investigated the performance of human crane operators when operating locally, remotely, with and without input shaping. The first study, using a portable tower crane, demonstrated the task completion time improvement that input shaping can provide for remotely operated, flexible systems. The second study investigated the influence of shaper duration on operator performance, revealing that longer duration shapers can increase the time required to complete a task. In addition, the influence of communication delay on crane operators was investigated using a bridge crane, with and without shaping. It was shown that input shaping provides substantial improvements in operator performance for low delay times. However, as the communication delay time increases, the improvements provided by input shaping decrease. The final study

again used the portable tower crane. For this study, however, two different payloads were used that resulted in double-pendulum dynamics. A multi-mode input shaping method was introduced that reduced oscillation at the two frequencies of the double-pendulum. The operators completed two obstacle courses, with and without shaping, locally and remotely operated. Input shaping provided significant improvements in task completion time and a dramatic reduction in the number of obstacle collisions.

CHAPTER IX

CLOSING

CHAPTER SUMMARY: *This chapter summarizes the work presented in this thesis, highlights the main thesis contributions, and presents possible avenues for extension of this research for future work.*

9.1 Dissertation Summary and Contributions

This dissertation has presented research directed toward the advancement of the state of the art in the control of vibratory systems, with cranes as the primary application example. The work included the most thorough evaluation of robust input shaping techniques completed to date. This evaluation highlighted the fundamental compromises in input shaper design. Through this analysis, a new input shaper was developed, the Specified Negative Amplitude–Specified Insensitivity (SNA-SI) shaper. This new shaper provides a continuous spectrum of solutions for the most fundamental compromise in shaper design between shaper duration, robustness, and high-mode excitation.

In addition to this thorough analysis of robust input shaping methods, a comparison was made between input shaping and two other command filtering methods, lowpass and notch filters. Input shapers were proven to be superior for reduction of vibration via command generation in mechanical systems. In addition it was shown that input shapers are also superior in this application in terms of ease of calculation and ease of implementation.

Another major advancement in input shaping theory presented in this dissertation was

the extension of input shaping into the multi-input domain. Few researchers have previously investigated this extension. The fundamental principle behind the multi-input shapers developed is to use multiple inputs to achieve performance that is not possible with a single input. Toward this end, several categories of multi-input shapers were presented and design methods for each was outlined. These included compensating inputs to overcome the structural limitations of one primary input, using additional actuators to improve the robustness of the control system, and utilizing multiple inputs to improve the rise time of the system, while maintaining low levels of vibration.

In addition to developing multi-input shaping methods, another new category of input shapers was presented. Input shapers were presented that reduced the perceived overtravel and overshoot in human operated systems. These shapers represent the first to explicitly consider these parameters in input shaper design; no similar shapers exist in the literature.

A series of operator studies was also presented. These studies sought to distill the important factors in the teleoperation of flexible systems, using cranes as the primary application. These studies presented a fundamentally different approach than the vast majority of teleoperation literature. The nature of many systems, cranes being one example, are not well suited to the force-feedback teleoperation methods popular in the literature. The studies showed that by improving the dynamics of the remote system, *i.e*. reducing vibration using input shaping, the performance of remote operators was drastically improved.

To summarize, major contributions include:

- **Dynamic Analysis of Mobile Cranes** – Chapter 5

  The dynamics of a mobile tower crane and a tower crane with double-pendulum payload dynamics are presented. The primary dynamic properties of each are discussed.

- **Methods to design of multi-input shaped commands** – Chapter 6

  Multi-Input shapers create multiple inputs to achieve performance that is not possible with a single input. Multi-input shaping design procedures are introduced that result

in shapers that use secondary actuators to reduce vibration, increase robustness, and speed system motion.

- **Methods to decrease the input shaper overtravel in human operated systems** – Chapter 7

  Traditional input shaping techniques increase the duration of an operator's command. To accurately position an input shaped system, a human operator must estimate the distance the system will travel as a result of this increased command duration. A new class of input shapers is designed to limit the overtravel.

- **A comparison of command filtering methods for vibration reduction via command generation in mechanical systems** – Chapter 4

  Digital filtering and input shaping are both well-known methods for shaping the reference commands for flexible systems. This thesis presents a comparison of digital filters and input shaping, showing that input shaping is the superior approach for vibration reduction in mechanical systems.

- **A new input shaper design method providing a continuous spectrum of solutions for optimizing the robustness, duration, and high-mode excitation compromise inherent in shaper design** – Chapter 3

  There is a fundamental compromise in input shaper design between robustness, shaper duration, and possible high-mode excitation. A new Specified Negative Amplitude-Specified Insensitivity (SNA-SI) shaper is developed to provide the shortest duration shaper for a given Insensitivity and maximum negative impulse amplitude.

9.2 Future Work

There is ample opportunity to extend the work presented in this thesis. Given that so few researchers have addressed several of the topics covered in this thesis, there is still much work to do.

One primary avenue of future work is the further generalization of the multi-input shaping methods presented in this thesis, with the goal of finding standardized shapers similar to traditional, single input shapers. The application of multi-input shaping to systems other than mobile cranes is another avenue of future research. The techniques developed here are equally applicable to other multi-input systems, with prime examples being overactuated systems such multi-stage positioning systems, micro/macro manipulators, and hard disk drives. However, application of multi-input shaping techniques to these systems is sure to uncover additional, interesting research topics. One of these is likely the extension of the multi-input methods to nonlinear applications. One final avenue of extension is toward the multi-input multi-output domain. The methods presented in this thesis are able to reduce vibration for multi-mode systems. However, there may be more efficient methods to solve multi-input shapers for multi-mode systems.

Another area ripe for future research is the development of shapers for reducing overshoot in human operated systems. One primary avenue should be to examine the performance of crane operators when using such shapers. Another avenue of extension is to limit the amount of maximum deviation from the desired final location. The shapers presented in this thesis only had constraints placed on the final position. Additional constraints on the maximum deviation may further improve performance.

Finally, there remains much work to be done to understand the interaction between human operators and crane control systems. This work includes not only further investigations into the teleoperation of cranes, but also into local operation. Further understanding of how human operators control crane will likely influence crane controller design, even further improving crane performance.

APPENDIX A

EXPERIMENTAL SETUPS

CHAPTER SUMMARY: *This appendix presents detailed descriptions of the three experimental setups used throughout this thesis. These include a 10-ton industrial bridge crane, a portable bridge crane, and a mobile, portable tower crane.*

A.1 10-Ton Industrial Bridge Crane

The 10-ton bridge crane shown in Figure 183 is located in the High-Bay of the Manufacturing Research Center (MaRC) building at the Georgia Institute of Technology. It has a workspace that is 6 meters high, 5 meters wide and 42 meters long. The crane is controlled using a Siemens programmable logic controller (PLC), which receives operator commands from one of a variety of user interfaces. Commands from the PLC are sent to Siemens Masterdrives Series AC-AC inverters, which ensure accurate execution of the commands. The crane also has laser sensors that provide accurate information of the bridge and trolley positions. An overview of the control system is shown in Figure 184. To measure payload response, the crane is also equipped with a Siemens vision system.

There are several different interfaces that may be used to operate the 10-ton bridge crane. The first is a traditional crane pendant shown in Figure 185. The pendant has a series of two position buttons that allow the user to command the crane at two different speeds in each cartesian direction. The crane may also be controlled using a joystick. The joystick allows the user to input a continuous range of velocities over a full 360°.

The third interface option is the Graphical User Interface (GUI) shown in Figure 186.

Figure 183: 10-ton Bridge Crane

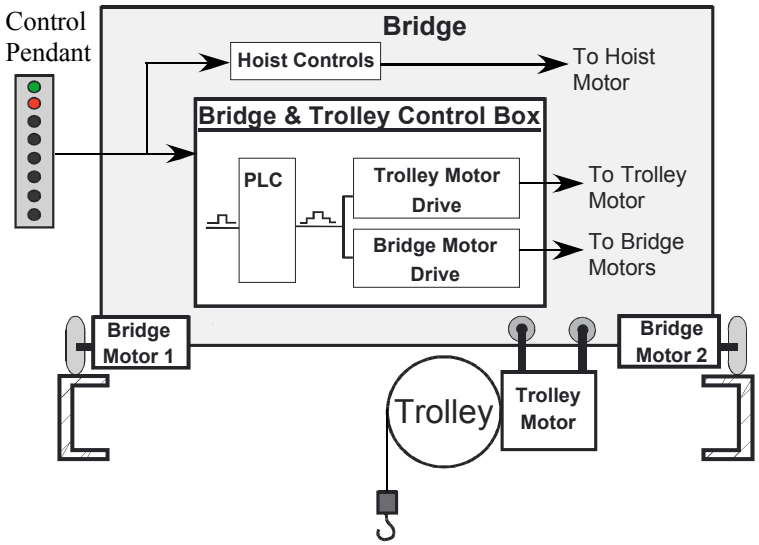

Figure 184: 10-ton Bridge Crane System Overview

Figure 185: 10-ton Bridge Crane Pendant

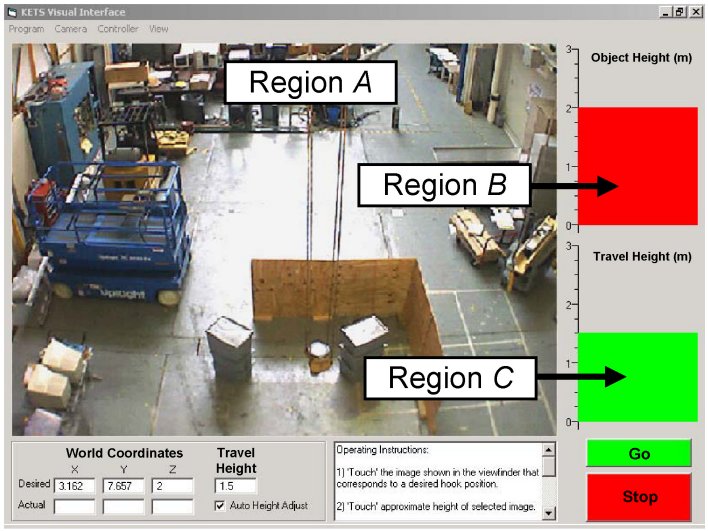

Figure 186: 10-ton Bridge Crane Graphical User Interface (GUI)

When using this mode of input, the user no longer specifies the crane's velocity, but rather choses a desired position in the workspace using the display. The user chooses a point from Region A of the interface, a live view of the crane workspace. The user must also choose the final positioning height in Region B of the interface. The user also has the option of choose the travel height of the hook by choosing a value from Region C.

The components of the machine vision system are shown in Figures 187 and 188. A Siemens vision sensor is mounted to the crane trolley, nearly directly over the equilibrium position of the hook. An LED array is mounted next to the camera. This LED array flashes to illuminate the marker shown in Figure 188, mounted to the top of the crane hook. The marker consists of six circles arranged in a circular array. This configuration allows up to three markers to be blocked before the camera loses its ability to determine the hook's position. In addition to measuring hook position for data recording during experiments, the machine vision system can be used for feedback. It has been used to implement a disturbance rejection algorithm on the crane [83].

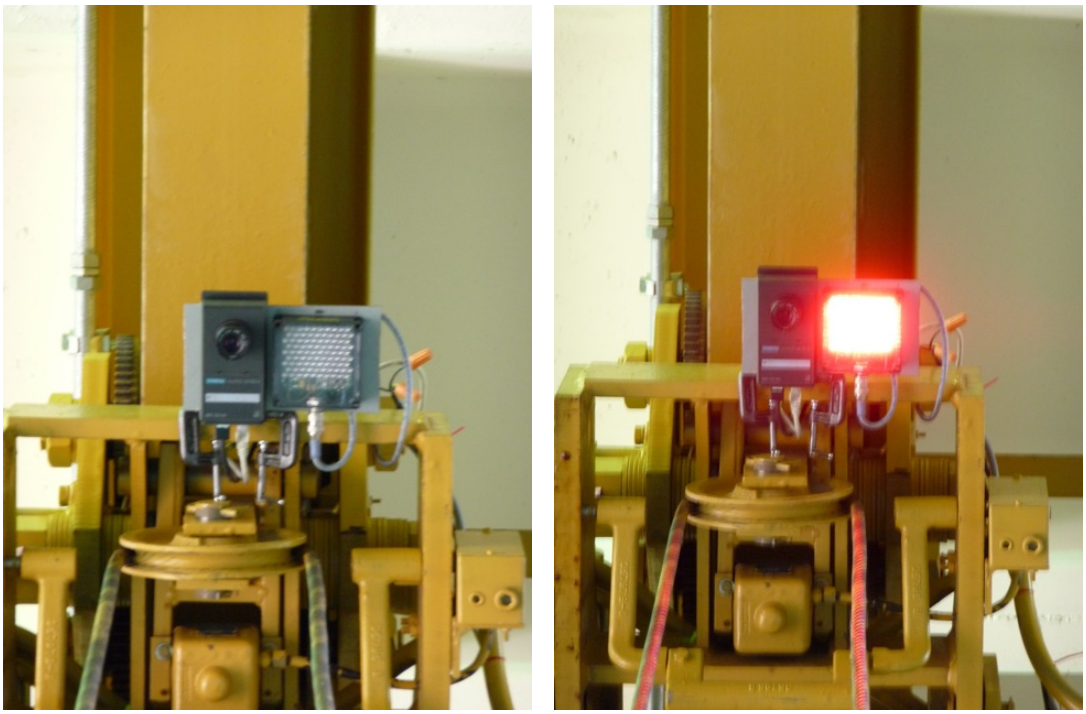

(a) Siemens Vision System and LED Array **(b)** LED Flash

Figure 187: 10-ton Bridge Crane Vision System

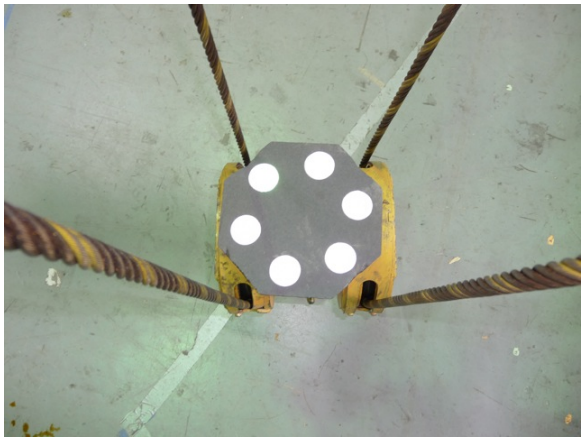

Figure 188: 10-ton Bridge Crane Retro-Reflective Marker

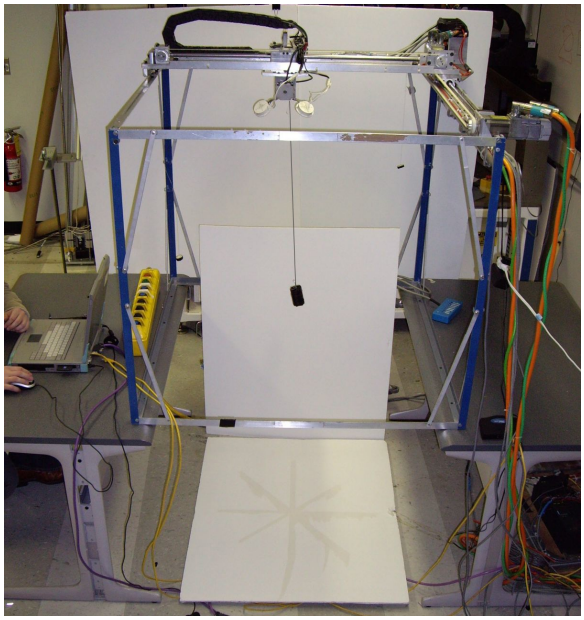

Figure 189: Portable Bridge Crane

A.2 Portable Bridge Crane

The 10-ton crane in the previous section is in active use in the MaRC High-Bay, making running large batteries of experiments or testing of prototype control systems difficult. To provide a more accessible experimental platform, the portable bridge crane shown in Figure 189 was constructed [29, 75]. It has many of the same features as the 10-ton crane.

The portable bridge crane has a workspace of approximately 1m×1m×1.6m. The overhead bridge and trolley are driven using Siemens synchronous AC servo motors attached to timing belts that provide motion in the x and y directions. The motors are controlled using a Siemens PLC using Proportional-plus-Integral (PI) Control with feedback from motor-mounted encoders. The crane is also equipped with a vision system to track payload position.

The portable bridge crane can be controlled via a traditional crane pendant, similar to that shown in Figure 185, or via the GUI shown in Figure 190(a). The upper left portion of the screen shows a real-time animation of the crane from an overhead view using the camera and encoder data. The square is the trolley position and the circle is the payload

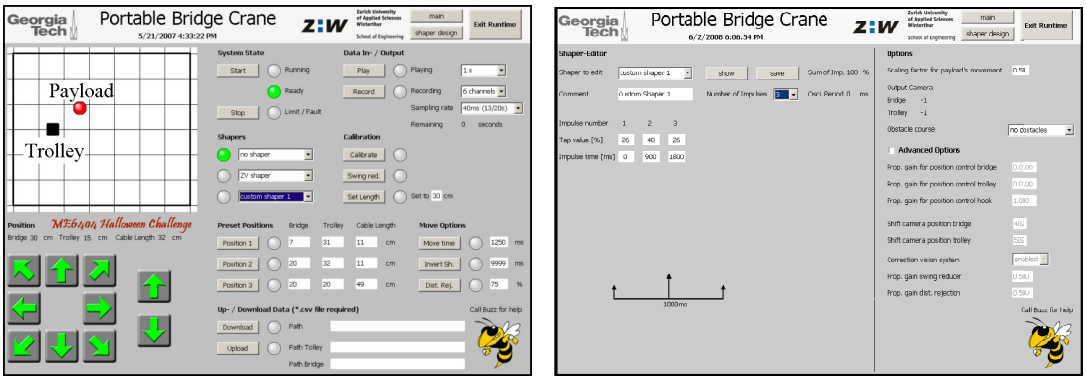

(a) Crane Control **(b)** Input Shaper Design and System Parameters

Figure 190: Portable Bridge Crane Graphical User Interfaces

position. The current configuration is also numerically displayed under the animation (trolley position, cable length, etc.). The crane can be manually driven using the directional arrows at the bottom left of the screen. In addition, velocity setpoints can be stored and then executed with the "Play" button. Other features include: input shaper selection, data recording, and a "Swing Reducer" that uses feedback from the camera to automatically dampen payload oscillation. An additional GUI screen, shown in Figure 190(b), allows the user to change key control system parameters. This portion of the interface also has a graphical input shaper design, to allow users to change input shaper parameters.

The portable bridge crane has teleoperation capabilities that allow it to be operated in real-time from anywhere in the world via the Internet. To achieve teleoperation, the controlling PC was equipped with UltraVNC. This program allows any user with Internet access to remotely control a target PC. In addition to the teleoperation capabilities, the portability of the crane allows it to provide a hands-on learning tool for students remote from Georgia Tech. For example, the crane was transported to Georgia Tech Lorraine in France during the fall of 2004. In the spring of 2006, it was used in an Atlanta-area high school.

(a) Mobile Tower Crane **(b)** Mobile Crane Base

Figure 191: A Mobile, Portable Tower Crane

A.3 Mobile, Portable Tower Crane

The mobile, portable tower crane, shown in Figure 191, has also been constructed for both research and educational purposes [30]. This crane has teleoperation capabilities that allow it to be operated in real-time from anywhere in the world via the Internet. The tower portion of the crane, shown in Figure 191(a) is approximately 2m tall with a 1m jib arm. It is actuated by Siemens synchronous, AC servomotors. The jib is capable of 340° rotation about the tower. The trolley moves radially along the jib via a lead screw, and a hoisting motor controls the suspension cable length. A VS-723 Siemens digital camera is mounted to the trolley and records the swing deflection of the hook. It can also be used for feedback control of the payload oscillation [30]. The measurement resolution of the camera depends upon suspension cable length. For the cable lengths used in this research, the resolution is approximately 0.08 degrees. This is equivalent to an approximate 0.14cm hook displacement at a cable length of 1m. The sampling rate of the camera is 50Hz.

Base mobility is provided by DC Motors with omni-directional wheels attached to each support leg, as shown in Figure 191(b). The base is under PD feedback control using

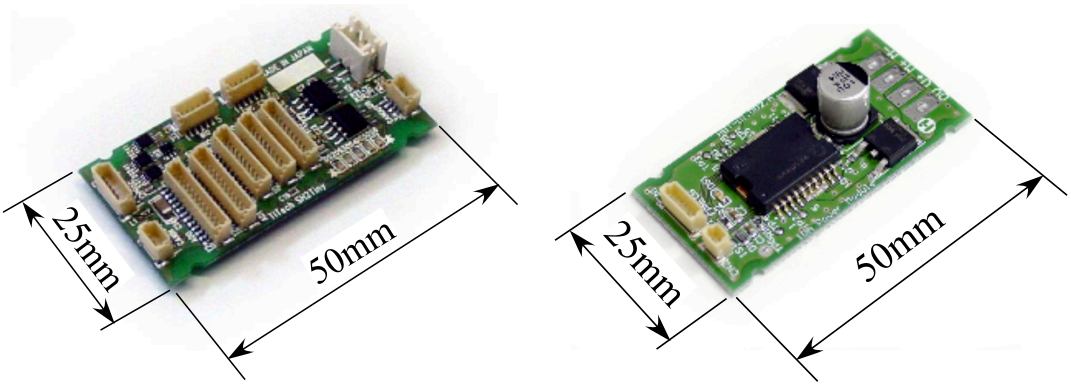

(a) HiBot *TiTechSH2 Tiny Controller*® **(b)** HiBot *1AxisDCMotor Module*®

Figure 192: HiBot Microcontroller and Motor Driver

two HiBot[1] *TiTechSH2 Tiny Controllers*®, each controlling two motors. These SuperH™-2 based microcontrollers use feedback from motor shaft mounted encoders to generate PWM signals for each motor driver. The DC motors are each driven with a HiBot *1Axis DCMotor Module*®, each of which is capable of providing 10A nominal current. The HiBot microcontroller and motor driver are shown in Figure 192.

During the fall of 2005, this crane was simultaneously used in courses at Georgia Tech and the Tokyo Institute of Technology (Tokodai). The crane has been tele-operated by researchers and students located throughout the United States, Japan, Korea, Switzerland, Spain, and Serbia [75, 76].

The tower crane can receive velocity commands from either a control pendant, shown in Figure 193, or via the GUI shown in Figure 194. As with the bridge crane, the upper left portion of the screen shows a real-time animation of the crane from an overhead view using the camera and encoder data. The square is the trolley position and the circle is the payload position. It also contains arrows to drive the crane, play and record features, and the "Swing Reducer" that uses camera feedback to dampen payload oscillations. The tower crane also receives its tele-operation capabilities via UltraVNC.

The mobile base may also be controlled independently of the tower portion of the crane

[1] http://www.hibot.co.jp/

Figure 193: Mobile Tower Crane Control Pendant

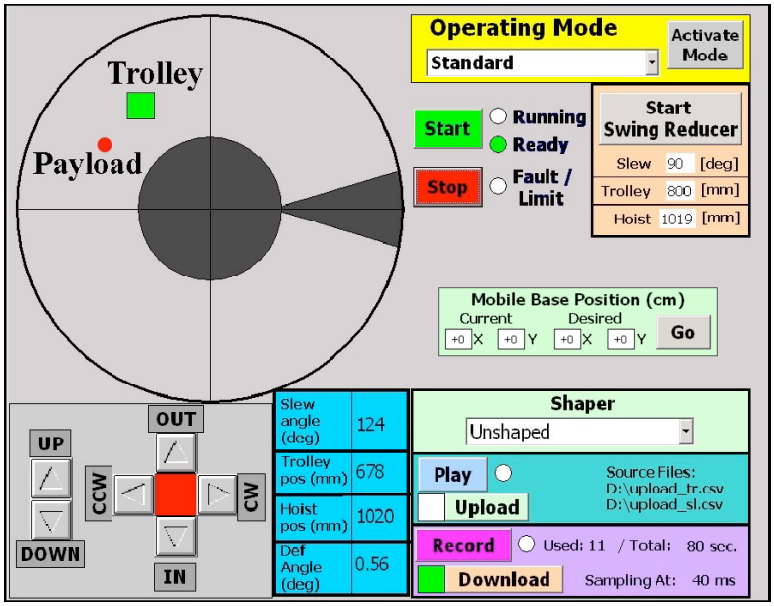

Figure 194: Mobile Tower Crane Graphical User Interface

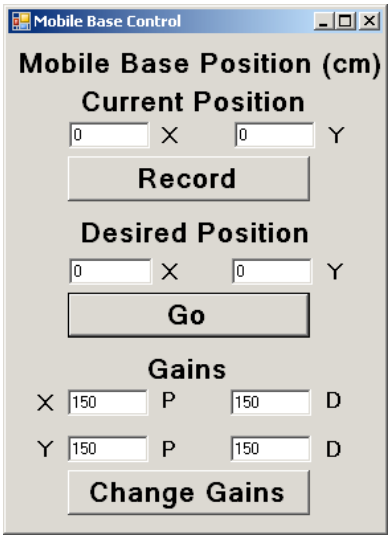

Figure 195: Mobile Tower Crane Base Graphical User Interface

using the much simpler interface in Figure 195. This interface allows for point-to-point positioning commands of the tower base, while recording the motion. The user also has the options of changing the controller gains for the *X* and *Y* directions.

Figure 196 shows the control layout of the tele-operated tower crane. The portable bridge crane shares a similar topography. A PLC sends velocity setpoints to the motor drives. The PLC receives the payload swing data from the camera and carries out the control algorithm. The motors are powered with Siemens Sinamic drives, which use the motor encoder signals to provide Proportional-plus-Integral (PI) velocity control of the motors.

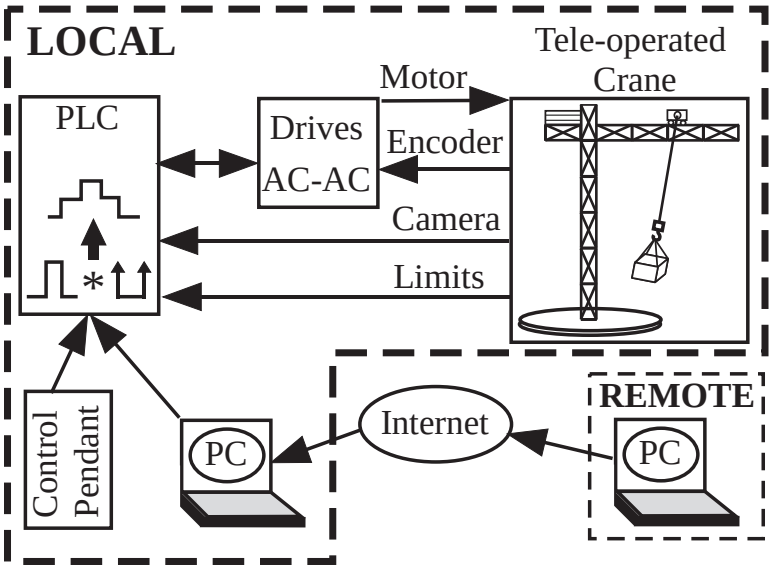

Figure 196: Mobile Tower Crane System Overview

REFERENCES

[1] Abdel-Rahman, E. M., Nayfeh, A. H., and Masoud, Z. N., "Dynamics and control of cranes: A review," *JVC/Journal of Vibration and Control*, vol. 9, no. 7, pp. 863 – 908, 2003. Rotary cranes;. 2.2

[2] Ando, N., Lee, J.-H., and Hashimoto, H., "Study on influence of time delay in teleoperation," *IEEE/ASME International Conference on Advanced Intelligent Mechatronics, AIM*, pp. 317 – 322, 1999. Teleoperation;Time delay;. 8.1

[3] Baumgart, M. D. and Pao, L. Y., "Cooperative multi-input shaping for arbitrary inputs," in *Proceedings of 2001 American Control Conference*, vol. 1, pp. 275–280, June 2001. 6

[4] Baumgart, M. D. and Pao, L. Y., "Discrete time-optimal command shapers and controls for multi-input multi-output systems," in *Proceedings of 2002 American Control Conference*, vol. vol.3, pp. 2279–84, May 2002. 6

[5] Baumgart, M. D. and Pao, L. Y., "Discrete time-optimal command shaping," *Automatica*, vol. 43, no. 8, pp. 1403 – 1409, 2007. Residual vibration;Command shaping;Derivative constraints;. 6

[6] Bhat, S. P. and Miu, D. K., "Precise point-to-point positioning control of flexible structures," *ASME J. of Dynamic Systems, Measurement, and Control*, vol. 112, no. 4, pp. 667–674, 1990. 4.1

[7] Blackburn, D. F., Singhose, W., Kitchen, J. P., Petrangenaru, V. P., Lawrence, J., Kamoi, T., and Taura, A., "Advanced input shaping algorithm for nonlinear tower crane dynamics," in *8th International Conference on Motion and Vibration Control*, (Daejeon, Korea), 2006. 2.2, 3

[8] Blevins, R., *Formulas for Natural Frequency and Mode Shape*. New York, NY: Van Nostrand Reinhold Co., 1979. 5.2.2

[9] Cutforth, C. F. and Pao, L. Y., "A modified method for multiple actuator input shaping," in *Proceedings of the 1999 American Control Conference*, vol. 1, pp. 66–70, 2-4 June 1999. 6

[10] Economou, D., Mavroidis, C., Antoniadis, I., and Lee, C., "Maximally robust input preconditioning for residual vibration suppression using low-pass fir digital filters," *Journal of Dynamic Systems, Measurement and Control, Transactions of the ASME*, vol. 124, no. 1, pp. 85 – 97, 2002. 4, 4.1, 4.1, 4.2.1, 4.4.1

[11] Ferrell, W., "Remote manipulation with transmission delay," *IEEE Transactions on Human Factors in Electronics*, vol. HFE-6, no. 1, pp. 24 – 32, Sept. 1965. 8.1

[12] Fiorini, P. and Oboe, R., "Internet-based telerobotics: Problems and approaches," in *Proceedings of the International Conference on Advanced Robotics*, (Monterey, CA, USA), pp. 765 – 770, 1997. 8.1

[13] Gao, J. and Chen, D., "Learning control of an overhead crane for obstacle avoidance," in *Proceedings of the 1997 American Control Conference*, vol. 5, (Albuquerque, NM, USA), pp. 3103 – 3104, 1997. 2.2

[14] Glossiotis, G. and Antoniadis, I., "Digital filter based motion command preconditioning of time varying suspended loads in boom cranes for sway suppression," *J. Vib. Control*, vol. 13, pp. 617 – 56, May 2007. 4

[15] Golafshani, A. R. and Aplevich, J., "Computation of time-optimal trajectories for tower cranes," in *Proceedings of IEEE Conference on Control Applications*, (Albany, NY, USA), pp. 1134 – 1139, 1995. 2.2

[16] Grosser, K. and Singhose, W., "Command generation for reducing perceived lag in flexible telerobotic arms," *JSME International Journal*, vol. 43, no. 3, pp. 755–761, 2000. 6.5

[17] Hazlerigg, A., "Automatic control of crane operations," in *IFAC 5th World Congress*, (Paris, France), pp. 28 –, 1972. 2.2

[18] Hokayem, P. F. and Spong, M. W., "Bilateral teleoperation: An historical survey," *Automatica*, vol. 42, no. 12, pp. 2035 – 2057, 2006. 8.1

[19] Huey, J., Fortier, J., Wolff, S., Singhose, W., Haraldsson, H. B., Sasaki, S. K., and Watari, E., "Remote manipulation of cranes via the internet," in *Proceedings of International Conference on Motion and Vibration Control*, (Daejeon, Korea), 2006. 8.1

[20] Hyde, J. and Seering, W., "Using input command pre-shaping to suppress multiple mode vibration," in *IEEE Int. Conf. on Robotics and Automation*, (Sacramento, CA), pp. 2604–2609, 1991. 8.5.1

[21] Kenison, M. and Singhose, W., "Input shaper design for double-pendulum planar gantry cranes," in *IEEE Conference on Control Applications*, (Hawaii), pp. 539–44, 1999. 5.2.2, 5.2.2

[22] Khalid, A., Huey, J., Singhose, W., Lawrence, J., and Frakes, D., "Human operator performance testing using an input-shaped bridge crane," *Journal of Dynamic Systems, Measurement and Control*, vol. 128, no. 4, pp. 835 – 841, 2006. 2.2, 8.1, 8.5.6

[23] Kim, D., Singhose, W., and Kenison, M., "Input shaping control of double-pendulum bridge crane oscillations," *Accepted to the Journal of Dynamic Systems, Measurement, and Control*, 2007. 2.2, 5.1.1, 8.1, 8.5.1, 8.5.1, 8.5.6

[24] Kim, J., "A TCP/IP-based remote control system for yard cranes in a port container terminal," *Robotica*, vol. 24, pp. 613 – 20, Sept.-Oct. 2006. 8.1

[25] Klaassens, J., Honderd, G., van Nauta Lemke, H., El Azzouzi, A., van der Veen, P., and de Vrind, M., "Time-optimal trajectory controller for container cranes using model-based predictive control," *J. A (Belgium)*, vol. 41, pp. 25 – 30, March 2000. time-optimal control;trajectory control;container cranes;model-based predictive control;gantry crane;position control;speed control;stabilisation;. 2.2

[26] Kozak, K., Singhose, W., and Ebert-Uphoff, I., "Performance measures for input shaping and command generation," *Journal of Dynamic Systems, Measurement and Control*, vol. 128, no. 3, pp. 731 – 736, 2006. 2.3.1

[27] Lawrence, J. and Singhose, W., "An analytical solution for a zero vibration input shaper for systems with coulomb friction," in *American Control Conference*, (Anchorage, AK), 2002. 3

[28] Lawrence, J. and Singhose, W., "Decreasing effects of coulomb friction in precision positioning using input shaping: Experimental verifications," in *Japan-USA Symp. on Flexible Automation*, (Hiroshima, Japan), 2002. 3

[29] Lawrence, J. and Singhose, W., "Design of minicrane for education and research," in *6th Int. Conference on Research and Education in Mechatronics*, (Annecy, France), 2005. 2.2, 3.8, A.2

[30] Lawrence, J., Singhose, W., Weiss, R., Erb, A., and Glauser, U., "An internet-driven tower crane for dynamics and controls education," in *7th IFAC Symposium on Advances in Control Education*, (Madrid, Spain), 2006. 2.2, 5.1.1, 8.1, A.3, A.3

[31] Lim, J., Ko, J., and Lee, J., "Internet-based teleoperation of a mobile robot with force-reflection," in *Proceedings of 2003 IEEE Conference on Control Applications*, vol. 1, (Istanbul, Turkey), pp. 680 – 5, 2003. 8.1

[32] Lim, S., Stevens, H., and How, J., "Input shaping design for multi-input flexible systems," *Journal of Dynamic Systems, Measurement and Control*, vol. 121, no. 3, pp. 443–7, 1999. 6

[33] Meckl, P. H., Arestides, P. B., and Woods, M. C., "Optimized s-curve motion profiles for minimum residual vibration," in *American Control Conference*, (Philadelphia, PA), 1998. 3

[34] Munir, S. and Book, W. J., "Control techniques and programming issues for time delayed internet based teleoperation," *Journal of Dynamic Systems, Measurement and Control*, vol. 125, no. 2, pp. 205–214, 2003. 8.1

[35] Niemeyer, G. and Slotine, J.-J. E., "Stable adaptive teleoperation," *IEEE Journal of Oceanic Engineering*, vol. 16, no. 1, pp. 152 – 162, 1991. 8.1

[36] Niemeyer, G. and Slotine, J.-J. E., "Telemanipulation with time delays," *International Journal of Robotics Research*, vol. 23, no. 9, pp. 873 – 890, 2004. 8.1

[37] Oboe, R. and Fiorini, P., "Design and control environment for internet-based telerobotics," *International Journal of Robotics Research*, vol. 17, no. 4, pp. 433 – 449, 1998. 8.1

[38] O'Connor, W. J., "A gantry crane problem solved," *Journal of Dynamic Systems, Measurement and Control, Transactions of the ASME*, vol. 125, no. 4, pp. 569 – 576, 2003. Mechanical displacement;System dynamics;. 2.2

[39] Oppenheim, A. V. and Schafer, R. W., *Digital Signl Processing*. Englewood Cliffs, NJ: Prentice Hall, Inc., 1975. 4.2.1, 4.5

[40] Pao, L. Y., "Multi-input shaping design for vibration reduction," *Automatica*, vol. 35, pp. 81–9, 1999. 6

[41] Pao, L. and Singhose, W., "Unity magnitude input shapers and their relation to time-optimal control," in *IFAC World Congress*, (San Francisco, CA), pp. 385–390, 1996. 2.3.1.2

[42] Pao, L., "Input shaping design for flexible systems with multiple actuators," in *Proceedings of the 13th World Congress International Federation of Automatic Control*, (San Francisco, CA, USA), pp. 267 – 72, 1997. 6

[43] Park, U. H., Lee, J. W., Lim, B. D., and Sung, Y. G., "Design and sensitivity analysis of an input shaping filter in the z-plane," *Journal of Sound and Vibration*, vol. 243, no. 1, pp. 157–171, 2001. 3.4.2.1

[44] Parker, G. G., Petterson, B., Dohrmann, C., and Robinett, R. D., "Command shaping for residual vibration free crane maneuvers," in *Proceedings of 1995 American Control Conference*, vol. vol.1, (Dept. of Structural Dynamics & Vibration Control, Sandia Nat. Labs., Albuquerque, NM, USA), pp. 934–8, American Autom Control Council, June 21-23 1995. 2.2

[45] Parker, G. G., Groom, K., Hurtado, J., Robinett, R. D., and Leban, F., "Command shaping boom crane control system with nonlinear inputs," in *Proceedings of IEEE Conference on Control Applications*, vol. 2, (Kohala Coast, HI, USA), pp. 1774 – 1778, 1999. 2.2

[46] Parks, T. and Burus, C., *Digital Filter Design*. New York: John Wiley & Sons, Inc., 1987. 4.2.1

[47] Robertson, M. and Singhose, W., "Closed-form deflection-limiting commands," in *American Control Conference*, vol. 3, (Portland, OR), pp. 2104–2109, June 8-10 2005. 4.5

[48] Rosch, O., Schilling, K., and Roth, H., "Haptic interfaces for the remote control of mobile robots," *Control Engineering Practice*, vol. 10, pp. 1309 – 13, November 2002. 8.1

[49] Sakawa, Y. and Shindo, Y., "Optimal control of container cranes," *Automatica*, vol. 18, pp. 257 – 66, June 1982. 2.2

[50] Schilling, K., Roth, H., and Spilca, C., "A tele-experiment on rover motor control via internet," *J. Robot. Syst.*, vol. 22, pp. 123 – 30, March 2005. 8.1

[51] Schilling, K. and Roth, H., "Control interfaces for teleoperated mobile robots," in *Proceedings of 7th IEEE International Conference on Emerging Technologies and Factory Automation*, vol. 2, (Barcelona, Spain), pp. 1399 – 403, 1999. 8.1

[52] Shan, J., Liu, H.-T., and Sun, D., "Modified input shaping for a rotating single-link flexible manipulator," *Journal of Sound and Vibration*, vol. 285, no. 1-2, pp. 187–207, 2005. 3.1.3

[53] Sheridan, T., "Telerobotics," *Automatica*, vol. 25, no. 4, pp. 487 – 507, 1989. 8.1

[54] Sheridan, T., "Teleoperation, telerobotics and telepresence: a progress report," *Control Engineering Practice*, vol. 3, no. 2, pp. 205 – 214, 1995. 8.1

[55] Sheridan, T. B., "Space teleoperation through time delay: Review and prognosis," *IEEE Transactions on Robotics and Automation*, vol. 9, no. 5, pp. 592 – 606, 1993. 8.1

[56] Singer, N., Singhose, W., and Kriikku, E., "An input shaping controller enabling cranes to move without sway," in *ANS 7th Topical Meeting on Robotics and Remote Systems*, vol. 1, (Augusta, GA), pp. 225–31, 1997. 2.2

[57] Singer, N. C. and Seering, W. P., "Design and comparison of command shaping methods for controlling residual vibration," in *IEEE International Conference on Robotics and Automation*, vol. 2, (Scottsdale, AZ, USA), pp. 888 – 893, 1989. 4

[58] Singer, N. C. and Seering, W. P., "Preshaping command inputs to reduce system vibration," *J. of Dynamic Sys., Measurement, and Control*, vol. 112, no. March, pp. 76–82, 1990. 2.3, 2.3.1, 3.1.1, 3.4.1, 4.1, 4.2.1, 4.5, 8.3.1

[59] Singer, N. C., Singhose, W. E., and Seering, W. P., "Comparison of filtering methods for reducing residual vibration," *European Journal of Control*, no. 5, pp. 208–218, 1999. 4

[60] Singh, T. and Heppler, G. R., "Shaped input control of a system with multiple modes," *Journal of Dynamic Systems, Measurement, and Control*, vol. 115, pp. 341–347, September 1993. 8.5.1

[61] Singh, T. and Vadali, S. R., "Robust time-delay control," *ASME Journal of Dynamic Systems, Measurement, and Control*, vol. 115, pp. 303–6, 1993. 4.1

[62] Singhose, W., *Command Generation for Flexible Systems*. Ph.d. thesis, Massachusetts Institute of Technology, 1997. 3.1.2.1

[63] Singhose, W., Biediger, E., Chen, Y.-H., and Mills, B., "Reference command shaping using specified-negative-amplitude input shapers for vibration reduction," *ASME J. of Dynamic Systems, Measurement, and Controls*, vol. 126, no. March, pp. 210–214, 2004. 2.3.1.2, 3.3, 3.3, 3.5, 3.7

[64] Singhose, W., Biediger, E., Okada, H., and Matunaga, S., "Closed-form specified-fuel commands for on-off thrusters," *AIAA J.of Guidance, Control, and Dynamics*, vol. 29, pp. 606–11, 2006. 4.5

[65] Singhose, W., Crain, E., and Seering, W., "Convolved and simultaneous two-mode input shapers," *IEE Control Theory and Applications*, vol. 144, no. Nov., pp. 515–520, 1997. 8.5.1

[66] Singhose, W., Derezinski, S., and Singer, N., "Extra-insensitive input shapers for controlling flexible spacecraft," *AIAA J. of Guidance, Control, and Dynamics*, vol. 19, no. 2, pp. 385–91, 1996. 3.1.2.2

[67] Singhose, W. and Grosser, K., "Limiting excitation of unmodeled high modes with negative input shapers," in *IEEE Conference on Controls Applications*, (Kohala, Hawaii), 1999. 3.3

[68] Singhose, W. and Mills, B., "Command generation using specified-negative-amplitude input shapers," in *American Control Conference*, (San Diego, CA), 1999. 3.5

[69] Singhose, W., Porter, L., Kenison, M., and Kriikku, E., "Effects of hoisting on the input shaping control of gantry cranes," *Control Engineering Practice*, vol. 8, no. 10, pp. 1159–1165, 2000. 2.2

[70] Singhose, W., Porter, L., Tuttle, T., and Singer, N., "Vibration reduction using multi-hump input shapers," *ASME Jouranl of Dynamic Systems, Measurement, and Control*, vol. 119, no. June, pp. 320–326, 1997. 3.1.2.1, 3.4.2.1

[71] Singhose, W., Seering, W., and Singer, N., "Shaping inputs to reduce vibration: A vector diagram approach," in *IEEE Int. Conf. on Robotics and Automation*, vol. 2, (Cincinnati, OH), pp. 922–927, IEEE, 1990. 2.3.2.2, 3.1.2, 3.4.2.1

[72] Singhose, W., Seering, W., and Singer, N., "Residual vibration reduction using vector diagrams to generate shaped inputs," *ASME J. of Mechanical Design*, vol. 116, no. June, pp. 654–659, 1994. 2.3.2.1, 2.3.2.2, 3.1.2, 3.1.2.1, 3.4.2.1, 4.1, 4.4.1, 4.5

[73] Singhose, W., Seering, W., and Singer, N., "Input shaping for vibration reduction with specified insensitivity to modeling errors," in *Japan-USA Sym. on Flexible Automation*, vol. 1, (Boston, MA), pp. 307–13, 1996. 4.1, 4.2.1, 4.2.1, 8.3

[74] Singhose, W., Singer, N., and Seering, W., "Time-optimal negative input shapers," *J. of Dynamic Systems, Measurement, and Control*, vol. 119, no. June, pp. 198–205, 1997. 2.3.1.2, 3.3, 3.6.2

[75] Singhose, W., Vaughan, J., Danielson, J., and Lawrence, J., "Using tele-operated cranes for advanced controls education," in *ASME International Mechanical Engineering Congress and Exposition*, (Seattle, Washington), 2007. 2.2, 3.8, A.2, A.3

[76] Singhose, W., Vaughan, J., Danielson, J., and Lawrence, J., "Use of cranes in system dynamics and controls education," in *Proceedings of the 17th IFAC World Congress*, (Seoul, Korea), July 6-11 2008. A.3

[77] Slawinski, E., Postigo, J. F., and Mut, V., "Bilateral teleoperation through the internet," *Robotics and Autonomous Systems*, vol. 55, no. 3, pp. 205 – 215, 2007. 8.1

[78] Smith, J., Kozak, K., and Singhose, W., "Input shaping for a simple non-linear system," in *American Control Conference*, vol. 1, (Anchorage, AK), pp. 821–6, 2002. 3

[79] Smith, O., *Feedback Control Systems*. New York: McGraw-Hill Book Co., Inc., 1958. 2.3, 2.3.1.1, 8.3.1

[80] Smith, O. J. M., "Posicast control of damped oscillatory systems," *Proceedings of the IRE*, vol. 45, no. September, pp. 1249–1255, 1957. 8.3.1

[81] Sorensen, K., Daftari, A., Singhose, W., and Hekman, K., "Negative input shaping: Eliminating overcurrenting and maximizing command space," *In Press: ASME Journal of Dynamic Systems, Measurement, and Control*, 2008. 6.3.3

[82] Sorensen, K., Singhose, W., and Dickerson, S., "A combined controller for precision crane positioning with minimal sway," in *IFAC World Congress*, (Prague, Czech Republic), 2005. 2.2

[83] Sorensen, K., Singhose, W., and Dickerson, S., "A controller enabling precise positioning and sway reduction in bridge and gantry cranes," *Control Engineering Practice*, vol. 15, pp. 825–837, July 2007. 2.2, A.1

[84] Starr, G. P., "Swing-free transport of suspended objects with a path-controlled robot manipulator," *J. of Dynamic Systems, Measurement and Control*, vol. 107, pp. 97–100, 1985. 2.2

[85] Vaughan, J., Singhose, W., Debenest, P., Fukushima, E., and Hirose, S., "Initial experiements on the control of a mobile tower crane," in *ASME International Mechanical Engineering Congress and Exposition*, (Seattle, Washington), 2007. 2.2

[86] Vaughan, J., Yano, A., and Singhose, W., "Comparison of robust input shapers," *In Press: Journal of Sound and Vibration*, 2008. 4.1, 4.5, 6.5, 8.3

[87] Vaughan, J., Yano, A., and Singhose, W., "Performance comparison of robust negative input shappers," in *2008 American Controls Conference*, (Seattle, Washington), June 2008. 6.5

[88] Vaughan, J., Yano, A., and Singhose, W., "Robust negative input shapers for vibration supressions," *Under Review at Journal of Dynamic Systems, Measurement, and Control*, 2008. 4.5, 6.5

[89] Wang, M. and Liu, J. N., "Interactive control for internet-based mobile robot teleoperation," *Robotics and Autonomous Systems*, vol. 52, no. 2-3, pp. 160 – 179, 2005. 8.1

[90] Wang, Z. and Surgenor, B., "Performance evaluation of the optimal control of a gantry crane," in *Proceedings of the 7th Biennial Conference on Engineering Systems Design and Analysis - 2004*, vol. 1, (Manchester, United Kingdom), pp. 869 – 878, 2004. 2.2

[91] Xue, X., Yang, S. X., and Meng, M. Q.-H., "Remote sensing and teleoperation of a mobile robot via the internet," in *Proceedings of 2005 International Conference on Information Acquisition*, (Hong Kong, China), pp. 537 – 542, 2005. 8.1

INDEX